Department of Electronic & Electrical engineering
UNIVERSITY COLLEGE LONDON

PULSED LASER DEPOSITION GROWTH OF BISMUTH OXIDE SUPERCONDUCTORS

AMIR SAJJADI

A thesis submitted to the University of London in fulfilment for the degree of Doctor of Philosophy.

Dedicated to the living memory of my parents

Abstract

The discovery of high temperature superconductivity in cuprate systems such as YBaCuO, Bi-Sr-Ca-Cu-O, and Tl-Ba-Ca-Cu-O has led to an unprecedented explosion in research in the field because of their potential for technological application. The prospect of integrating these materials in electronic devices depends on the ability to grow good quality thin films. One of the methods of film fabrication increasingly in use is pulsed laser deposition (PLD) technique. This thesis reports on the growth and properties of the $Bi_2Sr_2Ca_{n-1}Cu_nO_{4+2n+\delta}$ system (n=1, 2) thin films by PLD.

In order to deposit high temperature superconducting films uniformly over a large area a new deposition geometry is suggested. The geometry involves tilting the target by an angle θ away from its normal horizontal position. A detailed modelling with supporting experimental results of the new geometry is presented. The method is shown to produce homogenous films over an area of several square centimetre. It is also shown that the film uniformity and thickness is dependent on the angle of tilt, θ, and the substrate-target distance, a.

Ex-situ and in-situ thin film growth of the 2212 phase of the Bi-Sr-Ca-Cu-O system by PLD on MgO substrates is demonstrated. For ex-situ process, the growth parameters such as annealing temperature and duration are optimised. It is shown that the annealing temperature is crucial in obtaining a highly c-axis 2212 film. Also, the superconducting properties of the films are shown to be determined by the annealing period. With in-situ processing it is shown that phase control of BiPbSrCaCuO films is possible by varying the substrate temperature and oxygen pressure.

Superconducting thin films of the Pb-doped Bi-Sr-Ca-Cu-O system (2223 phase) on MgO substrates by PLD are demonstrated. In the initial programme of thin film growth of the 2223 phase, BiPbSrCaCuO films were deposited from a single (BiPb)SrCaCuO target. It is shown, however, that this approach is not effective in obtaining a high proportion of the 2223 phase (> 50%). This is found to be due to the evaporation of Pb at an early annealing stages from the film. To overcome this problem an approach of depositing multilayers of PbO between several layers of BiPbSrCaCuO is utilised. Using the multilayered (BiPb)SrCaCuO/PbO technique Pb could in sufficient quantity be doped in the BiSrCaCuO films to facilitate the growth of the 2223 phase. It is demonstrated that

with the multilayered method, superconducting $Bi_2Sr_2Ca_2Cu_3O_{10+\delta}$ films containing more than 85% 2223 phase could be grown by annealing at 854°C for 15 hours in air.

The effect of target composition on the thin film growth of the 2223 phase is also investigated. It is shown that an excess Ca and Cu over the stoichiometric composition is effective in promoting the formation of the 2223 phase significantly, however, excess Cu is found to also favour the formation of the $(Sr_{14-x,}Ca_x)Cu_{24}O_{41-y}$ phase. In this study it is also demonstrated that the growth of the 2223 phase depends strongly on the annealing temperature and duration and that the temperature range in which the 2223 phase is produced, in the multilayered BiPbSrCaCuO/PbO films, preferentially is exceedingly narrow. The optimum annealing temperature and duration for the formation of the 2223 phase with the multilayered technique is found to be 854°C (±1°C) for 15 hours in air. The effect of $Ar:O_2$ annealing of the multilayered films on the formation of the 2223 phase is also investigated. It is shown that $Ar:O_2$ annealing lowers the melting point of the BiPbSrCaCuO films considerably.

The critical current density of the 2223 BiPbSrCaCuO films is found to be dependent on the proportion of the $(Sr,Ca)_{14}Cu_{24}O_{41}$ phase in the films. It is shown that the presence of the $(Sr,Ca)_{14}Cu_{24}O_{41}$ phase lowers the critical current value of the film considerably. Critical current density values as high as $3.7x10^3$ and $1.0x10^4$ A/cm^2, in zero field at 70K were obtained for the 2223 BiPbSrCaCuO films.

The successful patterning of 2212 and 2223 films by wet etching process for device application is demonstrated. The design and development of a superconducting microstrip filter for space applications using the 2223 films is attempted. Although the device does not fully show the filter characteristic, the measured response is very similar in shape to the simulated response, though no sharp band-pass response is measured.

Acknowledgements

I would like to thank the Science and Engineering Research Council whose award made the work of this thesis possible.

I would like to convey my gratitude to my supervisor Prof Ian Boyd for his advise, guidance, support and for the valuable discussions we had which greatly contributed towards the success of this project.

Throughout the course of this project I received tremendous support and encouragement from the following people without whom this work would not have been completed.

My gratitude to Dr Francis Saba for his full hearted encouragement and for his assistance in carrying out X-ray diffraction measurements, Energy Dispersive analysis, scanning electron microscope, and target preparation can not be adequately expressed. I am grateful to Dr David Caplin for allowing me access to the resistivity equipment and organising assistance in critical current measurements which was carried out by Mr Gary Perkins, Mr Michael Cuthbert, and Dr Leslie Cohen. Equally I am grateful to Prof John Gallop for Microwave measurements at the National Physics Laboratory, Teddington, Dr Steve Best for IR measurements of department of Chemistry, UCL, and Prof Collin Gough for the magnetic measurements which were carried out at his laboratory at Birmingham University.

Most of the X-ray diffraction measurements were carried out at the chemistry department of Imperial College. Its members of staff were most accommodating in giving me unlimited access to the diffractrometer. In addition Mr Martin Vickers of department of Crystallography, Birkbeck College, and Dr Ian Wood of department of Geology, UCL, carried out numerous X-ray diffraction measurements on my behalf. For all their efforts I am grateful. My thanks to Mr Kevin Reeves, Institute of Archeology, UCL, for the use of electron-Probe Micro-Analysis.

The supporting team at the department, Mrs Mavis Small, Mrs Maureen Goldstein, Mrs Manju Karia and the workshop team at the department, Mr Morris Gillett, Allen Gorrod, Terevor Hamer, Allen Drury, and Jim van Sickle deserve special thanks for being extremely helpful.

Many thanks to my friends and colleagues at the department for their support and encouragement. I am grateful to Dr Glenn Tyrrell, Dr Frank Beech, Dr John Merkel, and Dr David Lacey for their kind efforts in proof-reading my thesis and their invaluable comments and suggestions.

Above all, I would like to thank my wife Nicoline and my daughter Minou whose love, unfailing support and understanding were a perpetual source of encouragement. I can never thank them sufficiently.

Contents

Chapter 2 Thin Film Growth and Deposition

Chapter 3 Pulsed Laser Deposition

Chapter 4 High Temperature Superconductors $Bi_2Sr_2Ca_{n-1}Cu_nO_{4+2n+\delta}$ System

Chapter 5 Experimental

Chapter 6 Uniform Large Area Deposition by PLD

Chapter 7 Thin Film Growth of $(BiPb)_2Sr_2CaCu_2O_x$ High T_c Superconductor

Chapter 8 Thin Film Growth of $(BiPb)_2Sr_2Ca_2Cu_3O_{10+\delta}$ High T_c Superconductor

Chapter 9 Critical Current Measurements of The $(BiPb)_2Sr_2Ca_2Cu_3O_x$ Films

Chapter 10 Patterning & Application of Superconducting BiPbSrCaCuO (2212, 2223) Films

Chapter 11 Conclusions and Future Work Suggestions

Chapter 1

Introduction

The discovery of high temperature superconductivity by Bednorz and Muller in 1986 revitalized superconductivity research and technology [1]. Since then, numerous copper oxide based compounds such as $YBa_2Cu_3O_{6.5+\delta}$ and $Bi_2Sr_2Ca_{n-1}Cu_nO_{4n+2+\delta}$ systems have been developed with increasing chemical complexity and higher critical temperatures. The current critical temperature record is being held by $HgBa_2Ca_2Cu_3O_{8+\delta}$ (Hg1223) compound, a copper based material with T_c of 134K [2].

The high critical temperature and large critical current density associated with some of these materials have not only attracted the attention of the scientific community but also activated the interest of the technological sectors. The possibility of using superconductors in electronic devices, such as SQUIDs and microwave filters, require the fabrication of these materials in the form of thin films. However, due to the multicomponent, anisotropic, and reactive nature of these materials, the growth of devise quality thin films has encountered a new set of challenges. Among the thin film deposition techniques Pulsed laser deposition (PLD) technique has overcome many of the challenges involved in depositing thin films of high temperature superconductors (HTS). The success of this technique has partly been attributed to the ease with which stoichiometric films could be deposited in a high-pressure oxygen ambient and controlled deposition rate.

The $Bi_2Sr_2Ca_{n-1}Cu_nO_{4n+2+\delta}$ system is possibly the most complex system among the high temperature superconductors. This system comprises three superconducting phases with critical temperatures, T_c, of 20K, 80K, and 110K. The 2223, has especially attracted the attention of the scientific community for its high T_c (110K). In this research programme growth and properties of high temperature superconducting thin films of the $Bi_2Sr_2Ca_{n-1}Cu_nO_{4+2n+\delta}$ system deposited with pulsed laser deposition (PLD) technique have been investigated. Research efforts were concentrated on the thin film growth of the 2212 phase and in particular the 2223 phase of this system. The application of the wet chemical etchant *Ethylene-diamine-tetra-acetic acid (EDTA)* in water in patterning of the 2212 and 2223 BiPbSrCaCuO films is also investigated. The design and development of a band-pass microstrip filter using the 2223 films is attempted and its performance discussed.

The layout of this thesis is as follow:

The growth of thin films in terms of different steps involved such as arrival of atoms, nucleation, clustering of the nuclei and the formation of a continuous film is briefly described in chapter two. The basic modes of growth i.e. layer growth, island growth, and a combination of the two, are outlined. the concept of crystallinity and orientation is briefly discussed. Finally, thin film deposition methods except pulsed laser deposition (PLD) are briefly described.

Chapter three deals with PLD as a thin film growth technique. The advantages and disadvantages of this technique are outlined. A description of the stages involved during ablation, namely, laser-target interaction, plasma formation and expansion and their effect on film growth is given in several sections. This is then followed by a section on the problem of particulates.

Chapter four is an introduction to high temperature superconductors in particular the BiSrCaCuO system. Among the topics covered are the crystal structure of the various phases in this system as well as the effects of Pb and oxygen in the growth of the 2223 phase. The topic of modulation in this system is briefly described. In this chapter thin film growth mechanism of HTS is briefly discussed. The general requirements for the fabrication of good quality HTS thin films are out-lined. This is followed by the choice of substrates for HTS. Finally, a brief discussion is presented on the different growth techniques used for thin film fabrication of HTS in relation to the general requirements.

Chapter five is devoted to the experimental set-up and the characterisation techniques of the films grown in this research programme.

In chapter six uniform film deposition over a large area using PLD is discussed. The uniform film deposition is achieved by simply tilting the target from its normal position. A mathematical model of a new geometry for uniform deposition over large areas is developed. It is shown that the film thickness d, is a function of θ, the angle of tilt and a, the distance between the substrate and the target.

In chapter seven in-situ and ex-situ thin film growth of $(BiPb)_2Sr_2CaCu_2O_x$ by PLD on MgO substrates are discussed. For ex-situ process, the growth parameters such as annealing temperature and duration, and for ex-situ process, oxygen pressure and substrate temperature, are optimised. With ex-situ process the annealing temperature is shown to be crucial for obtaining a highly c-axis 2212 film. Also, the superconducting properties of the films is shown to be determined by the annealing period. With in-situ process it is shown that phase control of BiPbSrCaCuO films is possible by varying the substrate temperature and oxygen pressure. The oxygen partial pressure-substrate temperature phase diagram for BiPbSrCaCuO films indicates that in order to obtain a pure c-axis 2212 BiPbSrCaCuO films both substrate temperature and oxygen pressure should be optimised.

Thin film growth of the 2223 phase on MgO substrates by means of ex-situ annealing is described in chapter eight. The partial substitution of Bi by Pb has shown to enhance the formation of the 2223 phase. In the initial programme of thin film growth of the 2223 phase, BiPbSrCaCuO films are deposited on MgO substrates from a single (BiPb)SrCaCuO target. It is shown, however, that this approach is not effective in obtaining a high proportion of the 2223 phase (> 50%) due to rapid evaporation of Pb from the film's surface during the early annealing stages. To overcome this problem an approach of depositing multilayers of PbO between several layers of BiPbSrCaCuO is utilised. Using the multilayered (BiPb)SrCaCuO/PbO technique Pb could in sufficient quantity be doped in the BiSrCaCuO films to facilitate the growth of the 2223 phase. This technique is found to be very effective in producing highly c-axis oriented 2223 thin films. The effect of parameters such as the deposition and post-annealing conditions in the growth of the 2223 films has been systematically investigated

In chapter nine the critical current measurements of the 2223 films are presented. The critical current density of BiPbSrCaCuO films is shown to be influenced by the different proportion of 2223/2212 or 2223/(SrCa)CuO phases present in the films.

Finally, the successful patterning of 2212 and 2223 films by wet chemical etching process is described in chapter nine. Also, the design and development of a superconducting microstrip filter for space applications using the 2223 films is attempted.

References

1- J. G. Bednorz, and.K. A. Muller. Z. Phys. B64, (1986), 189.
2- A. Schiling, M. Cautoni, J. D. Guo, and H. R. Ott. Nature. 363, (1993), 56.

Chapter 2

Thin Film Growth and Deposition

2.1 Introduction

Before proceeding with a discussion on thin film growth techniques it is necessary to briefly discuss the growth of thin films in general. In this chapter some fundamental issues such as nucleation and growth process together with modes of growth, crystallinity and orientation are briefly discussed. Thin film deposition methods except pulsed laser deposition (PLD) are briefly described.

2.2 Nucleation and film growth process

Thin films are usually grown by some sort of vacuum deposition or vapour reaction process. Since with these techniques film formation is accomplished from the vapour phase the steps involved with this process are briefly discussed in this section. A detailed discussion can be found in a number of excellent text books written on this subject of which references [1, 2] are two examples. Upon impingement of vapour atoms or molecules on the substrate, the vapour molecules can **i)** adsorb and stick permanently to the substrate or **ii)** adsorb and re-evaporate in a finite time or **iii)** immediately bounce off the substrate. The likelihood of conditions **(i, ii)** occurring as compared to condition **(iii)** is very high as the incident vapour immediately equilibrates thermally with the substrate, except for very light atoms with high incident energy which are expected to bounce off from the substrate surface. Assuming that the impinging atoms or molecules are adsorbed on the substrate, condensation is then initiated by the formation of small clusters through the combination of several adsorbed atoms. These clusters are called nuclei, and the process of cluster formation is referred to as nucleation. The nucleation rate J ($cm^{-2}s^{-1}$) depends on the arrival rate of atoms R and the activation energies of desorption ΔG_{des} and surface diffusion ΔG_{sd} [1].

$$J \alpha R (\sqrt{\Delta G^*}) \exp \{(\Delta G_{des}-\Delta G_{sd}-\Delta G^*)/K_BT\} \qquad (2.1)$$

where K_B is the Boltzman constant, and ΔG^* is the activation energy associated with formation of the critical nucleus radius r^*. The critical radius r^* is proportional to the surface energy, σ, over the difference in Gibbs free energy between the solid and the vapour phase, ΔG_V. In a simple capillary model of nucleation the activation energy ΔG^* is proportional to $\sigma^3/(\Delta G_V)^2$. ΔG_V is given by $(K_BT/V) \ln R/R_e$, where V is the volume of one molecule of the film material and ratio R/R_e is the supersaturation ratio[1]. The supersaturation ratio is the impinging rate of the vapour over the re-evaporation rate of the film material at the substrate. This indicates that at low substrate temperatures the nucleation rate is higher and the nuclei are smaller than at high temperatures where the nucleation rate is lower but the nuclei are larger [1]. The temperatures mentioned here are relative and the actual values depend on the material and growth conditions. The atomic process in the nucleation of 3-D clusters of deposited film atoms on a substrate is shown schematically in figure 2.1.

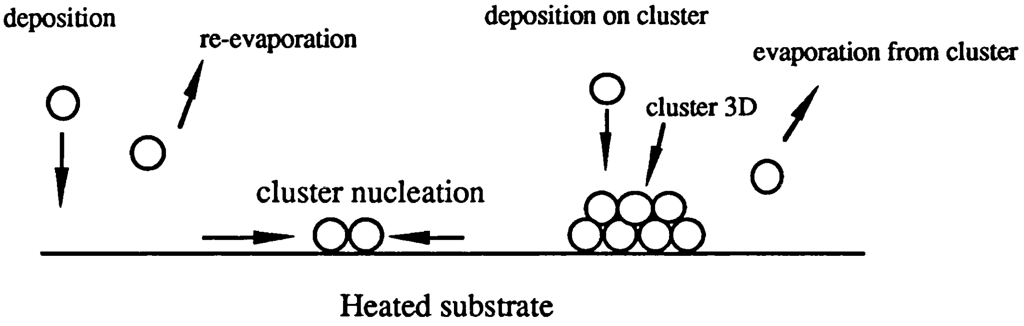

Figure 2.1- *Schematic diagram of nucleation and cluster formation of deposited film atoms on a substrate surface.*

In general the sequence of the nucleation and growth can be described as follows. In the initial stage the nuclei of fairly uniform size are formed. Growth of the nuclei is three dimensional, but the growth parallel to the substrate is greater than normal to it. This is probably because growth largely occurs by the surface diffusion of monomers on the substrate, rather than by direct impingement from the vapour phase. This is then followed by a coalescence of the nuclei and the formation of composite islands. The coalescence is characterised by a decrease in total projected area of the nuclei on the substrate and an increase in the nuclei heights. The formation of the islands result in the enlargement of the uncovered areas of the substrate and the formation of secondary nuclei between the islands by the impinging atoms and molecules. As the islands grow, large shape changes occur. However, these are confined mainly to the regions in the immediate vicinity of the junction of the islands. Consequently, the islands become elongated and join to form a continuous network structure in which the deposit material is separated by long, irregular, and narrow channels. As deposition continues secondary nucleation occurs in these channels. This process continuous until the final hole-free film is formed.

During the initial stages of film growth, islands are still quite small in size. As soon as they become large enough and meet, grain boundaries or lattice defects will be incorporated into the film, unless the islands coalesce to form a single crystal. The lattice defects can also grow in polycrstalline films as grains grow together. The most frequently occurring defects in evaporated films are dislocations. Dislocations can occur **i**) when two islands coalesce whose lattices are slightly rotated relative to one another, **ii**)when the substrate and the film have different lattice parameter, there will be a displacement misfit between islands, **iii**) near the edges of the holes during the earlier stages of film growth where stresses present, **iv**) when islands containing stacking faults bounded by the surface of the island coalesce.

2.2.1 Modes of nucleation and growth

The theories of the single crystal thin film growth propose three major modes of thin film formation which depend on the interactions between the atoms of the vapour and the substrates. These are **i**) layer by layer growth (also known as Frank van der Merwe), **ii**) Island-like growth (also known as Volmer Weber) and **iii**) a growth mechanism in which the film grows layer by layer in the initial stages and becomes island-like thereafter (also known as Stranski Krastanov) [2]. The growth mechanisms are illustrated in figure 2.2.

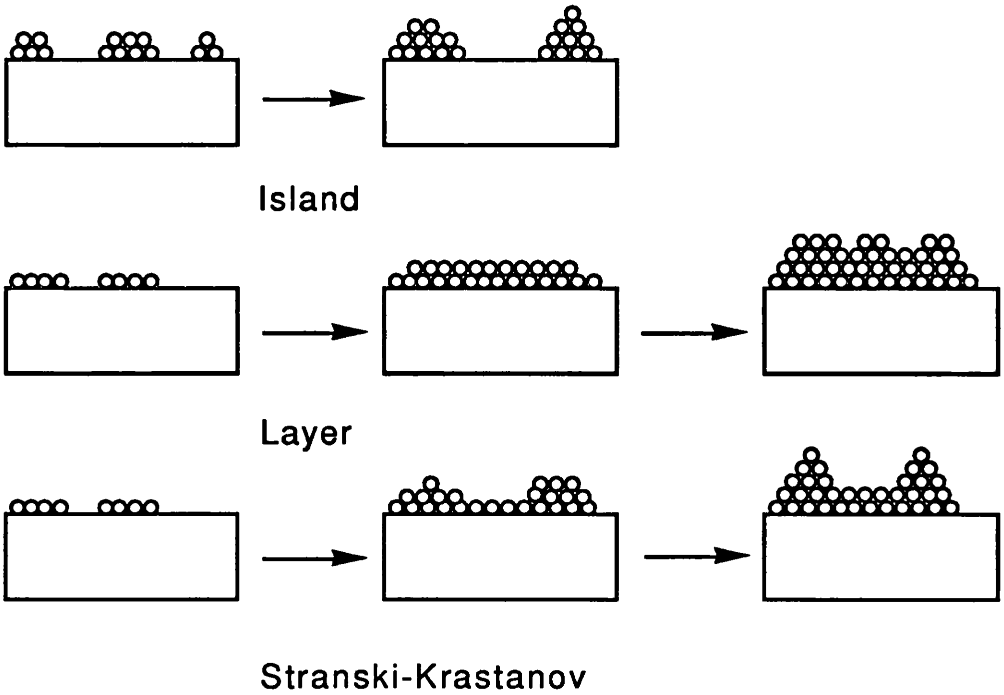

Figure 2.2- *Illustration of the three types of film growth mechanism [2].*

i) In the layer by layer growth the extension of the smallest nucleus occurs in two dimensions resulting in the formation of planar sheets. The atoms or the molecules in this case are more strongly bound to the substrate. For this type of growth to occur a good lattice match between the growing film and the substrate is required. **ii)** In the island growth the smallest stable clusters nucleate on the substrate and grow in three dimensions. This occurs when atoms or molecules bound strongly to each other than the substrate. An example of this type growth is found in many systems of metals. **iii)** In the Stranski Krastanov or intermediate combination of layered and island growth a transition from two to three dimensional growth takes place. After the formation of one or two monolayer the subsequent layer growth becomes unfavourable and islands form. This type of growth is believed to happen when there is a mismatch between the film and the substrate [1]. This type of growth is common and has been observed in the growth of semiconducting films.

The layer by layer or island growth modes could also be distinguished in terms of surface tension γ. The surface tension γ can also be interpreted as a force per unit length of boundary. The force equilibrium at a point where substrate and a 3D island of the deposited film meet requires

$$\gamma_S = \gamma_{S/F} + \gamma_F \cos\phi \qquad (2.2)$$

where γ_S is the surface tension of the substrate/vacuum interface, γ_F that of film/vacuum, $\gamma_{S/F}$ that of the substrate/film interface, and ϕ is the angle between γ_F and $\gamma_{S/F}$. The modes of growth can be distinguished by the angle ϕ [2].

i) for layer by layer growth: $\phi=0, \quad \gamma_S \geq \gamma_{S/F} + \gamma_F$ (2.3)

ii) for island growth: $\phi>0, \quad \gamma_S < \gamma_{S/F} + \gamma_F$ (2.4)

The modes of growth could also be influenced by the ratio between the vapour pressure of the impinging vapour and the vapour pressure of the re-evaporated material at the substrate, known as supersaturation, ξ. Equations 2.3 and 2.4 can be re-written as [2]

for layer by layer growth: $\gamma_S \geq \gamma_{S/F} + \gamma_F - (K_B T_S \ln \xi)/\text{constant}$ (2.5)

for island growth: $\gamma_S < \gamma_{S/F} + \gamma_F - (K_B T_S \ln \xi)/\text{constant}$ (2.6)

A transition from 3-D to 2-D growth is conceivable with increasing supersaturation, or a transition from 2-D to 3-D growth is possible with decreasing T_S.

2.2.2 Crystallinity and orientation of thin films

The deposition conditions (such as deposition rate and substrate temperature) and post-annealing temperatures can determine the crystallinity and orientation of the film. These factors can also influence the size of the grains in the case of crystalline films. Large grain sizes are naturally expected for increasing substrate or annealing temperature. This is because of an increase in the surface mobility which results in the film to decrease its total energy by growing large grains. Low substrate temperatures, on the other hand, lead to the formation of smaller grains [1].

The role of deposition rate on the size of the grains is less obvious, but can be rationalized on the basis that the impinging atoms which might have large surface mobility, could become buried under subsequent layers, at high deposition rates, before much diffusion can take place. In order for this to operate and have significant effect on the grain size a certain minimum rate must be exceeded. Below this threshold rate, grain size is limited by temperature. However, above this threshold the grain size decreases more and more for higher and higher deposition rates. Under ideal conditions the film grown on a single crystal is formed as a single crystal. This is known as epitaxy [1]. Both 2-D layered and 3-D island growth can result in epitaxial growth. In the layered growth, epitaxial growth with small misfit between the film and the substrate is possible up to a certain thickness, known as the critical thickness. Above this thickness the strain energy increases to such an extent that dislocations are introduced in order to reduce this energy. In the island growth, the islands not only spread on the surface of the substrate but also rotate in order to reach an epitaxial position with respect to the substrate.

2.3 Thin film growth techniques

In this section the main thin film growth techniques used for deposition and growth of HTS, except pulsed laser deposition, are described. Pulsed laser deposition technique is fully discussed in chapter 4. The main deposition techniques could be divided into two categories: **a**) Physical vapour deposition and **b**) Chemical vapour deposition. Physical vapour deposition can be divided into **i**) sputtering deposition, **ii**) thermal and electron beam evaporation **iii**) molecular beam epitaxy, and **iv**) pulsed laser deposition. Chemical vapour deposition can be divided into **i**) me talo-organic and **ii**) plasma assisted chemical vapour deposition. In the following sections a brief description of each technique including advantages and disadvantages is presented. Detailed discussion on the various deposition techniques can be found in a number of excellent books written on this subject of which reference [1] is one example.

2.3.1 Sputtering

Sputtering process is basically removal of material from the target surface by collision of high energy ions. The sputtering processes are divided into four categories: dc, rf, magnetron and reactive [1]. RF and dc sputtering systems are basically similar. The target in both systems is negatively biased (known as cathode) and the substrate (anode) which faces the target may be ground, positive or negatively biased. After the system has been evacuated, a gas, which could be Ar or a mixture of $Ar:0_2$, is introduced into the system to serve as a medium in which the discharge is initiated and sustained. Gas pressures usually range from a few to 100mtorr. Once a visible glow is maintained between the electrodes, a current flows and film condenses on the substrate. The film deposition is as a result of collision of positive ions in the discharge with the cathode plate (target) which causes ejection of neutral atoms and ions from the target surface through momentum transfer. These atoms and ions pass through the discharge region to eventually deposit on the substrate.

In the dc sputtering process the film deposition rate is proportional to the power or square of the current density and inversely proportional on the electrode spacing [1]. Highly resistive materials such as quartz (10^6 Ω-cm), however, can not be dc sputtered because the voltage required for the process could exceed 10^{12} volts. However, these materials can be sputtered by rf sputtering process. This is due to two properties of rf sputtering system operated above 50Hz. Firstly, electrons oscillating in the glow region may acquire enough energy to cause ionization collisions and sustain the discharge. Secondly, rf voltages can be coupled through any kind of impedance which means the electrodes need not be conductors. In rf sputtering system the target is capacitively coupled to the rf generator. This is to prevent the sputtering from both electrodes when ac electricity is applied.

Magnetron sputtering is the most widely commercially practised form of sputtering method. The systems success is its high deposition rate (up to 1μm/min for Al [1]) which is an order of magnitude higher than the conventional sputtering techniques. In this process both magnetic and electric fields are used. The electrons in the dual field environment experience the well-known Lorentz force in addition to the electric field force. In this system electrons ideally do not reach the anode but are trapped near the target enhancing the ionization efficiency. This is achieved by applying a magnetic field parallel to the target and perpendicular to the electric field.

2.3.2 Thermal & electron-beam evaporation

With thermal or resistive evaporation technique the energy for vaporization of the material is supplied by resistance or induction heating [1]. In thermal evaporation the source is either a filament or a resistive boat with a high melting point and low vapour pressures. The most commonly used filaments and resistive boats are tungsten and molybdenum. For evaporation to take place, the evaporant must wet the filament and be held by its surface tension. Resistively heated evaporation has the disadvantage of causing a possible contamination of the evaporated material from the crucible or heater.

With electron beam evaporation a stream of electrons is accelerate through fields of typically 5 to 10KV and focused onto the evaporant surface. Upon impingement, most of the kinetic particle energy is converted into heat. Since the energy is imported by charge particles, it can be concentrated on the evaporating surface while other portions of the evaporant are maintained at lower temperatures. Hence, interactions between evaporant and support material are greatly reduced. Therefore, this method of evaporation has become the most widely used vacuum evaporation technique for deposition of pure films [1].

2.3.3 Molecular beam epitaxy (MBE)

MBE technique essentially involves highly controlled evaporation in an ultrahigh-vacuum system ($\approx 10^{-10}$ torr). This technique is widely used for the growth of epitaxial semiconducting films. This is because the clean environment and the slow growth rate as well as independent control of the beam sources enables the precise fabrication of the film. Using this technique deposition of single monolayer to a micron thick film is possible. In general the growth rates of MBE are quite low (typically 36Å/min for materials such as GaAs.). Similar to the evaporation technique, for the growth of copper oxide superconductors, it implies the use of separate beam sources for each constituent element. The use of separate sources enables the desired layer by layer growth of these materials, which is a promising technique for making artificial structures.

2.3.4 Chemical vapour deposition

Chemical vapour deposition (CVD) process is reaction of a volatile compound to be deposited on a substrate with other gases to produce a non volatile solid. Most CVD systems employ a deposition chamber in which a mixture of gases are introduced from evaporation sources located out side the chamber. The evaporants decompose and interact on the substrate surface in the deposition chamber to form the film To increase the deposition rate and film thickness uniformity the deposition is usually carried out at low pressures, typically 1mbar. In a "hot-walled" reactor, the walls of the reactor are hot and heat is transmitted to the substrates. As a result the substrate temperature is lower than the the walls. In a"cold-walled" reactor the substrates are heated directly by resistive or rf inductive heating.

The major advantage of this technique is large area uniform film deposition. The main means of controlling the composition is by adjusting the rate of evaporation of the precursor into a constant stream of an oxygen rich carrier gas which then passes over the heated substrates in a separate chamber [1]. Metallo-organic CVD is the most widely used technique especially in the case of deposition of superconducting materials. The use of this method for laboratory research is not very widespread yet, but this technique is probably the most promising technique for commercial production work, because of its high throughput and its ability to coat complex shapes. Other advantages include relatively low cost of the equipment and operating expenses.

2.4 Summary

The processes involved in nucleation and growth of thin films were described briefly. It was explained that depending on whether the atoms or molecules bound strongly to each other or to the substrate, layered or island growth is obtained. Furthermore, under certain conditions a combination of both types of growth occur. The general requirements for thin film of HTS and the supporting substrates were out-lined and briefly discussed. Finally, a number of popular thin film deposition techniques in relation to HTS were described.

References

1- L. I. Maissel, and R. Glang. “Handbook of Thin Film Technology” Mcgraw-Hill publication, (1970).

2- M. Ohring. “The Materials Science of Thin Films”. Academic Press (1992).

Chapter 3

Pulsed Laser Deposition

3.1 Introduction

PLD is one of the main thin film growth techniques increasingly being used now a days for the growth of high temperature superconductor (HTS) such as BiSrCaCuO [1-3]. With this technique pulsed radiation is used to vaporize materials and to deposit thin films in a vacuum chamber. Although PLD, experimentally, is probably one of the simplest techniques among all film growth methods, however, the science involved in this process, especially the laser beam-solid interaction that leads to evaporation and ablation is very complex. In this chapter the central processes involved in the pulsed laser deposition (PLD) technique in particular, the ablation process that concerns laser target interaction, the formation of an ablation plasma, and plasma expansion are discussed.

3.2 Pulsed laser deposition technique

A simple experimental set-up used in this project is shown in figure 5.1 of chapter 5. The vacuum chamber basically consist of a target and a substrate. The target is normally a metal or a compressed pellet. The target is normally rotated to minimize the ablation and deposition of non-stoichiometric material formed around the edges during the ablation process. The laser beam is directed into the chamber and focused on to the target via suitable optical components. The chamber is usually kept under vacuum to provide a large mean free path of the evaporated material. PLD can also be accomplished in a reactive atmosphere such as O_2.

Both continuous wave (CW) and pulsed lasers can be used to remove material from an irradiated target. PLD in comparison with other thin film growth techniques such as evaporation, sputtering, chemical vapour deposition (CVD) and molecular beam epitaxy (MBE), has several advantages and disadvantages. Its most important advantage is i) the near stoichiometric transfer of the target materials to the substrate [1]. Other main advantages include:

ii) the ability to grow films at high oxygen pressures >10mbar.

iii) high growth rate, 1-145Ås^{-1} [4].

iv) versatility (from the stand point of its application to rather diverse processing conditions such as, variation of wavelength (1064-193nm), vacuum, and processing techniques including etching and patterning).

v) the use of multiple target sources which can be evaporated simultaneously by splitting and focusing the laser beam onto separate sources or by exposing individual targets to the laser beam sequentially.

vi) the ease of moving a focused beam on the target surface can also be used to improve film thickness uniformity over a large area and finally.

vii) dispensing the need for a crucible to hold the source materials.

The last advantage has two implications: Firstly, impurities from the crucible will be minimised; and secondly, highly reactive materials such as rare-earth metals can be evaporated without reacting with the crucible at high temperatures.

The main disadvantages of this technique are:
i) non uniform deposition over areas larger than 2cm. In chapter 6 of this thesis it is shown, that the uniformity of film thickness is directly proportional to the target-substrate distance. A large target-substrate distance results in a more uniform film. However, this is achieved at the expense of a lower deposition rate. The film uniformity can also be effected by other parameters such as laser spot size and deposition atmosphere.

ii) the change in the local stoichiometry of the material over the entire area of the substrate. This is associated with the composition of the plume which may have some angular dependence [5].

iii) presence of droplets on the film surface.

iv) degradation of the optical components in particular the laser viewport.

3.3 The ablation process

Although the exact mechanisms involved in PLD is not yet fully understood there are a number of models that provide a clear insight into the ablation process [6-8]. In this section a simple descriptive picture of this process is presented.

Laser ablation can be divided into three stages: (**i**) laser-target interaction (absorption, thermal conduction, and surface melting), (**ii**) laser interaction with the evaporated material leading to the formation of high-temperature expanding plasma, and (**iii**) anisotropic three-dimensional expansion of the laser-generated plasma giving rise to the characteristic forward-direct nature of the deposition [8]. Figure 3.1 illustrates schematic representation of the three separate regimes outlined above.

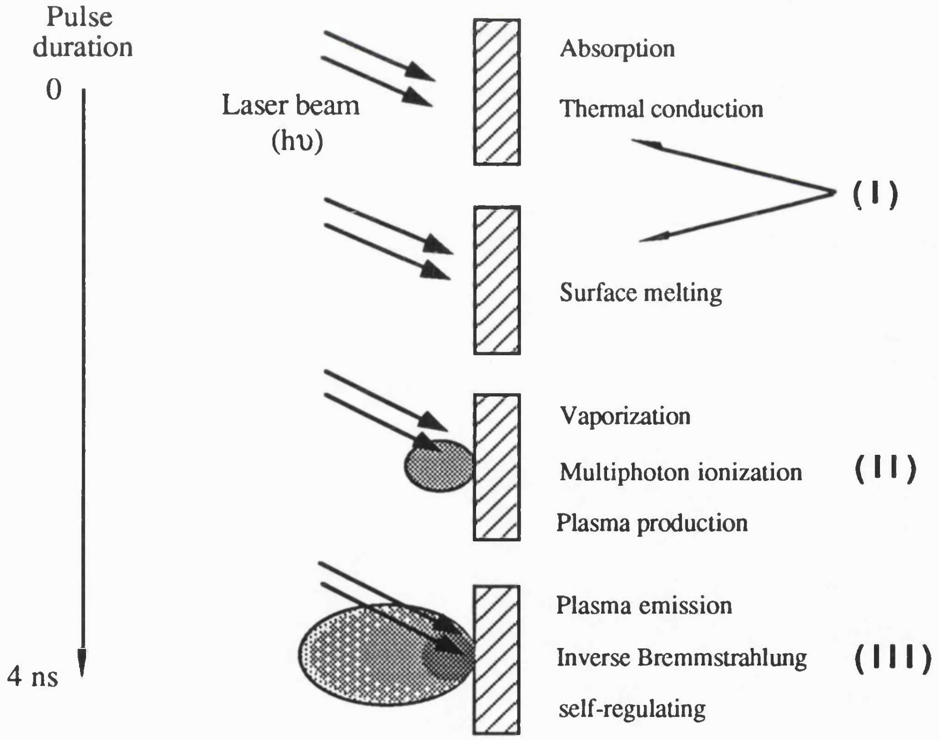

Figure 3.1- *Schematic representation of the laser target interactions, after S. R Foltyn et al. [9].*

3.3.1 Laser-target interaction (regime I)

The nature of laser-target interaction is predominantly determined by the target material and the characteristics of the incident laser beam such as its energy density, wavelength, and in the case of pulsed lasers, the pulse duration. Since in this project we discuss thin film growth of BiPbSrCaCuO material by PLD technique it is appropriate to consider the interaction of laser with high temperature superconductors.

For deposition of thin superconducting films, in general, a superconducting pellet, also known as a superconducting target is used. The targets are usually made from compressed oxide powders. The subsequent heat treatment process (annealing at >800°C) determines the varying degree of porosity and surface roughness of the pellets. This leads to a high coupling coefficient of the laser beam with the material. High temperature superconducting materials such as YBaCuO (123) or BiSrCaCuO are metallic and contain a high carrier concentration ($\approx 10^{21}/\mathrm{cm}^3$) at room temperature [8]. They also provide a low reflectivity to laser radiation ($R \approx 0.1$) [10, 9].

3.3.2 Target surface temperature

Short-pulse high energy lasers ($E > 10^7 \mathrm{W\ cm}^{-2}$) such as Q switched Nd-YAG lasers and excimer lasers provide a flux of high energy photons which upon interaction with the target material causes a sudden rise in the surface temperature, through photon absorption process, which can exceed its melting temperature (melting temperature,T_m, for BiSrCaCuO $\approx$1140°C [11]). The increase in the surface temperature depends on the target thermal and optical properties such as the absorption coefficient α_t, the thermal conductivity K, the specific heat C_v, the density ρ, and the reflectivity R as well as the laser energy density ϕ and the beam pulse duration τ. The approximate thickness of the material heated by the laser pulse is given by $(D\tau)^{1/2}$, where D is the thermal diffusivity and τ is the pulse duration of the laser.

By assuming that the optical and thermodynamic constants are independent of temperature and that the laser spot is homogeneous, the attainable maximum temperature and the heating rate can be estimated for two extreme cases, $(D\tau)^{1/2} \gg \alpha^{-1}$ and $(D\tau)^{1/2} \ll \alpha^{-1}$. In the case of $(D\tau)^{1/2} \gg \alpha^{-1}$, the energy absorbed during the laser pulse τ is $(1-R)\ \phi\tau$ which is used to heat a layer of thickness $(D\tau)^{1/2}$. The average temperature rise in this layer is given by [7],

$$\Delta T = \frac{(1-R)\,\phi\,\tau}{C_v\,\rho\,(D\tau)^{1/2}} \qquad (3.1)$$

In this case, the the laser intensity required to achieve a particular temperature is proportional to square root of pulse duration or pulse width.

In the case of $(D\tau)^{1/2} << \alpha^{-1}$, where the optical absorption depth α^{-1} is larger than thermal diffusion length, the temperature is dependent on the initial position of photons in the solid than the subsequent heat diffusion. The light absorption creates an exponential temperature profile along the depth z. In this case, the maximum temperature is proportional on pulse duration.

$$\Delta T\,(z) = \frac{(1-R)\,\alpha\,\phi\,\tau\,e^{-\alpha z}}{C_v\,\rho} \qquad (3.2)$$

3.3.3 The threshold energy

The black appearance of the HTS materials provide a high optical absorption coefficient $\alpha_t \geq 10^5$ cm^{-1}[11] and a low absorption depth, α^{-1}, ≈500Å for YBaCuO at 248nm [10]. Therefore Q-switched lasers such as Nd-YAG operating in the range of 266-1064nm and excimers (XeCl at 308nm, KrF at 248nm and ArF at 193nm) can deposit enough energy in a thin layer of material near the target surface for laser evaporation to take place. The high target absorption coefficient α_t plus the high coupling coefficient (1-R) of the target with the laser beam combined with the low thermal diffusivity result in a low vaporization threshold of these materials. This threshold represents the minimum energy required to heat the material to its evaporation temperature. This indicates that the threshold fluence, ϕ_{th}, is equal to the sum of melting fluence, ϕ_m, and the evaporating fluence, ϕ_e, of the irradiated materials. The threshold fluence is therefore strongly dependent on the wavelength and pulse duration of the laser beam. The dependence of ϕ_{th} on the laser wavelength is due to the variation in absorption coefficient of the material with wavelength. Assuming a total conversion of laser energy into heat energy on the target the values of ϕ_m, and ϕ_e can be given by [12].

$$\phi_m = \frac{\rho_s C_s (T_m - T_r) + L_m}{(1 - R_s)\, \alpha_s} \tag{3.3}$$

$$\phi_e = \frac{\rho_m C_m (T_e - T_m) + L_e}{(1 - R_m)\, \alpha_m} \tag{3.4}$$

where ρ_s is the mass density of solid, C_s is the temperature-averaged specific heat of the solid, T_m-T_r is the temperature increased required to melt the material, and L_m is the latent heat of melting. In equation 3.4 the symbols refer to the melt-to-evaporation phase transition. For YBaCuO at 248nm, this threshold energy has been estimated to be 110mJ/cm^2 [10]

3.3.4 The evaporation rate

By considering the energy absorbed in a thickness of ≈ $(D\tau)^{1/2}$, the amount of material evaporated per pulse can be calculated from energy balance. The energy deposited by the laser beam is equal to the energy needed to vaporize the surface layers plus the conduction losses by the precursor and the absorption losses by the plasma [8]. This can be represented as:

$$(1\text{-}R)\ [E\text{-}(\text{conduction losses} + \text{plasma losses})] = \Delta X_t\ [\rho\ C_p\ \Delta T + \Delta H] \tag{3.5}$$

where, R is the reflectivity, E corresponds to the incident laser energy, and ρ, C_p, ΔT,and ΔH are the mass density, heat capacity, temperature rise, and volume latent heat of the target material, respectively. The term Δx_t corresponds to the thickness of the target material evaporated per pulse. The heat conduction and plasma absorption losses represent the threshold energy, E_{th}, required for evaporation. The above equation can be written as:

$$\Delta x_t = \frac{(1 - R)(E - E_{th})}{(\rho\, C_v\ \Delta T + \Delta H)} \tag{3.6}$$

Since the latent heat of vaporization of the material is much higher than its specific heat content $\Delta H \geq \rho C_p \Delta T$, the above equation reduces to

$$\Delta x_t = \frac{(1-R)(E-E_{th})}{\Delta H} \qquad (3.7)$$

The equation (3.7) shows a linear relationship between evaporated material thickness and laser energy density, if the threshold energy, E_{th}, is assumed to be independent of E. At high laser energy densities (>3J/cm^2 shown later) the evaporated term, due to the change in plasma losses and variations in the reflectivity, may no longer show a linear relationship with the energy density [8].

To experimentally determine the dependence of the evaporated thickness with energy density, a bulk superconducting BiPbSrCaCuO target was irradiated with nanosecond (4ns) Nd-YAG laser pulses at different energy densities, and the evaporated material was collected on silicon substrates held at room temperature. The target-substrate distance was 3 cm. The chamber pressure during the deposition was maintained at 10^{-2} mbar. The laser beam spot size was 3.0mm. The laser energy was varied by inserting optical filters in the path of the laser beam. Since the ejected particles from the target in PLD follows a highly forward-directed distribution profile of the form $\cos^n \theta$ [13] with n=8-11, where θ is the angle between the surface normal and the direction of the ejected particles, therefore 90% of the deposition occurs within an angle of 30°. Thus, the evaporated material thickness measured by talystep (10Å resolution) was limited to that region where the maximum thickness is. Figure 3.2 shows a linear increase in evaporated thickness with an increase in energy density of the laser pulse up to 2.2J/cm^2. Above this energy density the evaporated thickness does not scale linearly with the energy density due to the change in plasma losses and variations in the reflectivity term of equation 3.7.

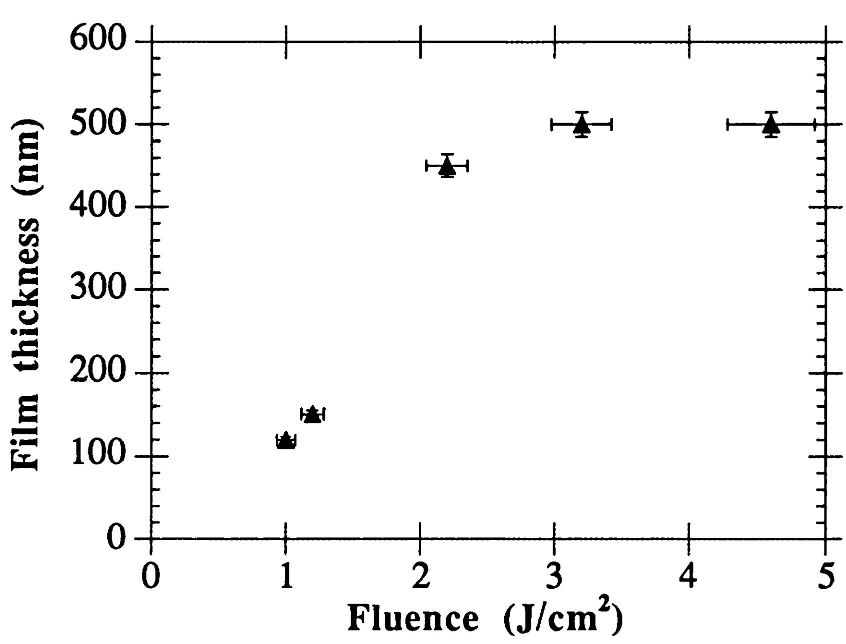

Figure 3.2- *Amount of the evaporated material as a function of pulse energy density. The thickness measurement were confined to the central deposition on the substrate.*

3.3.5 Plasma formation (regime II)

The interaction of high energy ($10^7 Wcm^{-2}$) pulse laser (ns duration) beams with a high temperature superconducting target leads to surface temperatures very much above the melting point of the material. The surface temperature of YBaCuO superconductor during laser-target interaction has been estimated to rise between 2000 and 3200K [14]. The high temperature generated at the target surface results in melting and evaporation of the material. The material is then ejected from the target surface by the vaporization pressure which creates a recoil pressure on the liquid melted layer. Also, the sudden rise in target surface temperature, >2000K, results in thermionic emission of positive ions and electrons as well as neutral atoms and molecules [15, 16]. Photoionization of the evaporated material leads to the formation of an expanding plasma above the target surface [17, 8] in the form a brilliant glow. Within the plasma near the target surface several types of ionization take place. These include impact ionization, photoionization, thermal ionization of photon-activated species [8].

Once the plasma has formed, it acts as a medium for the absorption of the incident laser beam which results in further heating of the plasma [8]. This absorption is said to occur by neutral atoms when the plume contains low densities of electrons and ions. However, when the density of the electrons and ions are high the absorption occurs by Bremmstrahlung process which involves the absorption of a photon by a free electron.

The plasma can be divided into two regions (I, II). Region (I) is the area immediate to the target surface (≈1mm from the target surface). In this region the density of ionized species near the target surface is high due to continuous interaction of the laser beam with the target. This area thus is constantly absorbing the laser radiation during the time interval of the laser pulse. In region (II) the electrons and ions concentration decreases rapidly with time, due to high expansion velocities of the leading plasma edge [8], causing the plasma to become transparent to the laser beam at the outer edge.

3.3.6 Plasma expansion (regime III)

The plasma expansion is thought to be one dimensional (1D), region (I), for a very short time (t <100ns) and 3D, region (II), for a longer time (t >300ns) [18]. Shortly after the formation of the plasma a momentum coupling between the target and the plasma does develop. As time passes the momentum exchange with the target surface decreases, due to the density gradient of the material in the plasma, resulting in the expansion of plasma [18]. The degree of plasma expansion is said to be inversely proportional to the dimension of the laser spot on the target [18]. This indicates that the distribution of the deposited materials can be controlled by varying the laser spot size.

Initially, the pressure gradients are much lower near the inner edge of the plasma compared to its outer edge. During this period more evaporated material is being injected into the inner edge of the plasma, while at the same time the outer edge is rapidly expanding. In this stage the density and the pressure of the plasma decreases exponentially from its inner edge [8].

After the termination of laser pulse the plasma continues to expand even though no more particles are injected into the plasma from the target. During the plasma expansion, the thermal energy is rapidly converted to kinetic energy with the plasma obtaining extremely high expansion velocities (3-10 times the speed of sound). Singh et al. [8] have shown that the plasma expansion in the direction perpendicular to the target is of the order of several mm, whereas in the parallel direction is of the order of 20-100μm [8]. This preferential expansion of plasma has been found to result from anisotropic expansion velocities of the plasma edges arising from the density gradients of the particles in the gaseous plasma [8].

The preferential expansion of plasma (at right angle with respect to target) gives rise to a highly forward peaked distribution $\cos^n\theta$ with $8<n<12$ (when ablating in vacuum), where θ is measured with respect to the target normal [13] of the evaporated material. In addition to this highly forward peaked distribution a $\cos\theta$ distribution of the evaporated material has also been observed [19] which is characteristic of thermal evaporation process. For YBaCuO superconductor, it has been shown that in addition to the angular distribution of the total material ejected from the target, there is also a variation in the composition of the evaporated material as a function of θ [19]. The highly forward peaked distribution has been shown to have the same stoichiometry as the target while the broad distribution ($\cos\theta$) is non-stoichiometric [19]. This indicates that there is always an element of the non-stoichiometric component in PLD of multicomponent materials such as YBaCuO or BiSrCaCuO.

3.4 Laser wavelength

As mentioned earlier the nature of laser-target interaction also depends on the laser wavelength. In order to understand the influence of laser wavelength on the growth of HTS materials it is necessary to consider the absorbance of the material. Figure 3.3 illustrates the absorbance spectra of a BiPbSrCaCuO (2212) film deposited by PLD technique on an MgO substrate and post-annealed for 1 hour at 850°C in air. The spectra shows differences of laser light penetration depth of almost 20% between near visible light of 400nm wavelength and the IR radiation of 1064nm wavelength on a 600nm thick BiSrCaCuO film. W. Kautek et al.[20] have reported a greater laser light absorption (at least two order of magnitude) in the IR region (1064nm) than the UV region (266nm) on YBCO films. These results indicate that the energy threshold for ablation of the material should increase in value with decreasing laser wavelength. Typical values estimated for energy threshold is $70mJcm^{-2}$ for 248nm radiation and $260mJcm^{-2}$ at 1064nm [12].

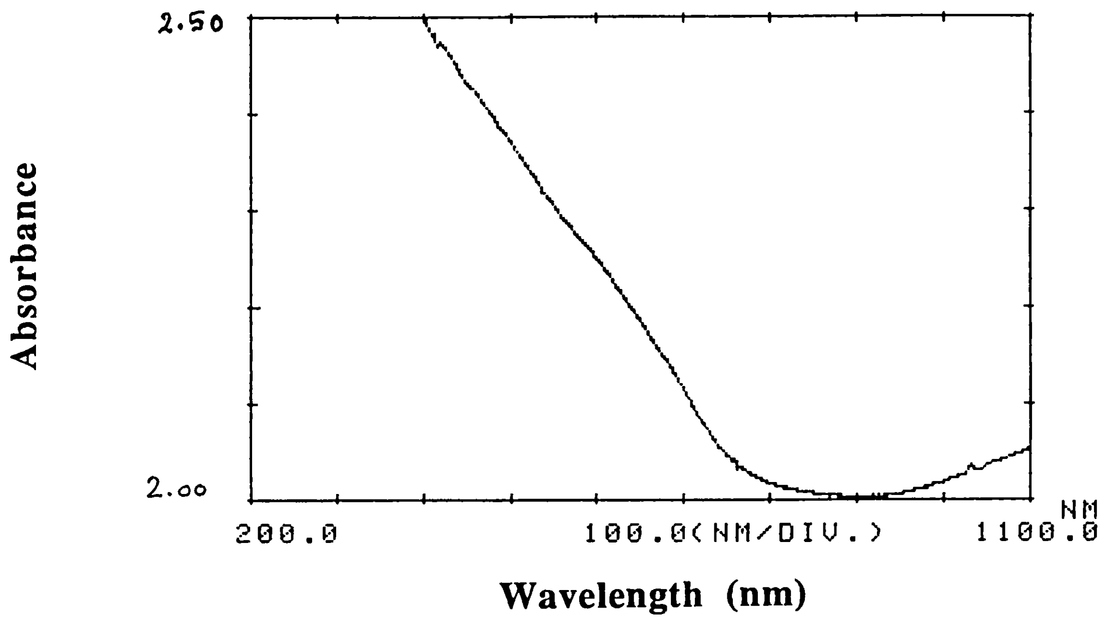

Figure 3.3- *Absorbance spectrum of a 2212 BiPbSrCaCuO film.*

The study done by W. Kautek et al. [20] on the effect of laser wavelength on YBCO targets using a Nd-YAG laser operated in the range of 266-1064nm wavelength reveals an interesting transformation of the target surface as a function of laser wavelength. They report that far-UV light at 266nm led to the formation of groves of the order of microns with smooth top and side faces thought to be resulted from solidification of a thin melt layer on the target surface. Visible light at 533nm, however, resulted in the disappearance of the original grain structures which were still intact after interaction with 266nm and the formation of large cones and extremely deep canyons, 100μm in depth with smooth tops but starting to become structured either by solidified splashes due to material eruption from the valley base, or by light induced boiling. A similar observation in the formation of cones and valleys was observed in laser ablation of a BiPbSrCaCuO (2212) target. Figure 3.4 shows an SEM photograph of a forest of cones of 86μm in depth and large valleys created after 1000 pulses of Nd-YAG laser operated at 532nm.

Figure 3.4- *SEM photograph of a BiPbSrCaCuO (2212) pellet after irradiation with 1000 pulses of 1.6J/cm^2.*

IR radiation of the target on the other hand resulted in a deep spongy structure which may indicate the rapid melting and vigorous boiling followed by rapid solidification of the surface. Comparing the structures obtained for IR radiation with the ones for visible and UV lead to the conclusion that UV and to a lesser extent visible radiation may result in the evaporation of much thinner region than for IR radiation. Also, IR radiation led to the formation of massive splashes on the substrate which were cornered in shape.

3.5 Film deposition

The ejected material in PLD contains two components, $\cos\theta$ and $\cos^n\theta$, to its profile with the latter superimposing the former. Since $\cos\theta$ profile is broader than $\cos^n\theta$ profile, the outer edges of the film are mainly a contribution of the former profile and consequently non-stoichiometric [19]. The presence of these two profiles and hence, non-uniformity of the films, would not be desirable for the application of high temperature superconductors.

A method of homogenizing the profile is to tilt the target with respect to its normal position. This has the effect of producing a uniform film over several centimetre square. However, the drawback of using this method is a substantial reduction in film thickness (i.e., longer deposition time is required). The description of this method including supporting experimental data is presented in chapter six of this thesis.

3.6 Stoichiometric transfer

It is generally agreed that stoichiometric transfer of the ablated species from the target to the substrate is possible under optimised growth conditions. Parameters such as target-substrate distance, deposition atmosphere and laser fluence as well as the collection angle [21-23, 5] could bring about a deviation from stoichiometry. Foote et al.[21], for instance, have shown no significant variation in chemical composition of the laser ablated YBaCuO (123) films, deposited under oxygen (O_2) partial pressure of 200mtorr with target-substrate distance of 5.5-6cm, with variation in laser fluence from 0.5 to 2.9J/cm^2. They, however, observed a substantial variation in chemical composition of YBaCuO films with target-substrate distance, even when depositing under O_2 partial pressure. Stoichiometric transfer of the elements were only observered when a balance between the O_2 partial pressure and target-substrate distance had been strick.

Others such as R. K. Singh et al. [8] have suggested that the compositional variation from multicomponent targets can occur during three separate phases of laser deposition. **i)** compositional deviation due to off-stoichiometric evaporation from the bulk target, **ii)** due to different sticking coefficients of the evaporating species, a factor that is not so important for deposition below 400°C substrate temperature, **iii)** spatial compositional variation due to different expansion velocities of the respective species.

3.7 Particulates

The presence of droplets on the deposited film surface is probably the major disadvantage of the PLD technique. The formation of the droplets is mainly attributed the laser-target interaction [24, 25]. Parameters such as laser fluence [26], laser wavelength [26, 27], target density [28] have shown to effect the formation of the droplets. Some of common ideas put forward include, **i)** superheating of the subsurface layer of the target surface by the laser beam which results in an explosive ablation **ii)** and the presence of trapped bubbles underneath the target surface.

Among the techniques used to reduce the droplet density the following are very popular and frequently utilized in PLD. The use of **i)** freshly polished target [29-31], **ii)** low laser wavelength (e.g UV lasers) [28], **iii)** velocity filters [32], **iv)** high density targets [28], two colliding laser beams [33,34]. None of these techniques, however, is known to eliminate the droplets totally.

E. van de Riet et al. [35] have shown, using a metal target, that the number of droplets can be reduced significantly by using higher laser fluences (6J/cm^2). However, at high laser fluence the target material could not be transferred congruently (ie, the original characteristic of the material may not be preserved). For congruent transfer of materials laser fluence of 3.2 J/cm^2 was found to be necessary. This indicates that the fluence required for a minimal droplet emission does not necessarily coincide with the fluence required for congruent transfer.

A. Zherikhin et al [36] have reported the presence of two types of droplets in their in-situ excimer (248nm) laser ablated YBaCuO films. Type (I) (>1μm) were reported to be dependent on the laser fluence only. To reduce the density of these droplets low laser fluence in the range of 2-3J/cm^2 is suggested [36]. The origin and nature of type (II) (<1μm) droplets are not fully clear. However, their presence is thought to be related to the anisotropy of crystalline growth of the superconducting YBaCuO (YBCO) material and the deposition parameters such as O_2 partial pressure and substrate temperature. They argue that since the velocity of crystal growth of YBCO in a dimension is larger than in the c dimension and since a-axis crystals could easily be present in a largely c-axis YBCO film, then the presence of these a -axis crystals could be seen as droplets when observed under SEM. Substrate temperatures above 770°C and low O_2 partial pressure e.g <10^{-2} torr reduced their density considerably [36].

3.8 Summary

In this chapter the advantages and disadvantages associated with the film growth by the PLD technique have been outlined. The ablation process in terms of the laser-target interaction and the formation of the laser plume and its expansion was discussed. Also a number of factors relating to the formation and prevention of the droplets on the film surface during the deposition process were outlined.

References

1- D. Dijkkamp, T. Venkatesan, X. D. Wu, A. Shaheen, N. Jisrawi, Y. H. Min-Lee, W. L. Mclean, and M. Croft, Appl. Phys. Lett. 51, (1987), 619.

2- K. Moorjani, J.Bohandy, F. J. adrian, B. F. Kim, R. D. Shull, C. K. Chiang, L. J. Swartzendruber, and L. H. Bennet,. Phys. Rev. B 36, (1987), 4036.

3- H. Tabata, T. Kawai, M. Kanai, O. Murata, S. Kawai. Jpn. J. Appl. Phys. 28(3), (1989), 430.

4- X. D. Wu, R. E. Muenchause,.S. R. Foltyn, R. C. Estler, R. C. Dye, C. Flamme, N. S. Nogar, A. R. Garcia, J. Martin, and J. Tesmer. Appl. Phys. Lett. 56(15), (1990), 14811483.

5- L. Lynds, B. R. Weinberger, D. M. Potrepka, G. G. Peterson, and M. P. Lindsay. Physica C, 159, (1989), 61-69.

6- A. Richter. Thin Solid Films. 188, (1990), 275-292.

7- J. T. Cheung. H. Sankur. CRC Critical Reviews in Solid State and Materials. Sciences. 15, (Issue 1), (1988), 63-108.

8- R. K. Singh, O. W. Holland, and J. Narayan. J. Appl. Phys. 68(1), (1990), 223.

9- S. R. Foltyn, R. E. Muenchausen, R. C. Estler, E. Peterson, W. B. Hutchinson, K. C. Ott, N. S. Nogar, and K. M. Hubbard. in Laser Ablation for Material Synthesis, edited by D. C. Payne and J. C. Bravman (Mater. Res. Soc. Symp. Proc. 191, Pittsburgh, PA, 1990), 205.

10- A. Inam, X. d. Wu, T. venkatesan, S. B. Ogale, C. C. Chang, and D. Dijjkanp. Appl. Phys. Lett.51, (1987), 1112.

11- S. de Unamuno and E. Fogarassy. Materials. Scie & Eng, B13, (1992), 29-33.

12- F. Beech, and I. W. Boyd in “Photochemical Processing of Electronic Materials”, edited by I. W. Boyd and R. B. Jackman (Academic Press, New York, 1991), 387-432.

13- R. A. Neifield, S. Gunapala, C. Liang, S. A. Ahaheen, M. Croft, J. Price, D. Simons, and W. T. Hill. Appl, Phys. lett. 53, (1988), 703.

14- T. Terashima, K. Iijima, K Yamamoto, Y. Bando, and H. Mazaki. Jpn. J. Appl. Phys. 27, (1988), 191.

15- R. K. Singh, and J. Narayan. Mater. Sci. Eng. B 3, (1989), 217.

16- T. P. Hughes. Plasma and laser light (Wiley, New York, 1975).

17- Zel’dovich and Raizer. Physics of Shock Waves and High Temperature Phenomena (Academic, New York, 1966).

18- J. C. Kools, T. S. Baller, S. T. De Zwart, and J. Dieleman. J. Appl. Phys. 71, (1992), 4547-4556.

19- T. Venkatesan, X. D. Wu, A. Inam, and J. B. Wachtman. Appl. Phys. Lett. 52, (1988), 1193-1195.

20- W. Kautek. Thin Solid Film. 191, (1990), 317-334.

21- M. C. Foote, B. B. Jones, B. D. Hunt, J. B. Barner, R. P. Vasquez, and L. J. Bajuk. Physica C, 201, (1992), 176-182.

22- D. B. Geohegan, D. N. Mashburn, R. J. Culbertson, S. J. Pennmcook, J. D. Budai, R. E. Valiga, B. C. Sales, D. H. Lowndes, L. A. Boatner, E. Sonder, D. Eres, D. K. Christren, and W. H. Christie. J. Matter. Res. 3, (1988), 1169.

23- S. Becker, and H. J. Dietze. Physica C, 167, (1990), 509-514.

24- V. S. Ban, D. A. Kramer. J. Mater. Sci. 5, (1970), 978.

25- K. Singh, D. Bhattacharya, and J. Narayan, Mrs 201, (1991), 322.

26- G. Koran, A. Gupta, R. J. Baserman, M. I. Lutyche, and R. B. Laibowitz. Appl. Phys. Lett. 55, (1989), 2450.

27- W. Kautek, B. Roas, and L. Schultz. J. Less-common Metals. 164-165, (1990), 292.

28- C. Scarfone, M. G. Norton, C. B. Carter, J. Li, and J. W. Mayer, MRS Symp. Proc. 191, (1991), 183.

29- D. S. Misra, and S. B. Palmer. Physica C. 176, (1991), 43.

30- J. F. Lawler, T. P. O'Brien, J. G. Lunney, and J. M. D. Coey. High T_C Superconductor Thin Films. edited by L. Correra. (Elsevier Science, B. V. Amsterdam, 1992), P. 475.

31- T. P. O'Brien, J. F. Lawler, J. G. Lunney, and W. J. Blau. Mater. Sci. Eng. B13, (1992), 9.

32- W. P. Barr. J. Phys. E2, (1969), 1024.

33- G. Koren, R. J. Baseman, A. Gupta, M. I. Lutwyche, and R. B. Laibowitz. Appl. Phys. Lett. 56, (1990), 2144.

34- H. Chiba, K. Murakami, O. Eryu, K. Shihoyama, T. Mochizuki, and K. Masuda, Jpn. J. Appl. Phys, (1991).

35- E. Van de Riet, C. J. C. M. Nillesen, and J. Dieleman. J. Appl. Phys. 74(3), (1993), 2008-2012.

36- A. Zherikhin, V. Bagratashvili, V. Burimar, E. Sobol, G. Shubini, and A. Sviridov. Physica C V198, (1992), 341.

Chapter 4

High Temperature Superconductors $Bi_2Sr_2Ca_{n-1}Cu_nO_{4+2n+\delta}$ System

4.1 Introduction

The phenomenon of superconductivity, the disappearance of the d.c electrical resistivity of certain metals and ceramics at low temperatures is probably one of the most unusual phenomena in solid-state physics. Superconductivity was discovered in 1911 by Kamerlingh Onnes [1]. He found that the resistance of mercury dropped to zero when cooled to the temperatures of liquid He. Over the years the highest critical temperature (T_c) has gradually increased from 4K for Hg to 23K for the compound Nb_3Ge.

In 1986 J. G. Bednorz and K, A. Muller [2] reported superconductivity in lanthanum barium copper oxide at temperatures as high as 30K. Since their initial work the search for new high temperature superconductors (HTS) has proceeded by substitution of chemical elements with similar properties into the original material. In 1987 lanthanum in the LaBaCuO was replaced by Yttrium to form a superconductor whose critical temperature was 90K [3]. Following this discovery, two families of compounds were found with even higher transition temperatures. These were $Bi_2Sr_2Ca_{n-1}Cu_nO_{4n+2}$, $Tl_2Ba_2Ca_{n-1}Cu_nO_{4n+2}$, with T_c of 110K and 125K respectively. Recently T_c up to 134K has been reported for $HgBa_2Ca_2Cu_3O_{8+\delta}$ (Hg1223) [4]. In the first section of this chapter some of the properties of superconductors including copper based HTS are described. This is then followed by a brief description of the BiSrCaCuO system in particular the 2201, 2212, and the 2223 phases. Finally the modulation in this system is briefly discussed. In the second section thin film growth of HTS are discussed and the general requirements are out-lined. This is followed by a discussion on the different deposition techniques used for the growth of HTS thin films. A detailed discusion of the properties of the superconducting materials is beyond this thesis. Interested readers are refered to excellent text books on this subject among which the followings were consulted(1, 2, 3).

4.2 Properties of superconductors

Probably the most outstanding property of a superconductor is the complete disappearance of the electrical resistivity at some critical temperature. The second fundamental property of a superconductor is that its normal resistance may be restored if a magnetic field greater than a critical value, B_C, is applied to the specimen. The third fundamental property is the Meissner effect. This is demonstrated by cooling a specimen which is initially in a constant magnetic field through the transition temperature for superconductivity. At this point the magnetic flux originally present is ejected from the superconductor.

Superconductors may be divided into two types (I, II) depending on the way in which they differ in transition from the superconducting state to the normal state when the applied magnetic field exceeds the critical magnetic field H_C. Type (I) superconductors are pure elements and are referred to as ideal superconductors which obey Silsbee's hypothesis. Non ideal or type (II) superconductors (alloys, oxides and high temperature copper oxide superconductors, HTS) do not obey Silsbee's hypothesis. This hypothesis states that a superconductor los es its zero resistance when, at any point on the surface, the total magnetic field strength, due to transport current and applied magnetic field, exceeds the critical field strength H_C. However if there is no applied magnetic field the only magnetic field will be that generated by any transport current, "self field", so in this case, the critical current will be that current which generates the critical magnetic field strength H_C at the surface of the conductor. The magnetization curve expected for type (I) and (II) are illustrated in figure 4.1(a, b).

1) A. C. Rose-Innes and E. H. Rhoderick, "Introduction to superconductivity", Second edition, Pergammon Press, U.K., (1978). 2) D. R. Tiley and J. Tiley, "Superfluidity and Superconductivity", Third edition, Adam Hilger, (1990). 3) G. Burns, "High-Temperature Superconductivity", Academic Press, USA, (1992).

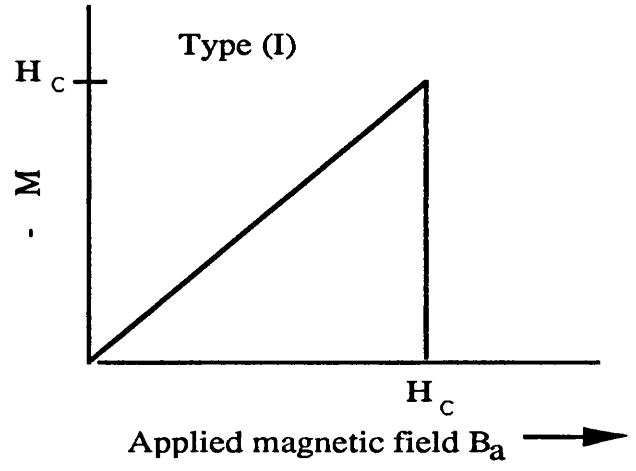

Figure 4.1 (a)- *Magnetization versus applied magnetic field for a type (I) bulk superconductor*

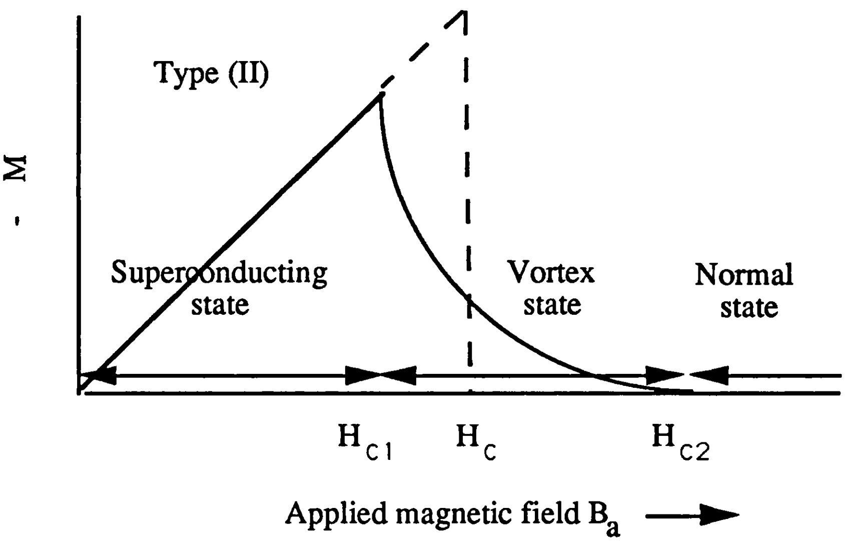

Figure 4.1 (b)- *Magnetization versus applied magnetic field of a type (II) bulk superconductor.*

The magnetization curve for type (I) superconductors exhibit a complete Meissner effect (i.e., perfect diamagnetism) and above the critical field H_c the entire specimen simultaneously becomes a normal conductor. In Type (II) superconductors the flux starts to penetrate the specimen at the lower critical field H_{c1}. At H_{c1} very fine filaments of the material become normal. Between H_{c1} and H_{c2}, the upper critical field, the material is in a mixed or vortex state. In this state the flux density is not zero ($B \neq 0$) and the Meissner effect is said to incomplete. As the applied magnetic field is further increased more normal filaments are produced, each supporting a flux line, and the magnetization or diamagnetic moment decreases. Only when the applied magnetic field reaches H_{c2} does the entire specimen become completely composed of normal filaments and only then the electrical resistance returns.

4.2.1 Penetration depth and the London equation

In the previous section it was mentioned that the perfect diamagnetism of a superconductor prevents electric currents flowing through the body of the material. However, this is not entirely true, because currents can not be confined entirely to the surface of the material. When a superconducting sample is in an applied magnetic field, the screening currents which circulate to cancel the flux inside must flow within a very thin surface layer whose thickness varies for different superconducting metals. Consequently, the flux density does not fall abruptly to zero at the boundary of the material but dies away within this region where the screening currents are flowing. For this reason the depth within which the currents flow is called the penetration depth. To explain this phenomena (penetration depth) and account for the Meissner effect, F. and H. London [5] suggested that the magnetic behaviour of a superconducting metal might be correctly described by modifying the Maxwell equation for a perfect conductor. They postulated that in the superconducting state the current density is proportional to the vector potential A of the local magnetic field with the constant of proportionality being λ_L. Thus

$$\mathbf{j} = \frac{-A}{\mu_0 \lambda_L^2} \tag{4.1}$$

where μ_0 is the permeability of free space. Equation (4.1) is known as the London equation. Using Maxwell equation, curl $\mathbf{B}=\mu_0 j_0$, and taking the curl of both sides it is possible to show that the London equation can lead to the Meissner effect.

$$\text{curl curl } \mathbf{B} = -\nabla^2 \mathbf{B} = \mu_0 \text{ curl } \mathbf{j} \tag{4.2}$$

By combining equations (4.1) and (4.2) we get

$$\nabla^2 \mathbf{B} = \frac{\mathbf{B}}{\lambda_L^{\,2}} \qquad (4.3)$$

where **B** is the applied magnetic field and λ_L is called the London penetration length. The solution to equation (4.3) depends on the boundary conditions. For a semi-infinite superconductor which extends on the positive side of x (i.e., x>0) and B_0 parallel to the surface in the x-direction then the solution has the form of

$$B(x)=B(0)\exp(-x/\lambda_L) \qquad (4.4)$$

The solution shows that **B** falls off exponentially within the superconductor. The London equation confirms the Meissner effect but at the same time it allows surface penetration by the field. The London equation can be regarded as a phenomenological empirical equation which is used to replace Ohm's law in superconductors and account for the Meissner effect.

4.2.2 Critical current density

The early researchers in superconductivity soon discovered that there is an upper limit to the amount of current that can be passed along a piece of superconductor if it is to remain resistanceless. In general, there can be two contributions to the current flowing on the surface of a superconductor. These are screening current J_H and transport current J_I. The total current density **J** is therefore the summation of the screening current and the transport current. According to London equation (equation 4.1) there is a relation between the supercurrent density at any point and the magnetic flux density at that point, and this relation holds whether the supercurrent is a screening current, a transport current or a combination of both. Hence, when a current flows on a superconductor, there will at the surface be a flux density B and a corresponding field strength $H=B/\mu_0$ which is related to the surface current density J_a.

If the total current flowing on a superconductor is sufficiently large, the current density at the surface will reach the critical value J_c and the associated magnetic field strength at the surface will have a value H_c. Conversely, a magnetic field of strength H_c at the surface is always associated with a surface supercurrent density J_c. This leads to Silsbee hypothesis. The maximum amount of transport current which can be passed along a piece of superconductor without resistance appearing is called the critical current of that piece. Clearly the stronger the applied magnetic field the smaller is this critical current. If there is no applied magnetic field the only magnetic field will be that generated by any transport current, so in this case, the critical current will be that current which generates the critical magnetic field strength H_c at the surface of the conductor.

The critical current density J_c in HTS has been moving up impressively from $10A/cm^2$ in 1987 when the first compound was discovered to the values exceeding $10^6A/cm^2$ at 77K in YBaCuO (123) films under the influence of its own fields [6]. The critical current density in YBaCuO is expected to be even higher if the grain boundary weak link and flux creep problems could be resolved. These current limiting factors has also been found in other HTS such as BSCCO and TBCCO [7].

4.2.3 Grain boundary & weak links

The presence of grain boundary weak links or Josephson-coupled weak links at most of the high-angle grain boundaries in HTS is well known [8-10]. This problem manifests itself more in bulk polycrystalline HTS than in thin films. This is due to the random orientation of the crystals in bulk materials. Since the transport current J_c is dominated by the weak link properties of the grain boundaries, the J_c in polycrystalline HTS is low and shows a strong field orientation dependence. The disorientation angle between adjacent grains generally dictate the current capability across the grain boundary [9]. The exact nature of the grain boundary weak link is still not too clearly understood. Some early reports suggest that this is due to the presence of microcracks or some sort of amorphous layers at the grain boundary. However, more detailed reports indicate the existence of cation compositional deviation [11-13] or oxygen deficiency at the grain boundaries [14] as the cause of weak link behaviour.

Several methods have been suggested in order to suppress the weak link behaviour in HTS. These include ozone gas heat treatment in bulk or thin films [14] which forces more oxygen atoms into the grain boundaries and the formation of crystallographic texture [15-17]. The former process has been shown to suppress the weak link behaviour and significantly increased the transport J_c by a factor of 4-10 in YBaCuO material [14]. On the other hand, the latter process with which the desirable texture (i.e., crystallographic alignment of grains parallel to the a-b conduction planes (CuO_2 planes) in HTS), can be introduced through melt texture processing and subsequent directional solidification has been shown to be most successful in overcoming the weak link problem in the bulk YBaCuO (123) superconductor [15, 16].

4.2.4 Flux creep

While the weak link problem in bulk HTS can be overcome by texturing , the high-field J_c could still be limited by the flux creep problem. This is believed to be due to the low density of strong flux pinning centres and the resultant flux motion (flux creep) in bulk materials [18]. Flux creep, is thermally activated flux motion in a magnetic field and is a recognised problem in all high-T_c superconductors [19-21]. This problem can be solved to some extent by enhancing the flux pinning centres through introduction of flux pinning defects in bulk HTS.

Several techniques have been shown to be effective in introducing these field defects and improving the pinning centres. These include irradiation of the material with fast neutrons, protons, ions or electrons [22, 23] and phase decomposition [24]. The irradiation technique depends on the use of a well controlled fluence in order to maximise the flux pinning without degrading the superconducting properties of the material. The phase decomposition technique is based on the dissociation of YBaCuO (124) into the 123 phase. This process is carried out by heating up the 124 material from its stability region below 800°C to above 900°C for a few minutes where 123 stability region is [25].

4.2.5 Theories

The fundamental idea underlying the modern theory of superconductivity is that the electrons pair up with one another due to a special type of attractive interaction. This interaction is indirect and caused by the way a positive ion in the crystal responds to the passage of an electron in its vicinity. The pairing of electrons is the basis of the Bardeen, Cooper, and Schrieffer (BCS) theory which was formulated in 1957 [26]. This theory in its most simple form states that if metallic mobile electrons interact attractively with each other they will condense into a ground state which is separated from the excited states by an energy gap Δ. In their BCS model they predicted that in zero magnetic field the critical temperature is given by

$$K_BT_c=1.13\ h\ \omega_D \exp\left[-1/NV\right] \tag{4.5}$$

where K_B is Boltzmann constant, ω_D is the vibration (Debye) frequency of the lattice, N is the number of available electronic states per unit energy in the solid (density of states at the fermi level), and V is the strength of the attractive (lattice mediated) electron-electron interaction. A similar formula is also predicted for the zero temperature energy gap

$$\Delta=2\ h\ \omega_D \exp\left[-1/NV\right] \tag{4.6}$$

The ratio of these two equation, (4.5, 4.6), gives a fundamental formula independent of the phenomenological parameters

$$\Delta(0) = 1.76\ K_BT_c \tag{4.7}$$

This result appears to hold for a large number of low T_C superconductors to within 10%. However, it fails in lead (Pb) and mercury (Hg) where the discrepancy is closed to 30%. Also, equation (4.5) indicates that the critical temperature T_C can be increased by increasing ω_D, N or V. This means no maximum transition temperature i.e., T_C can be increased by finding solids with larger and larger N, V, and ω_D which could be interpreted as over simplification. A more elaborate and accurate theory based on the BCS theory was developed by Eliashberg and McMillan [27]. This theory could calculate the energy gap Δ and the transition temperature accurately, by numerical methods, from precise experimental information about the lattice vibration.

In the case of HTS (oxides) many theories have been given to account for the high transition temperature they contain. While nearly all theories are based on pairing of the electrons [28-31], the origin of the pairing interaction that produces superconductivity remains an unresolved problem. Also, there is a suggestion that the pairing mechanism that yields high T_c superconductivity manifest itself above T_c [29] which is in contrast with the BCS theory.

4.2.6 The isotope effect

A consequence of lattice interaction is the isotope effect. This effect was demonstrated by Reynolds et al. in 1951 [32]. They showed that for low temperature superconductors like Hg the values of T_c for samples of different isotopes of the same element are roughly proportional to $M^{-1/2}$, where M is the atomic mass. This may be explained in terms of the frequency of the ionic vibration. If the elastic constant is unchanged the ionic frequency for any simple oscillator will be proportional to $M^{-1/2}$. The isotope effect thus demonstrates very convincingly that superconductivity is intimately connected with phonon interactions.

In HTS oxides such as $La_{2-x}Ba_x CuO_4$ the isotope effect is sufficiently large to indicate that the phonons play a major if not the sole role in mediating the effective attractive interactions between electrons [33]. However, in the case of $YBa_2Cu_3O_{6.5+\delta}$ or BiSrCaCuO the isotope effect is very much reduced [33,35]. This suggests that some non-phonon mechanism could be responsible for the high T_c in these materials.

4.3 High temperature superconductors

The discovery of La-Ba-Cu-O [2] with T_c between 30-40K resulted in the synthesis of many new superconducting copper oxide based materials with ever increasing chemical and structural complexity. Until recently, the highest T_c was held by $Tl_2Ba_2Ca_2Cu_3O_{10}$,

[36] a material whose processing requires the stoichiometric control of five elements, each with considerably different chemical characteristics. In 1993 another copper based superconducting oxide Hg-Ba-Ca-Cu-O (HBCCO) was discovered [4] with T_c recently approaching 134K [37].

A part from the obvious alternate arrangement of cations and anions, a common feature in HTS such as $YBa_2Cu_3O_{6.5+x}$, $Bi_2Sr_2Ca_{n-1}Cu_nO_{4n+2}$, $Tl_2Ba_2Ca_{n-1}Cu_nO_{4n+2}$, and $(La, Ba)_2CuO_4$, $(Nd, Ce)_2CuO_4$ is the existence of CuO_2 planes in the centre of their structure [38]. It is widely accepted that in HTS the superconductivity occurs within two-dimensional copper-oxygen arrays based on the joining of CuO_4 squares at their oxygen corners to form infinite CuO_2 planes [38]. Tokura et al. have proposed that the superconducting CuO_2 planes are separated by charge reservoir layers that act to control the charge on the superconducting planes (through chemical doping) either through transfer of holes or electrons [39]. Most copper oxide superconductors can be doped by either changing the oxygen anion content or by changing the metal cation. For instance, $YBa_2Cu_3O_{6.5+\delta}$ is an insulator for $\delta=0$, and becomes superconducting if the oxygen content increases to 7. Similarly, in La_2CuO_4 superconductivity can be introduced by partially substituting lanthanum with barium or strontium to form $(La, Ba)_2CuO_4$ [2]. Another common feature is the close similarity of part of their crystal structure with that of perovskite structure [39], shown in an idealized representation in figure 4.2.

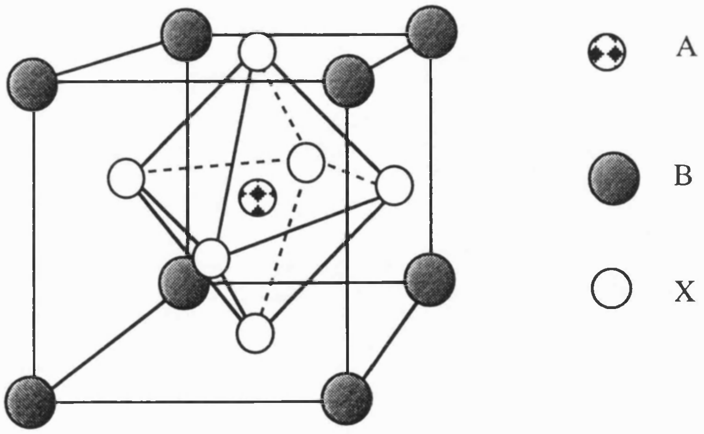

Figure 4.2- *Idealized structure of perovskite* ABX_3.

In this structure the A atoms is at the centre of an AX_6 octahedra which is positioned in the middle of a cubic cell with B atoms occupying each corner. In HTS these octahedra correspond to CuO_6 which are arranged in an square planar configuration.

To date, a number of common physical properties in HTS have been found. For instance, in p-type superconductors (holes are charge carriers) such as BSCCO and YBCO, superconductivity is observed when the nominal charge of Cu in the CuO_2 is +2.1 to +2.3. However, in n-type superconductors (electrons are charge carriers) such as $(NdCe)_2CuO_4$, superconductivity is observed when the nominal charge of Cu in the CuO_2 plane is +1.85 to+1.9 [40]. Also, there is a relation between T_c and the number of CuO_2 planes in materials such as BiSrCaCuO and TlBaCaCuO. In these materials T_c rises as the number of CuO_2 layers increases from single, to double, and reaches a maximum value in triple CuO_2 planes. However, T_c tend to saturate or decrease as the number of CuO_2 planes increases further [40]. Furthermore, the Cu-O distance in copper-based superconductors seem to play an important role. It has been shown that T_c increases with decreasing Cu-O distance for the $La_{2-x}A_xCuO_4$ superconductors [41].

4.3.1 The Y-Ba-Cu-O system

$YBa_2Cu_3O_{6.5+\delta}$ with δ=0.5 is the most well known copper oxide based high temperature superconductor with T_c as high as 92K. The crystal structure of the material can be considered as three stacks of perovskite-like cubes [42]. The yttrium Y and barium Ba atoms are at the centre of the cubes with copper Cu atoms occupying the corners. There are no oxygen atoms at the level of the Y atoms, but the oxygen sites on the Ba and Cu levels are fully occupied. The oxygen that is introduced upon doping enters the crystal structure in the copper plane between two adjoining Ba atoms, forming copper chains. The stacking sequence is hence Y-CuO_2-BaO-CuO-BaO-CuO_2......etc [38]. This means that a square planar CuO_4 chain and a BaO plane are sandwiched between infinite sheets of CuO_5 square pyramids [38]. The oxygen doping depends on temperature and oxygen partial pressure. At high temperatures and ambient pressure the oxygen content is almost 6.0. However, oxygen can be introduced into the material by cooling slowly in an oxygen atmosphere. Also, $YBa_2Cu_3O_{6.5+\delta}$ undergoes a tetragonal to orthorhombic phase transition upon oxygen doping. Two other superconducting phases in Y-Ba-Cu-O system that have been discovered are 248 and $Y_2Ba_4Cu_7O_{15}$ with the latter showing T_c of 80K and the former 40K [43].

4.3.2 The Bi-Sr-Ca-Cu-O system

In this section, the $Bi_2Sr_2Ca_{n-1}Cu_nO_{4n+2+\delta}$ system in term of its phase diagram and the three main superconducting phases namely, the 2201, the 2212, and the 2223 is discussed. Role of Pb in the enhancement of the 2223 phase is briefly described and finally the modulation in this system is briefly discussed.

4.3.3 Bi-Sr-Ca-Cu-O phase diagram

The $Bi_2Sr_2Ca_{n-1}Cu_nO_{4n+2+\delta}$ system is possibly the most complex system among the high temperature superconductors. The composition diagram of this system has been prepared by a number of authors [44-47]. Its phase diagram, shown in figure 4.3, constructed by binary oxides, namely alkaline-earth bismuthates and alkaline-earth cuperates, has been extended into ternary and recently, slightly into quaternary space [47]. The quaternary system Bi_2O_3-SrO-CaO-CuO has been shown to contain twenty one phases which includes a liquid phase when prepared at 850°C in air. This illustrates the complexity of phase formations associated with this system and the enormous task ahead of scientists to complete its phase diagram.

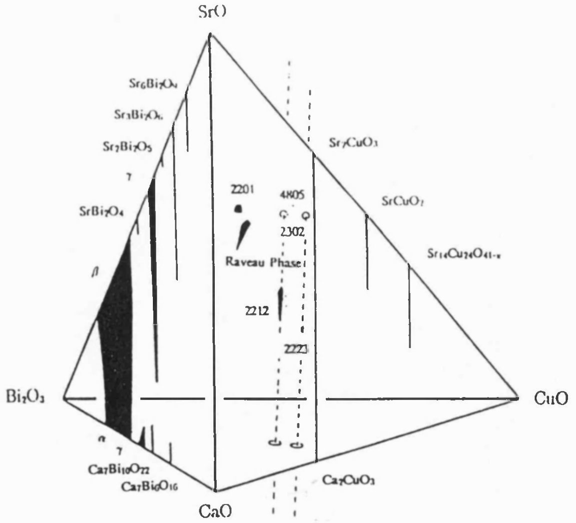

Figure 4.3- *Phases of the Bi-Sr-Ca-Cu-O system at 850℃ in air [47].*

In the high temperature superconducting $Bi_2Sr_2Ca_{n-1}Cu_nO_{4n+2+\delta}$ system the basic structural units are layers of $CaCuO_2$ and the n=1 compound. The combination of one $CaCuO_2$ layer with $Bi_2Sr_2CuO_6$ (n=1) gives $Bi_2Sr_2CaCu_2O_8$ (n=2), two layers of $CaCuO_2$ gives $Bi_2Sr_2Ca_2Cu_3O_{10}$ (n=3), and (n-1) layers gives $Bi_2Sr_2Ca_{n-1}Cu_nO_{4n+2+\delta}$. The $Bi_2Sr_2Ca_{n-1}Cu_nO_{4n+2+\delta}$ system comprises a number of superconducting phases which can be differentiated by the number of CuO layers in the crystal structure. The three main superconducting phases of this system are $Bi_2Sr_2Cu_1O_{6+\delta}$, $Bi_2Sr_2CaCu_2O_{8+\delta}$, and $Bi_2Sr_2Ca_2Cu_3O_{10+\delta}$ [48-50]. These phases are abbreviated as 2201 for n=1, 2212 for n=2, and 2223 for n=3 with superconducting temperature transition of 20K, 80K, and 110K respectively. Recently Kawai et al. [51] have reported on the formation of up to n=6 compounds of this system, however, no further improvement on the superconducting temperature transition, with the increase number of Ca, and CuO layers was detected.

X-ray diffraction studies have indicated that the crystal structure of the $Bi_2Sr_2Ca_{n-1}Cu_nO_{4n+2+\delta}$ system can be understood in terms of double Bi-O layers and perovskite type cuboid which are sandwiched between the Bi-O layers giving stacking sequences parallel to the c-axis of...BiO BiO SrO CuO [Ca,CuO,...] SrO BiO BiO [52]. Since the Ca layers are believed to be free of oxygen the Cu-O bonding in the crystal structure of the different phases differs significantly. For the n=1 phase one finds a single copper-oxygen layer consisting of elongated octahedral sharing corners. In the n=2 phase the octahedral is split into two pyramids each with their bases separated, and in the n=3 phase a square planar CuO_2 layer is inserted between the pyramids.

4.3.4 The 2201 phase

The $Bi_2Sr_2Cu_1O_{6+\delta}$ (n=1) compound is the "simplest" member of the $Bi_2Sr_2Ca_{n-1}Cu_nO_{4n+2+\delta}$ system. It has an incommensurate supercell based on an orthorhombic subcell; the structure has incommensurate components in both b and c directions [53]. The crystal structure of the subcell, shown in figure 4.4, contains single "CuO_2" sheets sandwiched between SrO layers, with Bi_2O_2 bilayers connecting adjacent Sr_2CuO_4 blocks [54-56]. Although its ideal stoichiometry is often given as 2201, it has been found to be either Bi rich or Sr deficient [57, 58]. In the former case the general formula is given by $Bi_{2+x}Sr_{2-x}Cu_1O_{6+\delta}$. The upper x limit is ≈0.4 but the lower x limit is temperature dependent and is in the range of 0.10-0.15 [58]. In the case of Sr deficiency compound the general formula is $Bi_2Sr_{2-x}Cu_1O_{6+\delta}$ with x=0.1-0.5. However, for x<0.1 a semiconducting phase is formed [57]. A second phase, non superconducting, with composition $Bi_{2.18}Sr_{2.14}CuO_{6+\delta}$ has also been reported with a=24.45Å, b=5.412Å, and c=21.97Å [57].

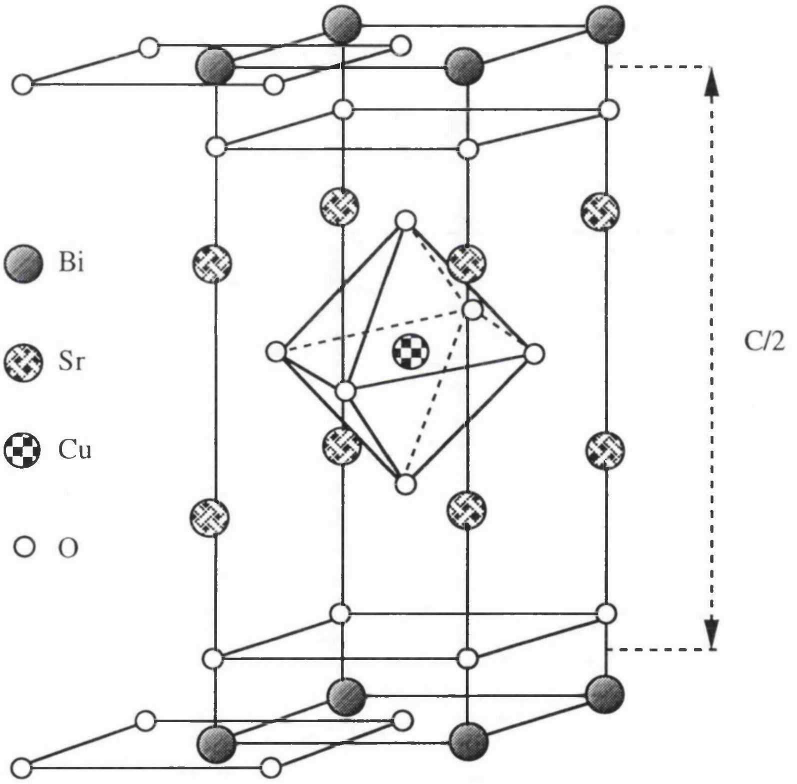

Figure 4.4- *Average crystal structure of the* $Bi_2Sr_2Cu_1O_{6+\delta}(n=1)$ *compound.*

4.3.5 The 2212 phase

The $Bi_2Sr_2CaCu_2O_{8+\delta}$ (n=2) compound is the second member of the $Bi_2Sr_2Ca_{n-1}Cu_2O_{4+2n+\delta}$ system. According to Sunshine et al. study based on single-crystal x-ray diffraction analysis, the crystals of $Bi_2Sr_2CaCu_2O_{8+\delta}$ exhibit an incommensurate superlattice (4.76xb) based on an orthorhombic subcell with dimensions 5.414x5.418x30.89Å [59]. Bordet et al. [60], based on x-ray powder diffraction analysis have reported a tetragonal unit cell with lattice parameters a=5.401(2), b=5.401(2), and c=30.83(2)Å for this phase. This is close to the subcell reported by Beskrovnyi et al. [61] which was based on neutron powder diffraction analysis.

The crystal structure of the subcell, shown in figure 4.5, may be considered as two alternating blocks, the oxygen deficient perovskite block and the rock-salt block. In the centre of the perovskite block there are two conducting CuO_2 planes which are separated by a sheet of Ca atoms. Because of the oxygen deficiency in the perovskite block, calcium is eight fold (cube) coordinated instead of the common dodecahedra coordination of large cations in perovskites. The coordination of copper is square-pyramidal in which, however, the apical oxygen is largely displaced leaving copper effectively in the square-planar bonding. The Sr sites are located at the boundary of both blocks and their surrounding is a mixture of the dodecahedra and octahedral coordinations. It involves nine close oxygen atoms. The Bi cations are in the centre of the rock-salt block and their coordination is octahedral. Such an arrangement would, however, be unstable since it brings four oxygen neighbours within the Bi layer to distance a/2=2.7Å which is out of the region of possible Bi^{3+}-O bonds (2.0-2.5Å). In fact, the Bi coordination is largely distorted and that is the main reason for the appearance of a super structure in this phase with a period of approximately 5a [61].

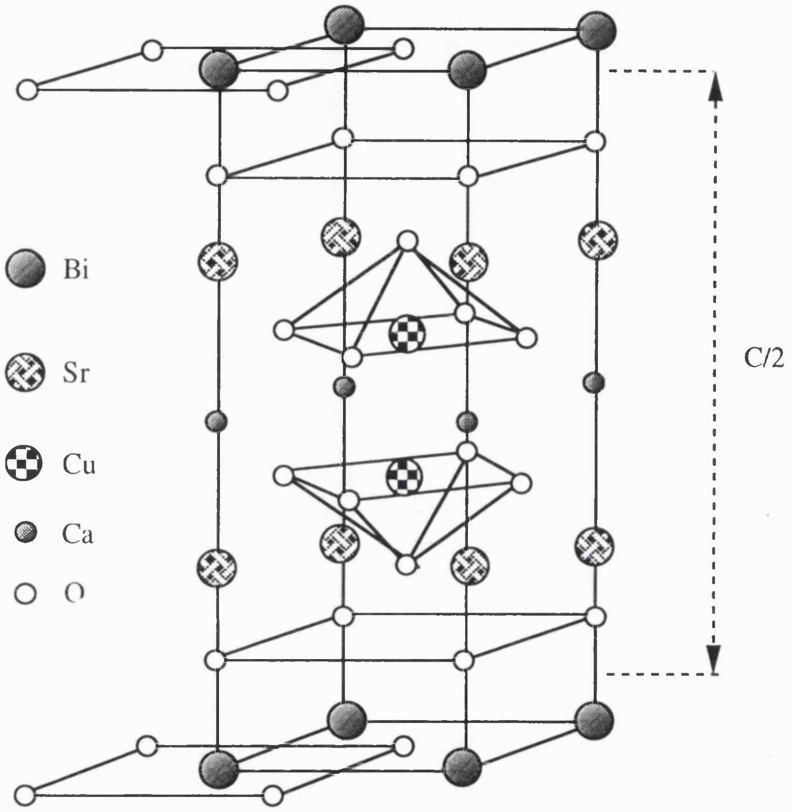

Figure 4.5- *Average crystal structure of the* $Bi_2Sr_2CaCu_2O_{8+\delta}$ *(n=2) compound.*

Several other compositions have been reported, such as $BiSrCaCu_2O_\delta$ (1112) [50], $Bi_4Sr_3Ca_3Cu_4O_{16+\delta}$ (4334) [52], and $Bi_2(SrCa)_3Cu_2O_{8+\delta}$ (2332) [52]. The superconducting temperature transition of these compounds is greater than 95K, however, zero resistance has been reported in the 80K region. The crystal structure of these phases show a tetragonal substructure with a varying between 5.39 and 5.4Å and c between 30.6-30.7Å depending on their compositions.

4.3.6 The 2223 phase

The third family member of the $Bi_2Sr_2Ca_{n-1}Cu_nO_{4n+2+\delta}$ system is the 2223 phase. The broad structural features of the 2223 phase reported in the literature have been evolved from an analogy with the corresponding triple Cu-O layer structure of $Tl_2Ba_2Ca_2Cu_3O_{10+\delta}$ (2223) with T_c of 125K in the Tl-Ba-Ca-Cu-O system [62]. The crystal structure of the 2223 subcell reported by Kijima et al. [63] indicate a tetragonal unit cell with lattice parameters a=5.407(6), b=5.407(6), and c=37.051(7)Å. Miehe et al. [64], on the other hand, based on neutron powder diffraction analysis have reported an orthorhombic sub cell with lattice parameters a=5.4029(3), b=5.4154(2), and c=37.074(2)Å for this phase.

The basic crystal structure of the subcell, shown in figure 4.6, is composed of the rock-salt block and the perovskite block. The rock-salt block is similar to the one in the 2212 phase. However, the perovskite block contains a square planar CuO_2 layer inserted between two square-pyramid copper layers. The square planar CuO_2 layer is separated from the square-pyramid copper layers by one sheet of Ca atoms on either sides. The enlargement in the perovskite block has resulted in an increase in the c-axis dimension of the subcell to c=37Å. Although the central Cu-O plane is perfectly flat, oxygen atoms on the two outer Cu-O planes are displaced slightly to the inner Ca planes in order to maintain the electrical charge balance [63].

The synthesis of the 2223 single phase by the usual solid state reaction technique has been recognized to be difficult. This is due to the existence of the liquid phase, the stacking faults in the crystal lattice [63, 64], formation of impurities such as Ca_2CuO_3, and intergrowths with lower T_c phase, $Bi_2Sr_2CaCu_2O_{8+\delta}$. At present, though several laboratories have effectively worked out the process of obtaining this phase almost isolated in ceramic samples [65] the conditions of preparation of this phase can not be considered as clarified, since highlights of the methods of preparation indicated in the various independent works are often contradictory. For instance, Endo et al. [66] have claimed that the crucial points to obtain a pure 2223 phase are strict control of slight Ca and Cu excess in the starting composition, and a low partial pressure of oxygen in the annealing atmosphere, which should be around 1/13 atom. By contrast, Green et al. [67] have shown that a low partial pressure of oxygen destabilizes the 2223 phase at the benefit of the 2212 phase. On the other hand, Shi et al. [68] have pointed out that the formation of the 2223 phase should result from the calcium and copper diffusion into regions of 2212 phase, and that in order to enhance this diffusion process, strong excess of calcium and copper in the starting composition are necessary. Therefore, one can speculate that the 2223 phase grows at the expense of the 2212 phase together with some impurity phases such as Ca_2CuO_3. However, according to Hatano et al. [69] rather than the starting composition, the principal parameter is the sintering temperature which should be sintered in a range corresponding to the occurrence of partial melting, so that the diffusion of the elements required for the formation of the 2223 phase is favoured.

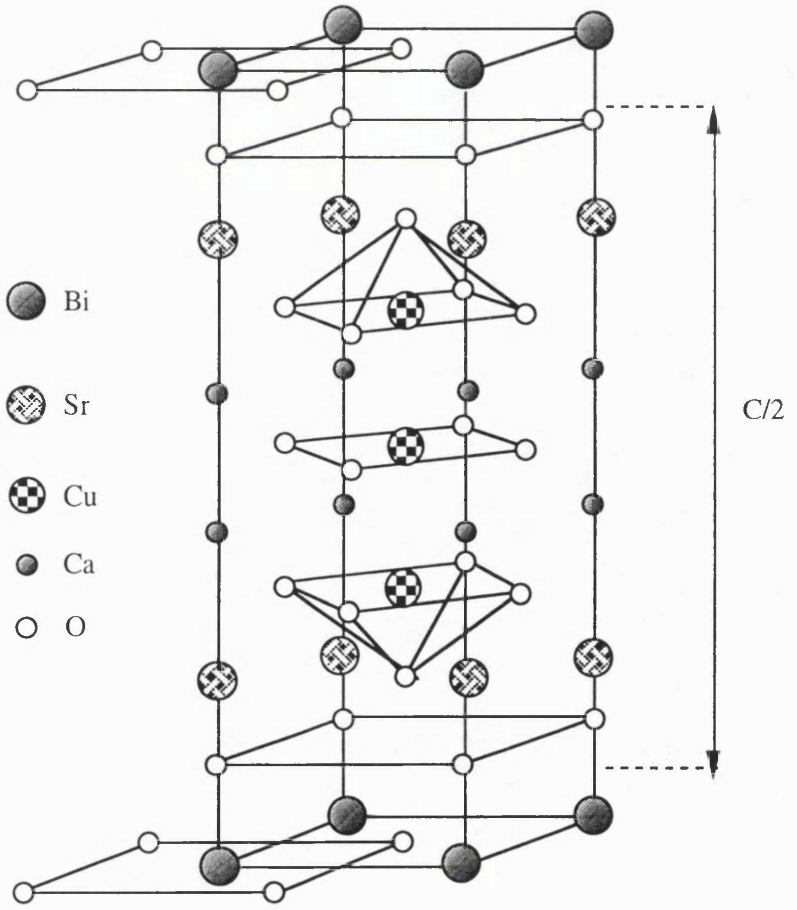

Figure 4.6- *Average crystal structure of the* $Bi_2Sr_2Ca_2Cu_3O_{10+\delta}$ *(n=3) compound.*

In 1988 Takona et al., Sunshine et al., and Ramesh et al. [71, 59, 70] reported that the partial substitution of Pb for Bi in the $Bi_2Sr_2Ca_2Cu_3O_{10+\delta}$ phase reduces the amount of stacking faults, increases the volume fraction, and enhances the crystallisation of the 2223 phase. In 1990 Chen et al. [72] proposed that the formation of the 2223 phase must be via the 2212 phase through a change in composition and structure because the 2212 phase is more thermodynamically and or crystallogrophically stable and the conversion into the 2223 phase only requires inserting Cu-O and Ca into the 2212 phase. They successfully illustrated this by the Ca_2PbO_4-catalysed reaction mechanism. They proposed the following sequence of transformation mechanisms for the formation of the 2212 phase, and the 2223 phase respectively.

$$2Bi_2Sr_2CuO_6 + Ca_2CuO_3 + CuO \longrightarrow 2Bi_2Sr_2CaCu_2O_8 \qquad (1)$$

$$2Bi_2Sr_2CaCu_2O_8 + Ca_2CuO_3 + CuO \xrightarrow{Ca_2PbO_4} 2Bi_2Sr_2Ca_2Cu_3O_{10} \qquad (2)$$

Their results indicated that the interdiffusion of $Bi_2Sr_2CaCu_2O_8$, Ca_2CuO_3, CuO, and Ca_2PbO_4 can lead to the emergence of the 2223 phase. In fact, recently a reverse process mechanism (2) was demonstrated by Dou et al. [73].

4.4 Role of lead in the enhancement of the 2223 phase

It is accepted that lead plays an active part in the growth of the 2223 phase, and that it effectively enters the crystal structure of the superconducting phase by principally substituting the bismuth atoms [74]. X-ray microanalysis of the lead doped 2212 phase reported by O.Eibi has shown that large amount of Pb incorporation into the crystal structure could substitute Sr and Ca sites as well as Bi sites [75]. X-ray diffraction studies on the basic structure of single crystal of the n=3 phase doped with Pb presented by Kijima et al. [76] has also shown substitution of Pb on Bi, Sr, and Ca sites. It is known that Pb substitutes Bi as Pb^{2+} and this substitution modifies the incommensurate superstructure in the BiPbSrCaCuO system [75].

Chen et al. [77] have shown that the growth of the 2223 phase can be illustrated by the Ca_2PbO_4 catalysed reaction mechanism. They concluded that the addition of the Ca_2PbO_4 in the mixture (2) did effectively speed up the growth of the 2223 phase. The catalytic reaction (2) can be explained as follows. The addition of Ca_2PbO_4 produces a lead-rich liquid phase and CaO when the sample is sintered above 822°C. Within the lead-rich phase the rate of interdiffusion among the 2212 phase, $CaCuO_3$ and CuO, can be increased beyond that of solid-state diffusion. The CaO decomposed from Ca_2PbO_4 can further react with CuO to form Ca_2CuO_3 and then accelerate the formation of the 2223 phase. Pb ions incorporated in the liquid phase possibly enhance the diffusion of calcium and copper into the 2212 phase and act as efficient nucleation and growth sites for either the formation or structural stabilization of the 2223 phase [78, 79]. On the other hand, it is possible that the Pb in the mixture lowers the partial melting temperature which could effectively enhance the growth rate of the 2223 phase [80]. Xu et al. [78] discovered a liquid phase with Cu-and Ca-rich composition and the 2212 phase in a Pb-free glass after annealing at 865°C and suggested that the presence of such a liquid phase was essential for the 2223 phase development in partially melted samples.

4.5 Effect of oxygen in the Bi system

The oxygen content of HTS such as $YBa_2Cu_3O_{6.5+\delta}$ plays an important role in its its superconducting properties. It has been illustrated that T_c in YBCO (123) varies from non-superconducting to 92K, depending on the processing parameters (such as annealing temperature and annealing atmosphere) which control the oxygen content [82-84]. For the structurally more complicated $Bi_2Sr_2Ca_{n-1}Cu_nO_{4n+2+\delta}$ system, conflicting results regarding the effect of oxygen content have been reported [85-87].

Unlike the Y-Ba-Cu-O system oxygen content of Bi-based superconductors (i.e., $Bi_2Sr_2Ca_{n-1}Cu_nO_{4n+2+\delta}$ system) has not been well characterised. However, it has become apparent that the effect of oxygen concentration on T_c and the lattice parameters in the $Bi_2Sr_2Ca_{n-1}Cu_nO_{4n+2+\delta}$ system in comparison with YBCO is very much smaller [88]. For the 2212 and the 2223 phases the established view is that T_c increases and decreases, respectively, with decreasing oxygen content (or increasing oxygen deficiency in the CuO_2 planes) [89-93]. A similar observation on reduction in T_c with decreasing oxygen content has also been made in Pb-doped BSCCO 2223 films by H. Hattori et al. [94]. This indicates that the oxygen content of these phases (2212 and 2223) can be regulated by annealing at high temperatures with an subsequent air quenching for 2212 samples and furnace cooling for 2223 samples. H. Hattori et al. [94] have also shown the change in lattice parameter c as a function of oxygen partial pressure from 10^{-5} to $1.5x10^2$ torr for films annealed at 600°C. The pattern shown in figure 4.7 indicates that the behaviour of the c parameter and T_c are not parallel.

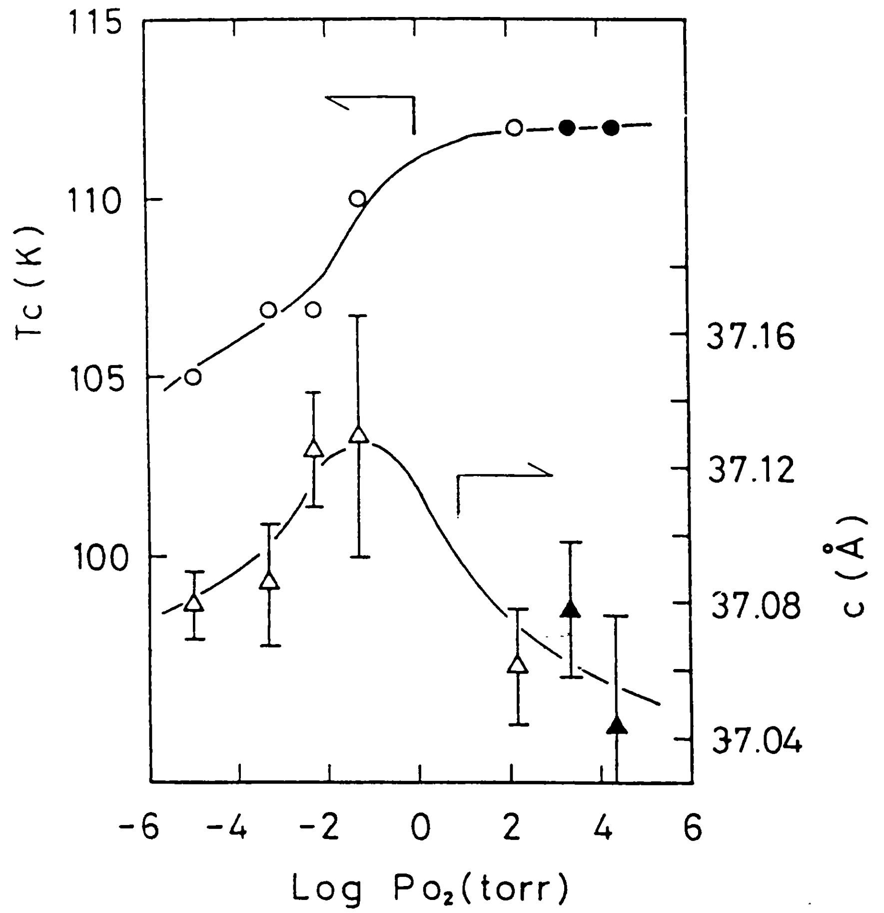

Figure 4.7- *Dependence of $T_{c,\ onset}$ and lattice parameter c on the oxygen partial pressure for films annealed at 400 and 600°C. Figure after H. Hattori et al. [94].*

In $YBa_2Cu_3O_\delta$ the c-axis dimension increases with decreasing oxygen partial pressure. However, the pattern here indicate that c-axis dimension goes through a peak with decreasing oxygen partial pressure and that the relation is not linear. A similar pattern has also been reported for Pb free 2212 phase by S. Miura et al.[95].

4.6 Modulation and superstructure in the BiSrCaCuO system

The topic of modulation in the crystal structure of the BCCO system is beyond the scope of thesis. However, in this section this in briefly discussed in order to highlight the complex crystal structure of this system. For more detailed analysis and description the references mentioned in this section should be consulted.

The crystal structure of the three phases in the $Bi_2Sr_2Ca_{n-1}Cu_nO_{4n+2+\delta}$ system are all modulated. In this system the n=1, 2, and 3 phases have incommensurate superstructures. These phases have been studied by a large number of authors and different models have been proposed. The n=2 phase has been studied most extensively, since it can be easily prepared and has a considerable high T_C. These authors have introduced a unit cell, which is enlarged five times with respect to the average structure parallel to the incommensurate direction of the wave vector of the modulation with lattice parameters a=5.4, b=27, and c=30.8Å [96].

The modulation in the Bi-based compounds has also been observed in the Tl compounds. However, the modulation in the Tl compounds is very weak. A number of groups [97-99] have shown that partial substitution of Bi by Pb leads to the formation of a superstructure which is different from that of the pure Bi compounds. The modulation vector is reported to be 8b. However, no sudden change occurs from the Bi-type to the Pb-type of modulation with increasing Pb content over a considerable region both modulations coexist [98, 100, 101]. Recently Torardi et al. [102] have reported on the lead doped 2201 (n=1) superconductor which contains no superstructure and is free of structural modulations. From single crystal x-ray analysis and results of the band electronic structure calculation, they concluded that the substitution of a lower-valent cation, Pb^{2+}, for the Bi^{3+} in the Bi-O sheets lowers the effective positive charge on the

Bi-O sheets, and consequently allows very little or no extra oxygen to be inserted into the double Bi-O layers so that lead-doped $Bi_2Sr_2CuO_6$ does exhibit structural modulation. Ikeda et al. [103] have also reported on modulation free superconductors in the lead-doped 2201 phase. The free modulation structure is obtained in a narrow range around Pb solubility limit in the $Bi_{2-x+y}Pb_xSr_{2-y}Cu_{1+y/4}O_\delta$ composition. To explain the modulation and the superstructure several models have been prepared, but none have successfully explained the structural data. A few prepared models include

a) an ordering of Bi depleted zones [104]

The superstructure model involving an ordering of Bi depleted and Bi enriched zones was first prepared by Maeda et al. [104] and elaborated in more detail by Matsui et al. [105]. This model was inspired by their very beautiful high resolution electron microscope images in the [010] orientation, which show clearly the modulation of position and intensity in the BiO phases and the tilting of perovskite columns. They suggested that there is either a periodic replacement of Bi by Sr and or Ca atoms accompanied by lattice distortions or that only distortions of the Bi site occur without atom replacement. In particular they simulated images for a model where three Bi atoms in ten are replaced by Sr. However, the proposed replacement of Bi by Sr in their model is not supported by single crystal x-ray diffraction patterns, nor is it in accord with x-ray microanalysis results which indicate that these superconductors may be deficient in Sr and Ca [106]. Also, this model has the correct symmetry in the [010] orientation.

b) an ordering of Sr vacancies [107]

The most serious attempt to explain the modulation has been reported by Gai et al. [108]. They suggested that the modulation is caused by a periodic absence of Sr atoms and the resulting relaxation of the lattice. Cheetham et al. [107] also confirmed that an ordering of Sr atom vacancies could be the cause of the superstructure. This model was based on x-ray microanalysis results which indicated a Sr deficiency in all samples tested. However, this model is not supported by the single crystal x-ray diffraction data, nor it is in agreement with the image contrast seen in high resolution electron microscopy (HREM) images which indicate that modulation is strongest in the BiO layer.

c) additional oxygen in the BiO planes [106, 109]
A detail model involving excess oxygen in the BiO layers was reported by Zandbergen et al. [106]. They justified their model by electron microscope image simulation and with chemical evidence from substitution experiments. They showed for example that Sr^{2+} can be partially replaced by La^{3+} and concluded that this must be accompanied by excess O^{2-} in the lattice for charge compensation. The substitution of 50% Sr^{2+} by La^{3+} led to a decrease in the modulation periodicity from 4.7 to 3.4 times the basic unit cell.

The model proposed by von Schnering et al. [110] for the bismuth compounds with n=1 and n=2 placed oxygen between two nearest Bi neighbour. This model was disputed on the ground that it could not be adopted for the isomorphous thallium compound as the mixed valance state in Bi is valid for Bi^{3+} and Bi^{5+}, whereas Tl^{5+} is not known to exist. However, the model of Bordet et al [111] which displaces the oxygen from the centre of the bismuth square (“rock-salt position”) towards two neighbouring bismuth atoms (“perovskite position”) does not require a high valency. In this case bismuth has three short and three long distant oxygen in its coordination sphere. Berdet et al. [111] model for the superstructure of the Bi-Sr-Ca-Cu-O materials is based on the presumably isomorphous but commensurate $Bi_{10}Sr_{15}Fe_{10}O_{46}$ investigated by Le Page et al [112]. By displacing oxygen further and further away from the “rock-salt position” until it occupies a site between two nearest neighbour bismuth atoms the “bridging position” of Le Page is obtained. This model for the position of extra oxygen is in agreement with the features obtained by electron diffraction [112].

4.7 Thin film growth of HTS

In this section thin film growth mechanism of HTS is briefly discussed. The general requirements for the fabrication of good quality HTS thin films are out-lined. This is followed by the choice of substrates for HTS. Finally, a brief discussion is presented on the different growth techniques used for thin film fabrication of HTS in relation to the general requirements.

4.7.1 Growth methods and mechanism of HTS thin films

Two general growth methods that have developed for the fabrication of thin films of HTS are ex-situ or post-annealed and in-situ growth techniques. With ex-situ growth, the deposited film is subjected to high temperature annealing in the range of 800-900°C to allow for the formation of HTS crystals. The high annealing temperature, however, may result in chemical reaction and interdiffusion of HTS film with the substrate. With in-situ growth technique, the deposited film does not require further post-annealing. In the HTS community, in-situ signifies a process in which the film is completely superconducting before removal from the deposition chamber. With this technique, the growth temperature is lower than in ex-situ, as it relies more on the surface, rather than bulk diffusion process. In the following section a brief discussion is presented on the various thin film deposition techniques used for HTS.

The growth mechanism of HTS films in particular YBaCuO has been investigated by a number of authors recently. It has been shown that it is conceivable to grow YBaCuO material in a layered by layered growth fashion at low temperatures and with low level of oxygen [113-115]. However, in general YBaCuO growth is believed to be via an island growth mechanism [116, 117]. A recent study has shown a consistent pattern in the morphology of YBaCuO films with deviation of composition from stoichiometry. For instance, copper poor films have shown to contain pitted surface and grow by the island growth mechanism and that pinholes are observed prior to coalescence of the nucleated islands where as copper rich films contain precipitate particles and tend to grow layer by layer in initial stages of film growth followed by 3-D growth resulting in the formation of out growths and pronounced grain structures [118].

The overall orientation of the HTS films has been reported to depend on the deposition conditions such as the substrate temperature. For instant, in PLD and sputtering growth of YBaCuO it has been reported that c-axis oriented films can be deposited on $SrTiO_3$ substrate in the temperature region of 750-830°C whilst 100°C lower an a-axis orientation can be grown [119-121]. The explanation of the occurrence of this behaviour has not been established yet. However, this has not prevented researchers from utilising this to their advantage by depositing an initial a-axis layer and then rising the substrate temperature for the main part of film growth, for better lattice matching, resulting in high quality films [122, 123]. The orientation of the film can also be influenced by the orientation of the substrate as (110) oriented YBaCuO films have been shown to grown on (110) $SrTiO_3$ substrates [124, 125].

4.7.2 General requirements for HTS thin films

For many applications as well as for fundamental studies, it is essential to grow high-quality superconducting thin films with high critical temperatures, T_C, and large critical current-carrying capabilities. The general requirements for device-quality thin films can be summarised as follows [126].

i) A high T_C

For industrial application of HTS, it is important to grow films with T_C above 77K (boiling point of nitrogen). Also, the superconducting film must have a high T_C layer all the way down to the interface region (substrate).

ii) A small transition width ΔT

ΔT is the transition width between the normal and the superconducting states. It is desirable that the film enters superconducting state over a narrow temperature range. This could also be interpreted as the degree of purity of the superconducting film. ΔT is particularly important in the case of multiphase materials such as BiPbSrCaCuO, where two or even three phases with different T_C could coexist in a film.

iii) High critical current density, J_C

This is dependent on the crystal structure, orientation, defects, and the presence of grain boundaries in the superconducting films. The large electrical anisotropy of HTS means that J_C is different along the c-axis and along the a and b-axes. The presence of grain boundaries in the HTS films is inevitable at present as all films are polycrystalline. In polycrystalline YBaCuO films J_C has been shown to decrease rapidly with an increase in the applied magnetic field from 10^{-2} to 10^{-1} Tesla. This rapid descent in J_C has been associated with a decoupling of Josephson weak links between grains.

iv) Smooth film surface

Smooth film surface is especially important for thin film multilayered device application of HTS such as superconducting/insulating/superconducting (S/I/S) junctions. In the extreme case, large surface roughness could result in the formation of randomly orientated crystals which in effect could result in the reduction of J_C.

v) Sharp interface between multilayered films and film/substrate

This is also very important in multilayered devices. This property requires that little interdiffusion and chemical reactions of layers take place. Interdiffusion of layers could result in the reduction of T_C and J_C in such materials.

4.7.3 Choice of substrates for HTS films

The choice of substrate is one of the most important material issues in the thin film growth of the HTS. An ideal substrate must have several properties. These include

i) Thermal expansion match

The requirement of good thermal expansion match between a superconductor and substrate is particularly important because of the brittleness of the superconductors. For instant, above a certain thickness YBaCuO films on Si substrates could develop cracks as a result of large difference in the thermal expansion coefficient of Si and YBaCuO [127].

ii) Minimum lattice mismatch

In the thin film growth process a large lattice mismatch could result in a displacement misfit between islands. Dislocations can result from this misfit when islands grow together.

iii) Chemical compatibility of the film with the substrate material

This is of a particular concern for the growth of high quality superconducting films. The constituents of YBaCuO or BiSrCaCuO are reactive with many substrates that might otherwise be good candidates (such as Si) [128]. The relative high temperatures required for growing in-situ films (>700°C) make the compatibility required more severe than it would be if high quality films could be grown at lower temperature. In the case of ex-situ films, the problem is even more severe, since the minimum temperature that the film and substrate must withstand is usually 850°C.

iv) Substrate surface

This is probably the most important property of a substrate since it is here that the film-substrate interaction occurs. For the growth of well oriented films it is important to used scratch free and flat substrates. The presence of defects on the substrate could prorogate into the deposited film in the formation of dislocations.

Single crystal substrates such as $SrTiO_3$, MgO, and $LaAlO_3$ can fulfil the above mentioned requirements in supporting the growth of high quality superconducting films. Despite its large lattice mismatch with BiSrCaCuO, MgO has been extensively used to support thin film growth of this material. This is because of its chemical stability at high temperatures, ready availability and reasonable cost. $LaAlO_3$, on the other hand, provides a good lattice match with BiSrCaCuO. However, it undergoes a phase transformation at 450°C which introduces crystalline defects in the superconductor. $SrTiO_3$ provides a good lattice match with BiSrCaCuO and YBaCuO. However, its high dielectric constant make this substrate undesirable for microwave application of HTS. Table (4.1) summarises the crystal, thermal, and dielectric properties of a number of single crystal substrates often used for thin film growth the Bi-Sr-Ca-Cu-O system.

Material	Lattice parameter (001) plane (Å)	Thermal expansion coefficient x10^{-6}/K	Dielectric constant at room temp	% Lattice mismatch with BiSrCaCuO
$SrTiO_3$	3.9	9.5	277	+2
MgO	4.2	13.5	9.65	9
$LaAlO_3$	3.79	10.0	23	-1

Table (4.1)- *Crystal, thermal, and dielectric properties of a number of substrates used for supporting BiSrCaCuO films.*

Due to high cost and restricted size of the single crystals it is desirable to grow thin films of HTS on substrates such as Si. In spite of serious problems with chemical reactivity, Si has also received considerable attention as a substrate material for supporting thin films of HTS due to the tantalizing possibilities of integrating semiconductors with superconductors. Although it is possible to grow YBaCuO films directly on Si substrates the chemical reactivity of Si with YBaCuO limits the electrical properties of the films. The chemical reactivity can be decreased or eliminated by the use of buffer layers between the substrate and the superconductor

4.7.4 Thin film growth of HTS by different deposition techniques

PLD has been extensively used for thin film deposition of HTS. The growth rate with this technique is typically 1Å per pulse. The deposition rate can be varied by changing the laser repetition rate as well as target-substrate distance and energy density. With this technique HTS films can be deposited in vacuum at room temperature or in high oxygen pressures at elevated substrate temperatures. HTS films deposited in vacuum require post-annealing in air or oxygen to yield superconductivity. On the other hand, films deposited at high substrate temperatures (>700°C) in an oxygen atmosphere (0.1 mbar) could be grown in-situ. The exact oxygen pressure depends on the deposition system.
With PLD, in-situ growth of multilayered HTS devices have been demonstrated with a remarkably simple fashion of rapidly changing the target material [129]. Excellent quality

YBaCuO films in terms of high T_c, >90K, and large J_c, $>10^{-6}A/cm^2$, have been grown with this technique [130]. HTS films deposited by PLD technique, however, is shown to be rough on the surface. The origin of this problem has been related to the high deposition rate [131]. To deposit very smooth films the material should be grown stoichiometric and epitaxial [132]. In c-axis YBaCuO films often a-axis outgrowths has also been observed. The a-axis outgrowths are said to be related to the film nucleation at off-stoichiometric areas or the possibility of faster growth direction along the b-axis with slower growth direction along the c-axis [131].

The main sputtering technique used for the deposition of HTS such as BiPbSrCaCuO is rf magnetron sputtering [133]. In the early days the sputtering process of HTS was mainly accomplished by using various target combinations such as separate oxide targets, stoichiometric targets and multiple non-stoichiometric targets. It soon became apparent that trial and error process combined with careful composition analysis was the method in achieving the ideal deposition conditions. This is because each system has a different configuration and the diffusion of the target species through the sputtering gas to the substrates differ from one system to another.

An advantage of sputtering technique is its ability to deposit HTS films over a large area (1 square inch) with uniform composition. A major problem with sputtering technique which has been addressed to a great extent is the resputtering of the sample by negative oxygen ions during in situ growth of the high temperature superconductors. This problem is not new and is not confined to HTS. This phenomenon has been fully investigated by Rossnagel and Cuomo [134]. The suggested methods of avoiding this problem are either to thermalise the energetic species or by working at a very high pressure or by what is known as "off-axis" sputtering at a modestly high sputtering pressure which encourages energy reducing collisions in atoms emanating from the target [135].

The re-sputtering effect results in non-stoichiometric and damaged film deposition. Although the use of off-axis sputtering technique solves the problem of resputtering, it reduces the deposition rate to typically 50nm/hr. This means that a run duration of 5 hours is required to yield a 2500Å film. Using the sputtering technique good quality BiPbSrCaCuO (2223 phase) films with $T_{c,\ zero}$ as high as 106.5K and J_c in excess of 4.1×10^4 Acm^{-2} at 77.3K have been demonstrated [136].

The evaporation technique was one of the first methods utilized to grow thin films of HTS. Because of the multicomponent nature of HTS and the differences in vapour pressure of each components, separate heat or beam sources for evaporation are used with this technique. A major disadvantage of this technique is that the evaporation rate of each element needs to be controlled in order to grow a stoichiometric film. Deviation of one percent in stoichiometry can have noticeable effects on superconducting properties or surface morphology of the films [137]. Also, evaporation must operate with a background pressure of around 10^{-4} mbar. Whereas for in situ deposition of HTS high oxygen levels are required. This conflict has been resolved by the use of various forms of reactive oxygen, often injected close to the substrates.

The major advantage of this technique is the ability of changing the composition of films continuously, and thus examine the effect of composition on film properties. The use of separate heat or beam sources also enables one to grow these materials in a layer-by-layer fashion on an atomic scale, which is a promising technique for making artificial structures considering the layered structure of these materials. In-situ YBCO films deposited by this technique have shown $T_{c,\ zero}$ in excess of 90K [138].

Both YBaCuO and BiSrCaCuO films have been deposited by MBE technique [139, 140]. To obtain oxidization and hence crystalization of the superconducting films in layered structure, a low temperature and low pressure growth environment is favourable. To bring the elements (such as Cu) into oxidation state, an activated species of oxygen is necessary. Terashima et al. [141] have suggested the use of partial pressure of oxygen near the substrate which could be 2 to 3 orders of magnitude higher than the rest of the system. Others have suggested oxidation by an rf plasma of O_2 gas [143] or the use of ozone, which has the advantage of lowering the crystallization temperature [142]. Watanabe et al. [143] have shown the successful growth of BiSrCaCuO (2201 phase) by MBE technique on $SrTiO_3$ (100) substrate at 300°C using $2x10^{-7}$ torr of NO_2. The use of an activated oxygen source in MBE technique is effective in keeping the pressure of the system low during the deposition so that the mean free path in the chamber could be long enough for the molecular beam not to scatter in collisions with the gas molecules in reaching the substrate.

With chemical vapour deposition of HTS the constituent metal atoms are deposited on a substrate by decomposing metal-organic molecules from a gas phase. Chemical vapour deposition has also reached a stage where BiSrCaCuO films can be made with good electrical properties [144]. The use of this method for laboratory research is not very widespread yet, but this technique is probably the most promising technique for commercial production work, because of its high throughput and its ability to coat complex shapes.

4.8 Summary

A number of the properties of low temperature superconductors were described in the beginning of this chapter. This was complemented with a brief discussion on the critical current density of superconductors and the current limiting factors such as the grain boundaries and flux creep. The high temperature superconductors were briefly discussed in terms of the common features in their crystal structures. This was followed by a discussion on the crystal structures of the three main superconducting phases within the $Bi_2Sr_2Ca_{n-1}Cu_nO_{4n+2}$ system and the influencing factors on the enhancement of the 2223 phase. This was followed by a brief discussion on the modulation in the BiSrCaCuO system. Finally, thin film growth of HTS in terms of growth mechanisms was discussed and the general requirements for thin film growth of HTS was out-lined. Also, thin film deposition and growth of HTS by different techniques was discussed.

References

1- H. K. Onnes, Akad. van Wetenschappen (Amsterdam) 14, 113, (1911), 818.

2- J.G.Bednorz, and.K. A. Muller. Z. Phys. B64, (1986), 189.

3- M. K. Wu, J. R. Ashburn, C. J. Torng, P. H. Hov, R. L. Meng, L. Gao, Z. J. Huang, Y. Q. Wang, and C. W. Chu, Phys. Rev. Lett. 58, (1987), 908.

4- A. Schiling, M. Cautoni, J. D. Guo, and H. R. Ott. Nature. 363, (1993), 56.

5- F. London and H. London. Proc. Roy. Soc. A149, (1935), 72.

6- D. K. Fork, D. B. Fenner, R. W. Barton, J. M. Phillips, G. A. N. Connel, J. B. Boyce, and T. H. Geballe. Appl. Phys. Lett. 57, (1990), 1161.

7- M. Kawasaki, E. Sarnelli, P. Chaudhri, A. Gupta, A. Kussmaul, J. Lacey, and W. Lee. (private communication).

8- J. W. Ekin. Adv. Ceram. Mater. 2, (1987), 586.

9- D. Dimos, P. Chaudhri, and J. Mannhart. Phys. Rev. B41, (1990), 4038.

10- D. C. Larbalestier, Physics today. 44, (1991), 74.

11- D. M. Kroeger, A. Choudhury, J. Brynestad, R. K. Williams, R. A. Padgest, and W. A. Coghlan. J. Appl. Phys. 64, (1988), 331.

12- Y. Gao, K. L. Merkle, G. Bai, H. L. M. Chang, and ZD. J. Lam. Physica C 174, (1991), 1.

13- S. E. Babcock and D. C. Larbalestier. Appl. Phys. Lett. 55, (1989), 393.

14- M. Kawasaki, P. Chaudhri, and A. Gupta. Phys. Rev. Lett. 68, (1992), 1065.

15- K. Salama, V. Selvamanickam, L. Gao, and K. Sun. Appl. Phys. Lett. 54, (1989), 2352.

16- P. J. McGinn, W. Chen, N. Zhu, U. Balachandran, and M. T. Lanagam. Physica C 165, (1989), 480.

17- R. L. Meng, C. Kinalidis, Y. Y. Sun, L. Gao, Y. K. Tao, P. H. Hor, and C. W. Chu. Nature, 345, (1990), 326.

18- S. Jin, and C. W. Chu (To be published as Chapter 11 of properties of HTS. Edited by S. Jin (Singapore: world scientific, 1993).

19- B. Soylu, N. Adamopoulos, D. M. Glowacka, and J. E. Evetts. Appl. Phys. Lett. 60, (1992), 3183.

20- M. Tinkham. Phys. Rev. Lett. 61, (1988), 1658.

21- T. T. M. Palstra, B. Batlogg, L. F. Schneemeyer, and J. V. Waszczak, Phys. Rev. B43, (1991), 3756.

22- R. B. van Dover, E. M. Gyorgy, L. F. Schneemeyer, J. W. Mitchell, K. V. Rao, R. Puzniak, and J. V. Waszczak. Nature, 342, (1989), 55.

23- W. Kritscha, F. M. Sauerzopf, H. W. Weber, G. W. Crabtree, Y. C. Chang, and P. Z. Jiang, Supercond, Sci. Technol. 5, (1992), 232.

24- J. L. Tallon, D. M. Pooke, R. G. Buckley, M. R. Presland, N. E. Flower, S. Gibson, and P. W. Gilberd. Appl. Phys. Lett. 59, (1991), 1239.

25- P. J. McGinn, W. Chen, N. Zhu, S. Segupta, and T. Li. Physica C176, (1991). 203.

26- J. Bardeen, L. N. Cooper, and J. R. Schrieffer. Phys. Rev. 106, 162, (1957); 108, (1957), 1175.

27- V. L. Ginzburg and L. D. Landau. "On the theory of superconductivity", Zh. Eksp. Teor. Fiz. vol 20, (1950), 1064-1068.

28- S. R. Ovshinsky. Chem. Phys. Lett. 195 (4), (1992), 455-456.

29- S. R. Ovshinsky. Proc. of the 3rd Int'l conf on supercoductivity, Munich, (1992).

30- B. H. Brandow "Los alamos National Laboratory" (to be published).

31- P. W. Anderson, Science. 235, (1987), 1196.

32- Reynolds, Serin, Wright, and Nebitt. phys. Rev. 78, (1950), 487.

33- T. A. Faltens, W. K. Ham, S. W. Keller, K J. Leary, J. N. Michaels, A. M. Stacey, H. C. zur Loye, D. E. Morries, T. W. Barbee III, L. C. Bourne, M. L. Cohen, S. Hoen and A. Zettl, Phys. Rev. Lett. 59, (1987), 915.

34- K. J. Leary, H. C. Zur Laye, S. W. Keller, T. A. Faltens, W. K. Ham, J. N. Michaels and A. M. Stacy, Phys. Rev. Lett. 59, (1987), 1236.

35- H. K. Yoshida, T. Hirooka, A. Oyamada, Y. Okabe, T. Takahashi, T. Sasaki, A. Ochiai, T. Suzuki, A. J. Mascarenhas, J. I. Pankove, T. F. Ciszek, S. K. Deb, R. B. Goldfarb and L. I. Yong Kang, Physica C. 156, (1988), 481.

36- Z. Z. Sheng, and A. M. Hermann, Nature, 332, (1988), 138.

37- S. N. Putilin, E. V. Antipov, O. Chmaissem, and M. Marezio. Nature. 362, (1993), 226.

38- R. J. Cava. Science. 247, (1990), 656-662.

39- Y. Tokura, H. Takagi, S. Uchida. Nature 337, (1989), 345.

40- T. Kawai. ISTEC Journal. Vol 2 (3), (1989), 19-24.

41- A. W. Sleight. Science. 242, (1988), 1519-1527.

42- P. C. W. Fung, and W. Y. Kwok. J. Supercond. Vol 4 (6), (1991), 415-422.

43- J. Karpinski, C. Beeli, E. Kaldis, A. Wisard, and E. Jilek. Physica C, 153-155, (1988), 830.

44- M. R. D. Guire, N. P. Bansal, D. E. Farrell, V. Finan, C. J. Kim, B. J. Hills, and C. J. Allen. Physica C. 179,)1991), 333.

45- S. J. Collocott and R. Driver. Physica C, 167, (1990), 598.

46- K. Schlze, P. Majewski, B. Hettich, and G. Petzow, Z. Metallkde. 81, (1990), 836.

47- P. Majewski, B. Hettich, K. Schlze, and G. Petzow, Procedings of the 2nd conference of the European Ceramic Sociatv, 11-14 August (1991.)

48- C. Michel, M. Hervieu, M. M. Borel, A. Grandin, F. Deslandes, J. Provost, and B. Raveau, Z. Phys, B68, (1987), 421.

49- M .A. Subramanian, C. C. Torardi, J. C. Calabrese, J. Gopalkrishnan, K. J. Morrissey, T. R. Askew, R. B. Flippen, U. Chowdhry, and A. W. Sleight. Science. 239, (1988), 1015.

50- H. Maeda, Y. Tanaka, M. Fukutomi, and T. Asano. Jpn. J. Appl. Phys. 27, (1988), L209.

51- T. Kawai, Y. Egami, H. Tabata, S. Kawi. Nature, Vol ....(1991), 349.

52- J. M. Trascon, Y. Le. Page, P. Barboux, R. G. Bagley, L. H. Greene, W. R. McKinnon, G. W. Hull, M. Giroud, and D. M. Wang. Phys. Rev, B37, 16, (1988), 9382.

53- B. C. Chakoumakos, J. D. Budcui, B. C. Sales, and E. Sonder. Mat. Res. Soc. Symp. Proc. 156, (1989), 3329.

54- C. C. Torardi, M. A. Subramanian, J. C. Calabrese, J. Gopalakrishnan, E. N. McCarron, K. J. Morrissey, T. R. Askew, R. B. Flippen, U. Chowdhry, and A. W. Sleight. Phys. Rev. B38, (1988), 225.

55- J. B. Torrance, Y. Tokura, S. J. Laplace, T. C. Huang, R. J. Savoy, and A. I. Nazzal. Solid. State. Commun. 66, (1988), 703.

56- M. Onada, and M. Sato. Solid. State. Commun. 67, (1988), 799.

57- B. C. Chakoumkos, P. S. Sales, and E. Sonder. J Mate Res, 4, 919890, 767.

58- D. C. Sinclair, J. T. S. Irvine, and A. R. West. Jpn. J. Appl. Phys, 29 (11), (1990), 2002.

59- S. A. Sunshine, T. Siegrist, L. F. Schneemeyer, D. W. Murphy, R. J. Cava, B. Batlogg, R. B. van Dover, R. M. Fleming, S. H. Glarum, S. Nakahara, R. Farrow, J. J. Krajewski, S. M. Zahurak, J. R. Waszczak, J. H. Marshall, P. Marsh, L. W. Rupp, Jr., and W. F. Peck, Phys. Rev. B38, (1988), 893.

60- P. Bordet, J. J. Capponi, C. Chaillout, J. Chenavas, A. W. Hewat, E. A. Hewat, J. L. Hodeau, M. Marezio, J. L. Tholence, D. Tranqui. Physica C. 153-55, (1988), 623.

61- A. I. Beskrvonyi, M. Dlouha, Z. Jirak, and S. Vratislaw, Physica C. 166, (1990), 79.

62- J. M. Tarascon, W. R. McKinnon, P. Barboux, D. M. Hwang, B. G. Bagley, L. H. Greene, G. W. Hull, Y. Le Page, N. Stoffel, and. Giroud. Phys. Rev. B38 (13), (1988), 8885.

63- N. Kijima, H. Endo, J. Tsuchiya, A. Sumiyama, M. Mizuno, and Y. Oguri. Jpn. J. Appl. Phys. 27, (1988), L821.

64- G. Miehi, T. Vogt, H. Fuess, and M. Wilhelm. Physica C. 171, (1990), 339.

65- H. W. Zandbergen, Y. K. Huang, M. J. Menken, J. N. Li, K. Kadowaki, A. A. Menovsky, G. van Tendeloo, and S. Amelinckx. Nature, 332, (1988), 620.

66- U. Endo, S. Koyama, T. Kawai. Jpn. J. Appl. Phys. 27 (8), (1988), L1476.

67- S. M. Green, Y. Mei, A. E. Manzi, and H. L. Luo. J. Appl. Phys, 66, (1988), 3703.

68- D. Shi, M. Tang, K. van Devoort, and H. Claus. Phys. Rev. B39, (1989), 9091.

69- T. Hatano, K. Aota, S. Ikeda, K. Nakanura, and K. Ogawa, Jpn. J. Appl. Phys. 27, (1988), L2055,

70- R. Ramesh, G. Thomas, S. M. Green, C. Jiang, Yu. Mei, M. L. Rudee, and H. L. Luo. Phys. Rev. B 38(10), (1988).

71- M. Takano, J. Takada, K. Oda, H. Kitaguchi, Y. Miura, Y. Ikeda, Y. Tomii, and H. Mazaki. Jpn. J. Appl. Phys. 27, (1988), L1041.

72- F. H. Chen, H. S. Koo, and T. Y. Tseng. Appl. Phys. Lett. 58(6), (1991), 637.

73- S. X. Dou, K. H. Song, H. K. Liu, C. C. Sorrell, M. H. Apperly, and N. Sarrides. Appl. Phys. Lett. 56, (1990), 493.

74- R. Ramesh, K. Remschnig, J. M. Tarascon, and S. M. Green. J. Mater. Res. 6(2), (1991).

75- O. Eibl,. Physica C. 168, (1990), 215.

76- K. Kijima, H. Endo, J. Tsuchiya, A. Sumiyama, M. Mi Zuno, and Y. Ouri. Jpn. J. Appl. Phys. 28, (1989), L787.

77- Y. L. Chen and R. Stevens. J. Am. Ceram. Soc. 75 (5), (1992), 1150-1159.

78- D. Shi, M. S. Boley, J. G. Chen, M. Xu, K. Van dervoort, Y. X. Liao, A. Zangvil, J. Akujieze, and C. Seqre. Appl. Phys. Lett. 54, (1989), 699.

79- M. Mizuno, H. Endo, J. Tsuchiya, N. Kijima, A. Suniyama, and Y. Oguri. Jpn. J. Appl. Phys. 27, (1988), L1225.

80- T. Hatano, K. Aota, S. Ikeda, K. Nakamura, and K. Ogawa, Jpn. J. Appl. Phys, 27, (1988), L2055.

81- Z. Xu, P. D. Han, L. Chang, A. Asthana, and D. A. Payne, J. Mater. Res. 5, (1990), 39.

82- A. W. Hewat, J. J. Capponi, C. Chaillout, M. Marezio, and E. A, Hewat. Solid State commun. 64, (1987), 30.

83- J. Stepien-Damn, T. Morawska-Koval, and Z. Damn, Reactive Solids. 7, (1989), 325.

84- S. Jin, H. M. O'ryan, P. K. Gallagher, T. H. tiefel, R. J. Cava, R. a. Fastnach, and G. W. Kammlott. Physica c 165, (1990), 8868.

85- W. A. groen and D. M. de Leeuw. Physica C. 159, (1989), 417.

86- D. E. Morris, C. T. Hultgren, A.M. Markelz, J. Y. T. Wei, N. G. Asmar, and J. H. Nickel. Phys. rev. B. 39, (1989), 6612.

87- R. G. Buckley, J. L. Tallon, I. W. M. Brown, M. R. Presland, N. E. Flower, P. W. Gilberd, M. Bowden, and N. B. Milestone. Physica C. 156, (1988), 629.

88-H. Niu, N. Fukushima, and K. Ando. Jpn. J. Appl. Phys. 27, (1988), L1442.

89- H. W. Zendbergen, W. A. Grone, F. C. Mijhoff, G. van Tendeloo, and S. Amelincks. Physica C 156, (1988), 325.

90- T. Tamegai, A. Watanabe, K. Koga, I. Oguro, and Y. Iye. Jpn. J. Appl. Phys. 27, (1988), L1074.

91- S. Kambe, T. Matsuoka, M. Kawai, and M. Takahasi, Physica C. 165, (1990), 25.

92- Y. Motoi, Y. Ikrda, H. Uwe, and T. Sakudo. Physica C 162-164, (1989), 929.

93- J. Zhao, M. wu, W. Razzaq, and M. S. Seehra. Physica C. 165, (1990), 135.

94- H. Hattori, K. Nakamura, and K. Ogawa. Jpn. J. appl. Phys. 29(1), (1990), L36-L39.

95- S. Miura, T. Yoshitake, T. Satoh, Y. Miyasaka, and N. Shohata. "Proc of Jpan Society of applied Physics". Fukuoka, (1989), 25-28.

96- S. Horiuchi, H. Meada, y. tanaka, and Y. Matsui. Jpn. J. Appl. Phys. 27, (1988), 1172.

97- J. Schneck, L. Pierre, J. C. Toledo, and C. Daguet. Phys. Rev. B39. (1989), 9624.

98- E. A. Hewat, J. Microsc. Spectrosc. Electron,.....(1988), 297.

99- R. Ramesh, G. van Tendeloo, G. Thomas, S. M. Green, and H. L. Lao. Appl. Phys. Lett, 53, (1988), 2220.

100- J. L. Tallon, R. G Buckley, P. W. Gilberd, and M. R. Presland. Physica C, 158, (1989), 247.

101- H. W. Zandbergen, and W. A. Groen, Physica C, 166, (1990), 282.

102- C. C. Torardi, E. M. Mc Carron, P. l. Gai, J. B. Parise, J. Ghoroghchian, D. B. Kang, M. H. Whangbo, J. C. Barry. Physica C. 176, (1991), 347.

103- Y. Ikeda, Z. Hiroi, H. Ito, S. Shimomura, M. Takano, and Y Bando. Physica C. 165, (1989), 189.

104- H. Meada, Y. Tanaka, M. Fukutomi, T. Asano, K. togano, H. Kumakura, m. Uehara, S. Ikeda, K. Ogawa, S. Horiuchi, and Y. Matsui, Proc. Intelaken, Physica C, 153, (1988), 602.

105- Y. Matsui, h. Meada, Y. Tanaka, and S. Horiuchi. Jpn. J. Appl. Phys. 2(27), (1988), L372.

106- H. W. Zandbergen, w. A. Groen, F. C. Mijlhoff, G. van Tendeloo, S. Amelinckx. Physica C 156, (1988), 325.

107- A. K. Cheetham, A. M. Chippindale, and S. J. Hibble. Nature. 333, (1988), 21.

108- P. L. Gai, and P. Day. Physica C. 152, (1988), 335.

109- R. J. Cava, B. Batlogg, S. A. Sunshine, T. Siegrist, R. M. Fleming, K. Rabe, L. E. Schneemeyer, d. W. Murphy, R. B. va Dover, P. K. Gallagher, S. H. Glarum, S. Nakahara, R. C. Farrow, J. J. Krajewski, S. M. Zahurak, J. V. Waszczak, J. H. Marshall, P. Marsh, L. W. Rupp, W. F. Peck, and E. A. Rietman. Proc. Interlaken, Physica C. 153-155, (1988), 560.
110- H. G. von Schnering, L. Walz, M. Schwarz, W. Becker, M. Harweg, T. Popp, B. Hettich, P. Muller, and G. Kampf, Angew. Chem. Int.(Ed Eng). 27, 574, (1988).
111- P. Bordet, J. J. Capponi, C. Chaillout, J. Chenevas, A. W. Hewat, J. L. Hodeau, M. Marezio, J. L. Tholence, and D. Tranqui, Physica C. 156, (1988), 189.
112- Y. Le page, W. R. McKinnon, J. M. Tarrascon, and P. Barboux. Phys. Rev. B40, (1989), 6810.
113- T. Terashima, K. Ijima, K. Yamamoto, K. Hirata, Y. Bando, and T. Takada. Jpn. J. Appl. Phys. 28, (1989), L987.
114- T. Terashima, Y. Bando, K. Ijima, K. Yamamoto, K. Hirata, K. Hayashi, K. Kamigaki, and H. Terauchi. Phys. Rev. Lett. 65, (1990), 2684.
115- T. Shimizu, H. Nonaka, and K. Arai. Appl. Phys. Lett. 59, (1991), 600.
116- H. P. Lang T. Frey, R. Sum, and H. J. Guntherodt, Proc, ICAM 91, Strasbourg (to be published).
117- S. Miyazawa, M. Sasaura, and M. Mukaida, Proc. ICAM 91, Strasbourg. (to be published).
118- F. Baudenbacher, K. Hirata, P. Berberich, H. Kinder, and W. Assman. Proc. ICAM 91and E-MRS Spring Meeting (1991), Strasbourg.
119- G. Linker, X. X. Xi, O. Meyer, Q. Li, and J. Geek. Solid State Commun. 69, (1989), 249.
120- Q. Li, D. Wu, and T. Venkatesan. Appl. Phys. Lett. 57, (1990), 1064.
121- H. Tsunge, and N. Matsukura, IEEE Trans. Mag. 27, (1991), 1009.
122- H. U. Habermeier, A. A. C. S. Lourenco, B. Leibold, J. Kircher, B. Friedl, and G. Lu. Proc. ICAM 91, and E-MRS spring Meeting (1991), Strasboug.
123- H. U. Habermeier, A. A. C. S. Lourenco, B. Leibold, J. Kircher, and J. Kohler. Solid State Commun. 77, (1991), 683.

124- T. Terashima, Y. Bando, K. Ijima, K. Yamamoto, and K. Hirata. Appl. Phys. Lett. 53, (1988), 2232.

125- Y. Enomoto, T. Murakami, M. Suzuki, and K. Moriwaki. Jpn. J. Appl. Phys. 26, (1987), L1248.

126- T. Venkatesan, X. D. Wu, A. Inam, M. S. Hedge, E. W. Chase, C. C. Chang, P. England, D. M. Hwang, R. Krchnavek, J. B. Wachtman, W. L. Mclean, R. Levi-Setti, J. Chabala, and Y. L. Wang. (Chemistry of high temperature superconductors 11, edited by D. Nelson and T. F. George), ACS Symp. Ser.377, 1988.

127- D. K. Fork, F. A. Ponce, J. C. Tramontana, N. Newman, J. M. Phillips, and T. H. Geballe. Appl. Phys. Lett. 58, (1991), 2432.

128- A. M. Campero, B. D. Hunt, L. G. Turner, M. C. Burell, and W. E. Balz. Appl. Phys. Lett. 52, (1988), 584.

129- X. D. Wu, R. E. Muenchausen, S. Foltyn, R. C. Estler, C. Flamme, N. Nogar, A. R. Garcia, J. Martin, and J. Tesmer. Appl. Phys. Lett. 56, (1990), 1481.

130- E. W. Chase, T. Venkatesan, C. C. Chang, B. Wilkens, W. L. Feldman, P. Barboux, J. M. Rarascon, D. L. Hart, X. D. Wu, and X. Inam. J. Mater. Res. 4, (1989), 1326.

131- C. C. Chang, X. D. Wu, R. Ramesh, X. X. Xi, T. S. Ravi, T., D. M. Hwang, R. E. Muenchausen, S. Foltyn, and N. S. Nogar. Appl. Phys. Lett. 57, (1990), 1814.

132- R. E. Somekh, Z. H. Barber. (Private communication).

133- J. S. Moodera, A. M. Rao, A. Kussmaul, and P. M. Tedrow. Appl. Phys. Lett. 57, (23), (1990), 2498-2500.

134- S. M. Rossnagel, and J. J. Cuomo. American Institute of Physics Conference Proc. 165, (1988), 106.

135- C. B. Eom, A. F. Marshall, S. S. Laderman, R. D. Jacowitz, and T. H. Geballe. Science, 249, (1990), 1549.

136- A. Tanaka, N. Kamehara, and K. Niwa. Appl. Phys. Lett. 55, (12), (1989), 1252-1254.

137- N. G. Chew, S. W. Goodyear, J. A. Edwards, J. S. Satchell, S. E. Blenkinsop, and R. G. Humphreys. Appl. Phys. Lett. 57, (1990), 2016.

138- V. Matijasevic, P. Rosenthal, K. Shinohara, A. F. Marshall, R. H. Hammond, and M. R. Beasley. J. Mate. Res, Vol (6), (1991), 682.

139- J. Kwo, M. Hong, D. J. Trevor, R. M. Fleming, A. E. White, R. C. Farrow, A. R. Kortan, and K. T. Short. appl. Phys. Lett. 51, (1988), 2683.

140- Y. Nakayama, H. Ochimizu, A. Maeda, A. Kawazu, K. Uchinokura, and S. Tanaka. Jpa. J. Appl. Phys. 28, (1989), L1217.

141- T. Terashima, K. Iijima, K. Yamamoto, K. Hirata, Y. Bando, and T. Takada. Jpn. J. Appl. Phys. 28, (1989), L987.

142- I. Bozovic, J. N. Eckstein, M. E. Klausmeier-Brown, G. F. Virshup, and K. S. Ralls. Mat. Res. Symp. Proc. Vol (275), (1992). 67-72.

143- S. Watanabe, M. Kawai, and T. Hanada. Jpn. J. Appl. Phys. Vol (29), No7, (1990), L1111-L1113.

144- E. Endo, H. Yamasaki, S. Misawa, S. Yoshida, and K. Lajimura. Nature. Vol (355), (1992), 327-328.

Chapter 5

Experimental

5.1 Introduction

In this chapter the experimental procedure for thin film deposition of BiPbSrCaCuO using PLD is described. This is followed by a brief description of the characterisation techniques used to analyse the properties of the films.

5.2 Experimental set-up and procedure

A detailed schematic diagram (top view) of the experimental set-up constructed and used for PLD of BiPbSrCaCuO thin films, described in this thesis, is illustrated in figure 5.1. The deposition set-up consisted of a custom made six way cross deposition chamber devised with various ports and optical components for handling the laser beam.

The optical components were positioned outside the deposition chamber to avoid damage from the ejected materials during the deposition process. Prior to deposition, the chamber was evacuated to a pressure of $\approx 10^{-5}$ mbar by a rotary and a diffusion pump. To obtain partial pressure of oxygen in the chamber, a needle-valve was used. The pressure inside the chamber was monitored by a pirani gauge from 10^{3} to 10^{-3} mbar and by a penning gauge from 10^{-3} to 10^{-6} mbar.

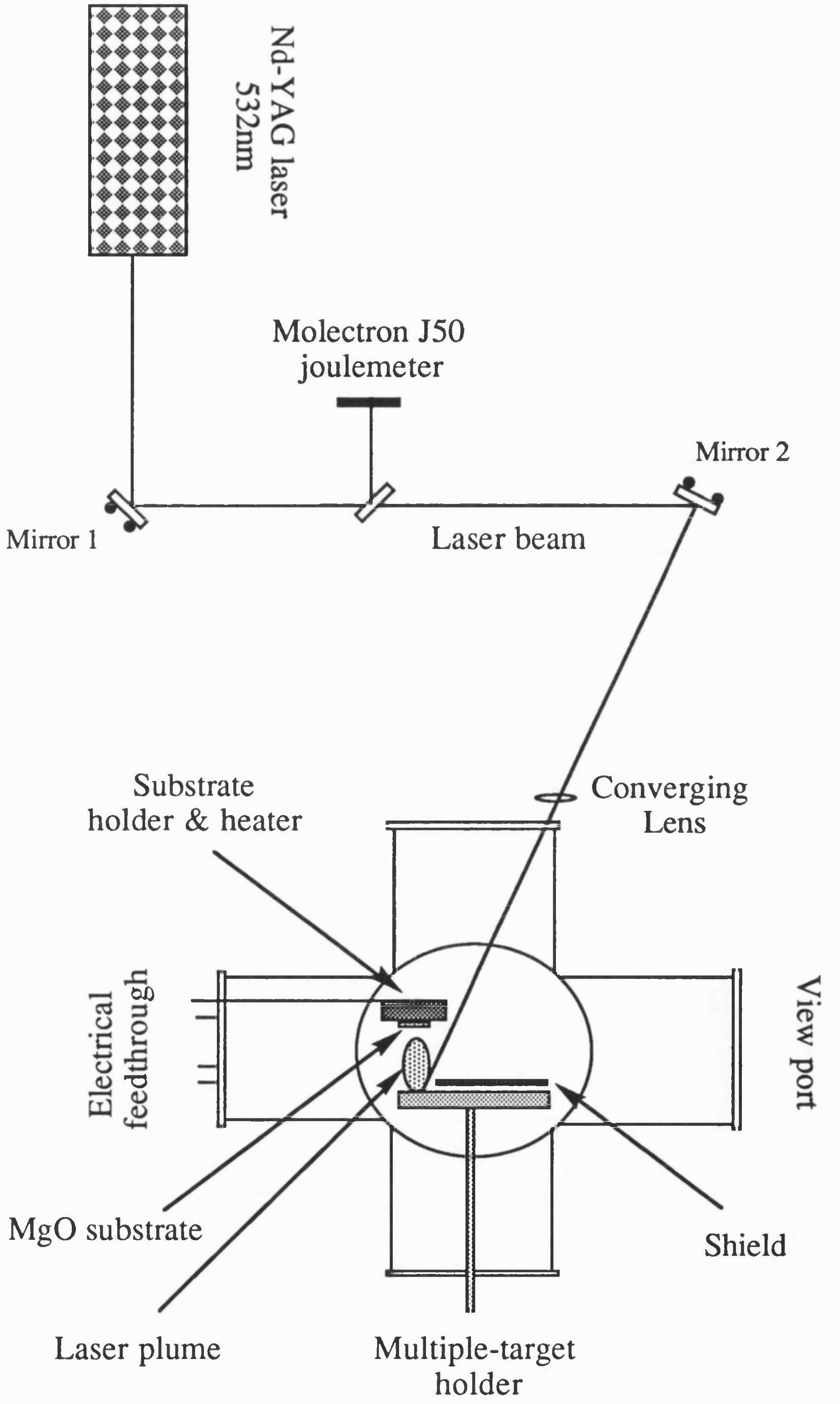

Figure 5.1- *Schematic diagram of the experimental set-up for pulsed laser deposition of the BiPbSrCaCuO thin films.*

The BiPbSrCaCuO films were deposited using a Nd-YAG laser (Quantle YG571C-10) operating at doubled frequency of 532nm with a repetition frequency of 10Hz and a pulse-width (FWHM) of 4ns and an average energy of 500mJ/pulse. The beam was guided by two turning mirrors through a converging lens (f=15cm) and a view port into the deposition chamber. The view port was cleaned routinely after several deposition runs. The beam was focused by the lens to a spot size of ≈3.0mm on the BiPbSrCaCuO target at an incident angle of 30°C.

The spatial characteristic of the laser beam intensity showed a double peaked distribution instead of the usual Gaussian distribution. At least two hot zones were also evident in the beam profile. The hot zones were detected after reducing the laser energy by neutral density filters placed in the path of the beam and subsequent analysis of the burn marks left on a fax paper. The hot zones were back-tracked through the optical components in the laser and found to originate from the rod in the cavity. The laser fluence at the target was measured using a Molectron J50 joulemeter

The targets (disk shaped BiPbSrCaCuO pellets of 12mm in diameter) were held in position by three adjustable screws inside a holder which was rotated externally by a dc motor with the speed of 5 Rev/min. The target rotation minimizes the ablation and deposition of non-stoichiometric material formed around the edges of each irradiated area, where melting and re-solidification takes place. Due to the preferential expansion of plasma (at right angle with respect to target) the substrates were placed in parallel with the target. The target-substrate distance could be varied between 2-4.2cm by moving the substrate holder back and forth.

Superconducting BiPbSrCaCuO films were grown on single crystal (001) oriented MgO substrates. The decision on the choice of substrate was based on **i)** chemical stability at high temperatures (>860°C) **ii)** ready availability; **iii)** economical grounds. For energy dispersive x-ray (EDX) and electron probe microanalyser (EPMA) analysis, BiPbSrCaCuO films were deposited at room temperature on Si substrates. The substrates were placed directly on the heater and kept in position either by a single stainless steel frame or silver paste. Two types of substrate resistive heaters, one home made and the other commercial Si nitride, were used for BiPbSrCaCuO film deposition at elevated substrate temperatures.

5.3 The multi-target holder

To deposit in-situ multilayered BiPbSrCaCuO/PbO films, as described in this thesis, a multi-target holder was designed in such a way as to accommodate up to five targets (BiPbSrCaCuO and PbO pellets). This was manufactured out of stainless steel at UCL (Department of Electronic & Electrical Engineering). A schematic diagram of the multi-target holder is shown in figure 5.2. Each target could be placed in the path of the laser beam manually, one at the time and rotated externally by a dc motor at the rate of 5rev/min. A shield was placed in front of the multi-target holder during the ablation process in order to protect the other targets from the ejected materials.

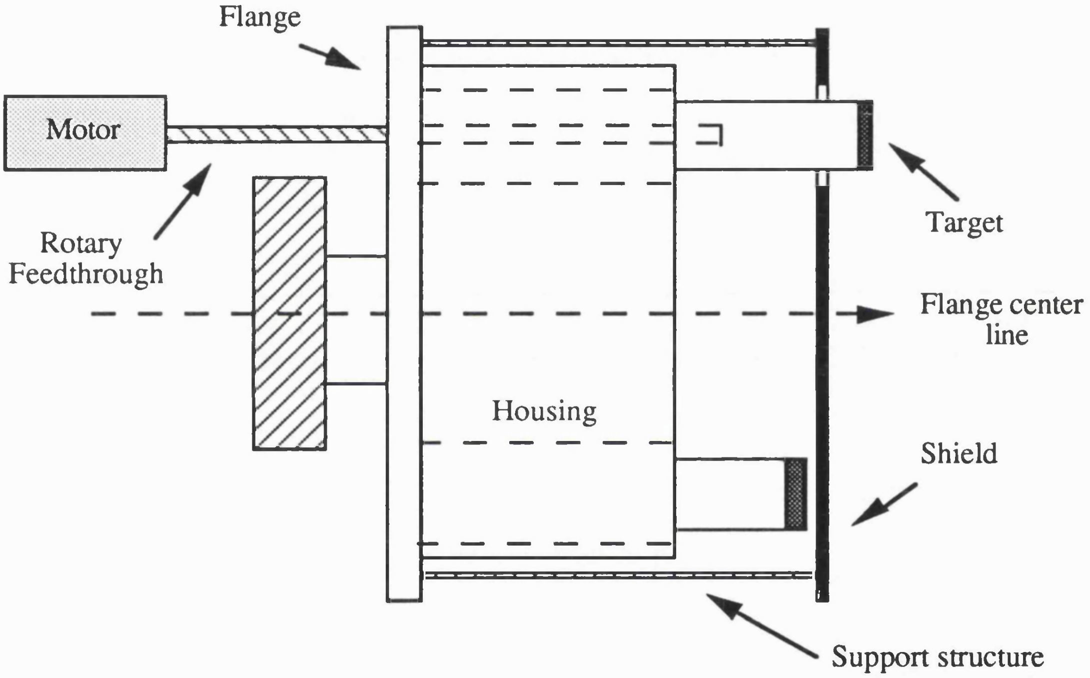

Figure 5.2- *Schematic diagram of the multiple target holder.*

5.4 Substrate heater and substrate temperature measurement

The home made substrate heater consisted of an alumina ceramic plate, 2.5mm in thickness, which was delicately machined with grooves on one surface. The heating wire (FeCrAlY) was inserted in the grooves and covered with alumina cement. A Chromel-alumel thermocouple wire was spot welded at one end on the back surface of the stainless steel frame, positioned directly on the heater. Therefore, the growth temperatures of the films which are referred to in this thesis, are of the heater and not the substrate.

5.5 The annealing furnace

Post-annealing of the deposited BiPbSrCaCuO films was carried out in a tube furnace (Carbolite furnaces, model number 6/90/968) which was computer controlled to run complicated annealing procedures. BiPbSrCaCuO films deposited on MgO substrates were placed on a gold foil inside a quartz boat. The boat was inserted into a large quartz tube of 110 cm in length and 6cm in diameter. The temperature of the substrate was monitored by a Chromel-alumel thermocouple wire placed in contact with the gold foil in the quartz boat.

5.6 Thin film characterisation

A detailed explanation of the characterisation techniques used for analysis of the films is beyond the scope of this thesis and therefore only a brief description is given. For more details the references given should be consulted.

5.6.1 Resistivity measurements

The resistivity as a function of temperature characterisation of BiPbSrCaCuO films were realised in an APD cryostat, using the Van der Pauw technique [1] at Imperial College (physics department). The film was placed on a sample holder and contacts to the film were arranged in a square geometry using silver paste and silver wires. In this configuration DC current (typically 10-100 μA) flows via two contacts distance L apart, through the film of cross sectional area A. The voltage ΔV is then picked up at the other two contacts. Resistance R is independent of contact and lead resistance, as long as the DVM's input resistance (which is typically in MΩ) is larger than the contact and lead resistance. The resistivity ρ in Ohm-cm of the film is then calculated from Ohms law ($\rho=RA/L$, where ρ is in Ωcm).

The thermo-electric effects in the leads and at the contacts could result in errors in the order of a few micro volts. To minimize this error, it is necessary to measure voltage response ΔV of the film with and without current flowing through it. By subtracting the two responses, ΔV can then be calculated. An alternative and better method used was to reverse the current. Reversing the current doubles the amount of measured points and since any heating effects in the resistive components do not change when the current is reversed, the measured data of the voltage response are more reliable. The voltage response of the film when current flows through it is then stored in a computer programme, Lutos 123.

5.6.2 Scanning electron microscope (SEM)

The scanning electron microscope is a very powerful and versatile analytical tool that has proven to be indispensable for characterising superconducting materials. The main advantage of SEM over the optical or transmission electron microscope for defining surface morphology is the greater depth of field of the SEM image. Because objects are viewed in the secondary electron image mode appear three-dimensional, interpretation of the SEM image is quickly assimilated [2].

In scanning electron microscope electrons are emitted from an electron gun (by thermionic or field emission) which are then accelerated down the column by a charge potential energy of typically 1-30KeV. Electromagnetic lenses and mechanical apertures are used to demagnify and focus the electrons to form an electron probe of small diameter and high current density. The lenses are adjusted to change the focal length of the primary electron beam to focus the image and to change the current density. The ability to change the focal length of the electronic lenses and size of the apertures allows the optimization of the spatial resolution and hence depth of field to obtain the desired image or signal.

In this technique the primary electrons of the electron beam interact with the specimen producing a large number of detectable signals [2]. Multiple scattering of the incident or primary electrons as they enter the specimen causes them to follow numerous trajectories. This diffusion of the electron beam is mainly dependent on the atomic number of the specimen and also on the energy of the primary electrons. As a result of incident electron-surface interactions x-rays, secondary electrons and visible and infrared light is generated.

The secondary electrons are of low energy (typically <50eV) and therefore escape only when created close to the surface of the specimen. For this reason secondary electrons mainly yield information about surface morphology. X-ray photons are generated by the elastic collision of the primary electrons with the atoms in the specimen which also results in the generation of back scattered electrons. The discrete energy released by this electron transition creates a characteristic x-ray photon. Every element has a specific atomic structure and therefore a unique set of x-rays. To analyse the energy and wavelength of x-ray radiation two techniques are used. These are energy dispersive x-ray spectroscopy (EDX) and wavelength dispersive x-ray pectroscopy (WDS).

5.6.3 Energy dispersive x-ray spectroscopy (EDX)

In EDX all x-rays between 1-20KeV can be seen simultaneously. Hence the time it takes to acquire enough data for quantitative analysis is greatly reduced [2]. This technique is widely used in investigating the composition of bulk materials or thick films. However, it can be limited in its accuracy (±10%) for quantitative analysis of thin films, <1μm in thickness. This technique was used for quantitative analysis of BiPbSrCaCuO films, as reported in this thesis.

5.6.4 Electron probe microanalysis (EPMA)

The electron probe microanalyser is capable of analysing thin films of up to 1μm in thickness. In this technique an electron beam of 1μm diameter impinges upon the area of interest on the film. This causes the excitation of the local atoms in that area, resulting in emission of x-rays which are characteristic of the elements present. The emitted x-rays are then directed into detectors built into the instrument. For quantitative analysis the use of standards is necessary. The standards are often pure elements. This technique provides a much higher accuracy (±3%) for quantitative analysis than EDX [2].

The electron probe technique is an effective tool in investigating the presence of different phases, segregation or grain boundaries in a sample. The probe can be used to scan along a line or over a large surface areas of about 200μm edge length, whereby the out put is displayed on a screen to show the elemental distribution [2]. The disadvantages of this method include the high cost of the equipment, the time required to analyse a sample and inadequate supply of standards.

EPMA quantitative analysis on BiPbSrCaCuO films were performed at the Centre for Material Research Institute of University College London using a JEOL JXA (8600) machine. A bulk BiPbSrCaCuO target and pure individual elements were used as standards for quantitative analysis of the films.

5.6.5 X-ray diffraction measurements

X-ray techniques based on monochromatic radiation are preferred over white radiation because the d spacing of the lattice planes in a crystal can be calculated from the observed diffraction angles. To determine the crystal orientation of thin films or polycrystalline bulk materials, the powder technique in conjunction with diffractometers is most commonly used [2]. In these instruments, the diffracted radiation is detected by counter tubes which move through the angular range of reflections. The intensities are usually recorded in a computer programme for data processing. An important feature of diffractrometers is their ability to focus into a sharp diffraction line the radiation which is Bragg-reflected from an extended specimen area. This reduces the signal to noise ratio considerably.

Bragg-Brentano diffractrometer has been used extensively in thin film work. With this technique the specimen is mounted in the centre of the diffractrometer and rotated by an angle θ around an axis in the film plane. The counter is attached to an arm rotating around the same axis by an angle 2θ twice as large as those of the specimen rotation. As the sample rotates the diameter of the focusing circle continuously decreases. Focusing is achieved by making the specimen a part of the circumference of a circle called focusing circle. In this technique only (hkl) planes parallel to the film plane contribute to the diffracted intensity.

X-rays are reflected by the ions present in any one plane of crystal. Considering ions are spaced a distance d apart and that the reflected rays from successive planes interfere constructively, then the path difference between the two rays is equal to $2d \sin \theta$, where θ is the angle of incidence. For the rays to interfere constructively, this path difference must be an integral number of wavelengths, leading to the Bragg condition

$$n\lambda=2d \sin\theta \qquad (5.1)$$

the integer n is known as the order of the corresponding reflection. The relationship between the lattice spacing, d, and Miller indecies (hkl) and the axes of an orthorhombic crystal (a, b, c)is given by,

$$\frac{1}{d^2}=\frac{h^2}{a^2}+\frac{k^2}{b^2}+\frac{l^2}{c^2} \qquad (5.2)$$

and for cubic crystal is given by,

$$d=\frac{a}{(h^2+k^2+l^2)^{1/2}} \qquad (5.3)$$

The x-ray diffraction scans provided in this thesis were recorded with Siemens x-ray diffractorometer equipment at Imperial College (Chemistry Department) using Bragg-Brentano x-ray geometry [3]. The radiation source used was CuKα radiation (1.5418Å).

5.6.7 Critical current measurements

Critical current measurements on the multilayered BiPbSrCaCuO/PbO 2223 films were carried out at Imperial College (Physics Department). The critical current densities of the films were calculated from magnetic measurements on a Vibrating Sample Magnetometer (VSM) (Oxford Instruments model 3001). This technique is described in detail in Angadi et al. [4].

5.6.8 Inductive measurements

The inductive characterization of the superconducting films was performed at Imperial College (Physics Department) on a modification of an AC susceptibility flux exclusion apparatus design at Ohio State University. The sample is laid on top of a spiral coil, which forms part of a resonant LC circuit, which in turn forms part of a electronic circuit kept at room temperature, containing a mixer and amplifiers. The DC voltage response versus frequency curve of the system contains a linear region in the vicinity of the resonant frequency (at around 1.04 MHZ). During its diamagnetic transition a superconducting sample induces a sudden change in the inductance of the flat spiral coil which shifts the DC voltage versus frequency curve. Thus, a DC voltage drop is recorded which depends crucially on the effective superconducting area screening the coil magnetic field.

References

1- L. J. Van der Pauw: Philips Research Reports 13(1), 1958.

2- L. I. Maissel and R. Glang. HandBook of Thin Film Technology. (sections 9-17, 9-18, 11-40) McGRAW-HILL publication.

3- B. D. Cullity "Elements of x-ray diffraction", Addison-Wesley, (1978).

4- M. A. Angadi, A. D. Caplin, J. R. Laverty, and Z. X. Shen. Physica C, 177, (1991), 479-486.

Chapter 6

Uniform Large Area Deposition by PLD

6.1 Introduction

In this chapter uniform film deposition over a large area using PLD is discussed. A mathematical model of a new geometry for uniform deposition over large areas is developed. It is shown that the film thickness **d**, is a function of θ, the angle of tilt and **a**, the distance between the substrate and the target.

6.2 Uniform deposition over large areas

Stoichiometric transfer of the species from target to substrate as well as high growth rate in PLD has put this technique in a unique position among various film deposition techniques. However, it has been suggested that this technique could be limited by its ability to deposit layers uniformly over a large area [1]. Neifield et al. [1] have shown that the ejected particles follow a profile of the form $\cos^n \phi$, where ϕ is the angle between the surface normal and the direction of the ejected particles. To overcome this limitation several methods including target scanning have been presented [2-4].

A probable solution to this problem is to simply tilt the target away from its normal horizontal position and hence create an angle of wobble on the target. A schematic diagram of the ablation system incorporating an angle θ on the target is shown in figure 6.1. In the following sections a mathematical model of this geometry is developed and theoretical and experimental data in support of this model is presented.

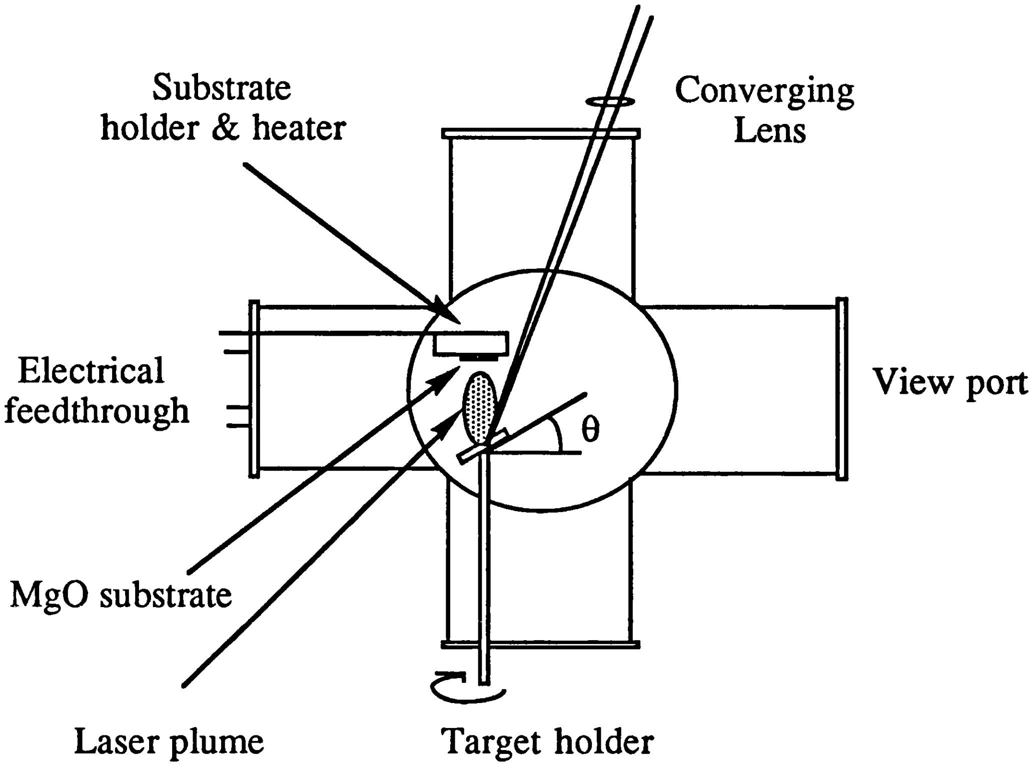

Figure 6.1- *Schematic representation of the laser-ablation system, with an angle of wobble on the target, applied for growth of thin films.*

6.3 Mathematical model for uniform film deposition over large areas

The growth of uniform superconducting films over large areas by PLD may be considered as a flux transfer problem. The concept of radiance in radiometry specifies, over large angles, the distribution of flux with respect to position and direction. It is defined as the flux per unit projected area and solid angle, L, given by

$$L = \frac{d^2 \phi}{d\omega \ \cos\theta \ dA} = \frac{d^2 \phi}{d\Omega \ dA} = \frac{d^2 \phi}{dT} \qquad (6.1)$$

where ω is the solid angle, A=area, θ is the angle subtended by ω with respect to the normal to A; Ω is the projected solid angle and T is the throughput.

The amount of flux transferred from the source to the receiver is found by considering a flux source of area δA_1 and a receiver of area δA_2, as is shown diagrammatically in figure 6.2.

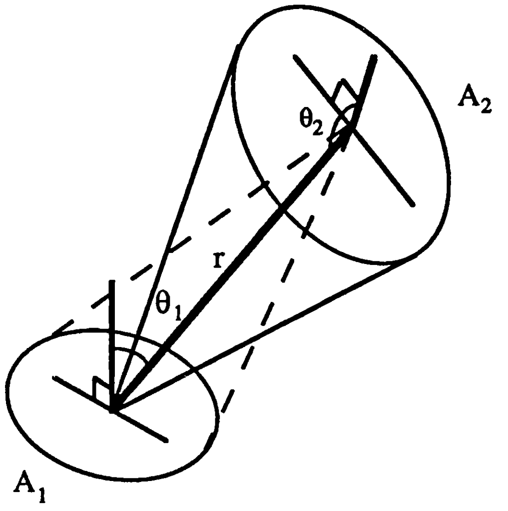

Figure 6.2- *Model of flux source of area δA_1 and a receiver of area δA_2. The distance between the flux and the receiver is r.*

The solid angle subtended by the receiver element at the source is then

$$\delta \omega_1 = \frac{\cos\theta_2 \; \delta A_2}{r^2} \tag{6.2}$$

and at the receiver by the source is

$$\delta \omega_2 = \frac{\cos\theta_1 \; \delta A_1}{r^2} \tag{6.3}$$

Therefore

$$L = \frac{\delta \phi}{\delta \omega_1 \; \cos\theta_1 \, \delta A_1} = \frac{\delta \phi}{\delta \omega_2 \; \cos\theta_2 \; \delta A_2} \tag{6.4}$$

This shows that the radiance L is a function of θ_1 and θ_2. By analogy to the radiance system then the ablation system shown in figure 6.3 can be modelled in the following manner:

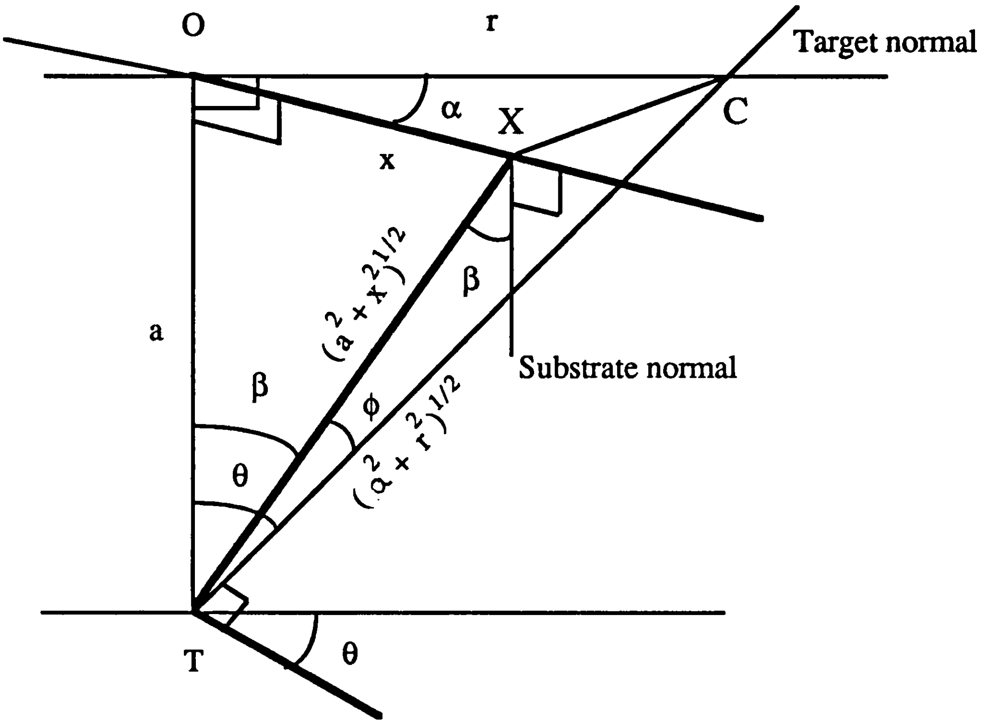

Figure 6.3- *Geometrical representation of the laser ablation system: T=Target, O=Centre of substrate, C=Centre of distribution and X=Point on substrate.*

Other parameters are TC= normal to target, OT= normal substrate, θ= target inclination, φ= angle CTX, β= angle CTO and α= angle XOC.

Applying the radiance equation to the ablation system

$$\delta\phi = L\delta A_T \cos\phi \left[\frac{\delta A_x \cos\beta}{a^2 + x^2}\right] \qquad (6.5)$$

where A_T is the target area, $\delta A_x = x\,\delta\alpha\,\delta x$ and

$$\cos\beta = \frac{a}{(a^2 + x^2)^{1/2}} \qquad (6.6)$$

It follows that

$$\frac{\delta\phi}{\delta A_T} = L\cos\phi\ \cos^3\beta \left(\frac{x}{a^2}\right) \delta\alpha\ \delta x \qquad (6.7)$$

The total flux received by the substrate from a point on the target is then

$$\frac{\phi}{\delta A_T} = \frac{1}{a^2}\int_0^x \frac{xa^3}{\left[(a^2 + x^2)^3\right]^{1/2}} \left[\int_0^{2\pi} L \left[\frac{a^2 + xr\cos\alpha}{\left[(x^2 + a^2)(a^2 + r^2)\right]^{1/2}}\right]^n d\alpha\right] dx \qquad (6.8)$$

For a Lambertian source such as a black body L is a constant and n=1. Considering the target as a black body, then

$$\frac{\phi}{\delta A_T} = \frac{1}{a^2}\int_0^x \frac{xa^3}{\left[(a^2 + x^2)^3\right]^{1/2}} \left[\frac{2L\pi a^2}{\left[(x^2 + a^2)(a^2 + r^2)\right]^{1/2}}\right] dx \qquad (6.9)$$

this can be re-written as

$$\frac{\phi}{\delta A_T} = \frac{2 L \pi a^3}{\left[(a^2 + r^2) \right]^{1/2}} \int_0^x \frac{x}{(x^2 + a^2)^{1/2}} dx \qquad (6.10)$$

However,

$$\cos\theta = \frac{a}{(a^2 + r^2)^{1/2}} \qquad (6.11)$$

and by letting $u^2=a^2+x^2$, the total flux received by the substrate could be rewritten as

$$\frac{\phi}{\delta A_T} = L\pi a^2 \cos\theta \left[\frac{-1}{(a^2 + x^2)} \right]_0^x = L\pi a^2 \cos\theta \left[\frac{1}{a^2} - \frac{1}{a^2 + x^2} \right] \qquad (6.12)$$

The flux at a point x on the substrate is found by considering the flux received by the small area $2\pi x \delta x$ on the substrate. By rotating the target, each point in the area the flux with respect to all the possible ϕ angles (β is fixed because **x** and **a** are fixed) for one rotation (from 0 to 2π).

By considering a point in this small area the total flux received at that point is

$$\frac{\delta \phi}{\delta A_T} = \frac{\cos^3\beta}{a^2\, 2\pi} \int_0^{2\pi} L \left[\frac{a^2 + xr\cos\alpha}{\left[(a^2 + x^2)(a^2 + r^2) \right]^{1/2}} \right]^n d\alpha \qquad (6.13)$$

The film thickness d of the deposited material at the point x is then given by

$$d = \frac{La}{2\pi\ (a^2 + x^2)^{3/2}} \int_0^{2\pi} \left[\frac{a^2 + xr\cos\alpha}{\left[(a^2 + x^2)(a^2 + r^2)\right]^{1/2}} \right]^n d\alpha \qquad (6.14)$$

This formula shows that the film thickness is a function of θ, the angle of tilt and a, the distance between the substrate and the target. By using equation 14, the atomic distribution for various angles of tilt (θ) were calculated and are shown in figure 6.4.

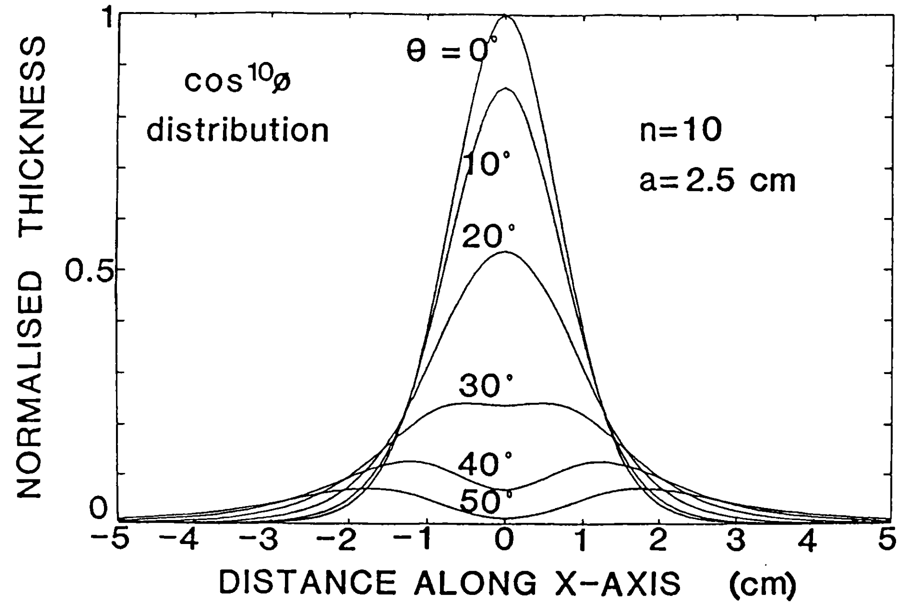

Figure 6.4- *Theoretical film thickness profile representation of the atomic distribution for various angles of tilt (θ).*

In agreement with the generally observed experimental result a $\cos^{10}\phi$ profile is calculated for the condition of θ=0. This implies that a high portion of the ablated species are deposited at the central region of the substrate followed by a sharp fall in film thickness away from this region. However, as θ is increased a smearing out of the profile is predicted, resulting in a more uniform film.

The uniformity of the deposited film also depends on the distance between the target and the substrate. Figure 6.5 shows derived film thickness profiles calculated as a function of substrate target distance **a** assuming a fixed θ of 30°.

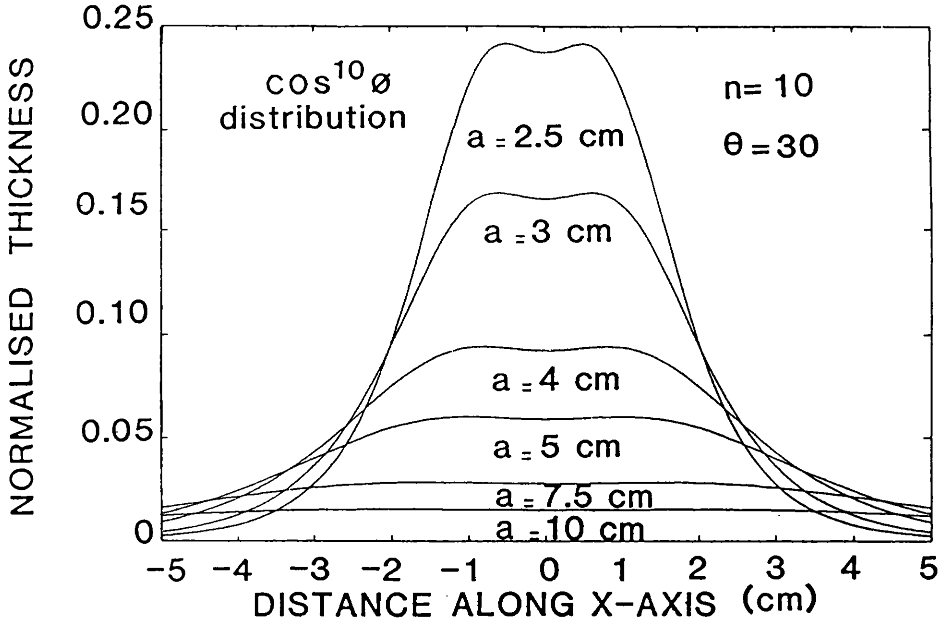

Figure 6.5- *Theoretical film thickness profile produced by cos* $^{10}\phi$ *distribution for various target-substrate distances.*

The patterns show that the larger the target-substrate distance the more uniform the films will be over a wider area. However, uniformity is achieved at the expense of a reduction in the film thickness.

6.4 Experimental studies for uniform film deposition by PLD

To verify the theoretical modelling of laser ablation experimentally, BiPbSrCaCuO films were deposited on Si or MgO substrates kept at room temperature from a 2212 target held at various tilting angles θ with respect to its normal plane of rotation. This was made possible by the design of a new target holder which could be tilted through ±30°, creating an angle, θ, to its normal axis of rotation. Figure 6.6 illustrates a schematic diagram of this target holder.

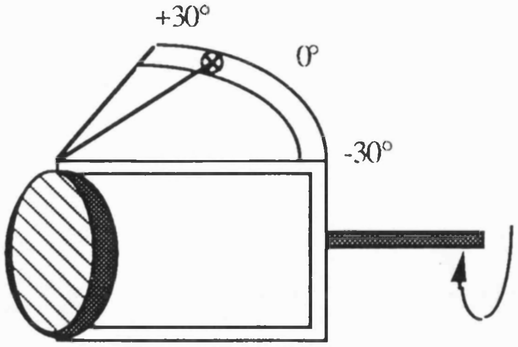

Figure 6.6- *Schematic diagram of the target holder.*

The films were grown using a Nd-YAG laser operating at 532nm (500mJ/pulse) with a repetition frequency of 10Hz and a pulse-width of 4ns. The beam was focused by a converging lens to a spot size of 3.0mm on a slowly rotating target (5 Rev/min). During the deposition the chamber pressure was kept at 1.0x10^{-2}mbar. The deposited films were shiny, amorphous, and insulating. The thickness of the deposited BiPbSrCaCuO films were were measured by Talystep (10Å resolution). Figure 6.7 shows the measured film thickness obtained, with a fixed at 2.5cm, for various tilting angles, θ, in the range of 0-30°.

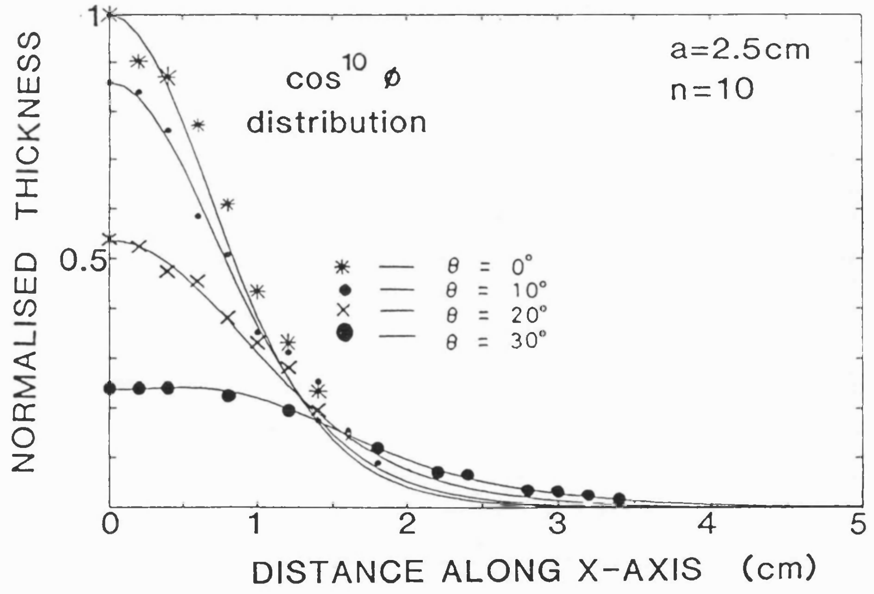

Figure 6.7- *Film thickness data obtained at various angles of tilt $\theta=0°$, $10°$, $20°$ and $30°$ compared with theoretical curves with target-substrate distance kept at 2.5cm.*

The patterns show that for θ=0° the measured data is consistent with a $\cos^{10}\phi$ distribution over the central region of the substrate. As θ° is increased a wider area in uniformity is obtained over the central region. At θ=30° the data supports the modelled profile of a uniform film covering $3cm^2$ in the central region. However, a reduction in film thickness is noticeable for θ=30° when compared with films deposited from θ=0°. This indicates that if thicker films are required longer deposition time is needed.

6.6 Conclusion

A mathematical model was presented for thin uniform film deposition incorporating an "angle of wobble" on the target. It was shown that film thickness d is a function of θ, the angle of tilt and a, the distance between the substrate and the target. Experimental data was presented that supported the numerical simulations of the mathematical model.

References

1- R. A. Neifield, S. Gunapala, C. Liang, S. A. Shaheen, M. Croft, J. Price, D. Simons, and W.T. Hill,. Appl. Phys. Lett. 53 (1988), 703.

2- P. V. Kolinsky, P. May, M. R. Harrison, P. Miller, and D. Jedamzik. Supercond. sci. Technol. 1 (1989), 333.

3- M. F. Davis, J. Wosik, K. Foster, S. C. Deshmukh, H. R. Rampersad, S. shah, P. Siemsen, J. C. Wolfe, and D. J. Economou. J. appl. Phys. Lett. 69, (10), (1991), 7182-7188.

4- M. Brown, M. Shiloh, R. B. Jackman, and I. W. Boyd. Appl. Surf. Sci. 43, (1989), 382.

Chapter 7

Thin Film Growth of $(BiPb)_2Sr_2CaCu_2O_x$ High T_c Superconductor

7.1 Introduction

In this chapter in-situ and ex-situ results of the thin film growth of $(BiPb)_2Sr_2CaCu_2O_x$ on MgO substrates are discussed. The aim of this study was to grow the 2212 phase of the BiSrCaCuO system by ex-situ and in-situ process. In that context the growth parameters such as annealing temperature and duration for ex-situ process and O_2 pressure and substrate temperature for in-situ growth process were optimised.

7.2 Target preparation

The targets were prepared by the solid state reaction of Bi_2O_3, PbO, $SrCO_3$, $CaCO_3$, CuO powders. The atomic ratios of Bi:Pb:Sr:Ca:Cu:O was (1.8: 0.32: 2: 1: 2). The powder mixture was well mixed and ground in a mortar with pestle before being pressed in a stainless steel die under 500Mpa to form a pellet of 12mm in diameter. The pellet was placed on a MgO single crystal plate and fired at 800°C for 20 hours. After the heat treatment the pellet was crushed, reground, and pressed under 500Mpa to form a new pellet. This was then heat treated at 845°C for a total annealing time of 96 hours with several intermediate grindings.

7.3 Ex-situ growth of $(BiPb)_2Sr_2CaCu_2O_x$ thin films

The incident Nd-YAG laser beam was focused on the BiPbSrCaCuO target to a spot diameter of ≈ 3.0 mm. During the deposition process the target was slowly rotated at a rate of 5 rev/min. The target-substrate distance was fixed at 3.5cm. BiPbSrCaCuO films were deposited in a vacuum pressure of $1x10^{-3}$mbar and in an oxygen partial pressure of $5x10^{-2}$mbar. The films were deposited on MgO substrates (001) orientation heated to temperatures not exceeding 550°C or held at room temperature. The MgO substrates were cleaned in acetone and ethanol for a few minutes and blown dry with nitrogen gas. Deposition time of 10 minutes resulted in film thickness of ≈1.2μm (as measured by talystep). The growth rate was estimated to be ≈20Å/s.

In the first set of experiments BiPbSrCaCuO films were deposited in a partial pressure of oxygen at various substrate temperatures. These films were subsequently annealed in a tube furnace in the temperature range of 850-900°C for various duration in air, followed by furnace cooling to room temperature. Annealing the films in the temperature range of 850-860°C in air resulted in the formation of the superconducting 2212 phase. However, the resistivity versus temperature of these films did not exhibited a zero resistance value even though $T_{c,\ onset}$ as high as 85K was obtained, see figure 7.1. The films exhibited a semiconducting behaviour at or above 870°C.

In the second set of experiments BiPbSrCaCuO films were deposited in a vacuum pressure of 1×10^{-3}mbar. These films were subsequently annealed in the tube furnace at a set temperature in the range of 840-860°C for various annealing periods, followed by air quenching. In general, all BiPbSrCaCuO films exhibited superconductivity. However, films that were annealed between 20-60 minutes showed a superior superconductivity transition temperature than those annealed for shorter or longer periods. Short time annealing (>20 minutes) resulted in the formation of the 2212 phase and large concentration of needle type crystals with composition $(Ca, Sr)_2CuO_3$. Annealing for longer than 60 minutes resulted in considerable film evaporation and degradation of the film superconducting properties. Figure 7.1 shows plots of $T_{c,\ onset}$ for $(BiPb)_2Sr_2CaCu_2O_x$ films deposited in oxygen and vacuum and annealed in the temperature range of 840-860°C. The data show that the optimum $T_{c,\ onset}$ for both sets of films is obtained at annealing temperature of 855°C. Figure 7.2 illustrates $T_{c,\ onset}$ and $T_{c,\ zero}$ for films deposited in vacuum and annealed at 850°C for different periods.

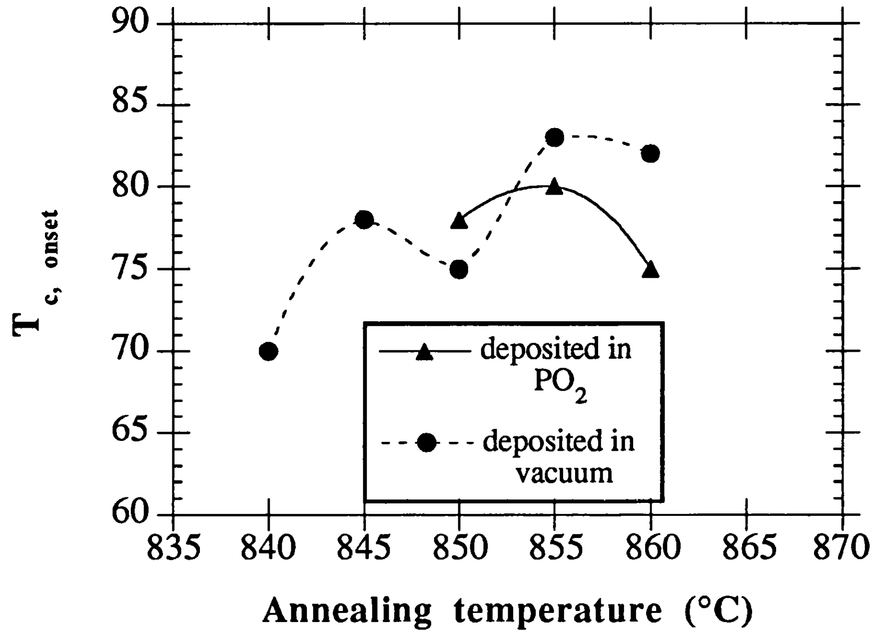

Figure 7.1- $T_{c,\ onset}$ *of* $(BiPb)_2Sr_2CaCu_2O_x$ *films as a function of different annealing temperatures for films deposited in oxygen and vacuum.*

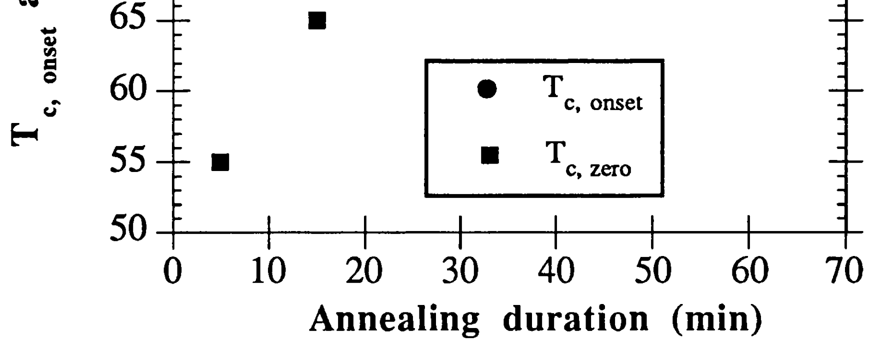

Figure 7.2- $T_{c,\ onset}$ *and* $T_{c,\ zero}$ *of 2212 films deposited in vacuum and annealed at 850°C for 5 to 60 minutes in air.*

The data set show a progressive improvement in $T_{c,\ zero}$ as a function of longer annealing period. The crystallinity of the films annealed in the temperature range of 840-860°C was investigated by XRD. The patterns shown in figure 7.3 indicate that the optimum annealing temperature for the growth of the 2212 phase is 845°C. Below this temperature the films are not textured. Annealing at higher temperatures results in the formation of other crystal orientation such as the (113) at 2θ=24.8°, the (115) at 2θ=27.5°, and the (117) at 2θ=31° of the 2212 phase. The formation of the 2201 phase at higher annealing temperature is due to the decomposition of the 2212 phase [5].

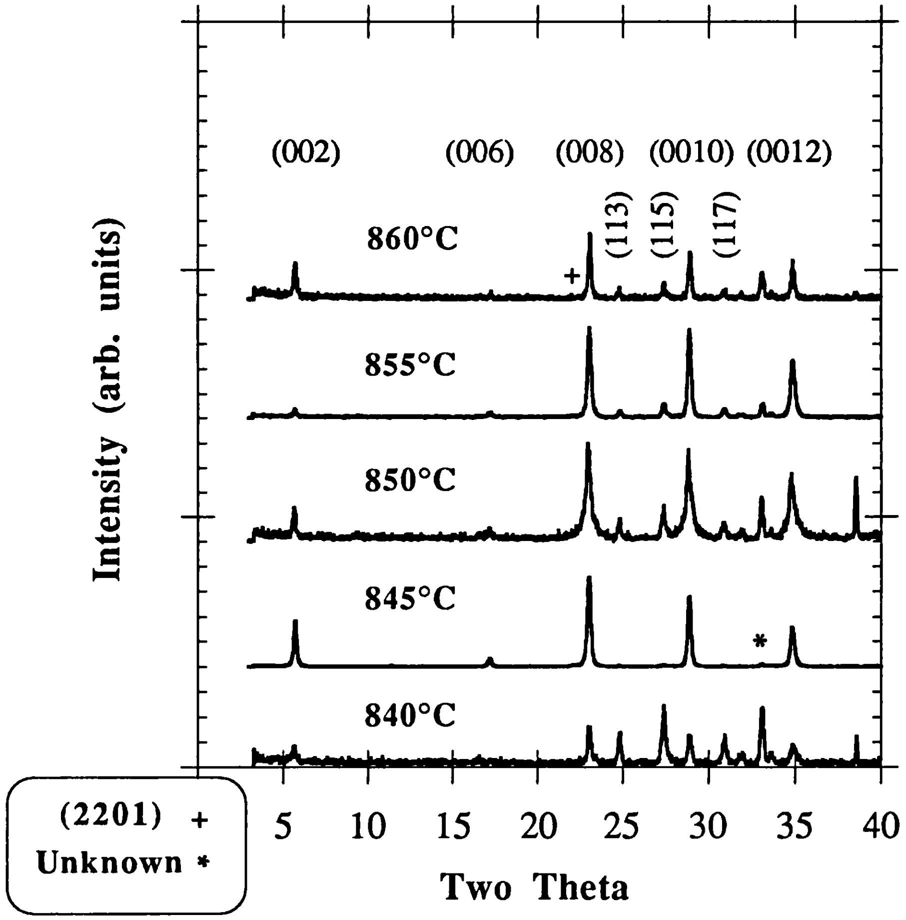

Figure 7.3. *X-ray diffraction patterns of (Bi, Pb)SrCaCuO thin films annealed between 840°C to 860°C for 20 min, in air. The symbols (+) and * are assigned to the (2201) and the unknown phases.*

Although x-ray diffraction pattern of the film annealed at 845°C shows an almost pure 2212 phase, the zero resistance value of this film did not exceed 65K, which is 15K below the ideal value (80K) for the 2212 phase. To investigate the reduction in $T_{c,\ zero}$, morphology of the film was examined by SEM and its chemical composition was analysed by EDX. The SEM observation shown in figure 7.6(a) revealed the presence of both needle and plate shaped crystals. Chemical analysis of the crystals by EDX identified the plate and needle shaped crystals as near 2212 and $(Ca, Sr)_2CuO_3$, respectively. Although the plate type crystals, shown in figure 7.6(a), are well connected with dimensions between 10-20μm, it is conceivable that the presence of the $(Ca, Sr)_2CuO_3$ phase in large concentration could act to influence the percolation path of current by deviating the composition of the grain boundaries from that of the ideal 2212 and hence result in degradation of $T_{c,\ zero}$ of the film.

Earlier it was mentioned that the concentration of the needle type crystals decreased considerably with longer annealing period from 5 to 20 minutes. To investigate the effect of longer annealing duration on the needle type crystals, BiPbSrCaCuO films were annealed up to 24 hours in air. To overcome film evaporation, the films were annealed next to the original target in a closed gold foil. The process of film-target encapsulation, however, lowered the annealing temperature for the formation of the 2212 phase from 845°C to 840°C. Figure 7.4 shows x-ray diffraction pattern of a typical BiPbSrCaCuO film annealed in air at 840°C for 16 hours. The pattern indicates a near pure 2212 phase with a high degree of c-axis orientation perpendicular to the substrate. The superconducting properties of this film, measured by the Van de Pauw and inductive techniques, shown in figure 7.5, indicate a substantial improvement in $T_{c,\ onset}$ to 85K and $T_{c,\ zero}$ to 80K with longer annealing duration. The inductive measurements of the film shown in the inset indicates that the film has entered into the superconducting state at 80K.

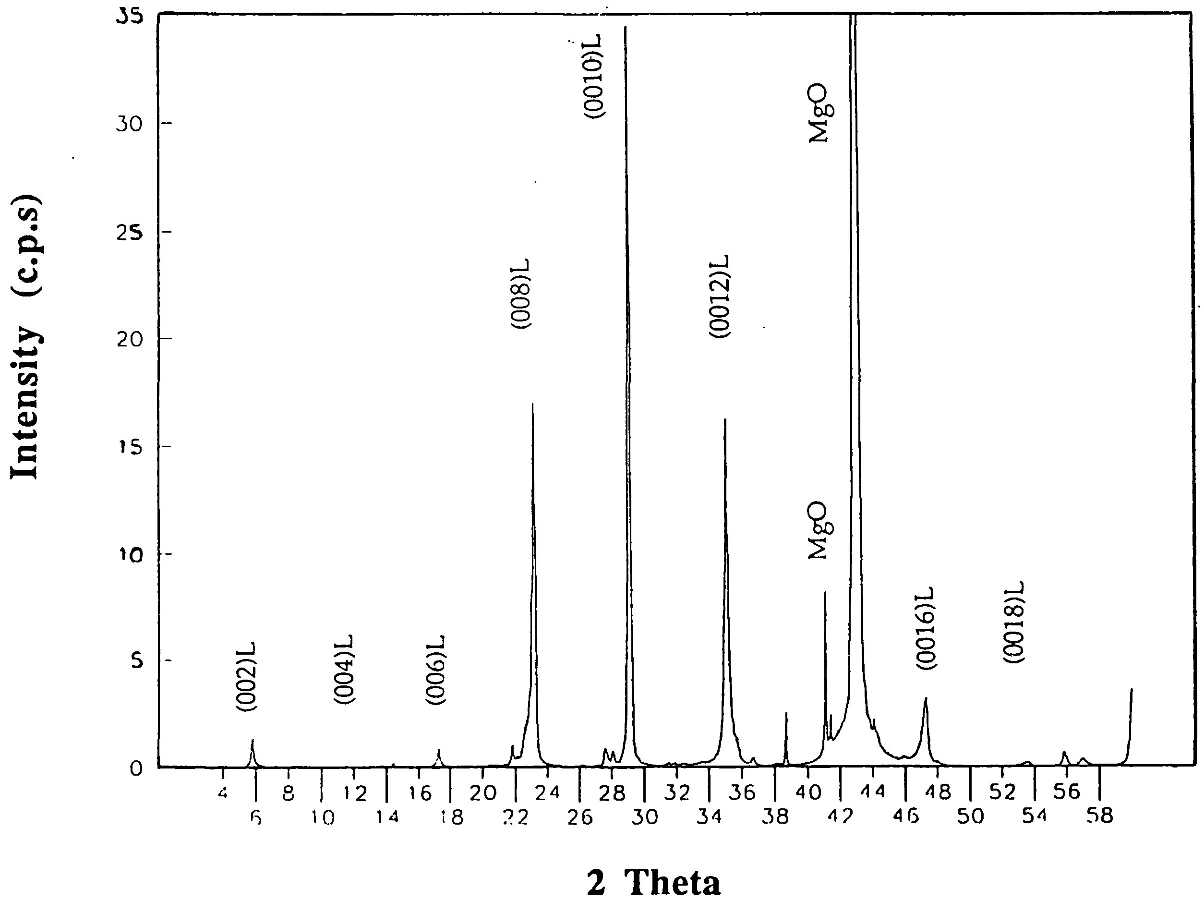

Figure 7.4- *X-ray diffraction pattern of the film annealed at 840 ℃ for 16 hours in air.*

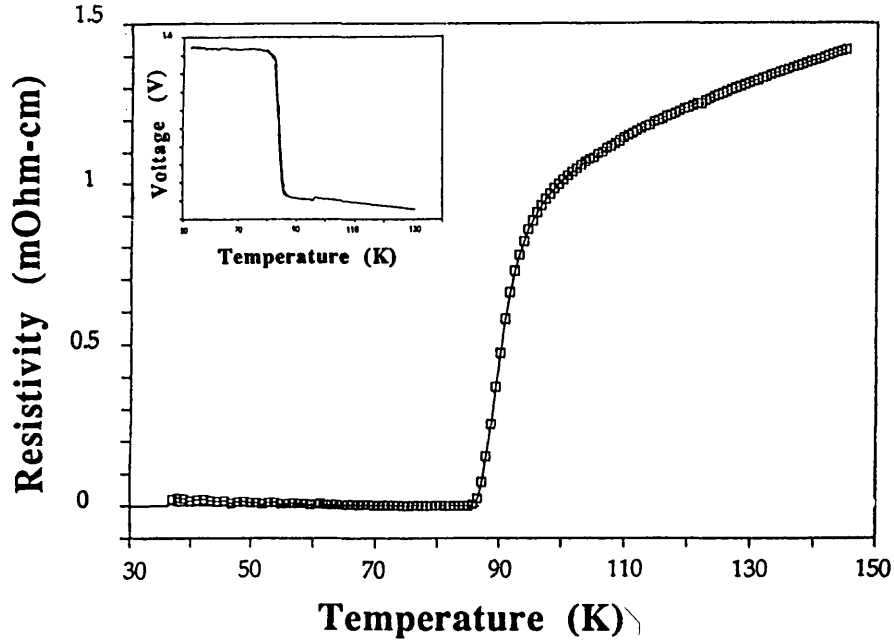

Figure 7.5- *Resistivity versus temperature of the film annealed at 840 ℃ for 16 hours in air. The inset shows inductive measurement o this film.*

The SEM micrograph of this film shown in figure 7.6 (b) illustrates the presence of very large well connected plate type crystals of 10s of microns in size as well as a few needle type crystals. However, comparatively the plate type crystals are much larger in dimensions and cover the whole of the film. The critical current density J_c of this film, measured by applied magnetic field technique and was found to be 1000 A/cm^2 in a zero field at 70K.

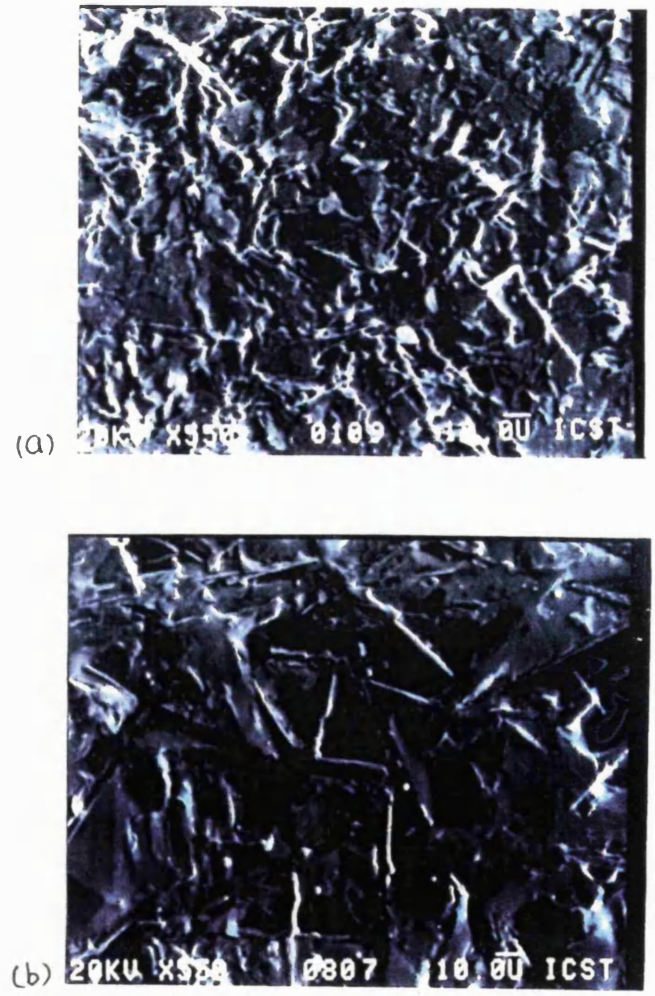

Figure 7.6- *SEM micrograph of the BiPbSrCaCuO films, a) annealed at 845 °C for 20 min, b) annealed at 840 °C for 16 hours, in air followed by air quenching.*

7.4 In-situ growth of BiSrCaCuO 2212 films by other groups

In-situ film growth of the 2212 phase with high T_C and reasonable J_C has been demonstrated by various deposition techniques including pulsed laser deposition and sputtering [6-8]. Table (7.1) summarises the growth parameters used by other groups for in-situ pulsed laser deposition of the 2212 phase.

T_s range (°C)	PO_2 (mbar)	$T_{c,\ zero}$	J_c (A/cm^2)	References
710-810	0.3	70	10^6 (at 4K)	[9]
600-700	10^{-2}	76	1.5×10^5 (at 40K)	[8]
700-750	0.2	73	not given	[10]
750-790	0.2	83	not given	[11]
700	0.1	not given	not given	[12]

Table (7.1)- *Summary of the PLD parameters used by other groups for in-situ deposition of the 2212 phase.*

The data in table (7.1) indicate that the substrate temperature lies between 600-810°C and the oxygen partial pressure (PO_2) between 0.07-0.4mbar for in-situ growth of the 2212 phase by PLD. The published reports on in-situ thin film growth of the 2212 phase by the sputtering technique, however, indicate the use of higher oxygen partial pressure, between 0.2-0.6mbar and lower substrate temperatures, between 630-690°C [7, 14, 15]. Figure 7.7 illustrates Oxygen partial pressure versus substrate temperature diagram for BiPbSrCaCuO, 2212 phase, grown by PLD and sputtering techniques. The data used for construction of this diagram was extracted from the literature.

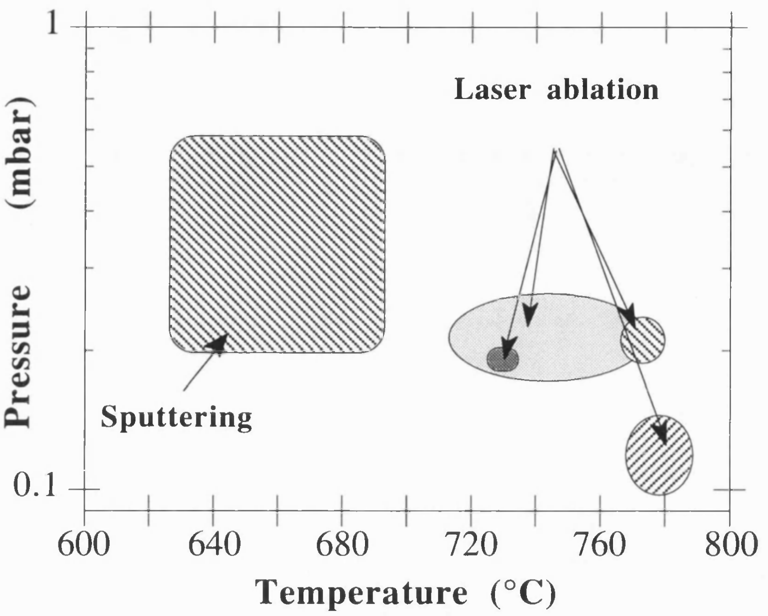

Figure 7.7- *Oxygen partial pressure versus substrate temperature diagram for BiPbSrCaCuO (2212 phase) grown with the pulsed laser deposition and sputtering techniques . Data from the following references [8-16].*

By comparing the published processing conditions employed for obtaining in-situ c-axis 2212 films in PLD and sputtering techniques, it emerges that PLD requires a higher growth temperature and a lower oxygen partial pressure than sputtering. The difference in growth temperature between the two techniques could be attributed to the nature of the kinetics of the evaporated materials. To lower the in-situ growth temperature in PLD, Y. Egami et al. [17] have used a gas mixture of $N_2O:O_2$ (1:1) instead of oxygen. They have shown that by using this gas mixture good quality 2212 films could be grown at substrate temperatures as low as 600°C.

7.5 In-situ growth of $(BiPb)_2Sr_2CaCu_2O_x$ thin films

The incident Nd-YAG laser beam was focused on the BiPbSrCaCuO target to a spot diameter of ≈ 3.0 mm. BiPbSrCaCuO films were grown on MgO substrates (001) orientation from targets with atomic ratios of Bi:Pb:Sr:Ca:Cu (1.68:0.32:1.75:1.82:2.75). The target-substrate distance was adjusted to 3.0 cm for these experiments. MgO substrates were cleaned in acetone and ethanol for a few minutes and blown dried with nitrogen gas. Before the deposition , the substrates were heated in the deposition atmosphere (O_2) to temperatures above deposition temperature for 5-10 minutes. The substrate temperatures indicated here are those of the heater and not of MgO substrates.

In the initial set of experiments the deposition pressure was kept constant at 0.02mbar, whilst the substrate temperature was varied from 650°C to 750°C. After the deposition the heater was turned off and the samples were cooled down naturally under oxygen pressure of 1 bar. The films then were taken out of the deposition chamber at temperatures below 200°C. Deposition duration of 2 minutes resulted in film thickness of ≈150nm. In the second set of experiments the oxygen pressure was varied from 0.5mbar to 0.01mbar while the substrate temperature was kept constant at 720 and 740. Figure 7.8 illustrates BiPbSrCaCuO films grown with different phases as functions of oxygen pressure and substrate temperature.

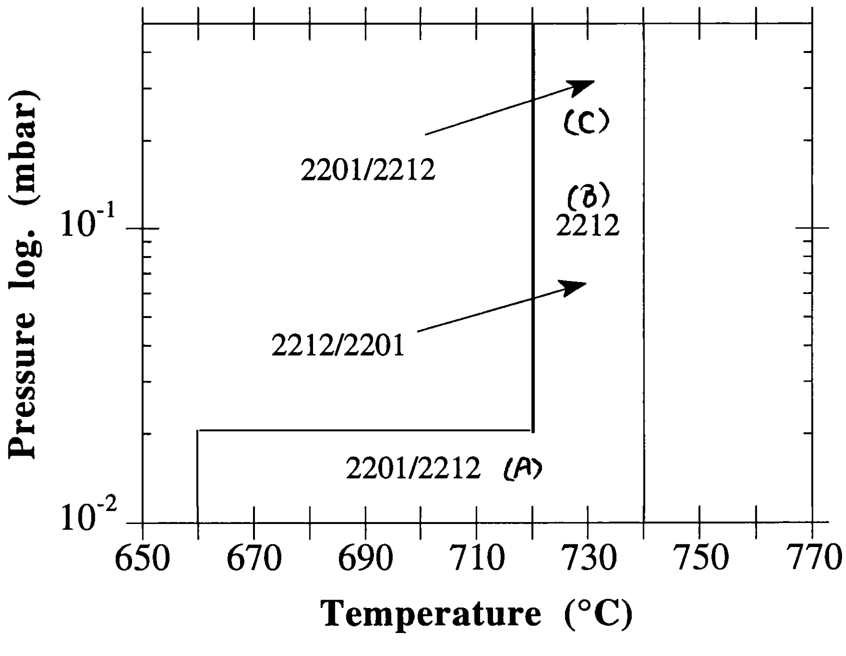

Figure 7.8- *Oxygen pressure-substrate temperature phase diagram for as grown thin BiPbSrCaCuO films.*

BiPbSrCaCuO films deposited in the temperature range of 660-740°C under oxygen pressure of $2x10^{-2}$mbar showed mixed phases of 2201/2212, with the 2201 phase being the main constituent. At substrate temperatures of 720-750°C range and oxygen pressures of 0.06-0.08mbar both phases were still present, however, in this region the 2212 phase is the main constituent. This pattern continues with increase in oxygen pressure and at pressures of around 0.1mbar a pure 2212 film is obtained. Keeping the substrate temperature constant whilst increasing the oxygen pressure further resulted in the formation of BiPbSrCaCuO mixed films of 2201/2212. Films deposited above 780°C in low oxygen pressure of $1.2x10^{-2}$mbar showed no sign of crystallization, indicating the amorphous state or decomposition of the material. Figure 7.9 illustrates XRD patterns of as-grown BiPbSrCaCuO films corresponding to the areas shown in figure 7.8.

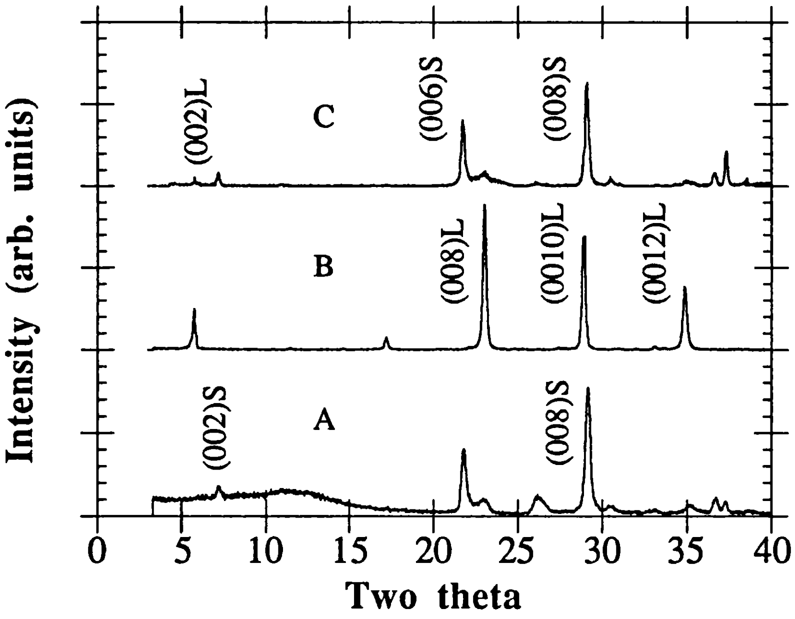

Figure7.9- *X-ray diffraction patterns of as-grown BiPbSrCaCuO films. A corresponds to* $PO_2=1.0x10^{-2}$*mbar with* $T_s=680°C$*, B corresponds to* $PO_2=1x10^{-1}$*mbar with* $T_s=720°C$*, and C corresponds to* $3x10^{-1}$*mbar with* $T_s=720°C$*.*

Unfortunately, the in-situ films generally presented poor superconducting properties even in the 2212 film. This was attributed to oxygen deficiency of the 2212 films. Figure 7.10 shows resistance versus temperature of the film grown at substrate temperature of 720°C with partial pressure of PO_2=0.1mbar. The film exhibits $T_{c,\ onset}$ of 80K and $T_{c,\ zero}$ below 40K. There are a number of methods that can be used to introduce oxygen into the deposited films in order to provide superconductivity. These include i) depositing at higher oxygen pressures ii) using plasma assisted laser deposition iii) conducting a low temperature annealing in the deposition chamber. The first method could result in the formation of mixed 2212/2201 phases as shown in the phase diagram, figure 7.8. The second method, however, entails an annealing stage at 400°C between 30 minutes to an hour in an oxygen atmosphere of 1 bar [11]. This method has been demonstrated to be an effective way of compensating the oxygen deficiency in the BiSrCaCuO (2212) films. The third method has been also shown an effective way of introducing oxygen into the 2212 films during the deposition process. Poulin et al. [11] have shown an increase of 5K in $T_{c,\ zero}$ value of the 2212 films by using this technique.

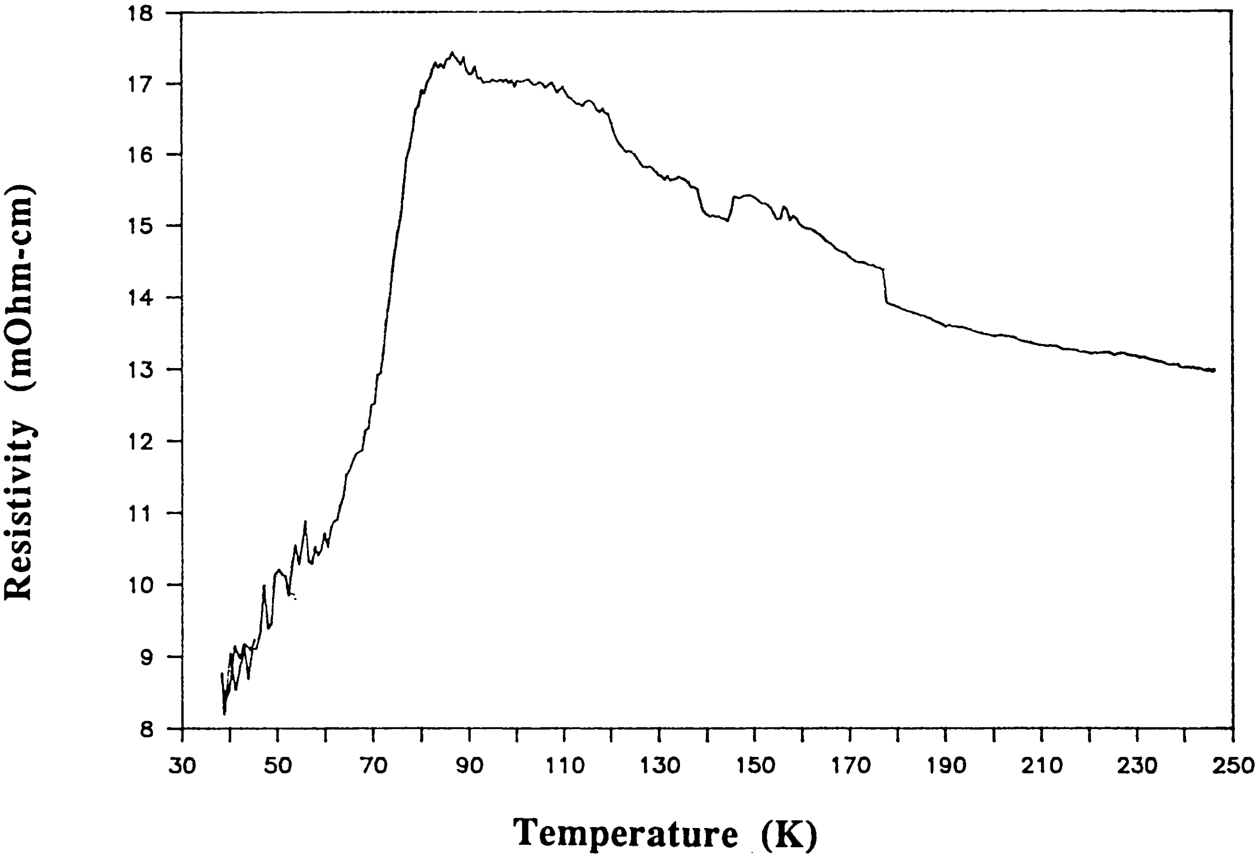

Figure 7.10- *Resistance versus temperature of a as-grown 2212 BiPbSrCaCuO film.*

The oxygen partial pressure-substrate temperature phase diagram for BiPbSrCaCuO films shown in figure 7.8 indicates that in order to obtain a pure c-axis 2212 BiPbSrCaCuO films both substrate temperature and oxygen pressure should be optimised. However, the conditions required for the growth of the crystalline 2212 phase might not necessarily correspond to the conditions needed for superconductivity of the film. This paradox is caused by the multiphase characteristic nature of the BiSrCaCuO system. An alternative approach, taken by many groups in this field [11, 17, 18] , is to optimise the conditions needed for superconductivity of the film and then through a trial and error process adjust the composition of the target for growing the required phase.

7.6 Conclusion

$(BiPb)_2Sr_2CaCu_2O_x$ thin films were grown on MgO substrates by ex-situ annealing process. In this process the annealing temperature was shown to be crucial for obtaining a highly c-axis 2212 film. Also, the superconducting properties of the films was shown to be determined by the annealing period. In-situ thin film growth of the 2212 phase was demonstrated by PLD technique. It was shown that phase control of BiPbSrCaCuO films is possible by varying the substrate temperature and oxygen pressure. The oxygen partial pressure-substrate temperature phase diagram for BiPbSrCaCuO films indicates that in order to obtain a pure c-axis 2212 BiPbSrCaCuO films both substrate temperature and oxygen pressure should be optimised. However, the conditions required for the growth of the crystalline 2212 phase might not necessarily correspond to the conditions needed for superconductivity of the film. This therefore entails adjustment of the target composition for a set of deposition parameters that yield superconductivity as well as crystallinity.

References

1- T. Kotani, H. Takei, and K. Tada. Physica C. 185-189, (1991), 447-448.

2- Z. Ivanov, and G. Brorsson. Appl. Phys. Lett. 55 (20), (1989), 2123-2125.

3- J. S. Moodera, A. M. Rao, A. Kussmaul, and P. M. Tedrow. Appl. Phys. Lett. 57, (23), (1990), 2498-2500.

4- E. Narumi, J. Lee, C. Li, S. Hosokawa, S. Patel, and D. T. Shaw. Appl. Phys. Lett. 59(24), (1991), 3180-3182.

5- F. S. Razavi, H. U. Habermeier, and P. Majewski. Max-Planck-Institute fur Festkorperforschung, (private communication).

6- M. Viret, J. F. Lawler, and J. G. Lunney. Supercond. Sci. Technol. 6, (1993), 490-496.

7- G. Poullain, R. Desfeux, and H. Murray. Physica C, 214, (1993), 195-203.

8- L. Ranno, R. M. defourneau, J. P. Enard, J. Perriere, and D. Martinez-Garcia. E-MRS, Fall (1992).

9- H. C. Yang, M. C. Kim, and H. Horhg. Jpn. Appl. Phys. 31, (1992), 44-46.

10- A. Agarwal, R. P. Gupta, W. S. Khokle, K. D. Kundra, P. R. Deshmukh, M. Singh, and P. D. Vyas. Supercond. Sci. Technol. 6, (1993), 670-673.

11- A. Kumar, L. Ganapathi, and J. Narayan. Appl. Phys. Lett.56, (20), (1990), 2034-2036.

12- J. S. Moodera, A. M. Rao, A. Kussmaul, and P. M. Tedrow. Appl. Phys. Lett. 57, (23), (1990), 2498-2500.

13- Y. Egami, H. Tabata, M. Kinugasa, T. Kawai, and S. Kawai. Jpn. J. Appl. Phys. 30(3B), (1991), L478-L481.

14- Y. Hakuraku, K. Nagayama, and T. Ogushi. Supercond. Sci. Technol. 4, (1991), 717-720.

Chapter 8

Thin Film Growth of $(BiPb)_2Sr_2Ca_2Cu_3O_{10+\delta}$ High T_c Superconductor

8.1 Introduction

The thin film growth of BiPbSrCaCuO (2223) by PLD technique using ex-situ annealing is discussed in this chapter. The objective of this study was to optimise the processing conditions necessary for the thin film growth of the 2223 phase. In that context, the effect of post annealing conditions (i.e., annealing temperature, duration, and atmosphere) as well as Pb doping concentration in the formation of this phase was investigated.

In the first section of this chapter, thin film growth of the 2223 phase from a single (BiPb)SrCaCuO target is described. It is shown, however, that this approach is not effective in obtaining a high proportion of the 2223 phase (> 50%). This is found to be due to the evaporation of Pb at an early annealing stages from the film (due to low melting point and high vapour pressure of Pb). To overcome this problem an approach of depositing multilayers of PbO between several layers of BiPbSrCaCuO was utilised. Using the multilayered (BiPb)SrCaCuO/PbO technique Pb could in sufficient quantity be doped in the BiSrCaCuO films to facilitate the growth of the 2223 phase. The characterisation of the films were carried out using EDX, EPMA, SEM, XRD, and resistivity methods.

8.2 The 2223 phase in the Bi-Sr-Ca-Cu-O system

The Bi-Sr-Ca-Cu-O system is possibly the most complex system among the high temperature superconductors. The phase diagram constructed by binary oxides, namely alkaline-earth bismuthates and alkaline-earth cuperates, has been extended into ternary and recently, slightly into quaternary space [1-4]. The quaternary system Bi_2O_3-SrO-CaO-CuO has been shown to contain twenty one phases which includes a liquid phase when prepared at 850°C in air. This illustrates the complexity of phase formations associated with this system and the enormous task ahead of scientists to complete its phase diagram.

The 2223 phase has especially attracted the attention of the scientific community for its high T_c (110K). The growth of the 2223 phase in pure form, however, has not been an easy task. This is due to a number of constraints associated with its growth mechanism. For instance, the Bi system contains five different cations if the partial substitution of Bi by Pb is included. These cations have dissimilar mobilities and reaction chemistry, resulting in inhomogeneous distribution of phases. Furthermore, the temperature range for the formation of the 2223 phase is limited and is critically dependent on the starting composition [5, 6]. In addition, since the 2223 phase has structural similarities to the 2212 and the 2201 phases intergrowths of these phases occur [7]. In fact the 2223 phase has been shown to be in equilibrium with the 2212, alkaline-earth cuperates, CuO and the liquid phase [4]. The phase equilibria of the 2223 phase are [4]

(i) 2223-2212-Ca_2CuO_3-$Sr_7Ca_7Cu_{24}O_{41-x}$
(ii) 2223-2212-Ca_2CuO_3
(iii) 2223-2212-Ca_2CuO_3-liquid phase
(iv) 2223-liquid phase-CuO
(v) 2223-CuO-$Sr_7Ca_7Cu_{24}O_{41-x}$

These constraints necessitate strict control over the starting composition and the processing conditions for obtaining the 2223 phase in pure form. Among the techniques used to grow this phase in large proportion partial substitution of Bi by Pb, excess Ca and Cu in the starting composition, and annealing in an Ar:O_2 atmosphere has been most successful [8-10].

8.3 The choice of composition

Among the nominal starting compositions $BiSrCaCu_2O_x$ (1112) [11], $Bi_2Sr_2Ca_2Cu_4O_x$ (2224) [9], $Bi_2Sr_2Ca_4Cu_5O_x$ (2245) [12], $Bi_2Sr_2Ca_6Cu_8O_x$ (2268) [13] have been reported to be most effective in obtaining a high volume fraction of the 2223 phase, although XRD patterns of these samples reveals the 2223 phase co-exists with both the

2212 and Ca_2CuO_3 phases. Other studies based on XRD and resistivity measurements have demonstrated that by controlling the starting composition and synthesis conditions it is possible to produce single phase 2223 BSCCO. For instance, Koyama et al. [14] have suggested $Bi_{1.84}Pb_{0.34}Sr_2Ca_2Cu_3O_x$. Sasokura et al. [15] have reported the growth of single phase 2223 over a wide range of compositions such as $Bi_{1.68}Pb_{0.32}Sr_{1.75}Ca_yCu_zO_w$ where $1.75 < y < 1.85$ and $2.65 < z < 2.85$. Calestani et al. [16] have reported $Bi_{1.3}Pb_{0.27}Sr_{1.33}Ca_2Cu_3O_x$ composition for the growth of this phase.

8.4 Sequence of phase development of 2223

The chemical reactions and the phase formation in the Bi-Sr-Ca-Cu-O system in relation to 2223 has been studied by a number of authors [9, 17]. A summary of these reactions as a function of the processing temperatures for two different compositions is outlined in table (8.1). Data was extracted from references [9, 17].

Temperature	Composition i) $Bi_{1.84}Pb_{0.34}Sr_{1.91}Ca_{2.03}Cu_{3.06}O_x$
400°C	CaO, Cu_2O, and 2201 begin to crystallize
550°C	Ca_2PbO_4, CuO form
700°C	$(Sr, Ca)_{14}Cu_{21}O_{41}$ begins to form
730°C	$2201+CaO+CuO \longrightarrow 2212$ (small quantity)
820°C	$Ca_2PbO_4 \longrightarrow CaO+PbO$ leading to the formation of the liquid phase and $2201+CaO+CuO \longrightarrow 22121$ $CaO+(Sr, Ca)_{14}Cu_{21}O_{41} \longrightarrow (Ca, Sr)_2CuO_3$
840°C	$2212+CaO+CuO \longrightarrow 2223$ (melt assisted diffusion)
860°C	$2223 \longrightarrow 2201+Cu_2O+(Ca, Sr)_2CuO_3$
870°C	$2212 \longrightarrow 2201+Cu_2O+(Ca, Sr)_2CuO_3$

continued overleaf

Composition **ii)** $(BiPb)_2Sr_2Ca_2Cu_4O_x$

	Product phases
560°C	Ca_2PbO_4, $CuBi_2O_4$
680°C	Ca_2PbO_4, 2201, $Ca_7Bi_{10}O_{22}$
810°C	2212, Ca_2PbO_4 (decreasing), 2201 (decreasing)
820°C	liquid phase, 2212 phase (growing rapidly)
845°C	2223, 2212, Ca_2PbO_4 (small quantity), $(Sr, Ca)_{14}Cu_{21}O_{41}$
856°C	2223 (decreasing), 2212, liquid phase

Table (8.1)- *Sequence of phase development as a function of processing temperature for $Bi_{1.84}Pb_{0.34}Sr_{1.91}Ca_{2.03}Cu_{3.06}O_x$ and $(BiPb)_2Sr_2Ca_2Cu_4O_x$ materials.*

The reaction mechanism for the formation of 2223 phase in Pb doped samples seem to begin at temperatures well below 850°C. The Ca_2PbO_4 phase formed at around 550°C is reported to decompose into CaO and PbO in the temperature range of 820-827°C [18, 19]. At this temperature, a Pb rich liquid phase is thought to form. This liquid phase accelerates the formation of the 2212 phase through a process of melt-assisted diffusion of CaO and CuO in the temperature range of 827-840°C [9, 17]. The composition of this liquid phase has been suggested as $(Ca, Sr)_2(Pb_{x+1}Bi_x)O_{4-x/2}$ by Chen et al.[9].

Between 840-845°C the addition of CaO and CuO to the 2212 phase, through melt-assisted diffusion, leads to the formation of the 2223 phase. This phase, however, decomposes to the 2212 and liquid phases at 856°C. The liquid subsequently leads to the formation of the 2201 phase [17]. The key to the formation of the 2223 phase appears to be the formation and decomposition of Ca_2PbO_4 phase. This phase forms the flux and pathway needed for diffusion of Ca^{2+} and Cu^{2+} to the reaction site. The small temperature range over which the 2223 phase exist explains why this phase is so sensitive to experimental conditions.

8.5 Thin film growth of the 2223 phase by other groups

To date, numerous film growth techniques including sputtering, electron beam evaporation [20], and PLD have been used to grow 2223 phase. Table (8.2) summarises the thin film processing conditions used in PLD and Sputtering techniques by other groups for the growth of this phase.

Growth technique	T_s(°C)	A. Temp (°C)	A. Time (h)	2223 %	$T_{c,\,zero}$	A. Temp range (°C)	Other factors	References
Sputtering	600	857	40	85	102	not given	none	[21]
PLD	R T	850	3	68	99.5	850-865	none	[22]
PLD	700	865	5	< 50	100	not given	Two step annealing	[23]
PLD	R T	855	138	85	< 98	850-860	Annealed next to a pellet	[24]
PLD	R T	850	60	85	100	not given	Two step annealing	[25]
Sputtering	250-400	850	3	85	115	not given	none	[26]
Sputtering	R T	850	3	90	106	850-870	Annealed next to a Pb pellet	[27]
Sputtering	400	851	1	>97%	106.5	848-853	none	[28]
PLD	R T	856	3 days	not given	70	854-859	none	[29]

Table (8.2)- *Summary of the processing conditions used by other researchers for thin film growth of the 2223 phase. In the above table* T_S *is the substrate temperature, A. Temp is the annealing tempertaure, and A. Time is the annealing time.*

The data shown in table (8.2) indicate that the annealing temperature range for the formation of the 2223 phase is very narrow and that the maximum proportion of the 2223 phase has been achieved at a particular temperature within that range. For instance, In a study by Tanaka et al. [28] the maximum proportion of this phase was reported by annealing the films at 851 (±1°C). This illustrates the sensitivity of this phase to the processing conditions and the need to have a fine control over the annealing temperature.

8.6 Target preparation and characterization

The targets were prepared by the solid-state reaction of Bi_2O_3 (99.999%), PbO (99.999%), $SrCO_3$ (99.995%) $CaCO_3$ (99.995%) and CuO high purity (>99.9999%) powders (Aldrich Chemical Ltd, Gillingham, Dorset, U.K). In the first stage, $SrCO_3$, $CaCO_3$ and CuO powders were thoroughly mixed and ground in a mortar with pestle. The powder was subsequently placed on a gold boat and fired at 910°C for 24 hours. The powder mixture was thoroughly mixed with Bi_2O_3 and PbO powders and ground in a mortar with pestle before being fired at 800°C for 24 hours. In the second stage, the powder mixture was well mixed and ground in a mortar with pestle before being pressed in a stainless steel die under 500Mpa to form a pellet of 12mm in diameter. The pellet was placed on a MgO single crystal plate and heat treated at 850°C for 25 hours. The pellet was then crushed, reground and pressed under 500Mpa to form a new pellet. This was subsequently heat treated at a final set temperature for a total time of 96 hours with several intermediate grinding. The atomic ratios of Bi:Pb:Sr:Ca:Cu elements and the final annealing temperatures used for various targets are summarised in table (8.3).

Bi	Pb	Sr	Ca	Cu	Sintering temperature T_s(°C)
1.84	0.32	1.91	2.25	3.06	856
1.7	0.4	1.6	2.4	3.6	854
1.68	0.32	1.75	1.82	2.75	858

Table (8.3)- *Starting composition and sintering temperature of the (BiPb)SrCaCuO targets.*

The targets were characterised by XRD and resistivity measurements. The XRD pattern of the pellet with composition $Bi_{1.68}Pb_{0.32}Sr_{1.75}Ca_{1.82}Cu_{2.75}O_x$ shown in figure 8.1 indicated the presence of both the 2212 and the 2223 phases with the latter phase being the main constituent. A Similar pattern of mixed 2223/2212 phases was also observed for the pellet with composition $Bi_{1.84}Pb_{0.32}Sr_{1.91}Ca_{2.25}Cu_{3.06}O_x$. The x-ray diffraction pattern of the $Bi_{1.7}Pb_{0.4}Sr_{1.6}Ca_{2.4}Cu_{3.6}O_x$ pellet, not shown here, only illustrated the presence of the 2212 phase and the $(Sr_{14-x}Ca_x)Cu_{24}O_{41-y}$ phase. The resistivity versus temperature of the pellet shown in figure 8.2 exhibits $T_{c,\ onset}$ of 110K and $T_{c,\ zero}$ of 102K.

$Bi_{1.68}Pb_{0.3}Sr_{1.75}Ca_{1.82}Cu_{2.75}O_x$

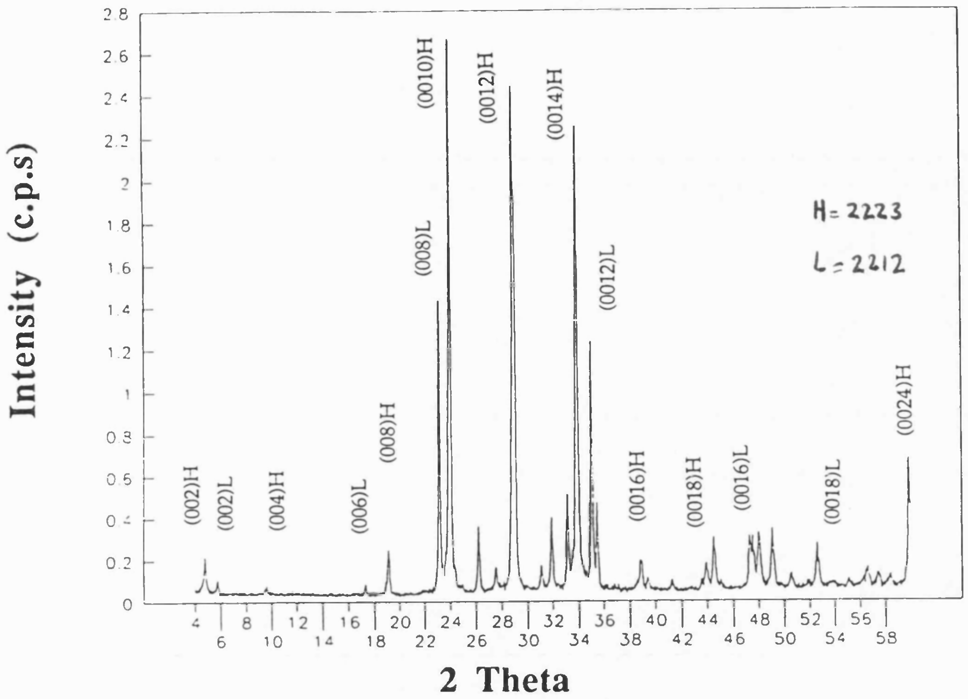

Figure 8.1- *X-ray diffraction pattern of the $Bi_{1.68}Pb_{0.32}Sr_{1.75}Ca_{1.82}Cu_{2.75}O_x$ pellet.*

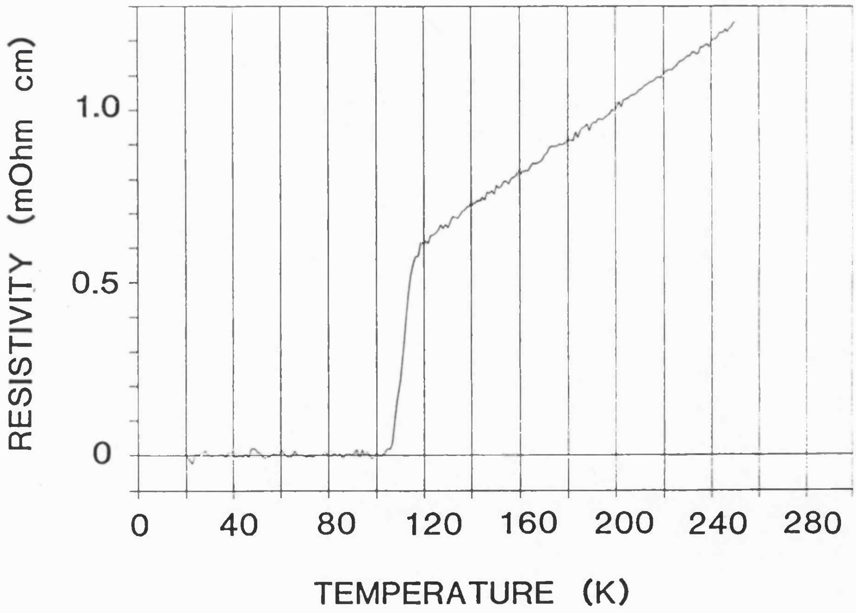

Figure 8.2- *Resistivity versus temperature curve of the $Bi_{1.68}Pb_{0.32}Sr_{1.75}Ca_{1.82}Cu_{2.75}O_x$ pellet.*

8.7 Thin film growth of $(BiPb)_2Sr_2Ca_2Cu_3O_x$

The experimental set-up for thin film deposition was discussed in detail in chapter 5. In brief, $(BiPb)_2Sr_2Ca_2Cu_3O_x$ films were deposited onto single crystal MgO substrates (001) orientation. Depositions were carried out by using a Nd-YAG laser operating at 532nm with pulse duration of 4ns at 10Hz. The incident laser beam was focused on the (BiPb)SrCaCuO target to a spot diameter of ≈ 3.0 mm. During the deposition process the target was slowly rotated at a rate of 5 rev/min. The target-substrate distance used in these experiments was 4.2cm which was the maximum distance possible, due to the limitation associated with the dimensions of the deposition chamber. Prior to deposition, MgO substrates were cleaned in acetone and ethanol for a few minutes and blown dry with nitrogen gas. To obtain crystallinity, deposited BiPbSrCaCuO films were post-annealed in a tube furnace followed by furnace cooling to temperatures below 100°C before leaving the furnace. The XRD diffraction peaks of the BiPbSrCaCuO films were indexed according to a=5.4, b=5.4, and c=21.97Å for the 2201 phase [30], a=5.40, b=5.40, and c=30.83Å for the 2212 phase [31], and a=5.40, b=5.40, and c=37.05Å for the 2223 phase [32].

8.7.1 Effect of laser fluence on film composition

Prior to the growth of the $(BiPb)_2Sr_2Ca_2Cu_3O_x$ films a series of depositions were carried out with different laser fluences in order to check the stoichiometric transfer of the material from target to substrate. The depositions were carried out from the $Bi_{1.68}Pb_{0.32}Sr_{1.75}Ca_{1.82}Cu_{2.75}O_x$ target under vacuum pressure of $1x10^{-5}$mbar. The ablated material was collected on Si substrates held at room temperature. The chemical compositions of the films were investigated by EDX technique. Figure 8.3 illustrates the average measurements taken at six different sites on the films. The large error associated with the EDX technique (≈10%) makes it difficult to conclusively state whether the relative stoichiometry of the elements changes over the range of laser flunces. However, it seems that there is Sr, Ca deficiency and excess Cu from that of the the ideal value in the films deposited with high laser fluences (> 3.4J/cm^2). The ideal values were calculated by normalising the total atomic percentage of cations to 100 resulting in the ratios Bi 20.2%, Pb 3.80%, Sr 21%, Ca 21.9%, and Cu 33.1%.

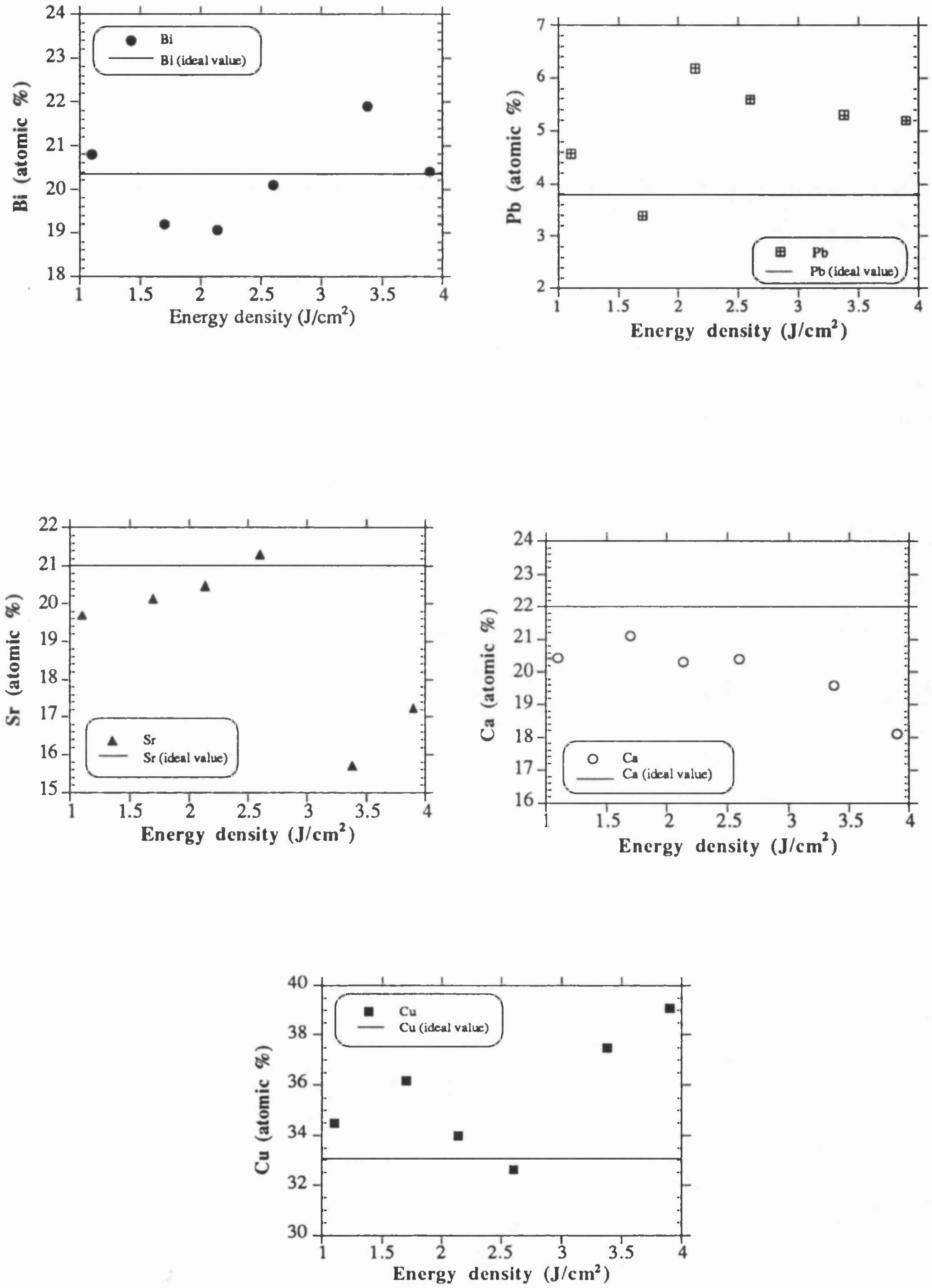

Figure 8.3- *Atomic % of the Bi, Pb, Sr, Ca, and Cu in films deposited in vacuum with various fluences from the* $Bi_{1.68}Pb_{0.32}Sr_{1.75}Ca_{1.82}Cu_{2.75}O_x$ *target.*

8.7.2 Thin film growth from a single target

The films were deposited on MgO substrates held at room temperature or heated to temperatures not exceeding 650°C, from a target with composition $Bi_{1.68}Pb_{0.32}Sr_{1.75}Ca_{1.82}Cu_{2.75}O_x$. The depositions were carried out under vacuum pressure of 1.0×10^{-2}mbar for 10 minutes. This resulted in a film thickness of 1.0μm (as measured by Taleystep), which represents a growth rate of ≈16Å/s. To ascertain the optimum annealing temperature and duration, (BiPb)SrCaCuO films were annealed in the temperature range of 830-877°C (±1°C) for various duration. Two types of post-annealing were investigated.

(i) using a constant temperature. With this method the film is inserted into the tube furnace at a set temperature. After annealing the film is furnace cooled to temperatures below 100°C.

(ii) using gradual heating at a rate of 5°C per minute from 90 to 490°C, followed by 10°C per minute to the set temperature.

Considerable evaporation occurred to films annealed for more than 15 hours by the first method. However, no noticeable film evaporation could be detected for films which were annealed by the latter method for a similar period of time. In the first set of experiments the films were annealed according to method (i). The (BiPb)SrCaCuO films annealed in the temperature range of 850-860°C between 10-15 hours showed $T_{c,\ onset}$ of 110K with $T_{c,\ zero}$ above 75K. The films annealed above 865°C exhibited a semiconducting behaviour in the normal state followed by a superconducting transition around 80K with $T_{c,\ zero}$ below 50K. The films annealed in the temperature range of 830-845°C illustrated a metallic behaviour in the normal state followed by a superconducting transition around 80K. However, $T_{c,\ zero}$ values of these films decreased with an increase in the annealing duration. Figure 8.4 shows $T_{c,\ zero}$ as a function of annealing duration for the BiPbSrCaCuO films annealed between 850-860°C. The patterns show that the films annealed at 850°C and 855°C illustrate a higher $T_{c,\ zero}$ values than those at 860°C.

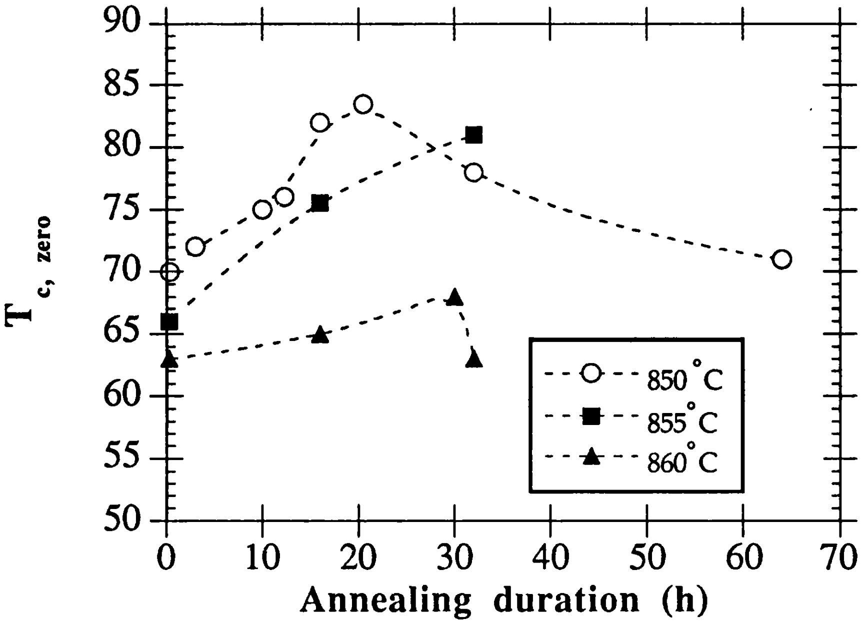

Figure 8.4- *$T_{c,\ zero}$ versus annealing duration for BiPbSrCaCuO films annealed at different temperatures. The dashed lines are possible profiles.*

The XRD patterns of the films annealed at 850°C and 855°C illustrated the presence of both the 2212 (L) and the 2223 (H) phases. The highest (002)H/(002)L peak ratio was 1:30 in the film annealed at 850°C for 16 hours. The XRD of the other films showed the presence of the 2212 phase only.

In the second set of experiments BiPbSrCaCuO films were annealed according to method (ii) from 5 minutes to 24 hours at 850°C and 855°C, respectively.. This method of annealing resulted an increase in the proportion of the 2223 phase. The highest proportion of the 2223 phase was observed in the film annealed for 24 hours at 855°C. The XRD pattern of this film is shown in figure 8.5.

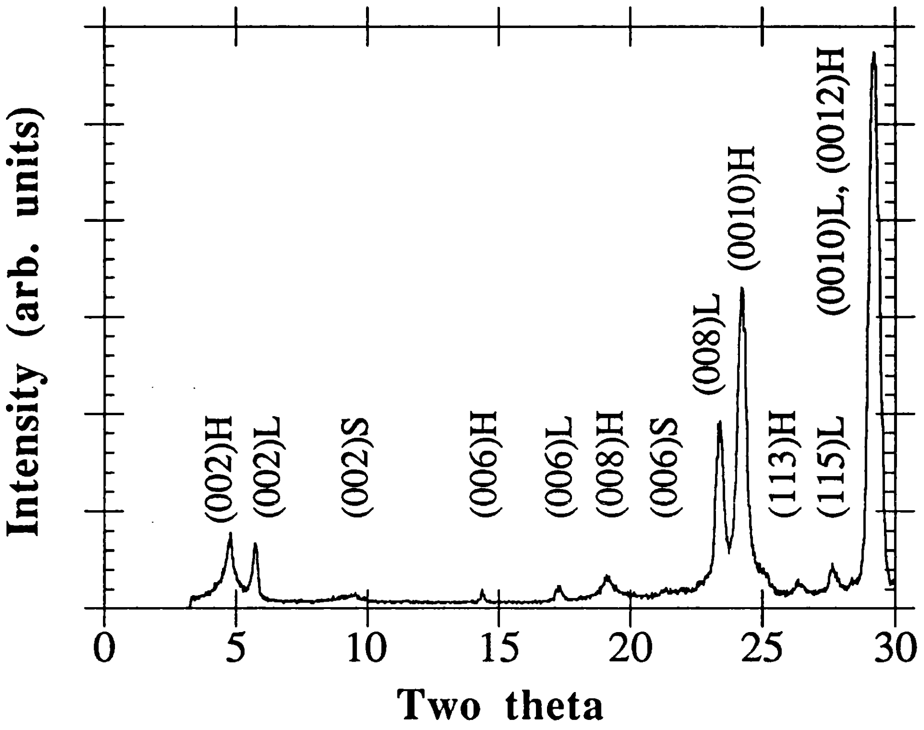

Figure 8.5- *X-ray diffraction pattern of the BiPbSrCaCuO film annealed at 855 °C for 24 hours. Letters H, L, and S are assigned to the peaks of the 2223, 2212, and the 2201 phases, respectively.*

The pattern shows the presence of the 2223, 2212, and 2201 phases with the 2223 phase being the main constituent. The resistivity versus temperature of this film shown in figure 8.6, however, indicates a small drop at 110K followed by a second transition at 80K with $T_{c,\ zero}$ of 58K. The low $T_{c,\ zero}$ value obtained is due to the low proportion of the 2223 phase present in this film (≈ 47%). According to J. Schneck et al. [33] in order to obtain $T_{c,\ zero}$ above 100K in Pb doped BiSrCaCuO films the proportion of the 2223 phase should be greater than 52%. This value is referred to as the percolation threshold.

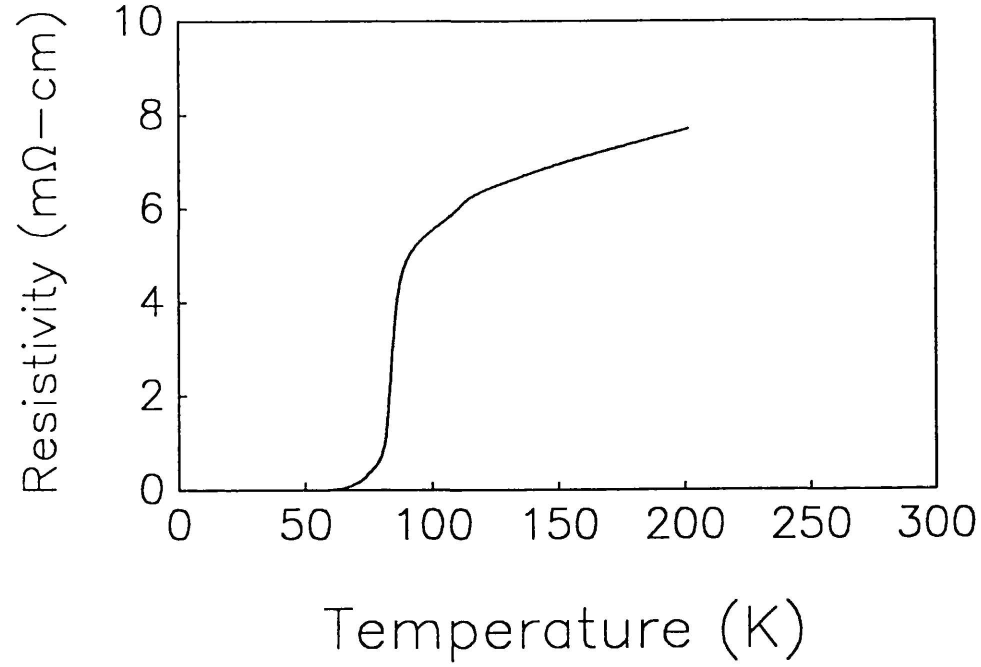

Figure 8.6- *Temperature dependence of resistivity of the film annealed at 855 °C for 24 hours in air.*

The phase developments of the BiPbSrCaCuO films investigated by EDX technique indicated a loss of Pb during the early annealing stage by as much as 98%. Unlike bulk BiPbSrCaCuO material, Pb could easily escape from the film surface, due to the film large surface to volume ratio. The presence of Pb in large amounts, however, is necessary for the formation of the liquid phase at 820°C and the eventual formation of the 2223 phase. To compensate for Pb loss other groups have taken the course of annealing the films next to a Pb rich target [34] or next to a Pb pellet [27]. The method that was developed and used to grow the 2223 phase as part of the project was to deposit multilayers of PbO between several layers of BiPbSrCaCuO. This method is fully described in the following section of this chapter.

8.7.3 Thin film growth of the 2223 phase using the multilayered BiPbSrCaCuO/PbO technique

With this technique two targets, 12 mm in diameter, were used. The BiPbSrCaCuO target preparation was described in detail in the last section. The PbO target was prepared from high purity PbO powders (99.999%). The powder was thoroughly mixed and ground in a mortar with pestle before being pressed in a stainless steel die under 200Mpa to form a pellet of 12 mm in diameter and 2 mm in thickness. The pellet was subsequently fired at 650°C for 12 hours. The targets were mounted on the multiple target holder, shown in figure 5.2 chapter 5, so that the process of multilayer film deposition could be performed in-situ. During the deposition the chamber pressure was kept at 1.0×10^{-5}mbar. The growth of homogenous multilayered films in an oxygen atmosphere on a heated substrate was not successful due to the high vapour pressure of PbO.

The material ablated sequentially from each target was collected on polished (001) orientation MgO substrates of dimensions 7.5x7.7x0.5 mm. The target-substrate distance was 4.2 cm. Figure 8.7 shows schematic diagram of the multilayer film structure.

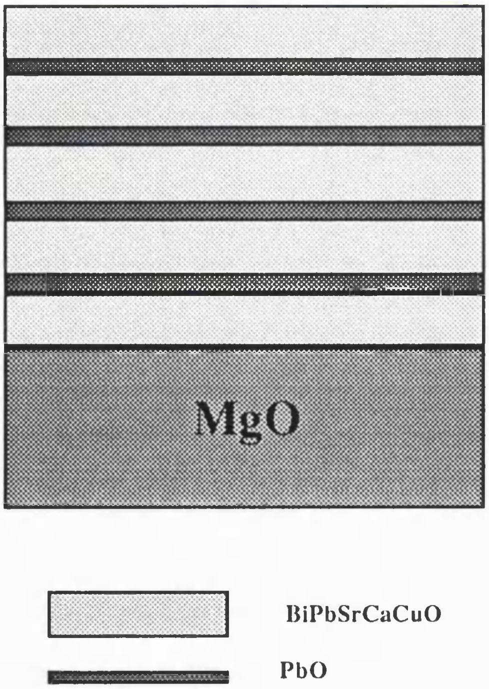

Figure 8.7-*Schematic diagram of the multilayer film structure*

The number of BiPbSrCaCuO and PbO layers deposited was fixed at 5 and 4. The BiPbSrCaCuO and PbO layer thicknesses deposited were back-calculated from a much thicker BiPbSrCaCuO and PbO films deposited separately on silicon substrates and measured by Talystep (10Å resolution). The deposited films were shiny and insulating. These were placed on a gold foil and post-annealed in a quartz tube furnace. The annealing temperature was monitored using a calibrated thermocouple close to the samples. The calibration was achieved at the known melting point of a Au sample placed next to the thermocouple in place of MgO. The heating rate was 10°C per minute to 810°C and 1°C per minute there after to avoid overshooting the set temperature. During the heating, the films were kept at 810°C for 30 minutes in order to facilitate the decomposition of Ca_2PbO_4 and the formation of the Pb rich liquid phase. The post-annealing cycle resulted in the reduction of the film thickness by as much as 30% to around 750nm due to the evaporation of the PbO layers at high temperatures.

8.8 Optimization of the growth conditions

In the following sections the effect of deposition and growth parameters on the multilayered BiPbSrCaCuO/PbO 2223 films are discussed as separate studies.

8.8.1 Laser fluence

In this study the effect of laser fluence on the phase developments of the multilayered BiPbSrCaCuO/PbO films is investigated. Multilayered BiPbSrCaCuO/PbO films were deposited on MgO substrates from a freshly sanded $Bi_{1.7}Pb_{0.4}Sr_{1.6}Ca_{2.4}Cu_{3.6}O_x$ target at different laser fluences. The number of BiPbSrCaCuO and PbO layers were fixed at 5 and 4, each being 200nm and 80nm in extent, respectively. This resulted in a total film thickness of 1.32μm. The substrate temperature was held at 250°C during the deposition of the films. The laser fluence was varied between 2.0-3.1J/cm^2 by inserting neutral density filters in the path of the laser whilst keeping the spot size constant. Care was taken to ensure that the total film thickness remained the same for all the films by adjusting the deposition time for each laser fluence. To yield crystallinity the multilayered films were subsequently post-annealed in air at 854°C for 15 hours. The XRD patterns of the multilayered BiPbSrCaCuO/PbO films deposited with various laser fluences and post-annealed at 854°C (±1°C) are shown in figure 8.8. The patterns show highly c-axis oriented films with the dominant diffraction peaks of the 110K phase (2θ=4.7, 23.9, 28.8, 33.8) as well as the minor 80K phase (2θ=5.7, 23.2,...). Two other peaks, high lighted by * symbol are also observed at 2θ=27.69 and 13.7 which is an indication of the presence of a third phase in these films. The magnitude of these peaks, however, decreases with the use of lower laser fluences and reaches a minimum value in film deposited at 2.6J/cm^2 before increasing in the film deposited at 2.0J/cm^2.

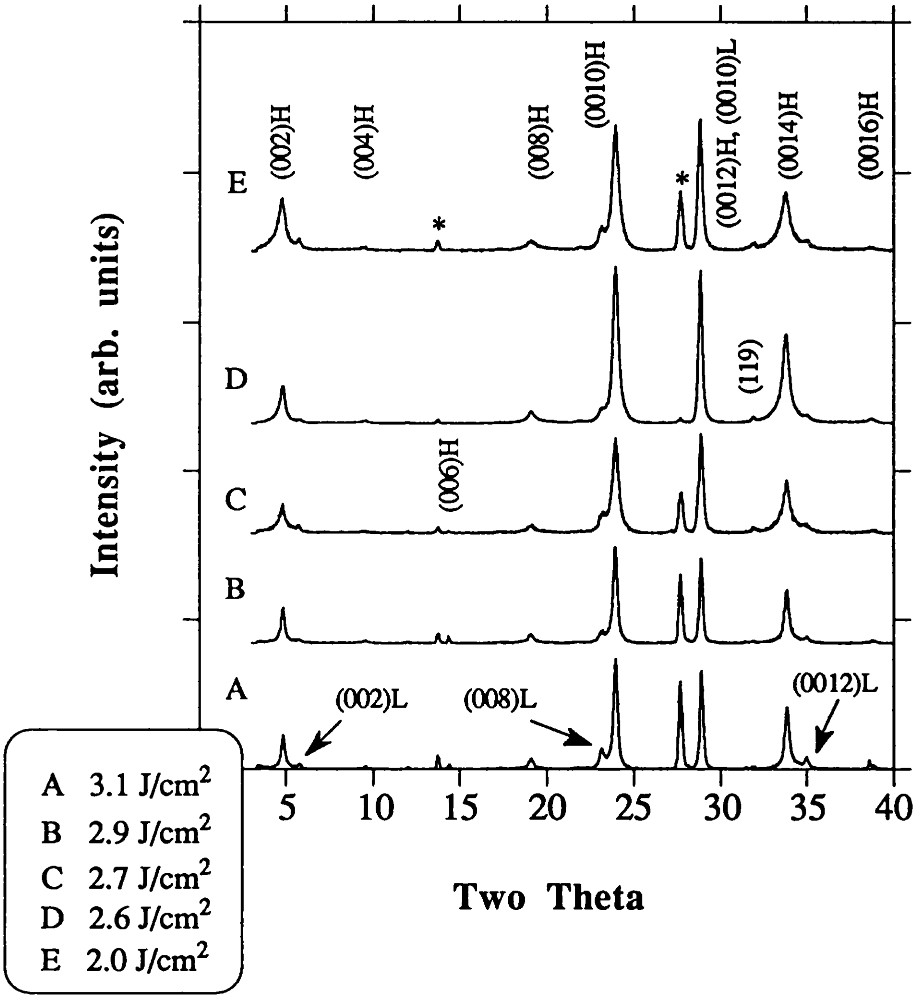

Figure 8.8- *X-ray diffraction patterns of the multilayered BiSrCaCuO/PbO films deposited with various laser fluences and post-annealed at 854 °C in air. The symbols H, L, and * are assinged to the peaks of the 2223, 2212, and unknown phases, respectively.*

The superconducting properties of these films were investigated by the Van der Pauw technique. The R-T curves shown in figure 8.9 indicate significant differences in the normal and superconducting states of the films. The most prominent feature of the R-T curves is the low temperature resistive tailing observed for all the films except for the film deposited at 2.6J/cm^2 which exhibits a metallic behaviour in the normal state followed by a single transition at 110K and $T_{c,\ zero}$ of 104K.

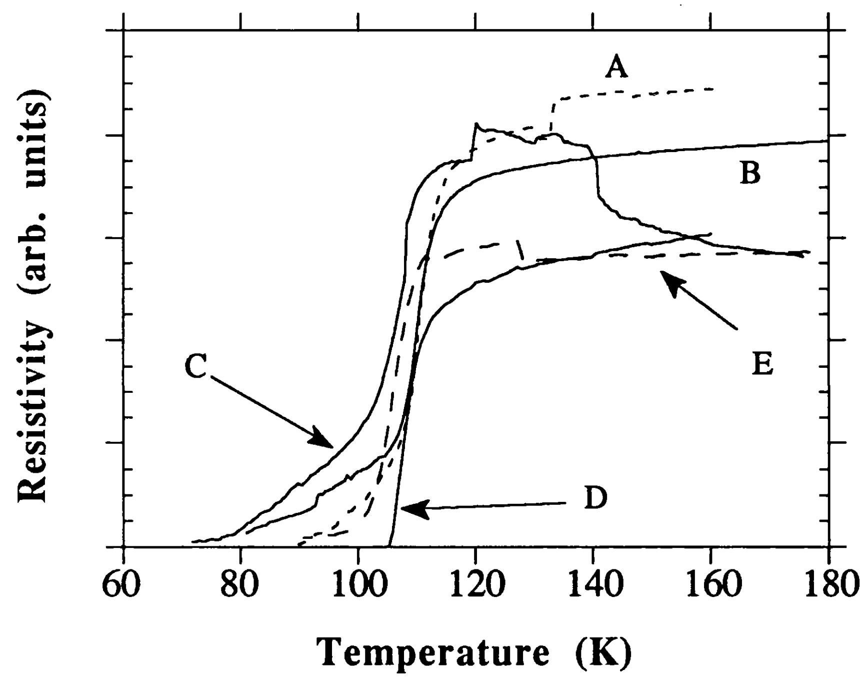

Figure 8.9- *Resistance versus temperature of the multilayered BiSrCaCuO/PbO films grown with various laser fluence and post-annealed at 854 °C in air.*

The microstructure of these films were investigated by SEM and are shown in figure 8.10 The micrographs show the presence of large needle shaped crystals embedded in array of plate type crystals. However, the frequency and the size of the needle type crystals decreases with the use of lower laser fluences. The composition of the films over large areas (approx 100μm per measurement) which included plate and needle type crystals was determined by EPMA technique. The average composition (sample of four different sites) of the film deposited at 3.1J/cm^2 was $Bi_{1.67}PbSr_{1.65}Ca_{2.48}Cu_{3.49}O_x$ which is near the composition of the target used. However, the average compisition of the films deposited at 2.9J/cm^2 and 2.7J/cm^2 showed a reduction in Cu and Ca and an increase in Bi and Sr molar ratios from that of the ideal values, respectively. Infact, the average composition of the film deposited at 2.6J/cm^2 was $Bi_{2.06}PbSr_2Ca_{2.22}Cu_3O_x$ which is near the ideal 2223. This pattern was reversed in film deposited at 2.0J/cm^2 which showed an average composition of $Bi_{1.94}PbSr_{1.76}Ca_{2.28}Cu_{3.3}O_x$. The composition of the needle shaped crystals were determined as $(Sr_{14-x}Ca_x)Cu_{24}O_{41-y}$.

(A)

(B)

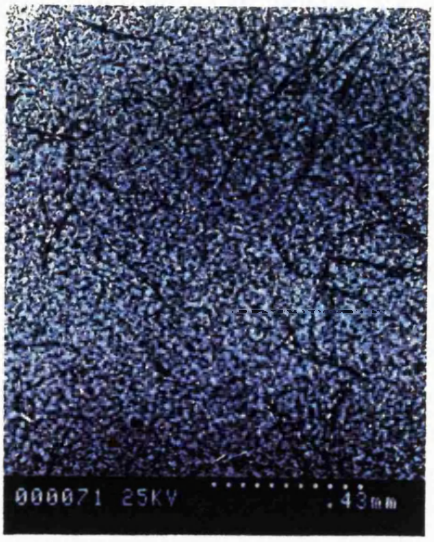

(C)

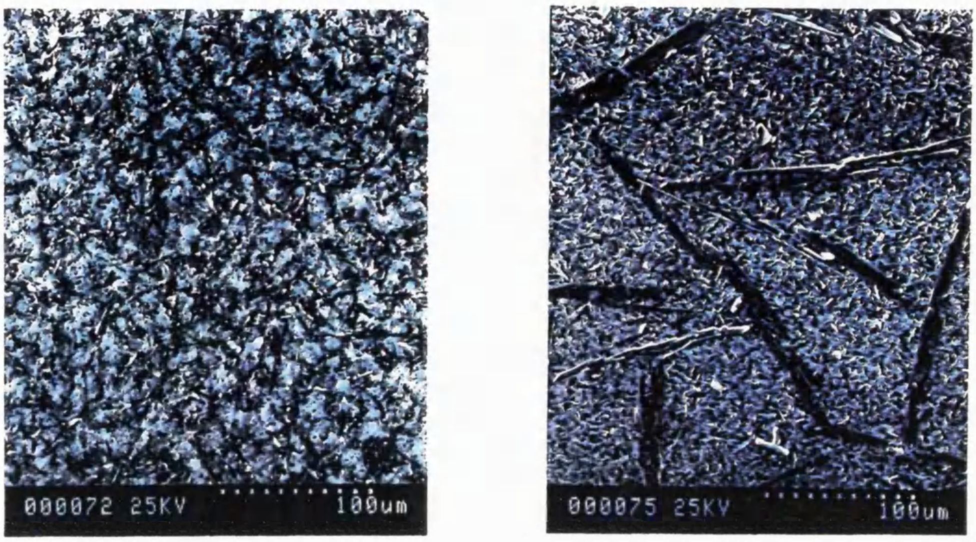

(D) (E)

Figure 8.10- *SEM micrographs of BiPbSrCaCuO films deposited with various laser fluences and annealed at 854°C for 15 hours in air.*

8.8.1.1 Discussion

The XRD patterns in conjunction with SEM observations and EPMA analysis of the (BiPb)SrCaCuO films in this study indicates that laser fluence does have some influence on the chemical composition of the deposited multilayered films and hence on the phase developments of the material upon annealing. The EPMA analysis indicated that the formation of the $(Sr_{14-x},Ca_x)Cu_{24}O_{41-y}$ phase is as a direct result of excess Cu in the deposited films. The formation of this phase has also been reported by Chen et al. [35] in the Cu rich 2224 (BiPb)SrCaCuO samples. The identification of the $(Sr_{14-x},Ca_x)Cu_{24}O_{41-y}$ phase from the XRD patterns of the films shown in figure 8.8 is, however, difficult since the intense peaks of this phase overlap with those of the 2223 and the 2212 superconducting phases. To illustrate the existence of $(Sr_{14-x}Ca_x)Cu_{24}O_{41-y}$ phase in these films, bulk $(Sr_{14-x}Ca_x)Cu_{24}O_{41-y}$ with x=0-7.7 was independently synthesised by solid-state reaction of $SrCO_3$, $CaCO_3$, and CuO high purity (>99.999%) powders. In the first stage, $SrCO_3$, $CaCO_3$ and CuO powders were thoroughly mixed and ground in a mortar with pestle. The powder mixture was subsequently pressed in a stainless steel die under 300Mpa to form a pellet of 12mm in diameter. The pellet was heat treated at 855°C (±1°C) for 24 hours in air. The XRD patterns of these pellets are shown in figure 8.11.

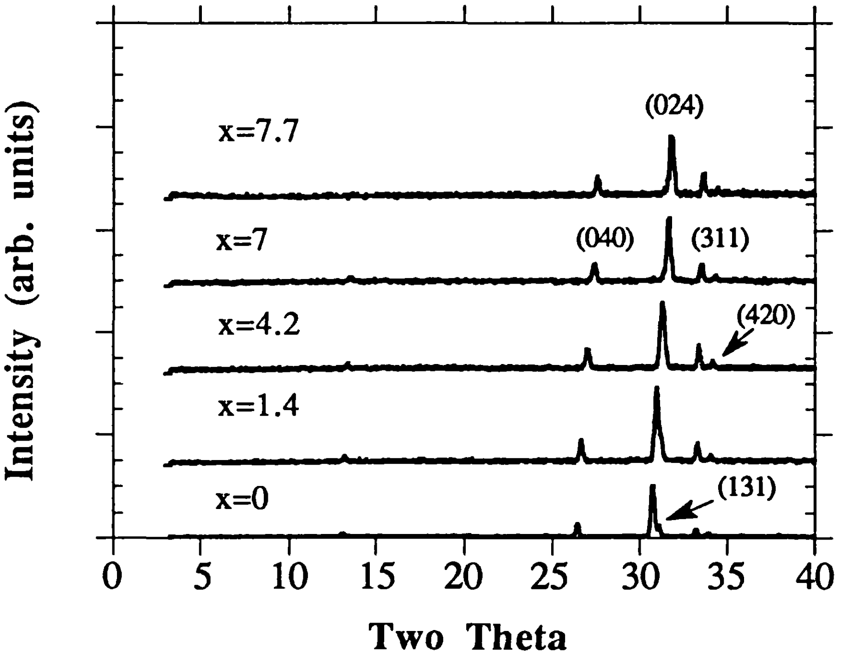

Figure 8.11- *XRD patterns of* $(Sr_{14-x}Ca_x)Cu_{24}O_{41-y}$ *targets with x= 0-7.7.*

The XRD diffraction peaks of the $(Sr_{14-x}Ca_x)Cu_{24}O_{41-y}$ phase were indexed by using the data provided by Roth et al [36]. From the XRD paterns it is apparent that the most intense peaks occur at 2θ=31.9°, 33.8°, and 27.7°. However, the first two peaks overlap with the diffraction peaks of the 2223 phase at (119), 2θ=31.9° and at (0014), 2θ =33.8°. Furthermore, the third peak overlaps with the 2212 phase at (115), 2θ=27.5°. However, by examining the XRD patterns of the $(Sr_{14-x}Ca_x)Cu_{24}O_{41-y}$ targets, the (020) at 2θ=13.7° and (040) peaks at 2θ=27.69° are determinable. It should also be noted that the position of the peaks in the XRD patterns, shown in figure 8.11, changes slightly according to the degree of Ca substitution of Sr sites. For instance, the position of (040) reflection changes from 2θ=26.7° for x=0 to 27.71° for x=7.7. This becomes more apparent by p l$\overset{t}{o}$ting the unit cell dimensions of the $(Sr_{14-x}Ca_x)Cu_{24}O_{41-y}$ phase as a function of the Ca concentration x as shown in figure 8.12 (a, b).

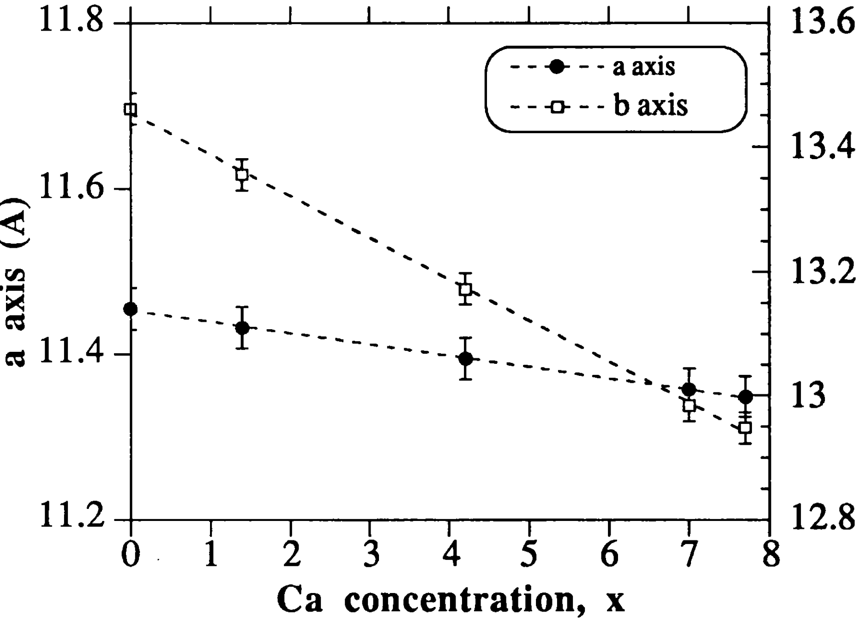

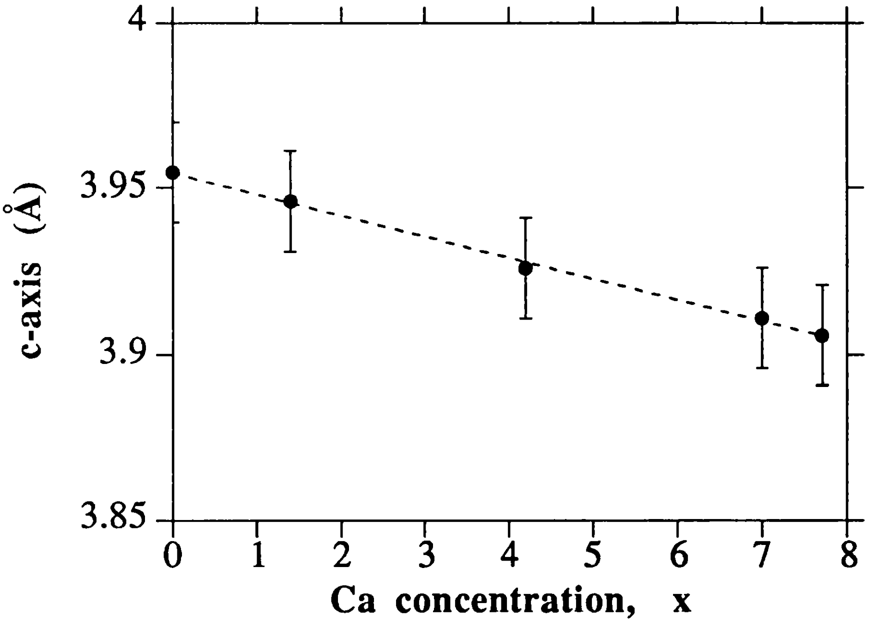

Figure 8.12 (a, b)- *a,b, and c axis dimensions as a function of Ca concentration, x, of the* $(Sr_{14-x}Ca_x)Cu_{24}O_{41-y}$ *phase.*

The R-T measurements of BiPbSrCaCuO films shown in figure 8.9 indicate low temperature resistive tailing except in the film deposited at 2.6J/cm^2. This effect could be attributed to the variation in the chemical composition of these films such as depletion in Sr and excess in Cu content from that of the ideal values. In a study Endo et al. [37] have shown that low temperature tailing occurs in Ca and Cu rich samples, which becomes smaller and finally disappear with an increase in Sr content. The presence of the non superconducting $(Sr_{14-x}Ca_x)Cu_{24}O_{41-y}$ is not thought to influnce the R-T behaviour of the films as its presence is not continuous throughout the microstructure [35]. On the other hand its presence has the effect of decreasing the critical current density of the films. This effect is investigated as a seperate study and is presented in chapter nine.

8.8.2 Effect of substrate temperature

The aim of this study is to investigate the effect of substrate temperature on the formation of the 2223 phase in the multilayered BiPbSrCaCuO/PbO films. In that context multilayered films were deposited on MgO substrates held between 25°C and 500°C from the $Bi_{1.7}Pb_{0.4}Sr_{1.6}Ca_{2.4}Cu_{3.6}O_x$ target. The deposition conditions were similar to those outlined in the previous section. The laser fluence used for the deposition of these films was 2.6J/cm^2. The number of BiPbSrCaCuO and PbO layers were fixed at 5 and 4, each being 200nm and 80nm in extent, respectively. This resulted in a total film thichness of 1.32μm. The films were post-annealed between 852-854°C (±1°C) for 15 hours in air. The R-T curves and XRD patterns of the BiPbSrCaCuO/PbO films deposited at various substrate temperatures are shown in figure 8.12 (a, b).

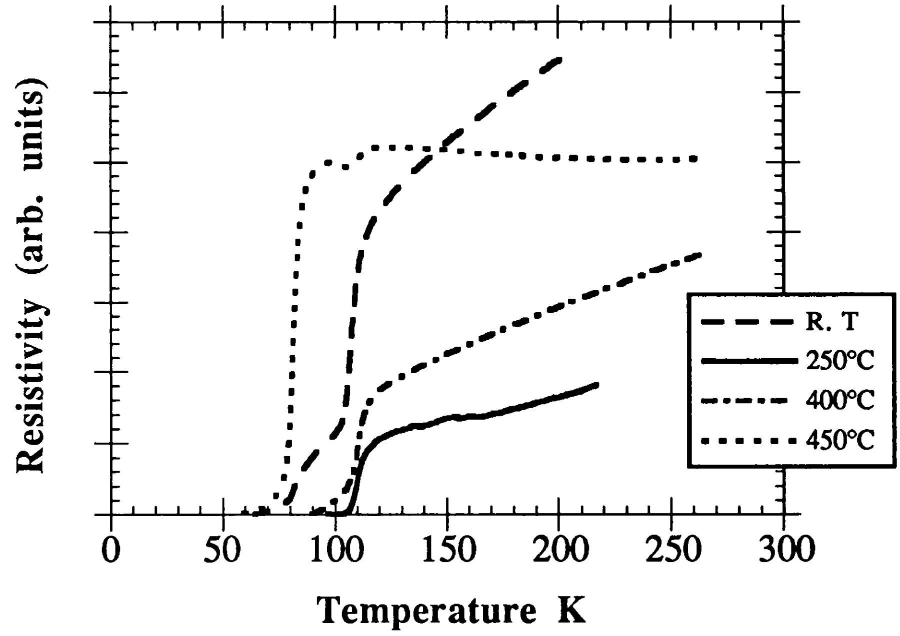

Figure 8.12 (a)- *Resistance versus temperature of multilayered superconducting BiPbSrCaCuO films as a function of the substrate temperature.*

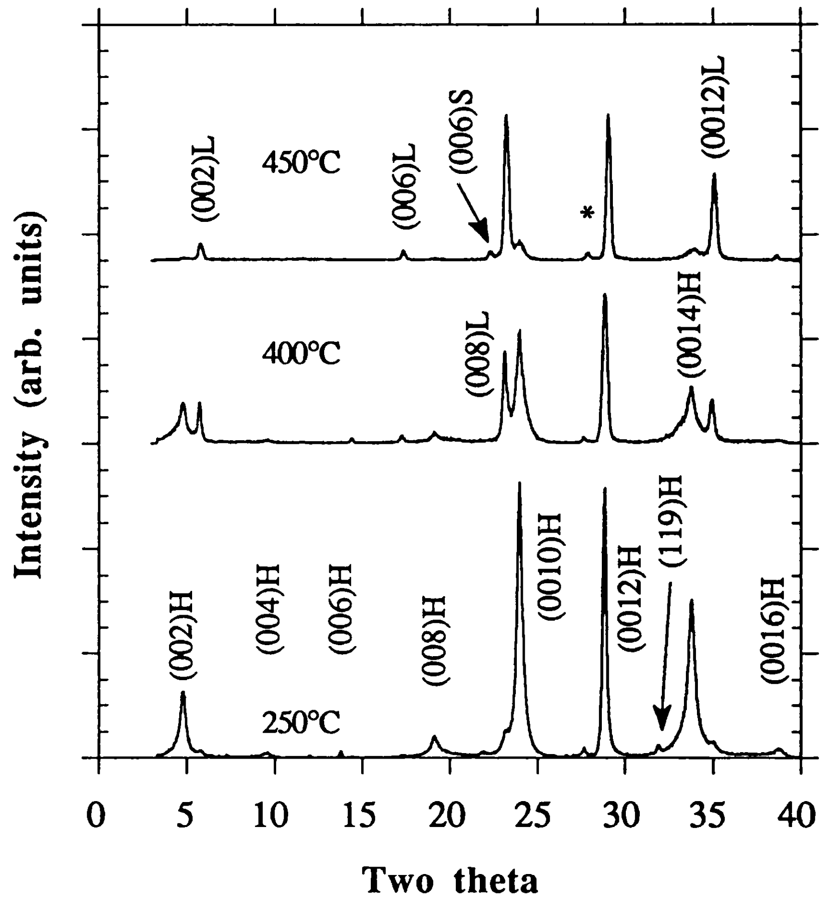

Figure 8.12 (b)- *X-ray diffraction patterns of the multilayered BiPbSrCaCuO/PbO films deposited at various substrate temperatures and post-annealed at 854 °C for 15 hours in air. Letters H, L, S, and * are assinged to the diffraction peaks of the 2223, 2212, 2201, and* $Sr_{14-x}Ca_xCu_{24}O_{41-y}$ *phases, respectively.*

The film deposited at room temperature exhibits a clear two-step resistive transition with $T_{c,\ zero}$ around 65K. The XRD pattern of this film, not shown in figure 8.12(b), illustrated the presence of similar proportion of the 2223 and the 2212 phases. The pattern also showed the presence of the (119), and (200) peaks of the 2223 phase and a high level of backround noise especially at the low angles between 4-20°. The high level noise could be an indication of the presence of an amorphous phase in the film. As the substrate temperature was increased to 250°C the films exhibits a single resistive transition of 110K and $T_{c,\ zero}$ above 100K with the XRD pattern showing a highly c-axis oriented 2223 (>85% purity) film. However, with further increase in the substrate temperature to 400°C, the R-T curve exhibits a low temperature tailing with complete zero resistance at 90K. This is despite the XRD pattern showing the 2223 as the dominant phase. The XRD pattern of the film deposited at 450°C shows that the 2212 phase is the main constituent. The R-T curve of this film exhibits a small resistivity drop at 110K followed by an 80K transition with $T_{c,\ zero}$ around 52K. Uniform film deposition became increasing difficult at substrate temperatures above 450°C due to high vapour pressure of PbO. In fact, substrate temperature of 490°C was found to the threshold temperature for multilayered BiPbSrCaCuO/PbO film deposition. Above this temperature BiPbSrCaCuO/PbO multilayered films could not be deposited.

The variation in the 2223 (H) phase and the 2212 (L) phase as a function of substrate temperature can be shown by plotting the XRD intensity of the (0014)H and (0012)L peaks as a function of the substrate temperature, T_S. The intensity plots of the (0014)H and the (0012)L diffraction peaks shown in figure 8.13 indicate that the 2223 phase increases in proportion with an increase in the substrate temperature and reaches a maximum level for the film deposited at 250°C. Above this temperature, however, the 2223 phase decreases rapidly and reaches a minimum value for the film deposited at 450°C where the peaks of the 2212 phase are dominant. The dependence of $T_{c,\ onset}$ and $T_{c,\ zero}$ of the films as a function of the substrate temperature shown in figure 8.14 indicate that the $T_{c,\ onset}$ is not effected for the films deposited below 450°C. However, $T_{c,\ zero}$ increases to a maximum value of 104.5K for film deposited at 250°C before decreasing with an increase in the substrate temperature.

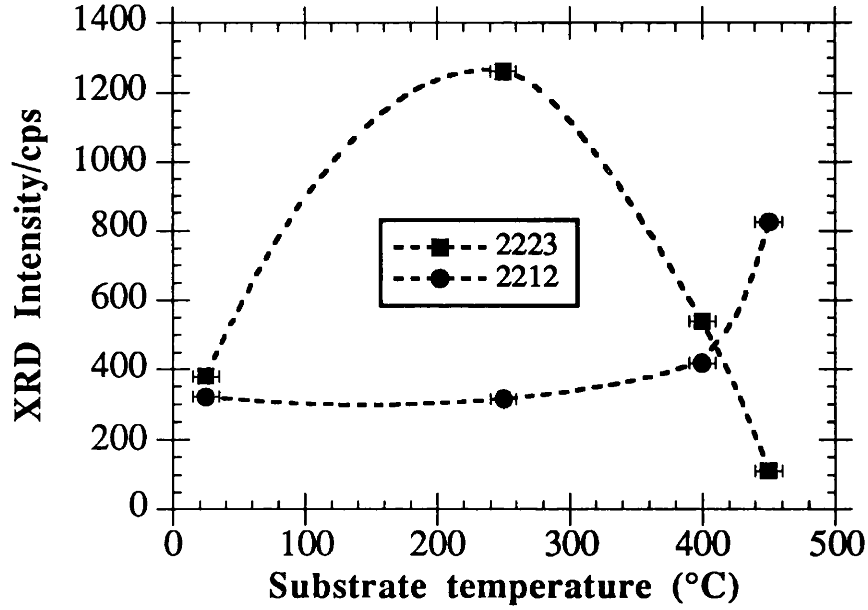

Figure 8.13- *Dependence of XRD intensity of the (0014)H and (0012)L of the diffraction peaks of the 2223, and 2212 phases, respectively on the substrate temperature. Dotted lines are possible profiles.*

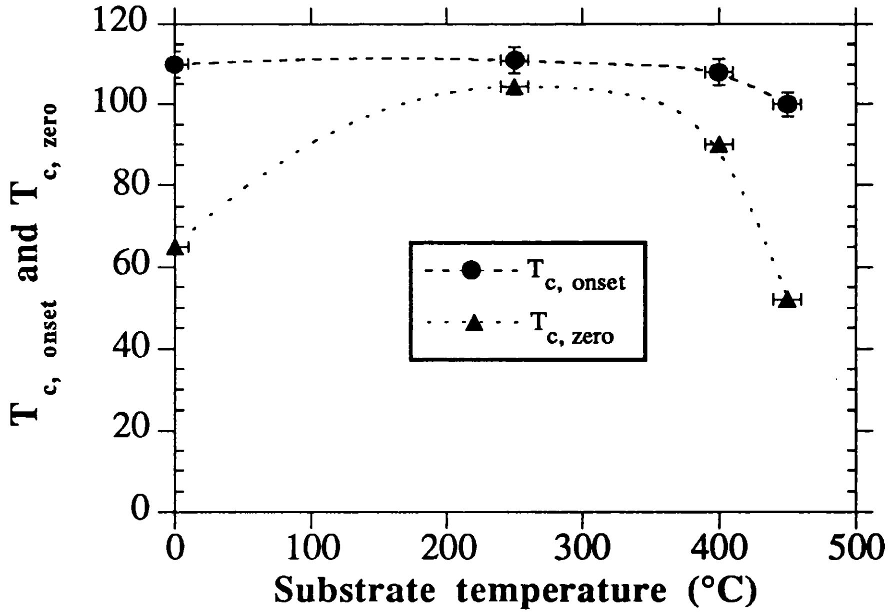

Figure 8.14- *Dependence of* $T_{c,\ onset}$ *and* $T_{c,\ zero}$ *on of the substrate temperature. Dotted lines are possible profiles.*

These results indicate that the superconducting properties of the multilayered films are quite sensitive to the substrate temperatures. The two-step resistive transitions obtained for the multilayered BiPbSrCaCuO/PbO films deposited at room temperature corresponds to the low proportion of the 2223 and high proportion of the 2212 phases present in the film. This is also illustrated by the intensity counts of the (0014)H and (0012)L diffraction peaks of the 2223 and the 2212 phases plotted in figure 8.13. In contrast with this film, the multilayered film deposited at substrate temperature of 250°C is highly c-axis oriented and shows a high XRD intensity count for the 2223 phase. The reduction in the proportion of the 2223 phase and $T_{c,\ zero}$ values of the films deposited at substrate temperatures above 250°C could be attributed to the reduction of Bi and Pb concentrations in these films. The EPMA analysis of the multilayered films showed a significant decrease in Bi concentration in the films deposited at and above 450°C. The reduction in Pb concentration is attributed to the low melting point and high vapour pressure of this material at high substrate temperatuers. This results in Pb deficiency in the multilayered BiPbSrCaCuO/PbO films and hence a reduction in the proportion of the 2223 phase and the $T_{c,\ zero}$ value respectively. The Bi deficiency has also been reported by Beker et al. [38] who observed a significant decrease in Bi concentration with an increase in substrate temperatures in the pulse laser deposition of BiPbSrCaCuO material using a Nd-YAG laser. In fact, based on X-ray fluorescence analysis (RFA) they have shown that due to low melting point of metallic Bi a depletion by 40-50% of the Bi content in the films deposited at 450°C, as compared to the Bi concentration in the initial target material, was detected. Similar Bi deficit in hot-deposited BiSrCaCuO thin films has also been reported by Tanaka et al. [39] who proposed deposition of Bi_2O_3 layers between several layers of BiSrCaCuO to avoid this deficiency.

8.8.3 Role of Pb in the multilayer film growth of the 2223 phase

The aim of this study is to investigate the effect of PbO thickness per layer in the multilayered BiPbSrCaCuO/PbO films on the formation of the 2223 phase. In the initial experiments SIMS and dot-mapping analysis were carried out on the multilayered films in order to confirm the layered structure of the films and the precipitation of PbO through the BiPbSrCaCuO layers after the post-annealing cycle. This is followed by the discussion of the results obtained for the multilayered films with various PbO thicknesses per layer.

The films were characterised by secondary ion mass spectroscopy (SIMS), EPMA (dot-mapping), XRD, and SEM. The R-T measurements were carried out with the Van der Pauw technique.

The deposition conditions were similar to those outlined in the last section with the Nd-YAG laser delivering pulses of 2.6J/cm^2 on the target. The multilayered BiPbSrCaCuO/PbO films were deposited on MgO substrates held at 250°C. The number of BiPbSrCaCuO and PbO layers deposited was fixed at 5 and 4, respectively.

8.8.3.1 SIMS and dot-mapping analysis

The SIMS depth profiles were conducted on a Atomika 6500 at Imperial College (Department of Material Science). A 15 KeV O_2^+ primary ion beam with a beam current of 150nA was used. For these experiments the BiPbSrCaCuO and PbO layers were each 200nm and 50nm in extent, respectively. This resulted in a total film thickness of 1.2µm. The films were either amorphous or annealed at 854°C for 1 hour in air. The SIMS analysis was carried out on both the annealed and un-annealed films while the dot-mapping was performed on the annealed film only.

The SIMS results of the non-annealed film and the annealed film are shown in figure 8.15 (a, b). In the SIMS depth profile of the un-annealed film, figure 8.15(a) some evidence of a layered structure in the form of a step fuction is visible. However, the sharpness of the interfaces could not be determined due to surface topography and pin holes in the film which resulted in a poor depth resolution. The SIMS depth profile of the annealed film, shown in figure 8.15(b), shows no evidence of the layered structure, suggesting the PbO was diffused during the annealing process.

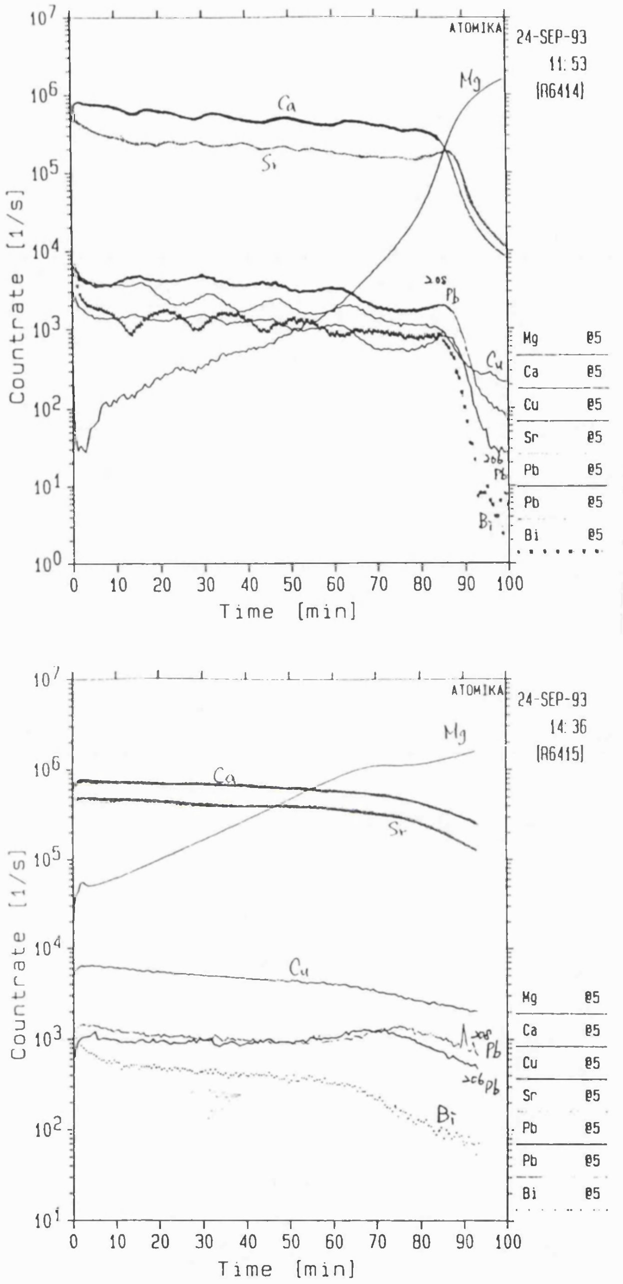

Figure 8.15 (a, b)- *SIMS analysis of the multilayered BiPbSrCaCuO/PbO films: a) as grown, b) annealed at 854 ℃ for 1 hour in air.*

The distribution of the diffused PbO layers in the annealed films was examined by the dot-mapping technique. The EPMA probe was programmed to scan an area on the film of about $1.5mm^2$. Figure 8.16 shows a photographic print of the multilayered film annealed at 854°C for 1 hour in air. In this picture colour red indicates the highest Pb concentration and colour green indicates the lowest Pb concentration in the film. The dot-mapping analysis indicates that upon annealing the multilayered BiPbSrCaCuO/PbO film PbO has diffused fairly uniformly through the BiPbSrCaCuO layers.

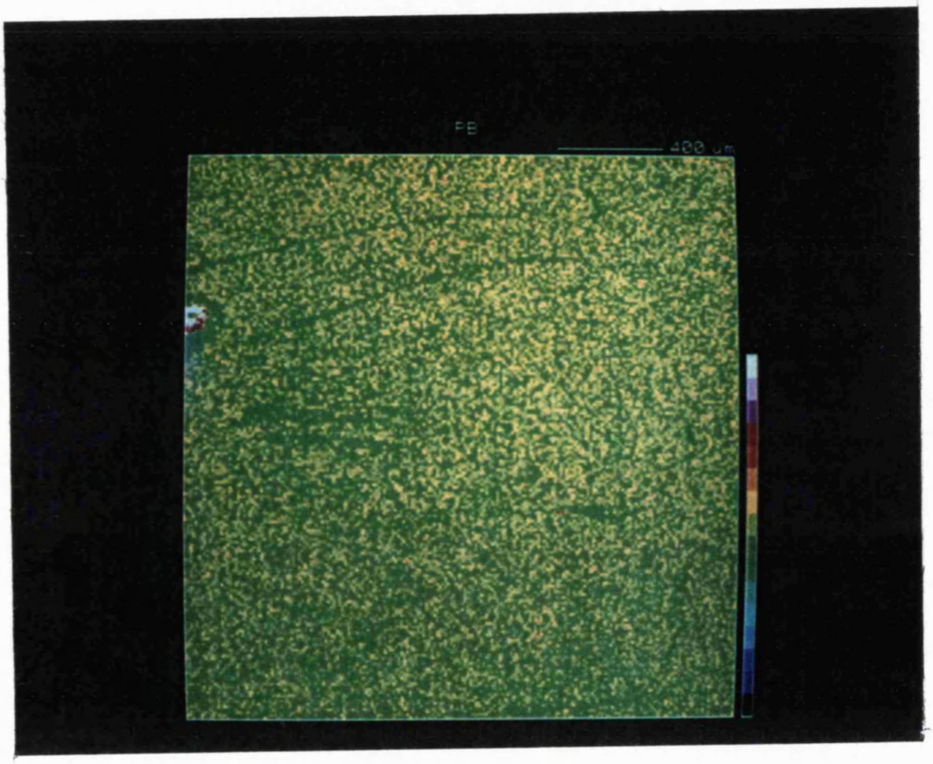

Figure 8.16- *Photograph of the dot-mapped area on the film annealed at 854°C for 1 hour in air.*

8.8.3.2 The role of PbO thickness

The effect of Pb concentration on the formation and growth of the 2223 phase was investigated by depositing multilayered films with various PbO thickness per layer. In that context the PbO and BiPbSrCaCuO thickness per each layer was varied from 13nm-266nm and 200-300nm, respectively.

In the first set of experiments the BiPbSrCaCuO layers in the multilayered BiPbSrCaCuO/PbO films were deposited from the $Bi_{1.68}Pb_{0.32}Sr_{1.75}Ca_{1.82}Cu_{2.75}O_x$ target. For these experiments each PbO layer was varied in thickness between 13-266nm while the BiPbSrCaCuO layer was fixed at 300nm per layer. This resulted in a total film thickness between 1.25-2.26μm. The films were subsequently annealed between 850-860°C for 1 hour in air.

The development of various phases with different PbO thickness per layer can be shown by plotting the XRD intensity of the chosen diffraction peaks of the phases present in the films [9]. Figure 8.17(a, b) illustrates the plot of the (0014)H, (0012)L, and (006)S diffraction peaks of the 2223, 2212, and 2201 phases, respectively against PbO thickness per layer for the mutilayered films annealed at 850°C and 854°C. In this plot the intensity of the peaks are normalised with respect to the peak of the highest intensity. The plots show that the 2223 phase increases in proportion with an increase in PbO thickness per layer and reaches an optimum amount in the films deposited with the PbO per layer, x, of 133nm and annealed at 850°C and 854°C. It should be noted that in both films the 2212 phase has remained the main constituent. With further increase in the PbO thickness per layer to 216nm the pattern in figure 8.17(b) shows the decomposition of the 2223 phase. By comparing the two plots it is also possible to conclude that with an increase in the PbO thickness per layer the required annealing temperature for the growth of the 2223 phase is lowered. For instance, in the film with x=80nm per layer a higher proportion of the 2223 is grown by annealing at 854°C than at 850°C. On the other hand, in the film with x=133nm per layer a higher proportion of the 2223 phase is grown by annealing at 850°C than at 854°C.

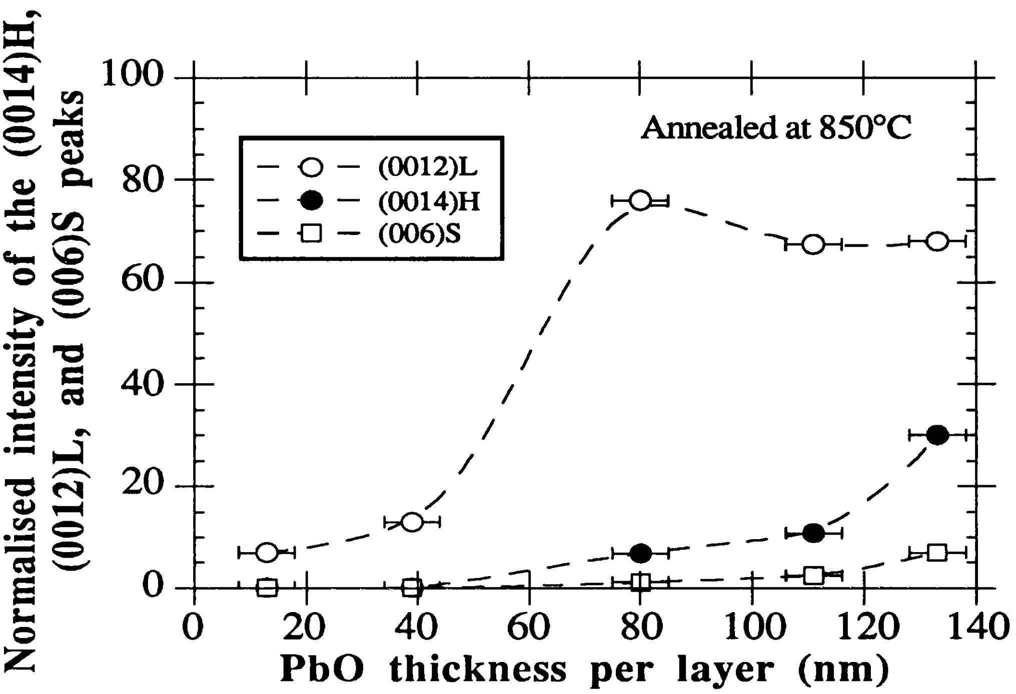

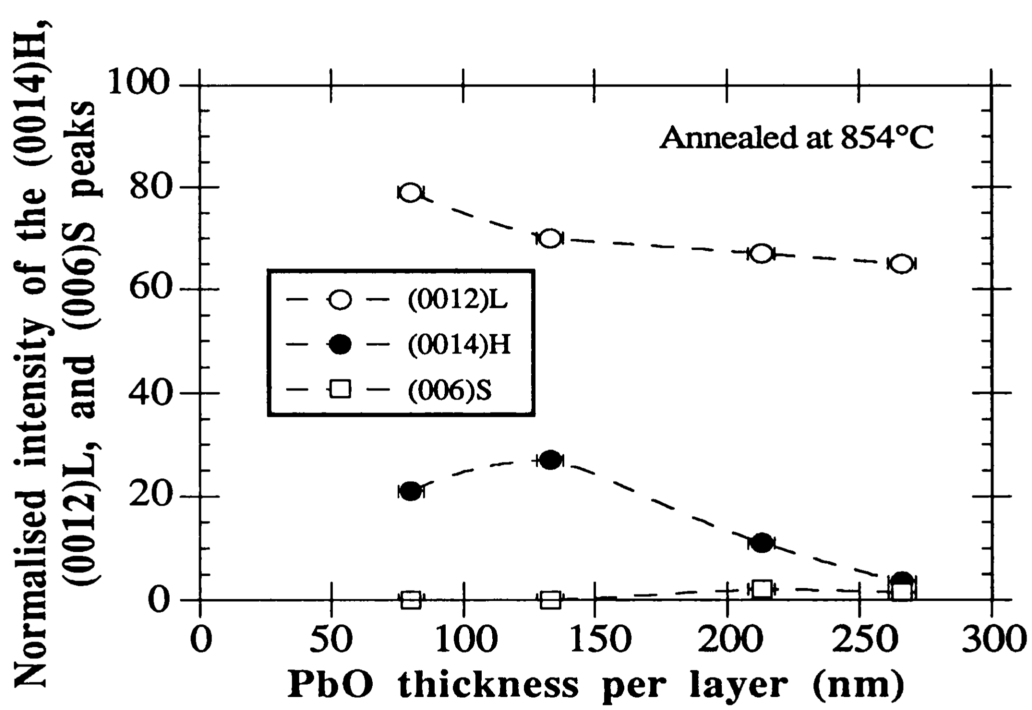

Figure 8.17 (a, b)- *Dependence of the XRD intensity diffraction peaks of the (0014)H, (0012)L, and (006)S of the 2223, 2212, and 2201 phases, respectively on the PbO thickness per layer. Dotted lines are possible profiles.*

In the second set of experiments the BiPbSrCaCuO layers in the multilayered films were deposited from the $Bi_{1.7}Pb_{0.4}Sr_{1.6}Ca_{2.4}Cu_{3.6}O_x$ target. The BiPbSrCaCuO and PbO thickness per layer in these films were 200nm and between 70-90nm, respectively. This resulted in total film thicknesses between 1.28-1.36µm.. The multilayered films were annealed at 854°C for 15 hours in air. The XRD patterns of the BiPbSrCaCuO/$(PbO)_x$ films with 70nm<x<90nm per layer is shown in figure 8.18. The patterns show a clear increase in the proportion of the 2223 phase with an increase in the PbO concentration per layer up to x=80nm. With further increase in the PbO thickness per layer to x=90nm, the XRD pattern shows the decomposition of the 2223 phase. The pattern also shows some evidence of the formation of the Ca_2PbO_4 phase. Further increase in the PbO thickness per layer, >90nm, resulted in the partial evaporation of the film during the post-annealing cycle.

The SEM observation of the heavily doped BiPbSrCaCuO/PbO films, x>90nm, showed the presence of plate and needle shaped crystals in the non evaporated areas. The composition of these needle shaped crystals were found to be $(Sr_{14-x}Ca_x)Cu_{24}O_{41-y}$. The formation of the long needle shaped crystals is attributed to partial film evaporation which causes an inhomogeneous distribution of the elements. Tanaka et al. [28] have reported the formation of Ca-Cu-O needle type crystals in heavily Pb doped films deposited from a near 2223 target by the sputtering technique.

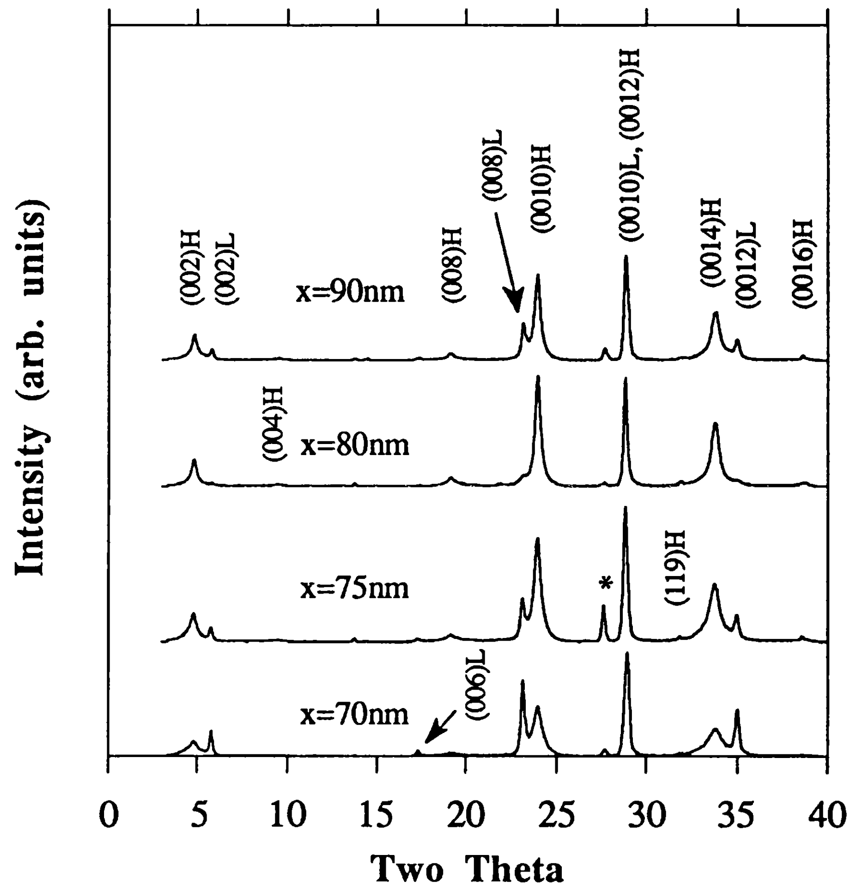

Figure 8.18 *XRD patterns of multilayered BiPbSrCaCuO/$(PbO)_x$ films with 90<x>70nm per layer. H, L, and * are assigned to the 2223, 2212, and $(Sr_{14-x}Ca_x)Cu_{24}O_{41-x}$ phases, respectively.*

The proportions or the relative volume-fractions of the 2223 (H) phase and the 2212 (L) phase have often been demonstrated by the plot of their intensity ratios of the (002)H/(002)L and (0014)H/(0012)L peaks [27, 28, 40]. Figure 8.19 shows the plot of the intensity ratios of the (0014)H/(0012)L+(0014)H as a function of PbO concentration, x, per layer. Similar results were obtained from the (002) peaks, however, to avoid confusion these are not plotted. The error bars are also omitted in order to avoid confusion. However, error of ±5nm should be considered for PbO thickness per layer.

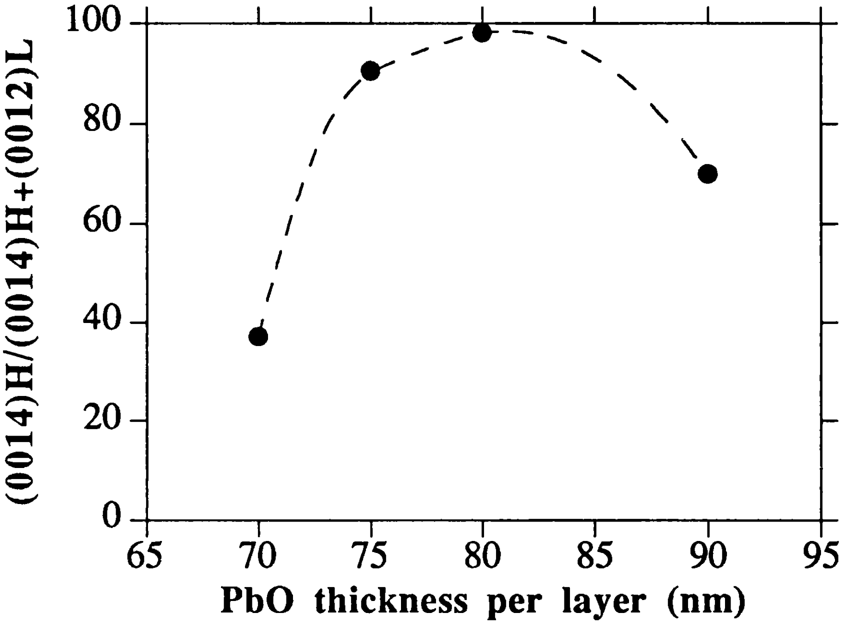

Figure 8.19- *Variation of (0014)H/(0012)L+(0014)H peaks as a function of PbO thickness per layer. Dotted line is a possible profile.*

The data clearly indicates that the 2223 phase increases with an increase in PbO thickness per layer up to 80nm. However, beyond 80nm the 2212 increases at the expense of the 2223 phase which is an indication that the 2223 phase partly decomposes into the 2212 phase. In fact Chen et al. [9] have shown that the 2223 phase decomposes into 2212 and the lead rich liquid phase in $(BiPb)_2Sr_2Ca_2Cu_4O_x$ samples.

The R-T curves of the films shown in figure 8.20 illustrate a gradual increase in $T_{c,\ zero}$ with an increase in PbO concentration per layer. The $T_{c,\ zero}$ in these films are ranging from 95K for film deposited with PbO thickness per layer of 70nm to 103.5K (ΔT=6.5K) for the film with PbO concentration per layer of 80nm. The resistance versus temperature curve of the film deposited with PbO thickness per layer of 90nm was not measured as the XRD of the film showed decomposition of the 2223 phase.

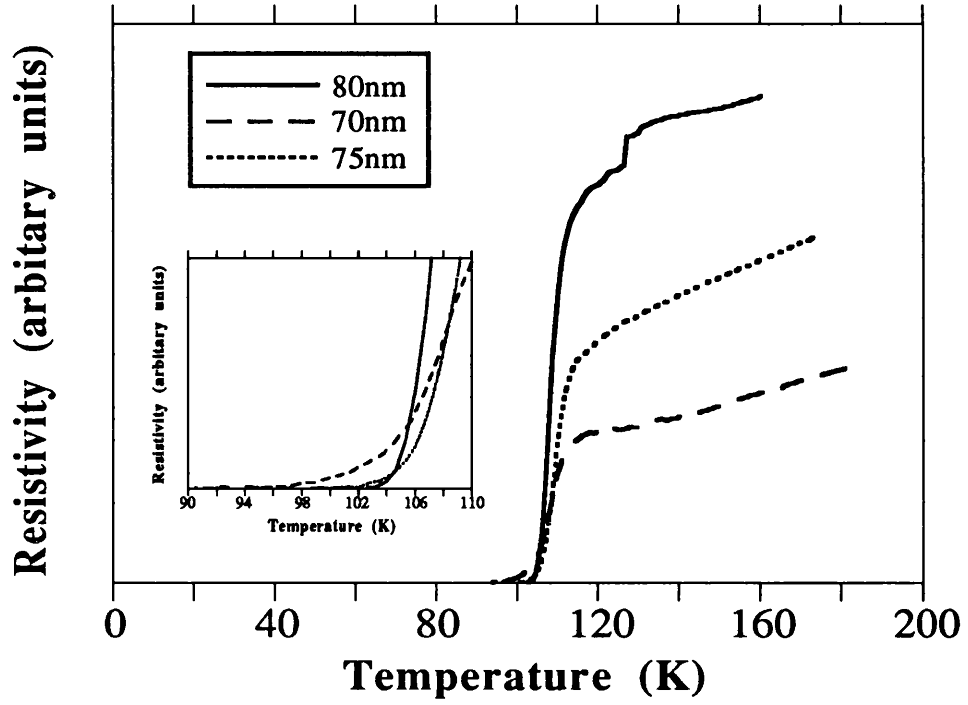

Figure 8.20- *R-T curves of the multilayered BiPbSrCaCuO/PbO films with PbO per layer ranging from 70nm to 80nm. These films were post-annealed at 854 °C for 15 hours in air.*

8.8.3.3 Discussion

In this study it was shown that PbO thickness per layer in the multilayered BiPbSrCaCuO/PbO films played an important role in the formation and enhancement of the 2223 phase. The dot-mapping analysis showed that the PbO layers in the multilayered BiPbSrCaCuO/PbO films percolates uniformly through the BiPbSrCaCuO layers. Several key conclusions can be made from this study. The patterns in figure 8.17 indicate that Pb lowers the required annealing temperature for the growth of the 2223 phase. The XRD patterns of the multilayered films shown in figure 8.18 clearly shows that at fixed annealing temperature and duration (854°C, for 15 hours) the proportion of the 2223 phase increases at the expense of the 2212 phase with an increase in the PbO thickness per layer. The optimum PbO thickness per layer for the multilayered films deposited from the $Bi_{1.7}Pb_{0.4}Sr_{1.6}Ca_{2.4}Cu_{3.6}O_x$ target was found to be 80nm. Beyond this value, the formation of the Ca_2PbO_4 phase and an increase in the proportion of the 2212 phase was observed. The partial melting of the heavily PbO doped, >90nm per layer, multilayered film indicates that PbO lowers the melting point of the BiPbSrCaCuO film. Finally, the XRD pattern of the film with PbO thickness per layer of 90nm indicates that the 2223 phase decomposes into the 2212 and $(Sr_{14-x}Ca_x)Cu_{24}O_{41-y}$ phases in the case of the films deposited from the $Bi_{1.7}Pb_{0.4}Sr_{1.6}Ca_{2.4}Cu_{3.6}O_x$ target. This is in agreement with Chen et al. [9] proposal that the 2223 phase decomposes into the 2212 phase and an amorphous liquid phase. They have suggested that the formation of the $(Sr_{14-x}Ca_x)Cu_{24}O_{41-y}$ phase in 2224 samples is due to the crystallization of the Bi-deficient liquid phase.

8.9 Optimization of the annealing conditions

In the following sections a series of studies on the optimization of the annealing conditions are presented. In these studies the effect of annealing temperature, duration, and atmosphere on the formation of the 2223 phase in the multilayered BiPbSrCaCuO/PbO films is discussed.

8.9.1 The role of annealing temperature

The published results indicate that the temperature range for the formation of the 2223 phase is narrow and its thermal stability limited, which results in a propensity for multiphase formation [41]. The temperature range for bulk synthesis of the 2223 phase usually employed is between 845°C and 870°C, depending on the starting composition and annealing atmosphere. The temperature range for the formation and growth of the 2223 phase in large volume in thin films, however, has been reported to be between 850-860°C which is even narrower than in the case of bulk samples [42, 27, 28]. In this study the effect of annealing temperature and annealing duration on the formation of the 2223 phase in the multilayered BiPbSrCaCuO/PbO films is investigated. These effects were systematically investigated on the multilayered BiPbSrCaCuO/PbO films deposited from three (BiPb)SrCaCuO targets with various nominal starting compositions (see table 8.3). The films were charecterised by XRD, EPMA, and resistivity techniques.

To ascertain the optimum annealing temperature and examine the effect of the starting composition, multilayered BiPbSrCaCuO/PbO films were grown from three targets with different compositions on MgO substrates (001) orientation. The number of BiPbSrCaCuO and PbO layers deposited was fixed at 5 and 4, respectively each being 200nm and 80nm in extend, respectively. This resulted in a total film thickness of 1.32μm. The substrate temperature was kept at 250°C during the depositions. The films were post-annealed at a fixed temperature in the range of 848-857°C for 15 hours in air.

In the first set of experiments multilayered BiPbSrCaCuO/PbO films were deposited from the target with the nominal starting composition of (2: 1.75: 1.82: 2.75) and annealed in the temperature range of 845-860°C. Figure 8.21 shows $T_{c,\ onset}$ and $T_{c,\ zero}$ values of the films annealed at various temperatures for 1 hour in air. The patterns show a fairly uniform $T_{c,\ onset}$ and $T_{c,\ zero}$ values for the films annealed between 850-860°C.

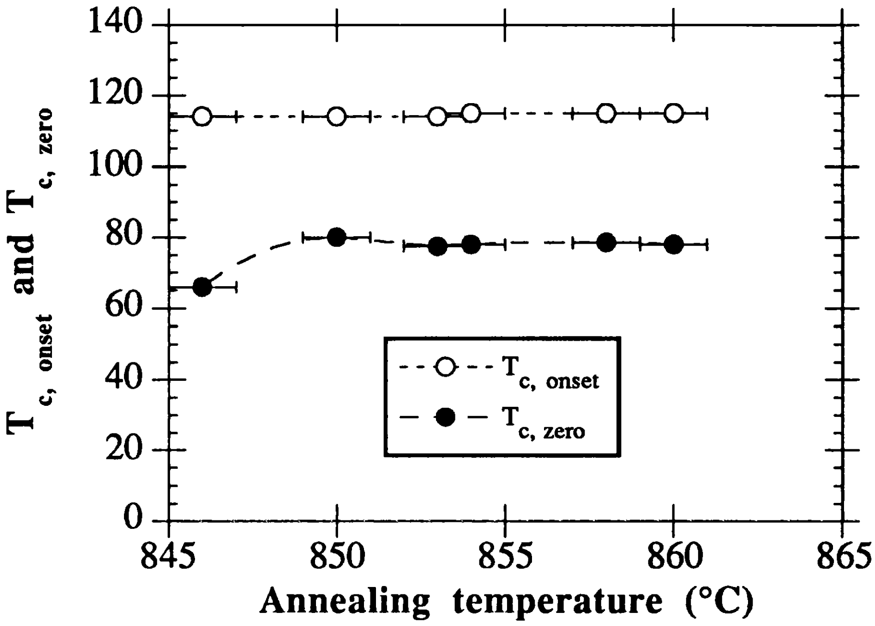

Figure 8.21- *The dependence of* $T_{c,\ onset}$ *and* $T_{c,\ zero}$ *of the multilayered films on the annealing temperature.*

The XRD patterns of the films, not shown here, illustrated the presence of the 2223 phase in small amount, ≈10%, after 1 hour and ≈15% after 3 hours annealing at 858°C in air. With further increase in the annealing duration to 15 hours, however, the proportion of the 2223 phase decreased. The small relative amounts of 2223 phase is thought to be due to the insufficient Cu in the starting composition of the films. Chen et al. [9] have shown that excess Cu from the ideal value in the starting composition effectively lowers the melting temperature of the material and helps to increase the volume fraction of the 2223 phase.

In the second set of experiments, multilayered BiPbSrCaCuO/PbO films were deposited from the $Bi_{1.84}Pb_{0.32}Sr_{1.91}Ca_{2.25}Cu_3O_x$ target. The films were post-annealed in the temperature range of 848-856°C for 15 hours in air followed by furnace cooling to room temperature. The XRD patterns of these films are illustrated in figures 8.22.

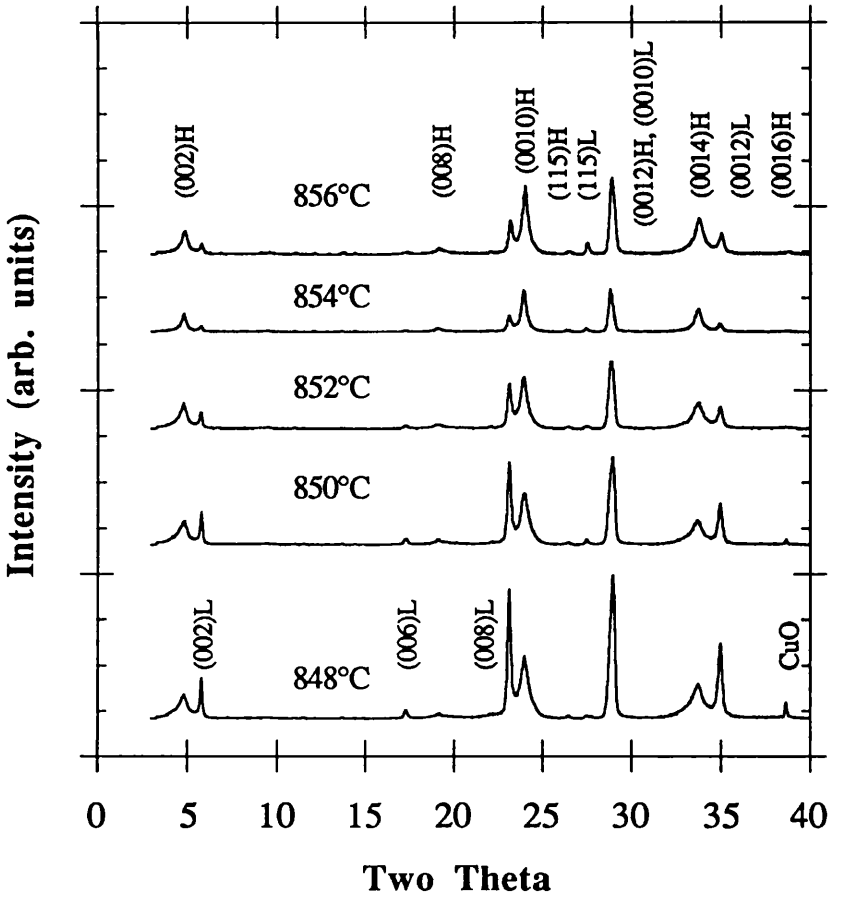

Figure 8.22- *XRD patterns of the multilayered BiPbSrCaCuO/PbO films grown from the $Bi_{1.84}Pb_{0.32}Sr_{1.91}Ca_{2.25}Cu_{3.06}O_x$ target and nnealed in the temperature range of 848-856 °C for 15 hours in air. Letters H and L are assigned to the peaks of the 2223 and 2212 phases, respectively.*

The development of different phases with the annealing temperatures can be shown by plotting the XRD intensities of the chosen diffraction peaks of the phases present in the films against annealing temperature. Figure 8.23 shows the plot of the (0014)H diffraction peak of the 2223 phase ($2\theta=33.8°$), (0012)L diffraction peak of the 2212 phase ($2\theta=34.82°$), and (006)S diffraction peak of the 2201 phase ($2\theta=21.9°$) as a function of the annealing temperature. In this plot the intensity of the peaks are normalised with respect to the peak with the highest intensity shown in figure 8.22.

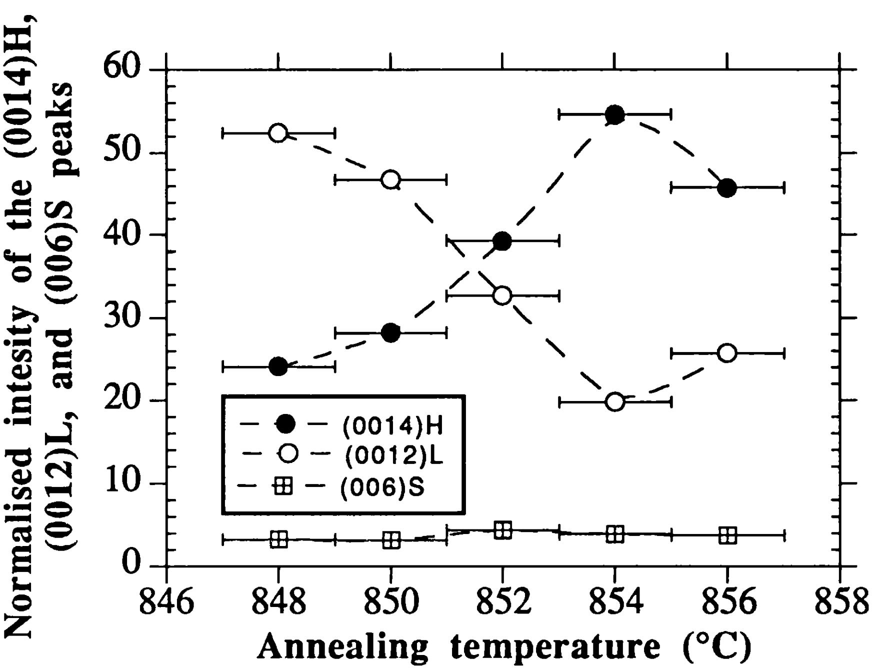

Figure 8.23- *Normalised intesity of the (0014)H, (0012)L, and (006)S peaks of the 2223, 2212, 2201 phases as function of the annealing temperature. Dotted line are a possible profile.*

The patterns indicate that the 2223 phase grows at the expence of the 2212 phase with an increase in the annealing temperature up 854°C. Beyond 854°C the 2223 is decomposed into the 2212 phase. There is also a constant level of the 2201 phase present in the films which seem not to be effected by the annealing temperature. Finally, multilayered BiPbSrCaCuO/PbO films were deposited from the $Bi_{1.7}Pb_{0.4}Sr_{1.6}Ca_{2.4}Cu_{3.6}O_x$ target. The films were annealed in the temperature range of 852-857°C for 15 hours in air, followed by furnace cooling to room temperature. The XRD patterns of the films are shown in figure 8.24.

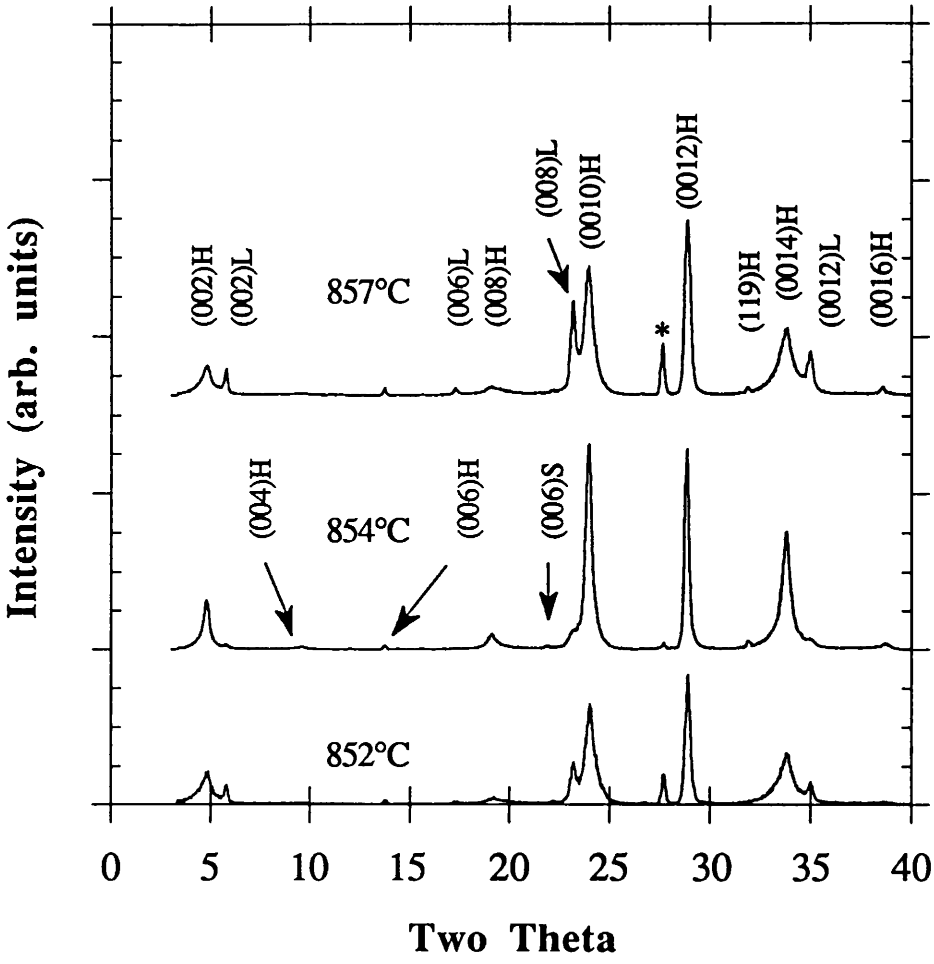

Figure 8.24- *XRD patterns of the multilayered BiPbSrCaCuO/PbO films grown from the* $Bi_{1.7}Pb_{0.4}Sr_{1.6}Ca_{2.4}Cu_{3.6}O_x$ *target and annealed in the temperature range of 852-857°C for 15 hours in air. Letters H, L, and * are assigned to the 2223, 2212 and the* $(Sr_{14-x,}Ca_x)Cu_{24}O_{41-y}$ *phases, respectively.*

The XRD patterns indicate the presence of the 2223, 2212, and 2201 phases as well as the $(Sr_{14-x},Ca_x)Cu_{24}O_{41-y}$ phase in the films deposited from the $Bi_{1.7}Pb_{0.4}Sr_{1.6}Ca_{2.4}Cu_{3.6}O_x$ target. Similar to the plot in figure 8.23, the development of different phases with annealing temperatures in these films is plotted by choosing the

(0014), (0012), (006), and (040) peaks of the 2223, 2212, 2201, and $(Sr_{14-x}, Ca_x)Cu_{24}O_{41-y}$ phases. This is shown in figure 8.25. In this figure the (040) peak of the $(Sr_{14-x}, Ca_x)Cu_{24}O_{41-y}$ phase is abriviated as (040)A.

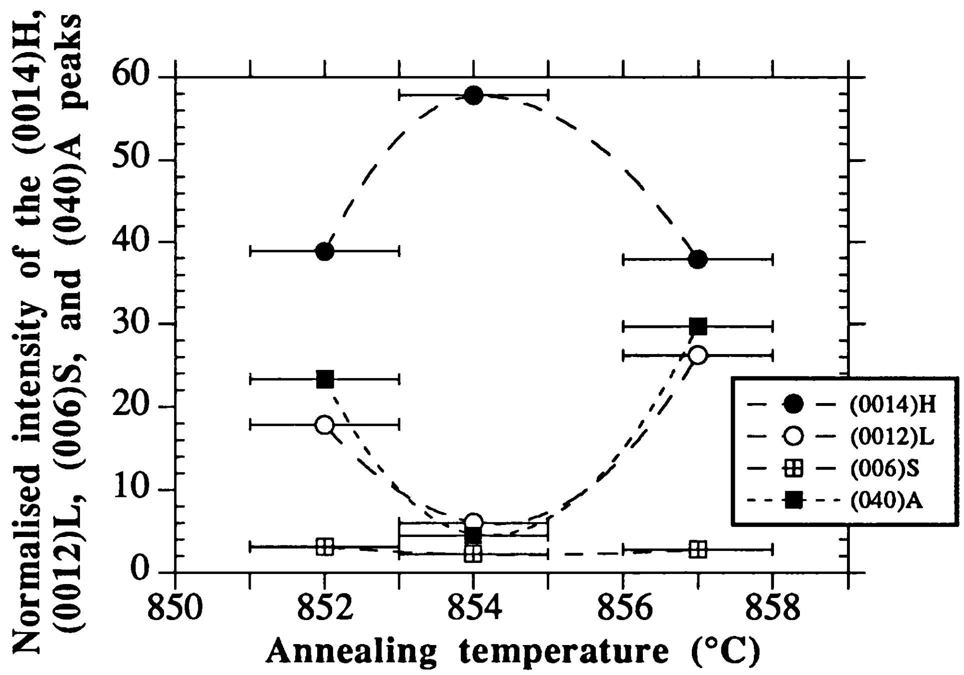

Figure 8.25- *Normalised intesity of the (0014)H, (0012)L, (006)S, and (040)A peaks of the 2223, 2212, 2201,* $(Sr_{14-x},Ca_x)Cu_{24}O_{41-y}$ *phases as function of the annealing temperature. Dotted lines are possible profiles.*

The patterns in the phase developments of the multilayered films deposited from the $Bi_{1.7}Pb_{0.4}Sr_{1.6}Ca_{2.4}Cu_{3.6}O_x$ target indicate also that the 2223 phase grows at the expence of the 2212 phase. Similar to the observation made in figure 8.23, there is a constant level of the 2201 phase present in these films, however, at a lower proportion. Also, the $(Sr_{14-x},Ca_x)Cu_{24}O_{41-y}$ and 2212 phases seem to go through a minimum proportion when the 2223 phase is at the maximum proportion. The resistivity versus temperature of the films deposited from the two targets and annealed in the temper$\overset{a}{t}$ ure range of 848-857°C for 15 hours in air is illustrated in figure 8.26 (a,b).

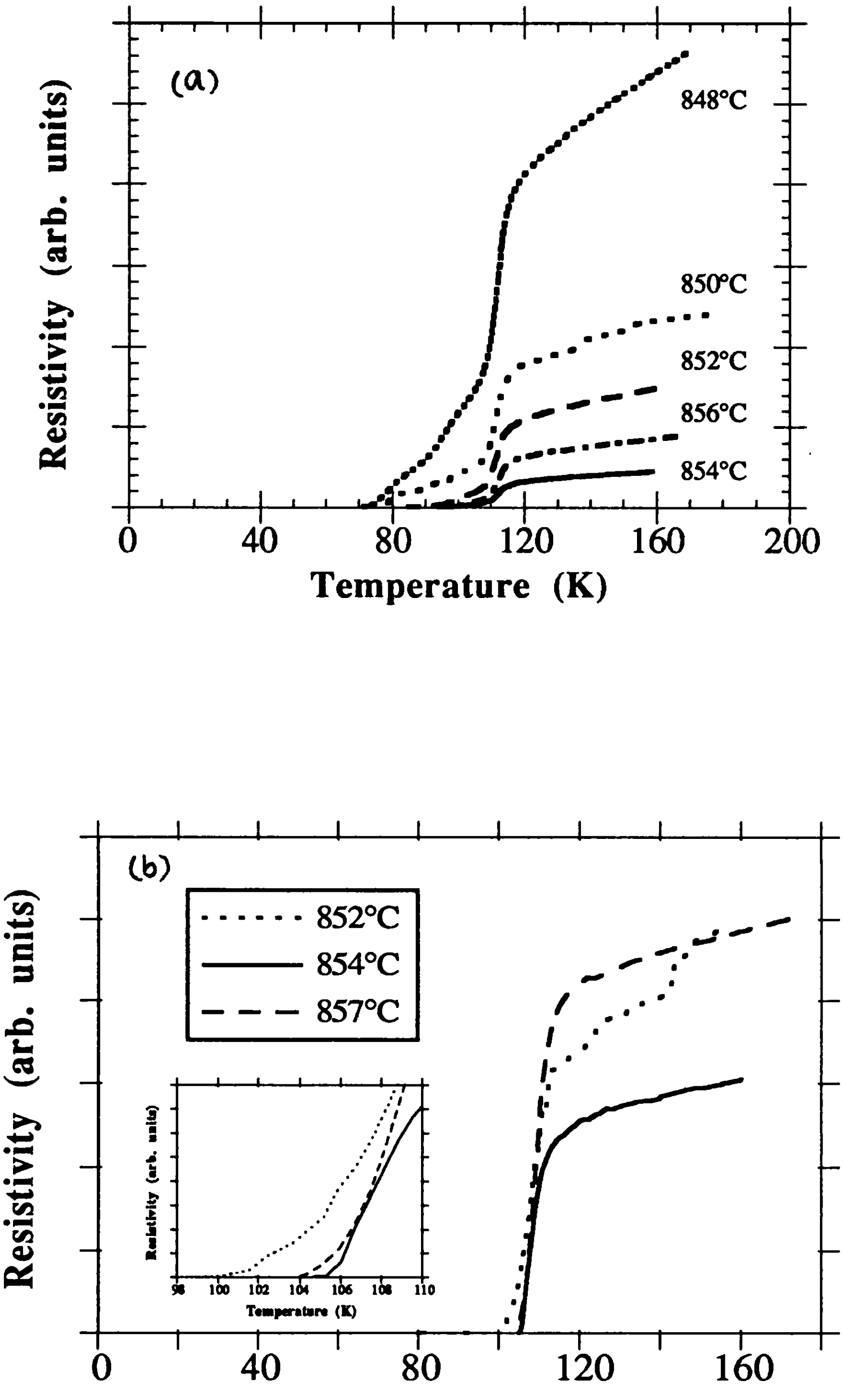

Figure 8.26(a, b)- *R-T curves for films deposited from the* $Bi_{1.84}Pb_{0.32}Sr_{1.91}Ca_{2.25}Cu_{3.06}O_x$ *and* $Bi_{1.7}Pb_{0.4}Sr_{1.6}Ca_{2.4}Cu_{3.6}O_x$ *targets and annealed in the temperature range of 852-857°C for 15 hours in air, respectively.*

The R-T curves of the multilayered films deposited from the $Bi_{1.84}Pb_{0.32}Sr_{1.91}Ca_{2.25}Cu_{3.06}O_x$ target show a progressive improvement in the $T_{c,\ zero}$ value with higher annealing temperatures. However, it is noted that the $T_{c,\ zero}$ does not increase above 100K in these films, even in the film annealed at 854°C which contains the highest proportion of the 2223 phase. The low resistive-tailing in the R-T curves is due to a high proportion of the 2201 phase present in these films, as indicated by the XRD patterns. The R-T curves of the films deposited from the $Bi_{1.7}Pb_{0.4}Sr_{1.6}Ca_{2.4}Cu_{3.6}O_x$ target show $T_{c,\ zero}$ ranging from 98K in film annealed at 852°C to 104.5K in film annealed at 854°C. This is despite the presence of the $(Sr_{14-x},Ca_x)Cu_{24}O_{41-y}$ phase in these films. Figure 8.27 shows plot of $T_{c,\ onset}$ and $T_{c,\ zero}$ for films grown from the $Bi_{1.7}Pb_{0.4}Sr_{1.6}Ca_{2.4}Cu_{3.6}O_x$ target. The pattern shows that while $T_{c,\ onset}$ increases slightly from 110K to 112K, $T_{c,zero}$ increases substantially from 98K in film annealed at 852°C to 104.5K in film annealed at 854°C. With further increase in the annealing temperature to 857°C, however, $T_{c,\ zero}$ decreases slightly to 104K.

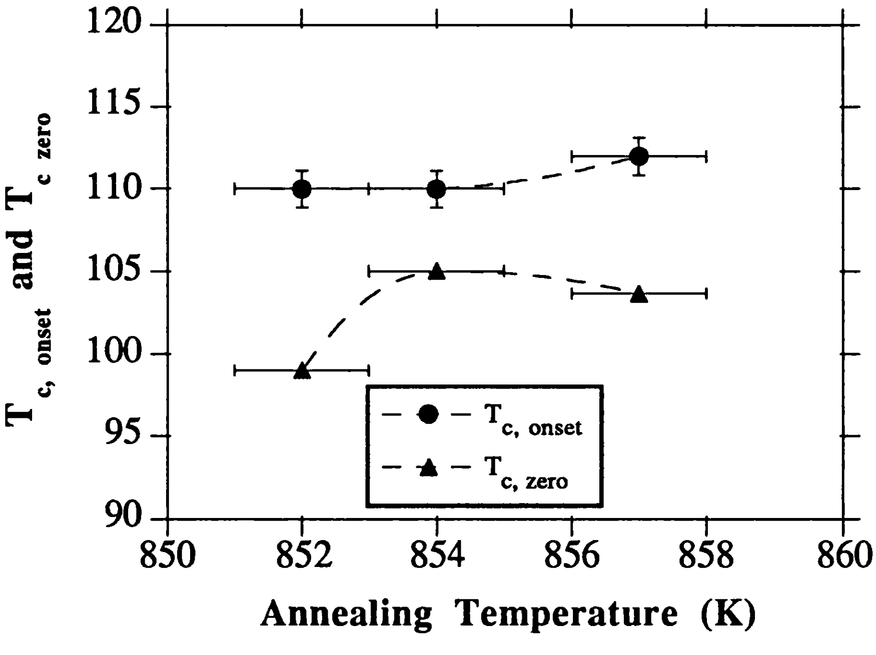

Figure 8.27- *$T_{c,\ onset}$ and $T_{c,\ zero}$ as a function of the annealing temperature for films deposited from the $Bi_{1.7}Pb_{0.4}Sr_{1.6}Ca_{2.4}Cu_{3.6}O_x$ target. Dotted line are possible profiles.*

8.9.2 The role of annealing duration

In this study the effect of the annealing period on the formation of the high T_c phase, 2223, in the multilayered BiPbSrCaCuO/PbO films is investigated. The deposition conditions and parameters were similar to those described in the previous section. In this study the films were deposited from the $Bi_{1.84}Pb_{0.32}Sr_{1.91}Ca_{2.25}Cu_{3.06}O_x$ and $Bi_{1.7}Pb_{0.4}Sr_{1.6}Ca_{2.4}Cu_{3.6}O_x$ targets. These films were subsequently annealed for different duration at 854°C in air followed by furnace cooling to temperatures below 100°C before leaving the furnace. The annealing temperature of 854°C was shown in the previous study to be the optimum temperature for the growth of the 2223 phase in large proportions for the multilayered BiPbSrCaCuO/PbO films. The films were characterised by XRD, EPMA, and resistivity techniques. In the first set of experiments multilayered films were deposited from the $Bi_{1.84}Pb_{0.32}Sr_{1.91}Ca_{2.25}Cu_{3.06}O_x$ target. The development of various phases with the annealing duration can be shown by plotting the XRD intensities of the chosen peaks of the phases present in the films. Figure 8.28 shows the plot of the (0014)H diffrcation peak of the 2223 phae, (0012)L diffraction peak of the 2212 phase, and (006)S diffrcation peak of the 2201 phase as a function of the annealing duration.

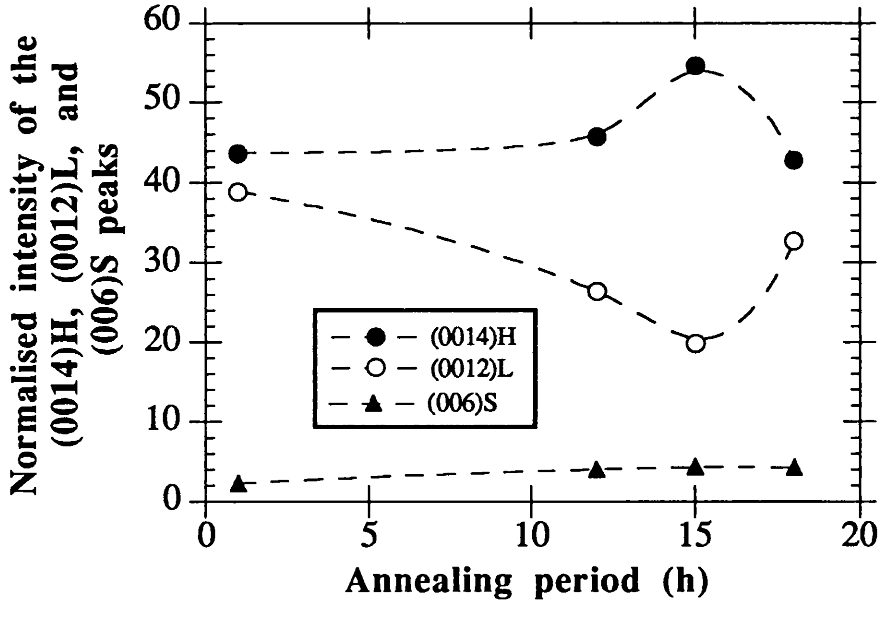

Figure 8.28- *Normalised intensities of (0014)H, (0012)L, and (006)S diffraction peaks of the 2223, 2212, and 2201 phases, respectively.*

The patterns show that the intensity of the (0014)H diffraction peak of the 2223 phase increases gradually and that of the (0012)L diffraction peak of the 2212 phase decreases rapidly with an increase in the annealing duration up to 15 hours. Beyond this optimum duration, however, the patterns show slight increase in the 2212 and 2201 phases. This indicates that the 2223 decomposes into the 2212 and the 2201 phases in the films deposited from the $Bi_{1.84}Pb_{0.32}Sr_{1.91}Ca_{2.25}Cu_{3.06}O_x$ target. In the second set of experiments the multilayered films were grown from the $Bi_{1.7}Pb_{0.4}Sr_{1.6}Ca_{2.4}Cu_{3.6}O_x$ target. The films were annealed at 854°C between 1-18 hours in air. The XRD patterns of these films are shown in figure 8.29.

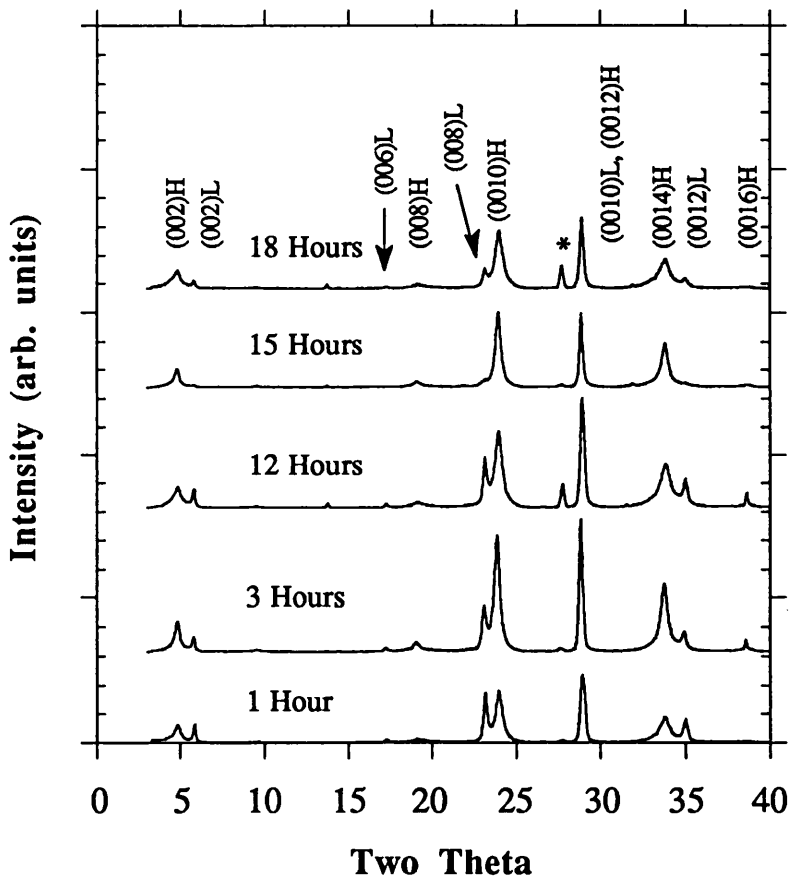

Figure 8.29- *XRD patterns of the multilayered films annealed at 854 ℃ between 1-18 hours in air. Letters H, L, *, are assinged to the peaks of the 2223, 2212, and $(Sr_{14-x},Ca_x)Cu_{24}O_{41-y}$ phase, respectively.*

The XRD patterns show that the 2223 phase increases in proportion at the expence of the 2212 phase with an increase in the annealing duration up to 15 hours. Beyond the optimum annealing time, 15, the pattern show an increase in the proportion of the 2212 and the $(Sr_{14-x},Ca_x)Cu_{24}O_{41-y}$ phases. The EPMA analysis of the film annealed for 18 hours indicated that the 2212 phase is rich in Bi and Sr. The average composition of the 2212 phase was found to be $Bi_{4.4}Sr_{2.71}Ca_{1.15}Cu_{1.8}O_x$.

The R-T curves of the films deposited from the $Bi_{1.84}Pb_{0.32}Sr_{1.91}Ca_{2.25}Cu_{3.06}O_x$ and $Bi_{1.7}Pb_{0.4}Sr_{1.6}Ca_{2.4}Cu_{3.6}O_x$ targets annealed at 854°C between 1-18 hours is illustrated in figure 8.30(a,b). The patterns show a progressive improvement in the $T_{c,\ onset}$ with an increase in annealing period for both sets of films. However, it is noted that for the films deposited from the $Bi_{1.84}Pb_{0.32}Sr_{1.91}Ca_{2.25}Cu_{3.06}O_x$ target, $T_{c,\ zero}$ does not exceed 97.5K even for the film annealed for 18 hours. On the other hand, the films deposited from the $Bi_{1.7}Pb_{0.4}Sr_{1.6}Ca_{2.4}Cu_{3.6}O_x$ target and annealed for various duration showed $T_{c,\ zero}$ above 98K. This is despite the presence of the $(Sr_{14-x},Ca_x)Cu_{24}O_{41-y}$ phase in these films.

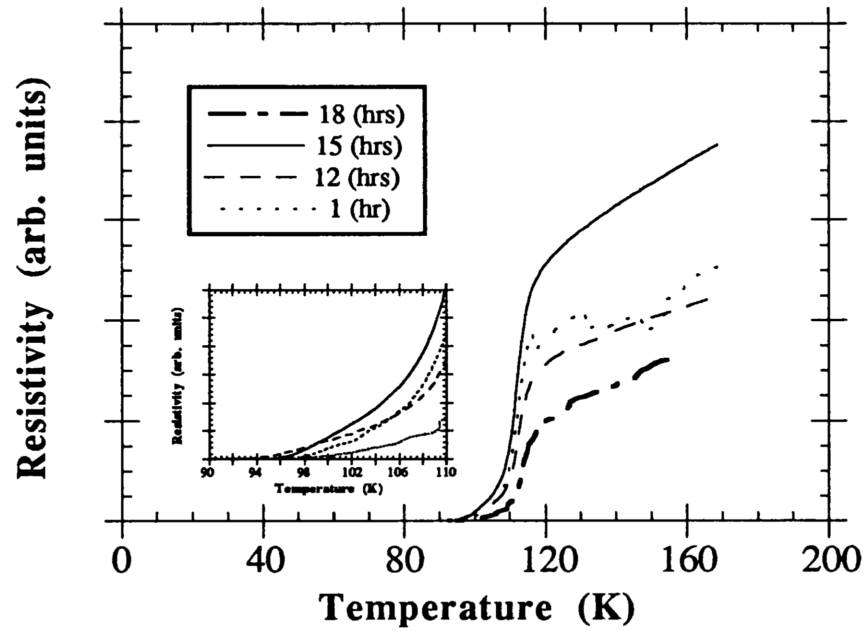

Figure 8.30(a)- *R-T curves of the films deposited from the $Bi_{1.84}Pb_{0.32}Sr_{1.91}Ca_{2.25}Cu_{3.06}O_x$ target and annealed form 1-18 hours at 854 °C in air.*

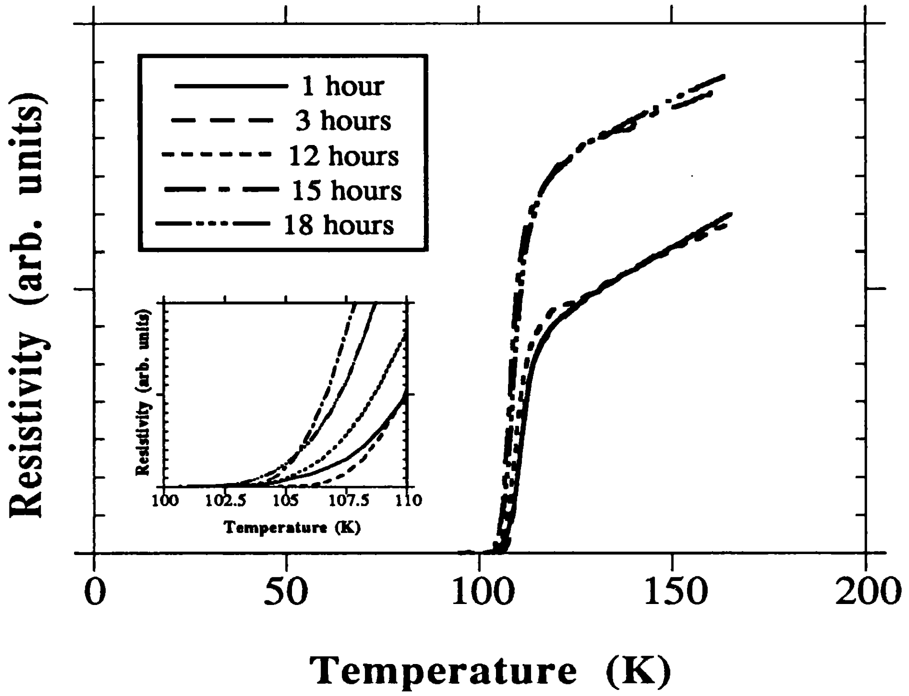

Figure 8.30(b)- *R-T curves of the films deposited from the $Bi_{1.7}Pb_{0.4}Sr_{1.6}Ca_{2.4}Cu_{3.6}O_x$ target and annealed for various duration.*

Figure 8.31 shows plot of $T_{c,\ onset}$ and $T_{c,\ zero}$ for films grown from the 2234 target as a function of the annealing period. The pattern shows that while $T_{c,\ onset}$ remains between 110K-112K in these films, $T_{c,zero}$ increases from 98K in the film annealed for 5 hours to 105.5K in the film annealed for 15 hours at 854°C. With further increase in the annealing period to 18 hours, however, $T_{c,\ zero}$ decreases slightly to 102K.

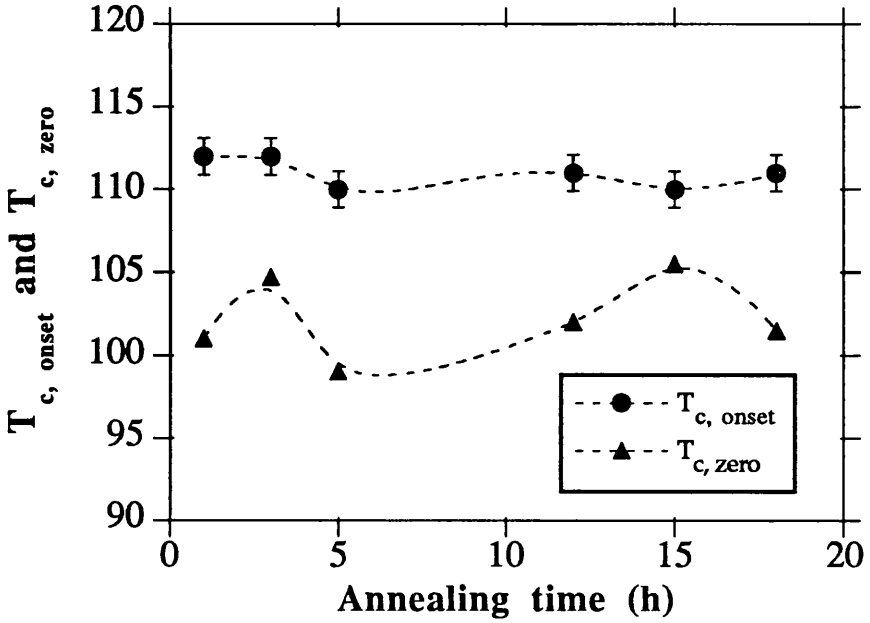

Figure 8.31- $T_{c,\ onset}$ *and* $T_{c,\ zero}$ *of films deposited from the* $Bi_{1.7}Pb_{0.4}Sr_{1.6}Ca_{2.4}Cu_{3.6}O_x$ *target. Dotted lines are possible profiles.*

8.9.2.1 Effect of annealing duration on Pb concentration

The EPMA analysis on the annealed multilayered BiPbSrCaCuO/PbO films indicated that Pb concentration decreased most rapidly during the first hour of annealing, and more slowly thereafter up to 3 hours. In fact, in films annealed for more than 5 hours only a very small concentration of Pb was detected. Figure 8.32 shows the dependence of the Pb thickness for films deposited at 250°C with PbO concentration of 80nm per layer as a function of high temperature annealing duration.

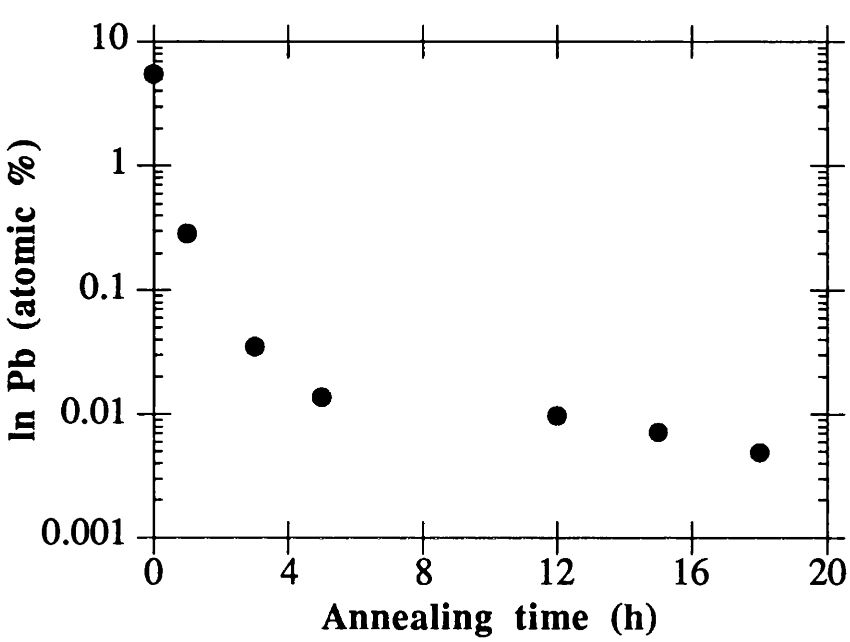

Figure 8.32- *Dependence of Pb (atomic %) on annealing period.*

In the diagram above the first data point is taken from EDX analysis of a single layer un-annealed BiPbSrCaCuO film deposited on a Si substrate. This data corresponds to Pb atomic percentage of 5.3% and its presence on the graph is for a guide only. In the multilayered films, Pb atomic percentage is expected to be much higher than this. The diagram shows that Pb molar fraction reaches 0.027 within the first hour of annealing at 854°C in air. This value decreases to 0.0034 after 3 hours and 0.0013 after 5 hours of annealing.

8.9.3 Discussion

By studying the XRD patterns of the multilayered films shown in figure 8.22, 8.24 a clear picture in the phase developments of the films with the annealing temperature emerges. The XRD patterns of the films deposited from the $Bi_{1.84}Pb_{0.32}Sr_{1.91}Ca_{2.25}Cu_{3.06}O_x$ and $Bi_{1.7}Pb_{0.4}Sr_{1.6}Ca_{2.4}Cu_{3.6}O_x$ targets indicate that the 2223 phase grows at the expense of the 2212 phase with an increase in the annealing temperature up to 854°C. When the optimum annealing temperature is exceeded, there is an increase in the proportion of the 2212 phase in the films deposited from the two targets and an increase in the proportion of the $(Sr_{14-x},Ca_x)Cu_{24}O_{41-y}$ phase in the film deposited from the $Bi_{1.7}Pb_{0.4}Sr_{1.6}Ca_{2.4}Cu_{3.6}O_x$ target. Therefore it is possible to conclude that the 2223 phase decomposes in accordance with

$$2223 \longrightarrow 2212 + (Sr_{14-x},Ca_x)Cu_{24}O_{41-x} \qquad (8.2)$$

in the case of the film deposited from the $Bi_{1.7}Pb_{0.4}Sr_{1.6}Ca_{2.4}Cu_{3.6}O_x$ target at 857°C, and

$$2223 \longrightarrow 2212 + (Ca, Sr)_2CuO_3 \qquad (8.3)$$

in the case of the film deposited from the $Bi_{1.84}Pb_{0.32}Sr_{1.91}Ca_{2.25}Cu_{3.06}O_x$ target at 856°C. The $(Ca,Sr)_2CuO_3$ phase was detected by EPMA analysis of the films. However, the presence of this phase could not be verified from the XRD patterns shown in figure 8.22. This is due to the overlapping of the diffraction peaks of this phase with those of the 2223 and 2212 phases. Chen et al. [9] have shown that the 2223 phase decomposes at 856°C in 2224 samples, to form the 2212 and liquid phases. They have proposed that the formation of the secondary phases such as $(Sr_{14-x},Ca_x)Cu_{24}O_{41-y}$ in the 2224 sample and $(Ca,Sr)_2CuO_3$ in the 2223 samples is due to the crystallization of the Bi-deficient liquid phase. The presence of the 2201 phase in the samples is related to the formation mechanism of the 2223 phase which is via the reaction between the 2201 precipitates and Ca^{2+} and Cu^{2+} from the liquid phase. This indicates that in this process it is conceivable for some of the 2201 phase to remain un-reacted. Also the slight increase in the proportion of the 2201 phase in the film annealed at 856°C is due to the decomposition of the 2212 phase.

The 2223 phase also grows with longer annealing duration. The XRD patterns of both sets of films deposited from the two targets and annealed up to 18 hours in air indicate that the 2223 phase increases at the expense of the 2212 phase. Beyond the optimum annealing time of 15 hours, however, the 2223 phase decomposes in accordance with (8.2) and (8.3) for the two compositions.

In summary several key conclusions can be made from the two studies. The amount of the 2223 phase that forms using the multilayered BiPbSrCaCuO/PbO technique depends strongly on the annealing temperature and duration and that the temperature range in which the 2223 phase is produced preferentially is exceedingly narrow. The form of the plots in figures 8.23 and 8.25 indicate that with the multilayered (BiPbSrCaCuO/PbO) technique, annealing temperature of 854°C is optimum for both compositions. However, the volume fraction of the 2223 phase is sensitive to the composition of the film. This leads to the conclusion that excess Cu in the composition significantly increases the volume-fraction of the 2223 phase. However, the drawback of using excess Cu is the formation of the $(Sr_{14-x},Ca_x)Cu_{24}O_{41-y}$ phase. Therefore in order to enhance the formation of the 2223 phase and avoid the growth of the $(Sr_{14-x},Ca_x)Cu_{24}O_{41-y}$ phase adjustment to the target composition is necessary. Another important conclusion is that the presence of the 2212 phase in the microstructure of the films is as a result of the fact that the 2223 and the 2212 phases can coexist thermodynamically at 854°C.

8.9.4 The role of atmosphere

The effect of post annealing atmosphere on the formation of the 2223 phase in the BiSrCaCuO system has been investigated by a number of researchers [10, 14, 43, 44]. For instance, Koyama et al. [14] have reported that the growth of the 2223 phase is facilitated by annealing the sample in an oxygen partial pressure of P_{O_2}=1/13 atmosphere. Endo et al. [10] have in fact demonstrated the growth of single 2223 phase by annealing BiPbSrCaCuO samples in an Ar:O_2 atmosphere. In this study the effect of annealing in an Ar:O_2 atmosphere on the formation of the 2223 phase in the multilayered BiPbSrCaCuO/PbO films is investigated and the results are discussed. The films were characterised by XRD and resistivity techniques.

To ascertain the optimum annealing temperature and examine the effect of the post-annealing atmosphere several multilayer BiPbSrCaCuO/PbO films were deposited on MgO substrates held at 250°C from the $Bi_{1.7}Pb_{0.4}Sr_{1.6}Ca_{2.4}Cu_{3.6}O_x$ target.. The deposition conditions were similar to those described in the previous sections. In the first set of experiments these films were post-annealed in an Ar:O_2 mixture, with an oxygen partial pressure of P_{O_2}=1/13 atmosphere in the temperature range of 830-850°C for 15 hours. The development of different phases with the annealing temperatures can be shown by plotting the XRD intensity of the chosen diffraction peaks of the phases present in the films against the annealing temperature. Figure 8.32 shows the plot of the (0014)H diffraction peak of the 2223 phase (2θ=33.8°), (0012)L diffraction peak of the 2212 phase (2θ=34.82°), and (040) diffraction peak of the $(Sr_{14-x},Ca_x)Cu_{24}O_{41-y}$ phase as a function of the annealing temperature. In this figure the (040) diffraction peak of the $(Sr_{14-x},Ca_x)Cu_{24}O_{41-y}$ phase is abbreviated as (040)A.

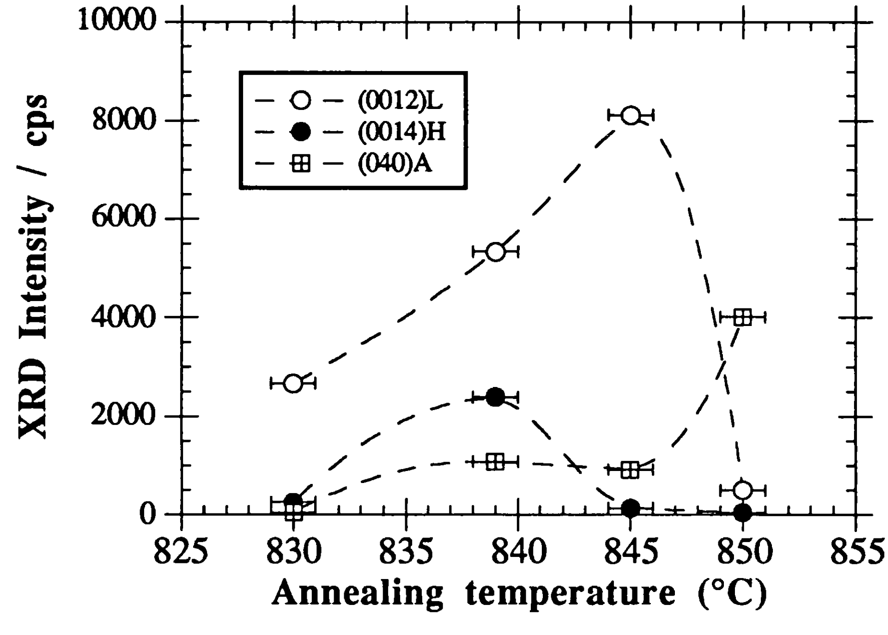

Figure 8.32- *Reaction temperature dependence of XRD intensities of the (0014)H, (0012)L, and (040) diffractions for 2223, 2212, and $(Sr_{14-x},Ca_x)Cu_{24}O_{41-x}$ phases. Dotted lines are possible profiles.*

The patterns show that the proportion of the 2223 phase steadily increases with an increase in the annealing temperature and reaches a maximum value for the film annealed at 839°C for 15 hours. With further increase in the annealing temperature to 845°C, however, the proportion of this phase decreases rapidly and reaches a minimum value in the film annealed at 850°C. The 2212 phase, on the other hand, is the major constituent in all the films except in the film annealed at 850°C where the $(Sr_{14-x},Ca_x)Cu_{24}O_{41-y}$ phase is the main constituent. In fact, the film annealed at 850°C was partially melted. This indicates that Ar:O_2 annealing lowers the melting point of the multilayered films.

In the second set of experiments the effect of re-annealing the BiPbSrCaCuO films containing large proportion of the $(Sr_{14-x},Ca_x)Cu_{24}O_{41-y}$ phase in an Ar:O_2 gas mixture was investigated. The films were re-annealed in an Ar:O_2 gas mixture, with oxygen partial pressure of 1/13 at 710°C for various duration. Figure 8.33 shows the XRD pattern of a BiPbSrCaCuO film re-annealed at 710°C for a total period of 4 hours in Ar:O_2 atmosphere followed by furnace cooling to room temperature.

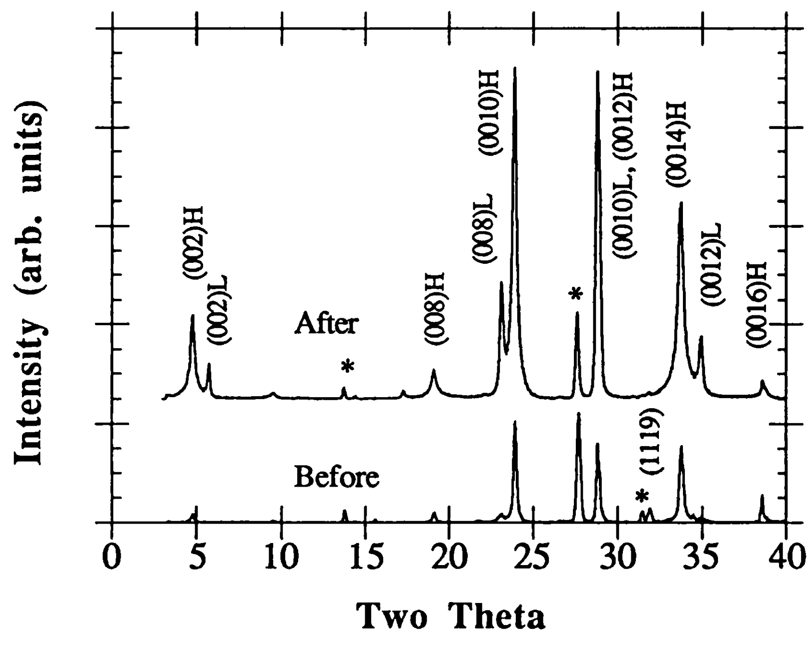

Figure 8.33- *XRD patterns of the BiPbSrCaCuO/PbO film annealed in air at 854 °C for 15 hours (lower pattern) and then re-annealed at 710 °C for a total period of 4 hours in Ar:O_2 atmosphere.*

The patterns show that the proportion of the $(Sr_{14-x},Ca_x)Cu_{24}O_{41-y}$ phase has decreased substantially after re-annealing the film in an Ar:O_2 (1/13) atmosphere at 710°C for 4 hours. It should be noted that the (040) peak of the $(Sr_{14-x},Ca_x)Cu_{24}O_{41-y}$ phase is the major peak in the film before the re-annealing process. The reduction in the proportion of the $(Sr_{14-x},Ca_x)Cu_{24}O_{41-y}$ phase indicates that this phase is unstable in an Ar:O_2 atmosphere at 710°C. The effect of re-annealing duration on the $(Sr_{14-x},Ca_x)Cu_{24}O_{41-y}$

phase was also investigated. It was found that re-annealing time of 2 hours resulted in a substantial reduction in the proportion of this phase. Beyond this optimum duration an increase in the proportion of the 2212 phase was observed. Figure 8.34 shows the R-T measurement of a typical BiPbSrCaCuO film, before and after re-annealed in Ar:O_2 (1/13) atmosphere at 710°C for 2 hours. The curves show that $T_{c,\ zero}$ increases substantially from 81K to 96K after the re-annealing process. It should be noted that before the re-annealing process, the (040) diffraction peak of the $(Sr_{14-x},Ca_x)Cu_{24}O_{41-y}$ phase was the highest peak in this film. The improvement in the $T_{c,\ zero}$ value of the film after the re-annealing process could be due to a number of possibilities. These include a change in the oxygen concentration of the phases present in the film, a better connectivity at the grain boundaries, or redistribution of the elements.

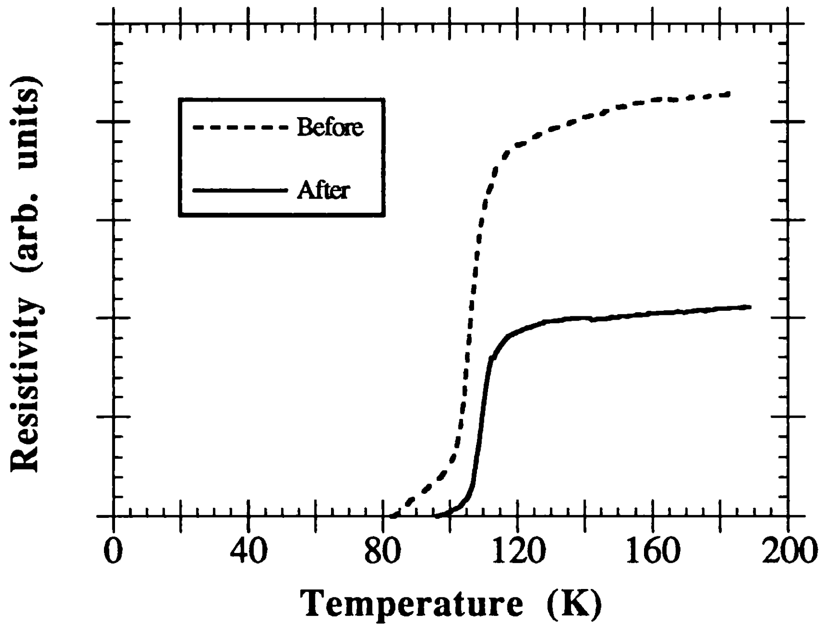

Figure 8.34- *Resistivity versus temperature of the BiPbSrCACuO film before and after Ar:*O_2 *re-annealing at 710°C for 2 hours.*

8.9.5 Conclusion

The objective of this study was to optimize the thin film growth conditions of the $Bi_2Sr_2Ca_2Cu_3O_{10+\delta}$ high T_c superconductor by PLD technique. Thin films of the 2223 phase were deposited by single layer and multilayered methods. It was demonstrated that with the latter method, superconducting $Bi_2Sr_2Ca_2Cu_3O_{10+\delta}$ films containing more than 85% 2223 phase could be grown by annealing at 854°C for 15 hours in air.

Several key conclusions can be drawn from the results presented in this study. It was demonstrated that addition of Pb is essential for the formation of the 2223 phase in high proportions. It was further shown that Pb lowers the formation temperature of the 2223 phase and also the melting temperature of the $Bi_2Sr_2Ca_2Cu_3O_{10+\delta}$ films. The effect of target composition on the thin film growth of the 2223 phase indicated that an excess Ca and Cu over the stoichiometric composition is effective in promoting the formation of the 2223 phase significantly, however, excess Cu was found to also favour the formation of the $(Sr_{14-x,}Ca_x)Cu_{24}O_{41-y}$ phase. This implies that in order to grow thin films of the 2223 phase without the impurity phase it is essential to use correct starting composition.

In this study it was also demonstrated that the growth of the 2223 phase depends strongly on the annealing temperature and duration and that the temperature range in which the 2223 phase is produced, in the multilayered BiPbSrCaCuO/PbO films, preferentially is exceedingly narrow. The optimum annealing temperature and duration for the formation of the 2223 phase with the multilayered technique was found to be 854°C±1°C for 15 hours in air. Beyond the optimum values, however, the 2223 phase was shown to decompose to form the 2212 phase and a Bi deficient phase. The presence of the 2212 phase in the microstructure of the films, under the optimum conditions, is a demonstration that the 2223 and the 2212 phases can coexist thermodynamically. It was show that the $Ar:O_2$ annealing of the multilayered films, lowers the melting point of the BiPbSrCaCuO films considerably. The re-annealing of the BiPbSrCaCuO films containing a high proportion of the $(Sr_{14-x,}Ca_x)Cu_{24}O_{41-y}$ phase illustrated that the $(Sr_{14-x,}Ca_x)Cu_{24}O_{41-y}$ phase is unstable in a low oxygen atmosphere.

References

1- M. R. D. Guire, N. P. Bansal, D. E. Farrell, V. Finan, C. J. Kim, B. J. Hills, and C. J. Allen. Physica C. 179, (1991), 333.

2- S. J. Collocott and R. Driver. Physica C, 167, (1990), 598.

3- K. Schlze, P. Majewski, B. Hettich, and G. Petzow, Z. Metallkde. 81, (1990), 836.

4- P. Majewski, B. Hettich, K. Schlze, and G. Petzow, Procedings of the 2nd conference of the European Ceramic Sociatv, 11-14 August (1991.)

5- U. Endo, S. Koyama and T. Kawai. Jpn. J. Appl. Phys, 27(8), (1988), L1476-L1479.

6- W. Lo, Y. L. Chen, T. B. Tang and R. Stevens. Br. Cream. Trans. J, 89, (1990), 218-222.

7- Z. Xu, P. D. Han, L. Chang, A. Asthana, and D. A. Payne. J. Mater. Res, 5(1), (1990), 39-45.

8- M. Takano, J. Takada, K. Oda, H. Kitaguchi, Y. Miura, Y. Ikeda, Y. Tomii, and H. Mazaki. Jpn. J. Appl. Phys. 27, (1988), L1041

9- Y. L. Chen and R. Stevens. J. Am. Ceram. Soc. 75 (5), (1992), 1150-1159.

10- U. Endo, S. Koyama and T. Kawai. Jpn. J. Appl. Phys, 27(8), (1988), L1476-L1479.

11- M. Takano, J. Takada, K. Oda, H. Kitaguchi, Y. Miura, Y. Ikeda, Y. Tomii, and H. Mazaki. Jpn. J. Appl. Phys. 27(6), (1988), L1041-L1043.

12- D. Shi, M. Tang, M. S. Boley, M. Hash, K. Vandervoort, H. Claus and Y. N. Lwin. Phys. Rev. B: Condens Matter, 40(4), (1989), 2247-2253.

13- A. Sumiyama, T. Yoshitomi, H. Endo, J. Tsuchiya, W. Kijima, M. Mizuno, and Y. Oguri. Jpn. J. Appl. Phys. 27(4), (1988), L542-L544.

14- S. Koyama, U. Endo, and T. Kawai. Jpn. J. Appl. Phys, 27(10), (1988), L1861-L1863.

15- H. Sasakura, S. Minamigawa, K. Nakahigashi, M. Kogachi, S. Nakanishi, N. Fukuoka, M. Yoshikawa, S. Noguchi, K. Okada and A. Yanase. Jpn. J. Appl. Phys, 28(7), (1989), L1163-L1166.

16- G. Calestani, C. Rizzoli, G. D. Andreetti, E. Buluggiu, D. C. Giori, A. Valenti, A. Vera and G. Amoretti. Physica C, 158, (1989), 217-224.

17- W. Wonge-Ng, C. K. Chiang, S. W. Freiman, L. P. Cook, and M. D. Hill. J. Am. Ceram. Soc. Bulletin 71 (8), (1992).

18- G. Zorn, B. Seebacher, B. Jobst, and H. Gobel. Physica C. 177, (1991), 494-508.

19- W. Wong, C. K. Chiang, S. W. Freiman, L. P. Cook, N. M. Hwang, and M. D. Hill. Mater. Res. Soc. Symp. Proc, 169, (1990), 123-128.

20- C. E. Rice, A. F. Levi, R. M. Fleming, P. Marsh, K. W. Baldwin, M. Anzlowar, A. E. White, K. T. Short, S. Nakahata, and H. L. Store, Appl. Phys. lett. 52, (1988), 1828.

21- A. Marino, T. Yasuda, E. Holguin, and L. Rinderer. Physica C, 210, (1993), 16-20.

22- A. L. Li, I. Shih, and A. A. Gundjian. Physica C. 208, (1993), 64-68.

23- S. Ohya, K. Kobayashi, Y. Hirabayashi, Y. Kurihara, and S. Karasawa. Jpn. J. Appl. Phys. 28(6), (1989), L978-L980.

24- A. A. Youssef, T. Fukami, T. Yamamoto, and S. Mase. Jpn. J. Appl. Phys. 29(1), (1990), L60-L63.

25- J. Levoska, T. Murtoniemi, and S. Leppavuori, J. Less-Common Metals, 164&165, 1362 (1990).

26- Y. Hakuraku, Y. Aridome, D. Miyagi, N. G. Suresha, and T. Ogushi. Jpn. J. Appl. Phys. 28(5), (1989), L819-L822.

27- H. Hayakawa, M. Kaise, K. Nakamura, and K. Ogawa. Jpn. J. Appl. Phys. 28(6), (1989), L967-L969.

28- A. Tanaka, N. Kamehara, and K. Niwa. Appl. Phys. Lett. 55(12), (1989), 1252-1254.

29- M. Viret, J. F. Lawler, and J. G. Lunney. Supercond. Sci. Technol. 6, (1993), 490-496.

30- B. C. Chakoumkos, P. S. Sales, and E. Sonder. J. Mate Res, 4, 919890, 767.

31- P. Bordet, J. J. Capponi, C. Chaillout, J. Chenavas, A. W. Hewat, E. A. Hewat, J. L. Hodeau, M. Marezio, J. L. Tholence, D. Tranqui. Physica C. 153-55, (1988), 623.

32- N. Kijima, H. Endo, J. Tsuchiya, A. Sumiyama, M. Mizuno, and Y. Oguri. Jpn. J. Appl. Phys. 27, (1988), L821.

33- J. Schneck, J. Toledano, L. Pierre, A. Litzler, J. Less-common. Metals. 164 & 165, (1990), 545-552.

34- M. R. Tseng, J. J. Chu, Y. T. Huang, and P. T. Wu, J. Appl. Phys. 67, (1990), 2657.

35- Y. L. Chen, R. Stevens. J. Am. Ceram. Soc. 75 (5), (1992), 1142-1149.

36- R. S. Roth, C. J. Rawn, B. P. Burton, F. Beech. J. Res. Nati. Inst. stand. Technol. 95(3). (1990), 291-335.

37- U. Endo, S. Koyama and T. Kawai, Jpn. J. Appl. Phys, 28(2), (1989), L190-L192.

38- S. Beker and H. J. Bietze, Physica C. 167, (1990), 509-514.

39- A. Tanaka, T. Machi, N. Kamehara, and K. Niwa, Appl. Phys. Lett. 54, (1990), 1362.

40- M. Lelental, T. N. Blanton, C. L. Barnes, H. J. Romanofsky, Physica C. 193, (1992), 395-400.

41- W. Lo, Y. L. Chen, T. B. Tang, and R. Stevens. Br. Ceram. Trans. J. 89, (1990), 218-222.

42- A. Marino, T. Yasuda, E. Holguin, and L. Rinderer. Physica C. 210,)1993), 16-20.

43- H. Hattori, K. Nakamura, and K. Ogawa. Jpn. J. appl. Phys. 29(1), (1990), L36-39.

44- W. S. Um, D. H. Kim, K. No, and H. G. Kim. Jpn. J. Appl. Phys. 31(3), part 1, (1992), 775-779.

Chapter 9

Critical Current Measurements of The $(BiPb)_2Sr_2Ca_2Cu_3O_x$ Films

9.1 Introduction

In this chapter the critical current density, J_c, of the $(BiPb)_2Sr_2Ca_2Cu_3O_x$ films deposited by PLD using the multilayered BiPbSrCaCuO/PbO method is discussed. The aim of this study is to investigate the effect on the critical current density of the presence of 2212 and $(Sr,Ca)_{14}Cu_{24}O_{41}$ phases in the 2223 films. This is followed by a discussion of the coupling mechanism between superconducting grains in the films.

9.2 Critical current density

Superconducting thin films with high T_c and large critical current have been grown by various film growth techniques. However, because the superconducting materials often contain weak links, the current does not necessarily circulate through the entire film. For instance, in polycrystalline films, the critical current within a single grain is usually many orders of magnitude higher than the macroscopic intergranular critical current. Consequently, the value of J_c depends on the length on which the measurement is taken. This is known as the length scale.

The critical current density of superconducting thin films can be determined by transport and magnetic measurements. In the transport measurements, the film is usually patterned to a bridge shape. The length scale here is equal to the length of the bridge. The disadvantage of patterning the film is that it might make it unsuitable for other uses. Magnetic measurements on the other hand are non destructive. With this technique, J_c is obtained from the irreversible magnetisation ΔM, as measured in a hysteresis loop. The length scale, $\wedge$, in this technique is proportional to the magnetic moment dm/dH of the film. A method of measuring both J_c and $\wedge$ in a sample is to subdivide the sample into smaller scales until the zero field ΔM does become proportional to sample dimension. An alternative method proposed by Angadi et al. [1] is to consider the critical state of a sample in an applied field that is large compared with the penetration field. In this case, the critical current density , is nearly the same throughout the sample. Angadi et al have demonstrated that with this method the length scale can directly be measured from the initial slope as the field is reduced on the reverse leg of a hysteresis loop.

Using this technique, the length scale and the critical current density of several $(BiPb)_2Sr_2Ca_2Cu_3O_x$ films containing various ratios of the 2223, 2212, and $(Sr,Ca)_{14}Cu_{24}O_{41}$ phases were measured. Critical current measurements were carried out at Imperial College, Department of Physics. The critical current densities of the films were calculated from magnetic measurements on a vibrating sample magnetometers (VSM) (Oxford Instruments model 3001). This technique is described in Angadi et al. [1].

9.3 Critical current measurements

The presence of multiphases in the superconducting films has been reported to reduce the critical current density of these films [2]. In order to quantify this, a few highly c-axis oriented BiPbSrCaCuO films containing various percentage ratios of the $2223/2212/(Sr,Ca)_{14}Cu_{24}O_{41}$ phases were selected for critical current measurements. The relative percentages of the various phases were estimated from x-ray diffraction patterns of the films by considering the (002) and (0014) peaks of the 2223 phase, the (002) and (0012) of the 2212 phase, and the (004) peak of the $(Sr,Ca)_{14}Cu_{24}O_{41}$ phase.

The films were square in shape with dimensions 5x5mm and thicknesses of 750nm, as determined by talystep (10Å resolution). The magnetisation measurements in these films were performed for the magnetic field perpendicular to the plane of the substrate and along the film c-axis.

9.3.1 Resistivity characterisation

Prior to J_c measurements, the superconducting properties of the films was investigated with the Van der Pauw technique. Figure 9.1 shows resistance versus temperature (R-T) curves of the films

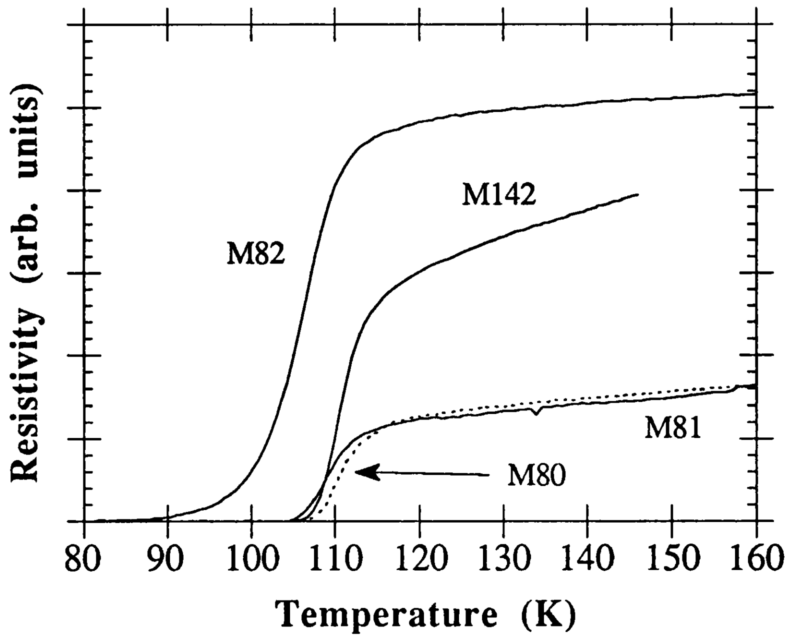

Figure 9.1- *R-T curves of $(BiPb)_2Sr_2Ca_2Cu_3O_x$ used for critical current density measurements.*

The films with the highest proportion of the 2223 phase (i.e., >78%) exhibited $T_{c,\ onset}$ of 110K with $T_{c,\ zero}$ above 100K. However, the film with the lowest proportion of the 2223 phase (59%) exhibited $T_{c,\ zero}$ of 87K.

9.3.2 Length scale measurements

In order to clarify whether the current in the $(BiPb)_2Sr_2Ca_2Cu_3O_x$ films is limited by the grain boundaries, the length scale of the current loops, i.e., the diameter of the intergranular screening currents, were determined from the magnetic response of the films. Angadi et al. [1] have shown that the length scale, Λ, of the current loops can be calculated by using the following formula.

$$\Lambda = \frac{dm}{dH}\,\frac{\left[\ln\left(\frac{8R}{t}\right)\right]-\frac{1}{2}}{\pi\ A} \qquad (9.1)$$

where R, A and t are the radius, area and thickness of the measured film respectively. Because the BiPbSrCaCuO films are square shaped the value of its effective radius, $\sqrt{A/\pi}$, was used as the radius of the film. The length scale values for the BiPbSrCaCuO films with various 2223/2212/$(Sr,Ca)_{14}Cu_{24}O_{41}$ phase proportions were calculated by inserting the gradient of the reverse leg of the hysteresis loop for each film into equation (9.1). These values together with the relative proportions of the various phases as well as $T_{c,\ zero}$ of the films are summarised in table (9.1).

Film code	2223 %	2212 %	$(Sr,Ca)_{14}Cu_{24}O_{41}$ %	Length scale (mm) at 30K	$T_{c,\ zero}$(K)
M82	59	27	14	7.8×10^{-3}	87
M80	78	8.3	13.7	2.87×10^{-2}	105.5
M81	80	15	5	0.22	104.5
M142	78	20	2	2.3	105

Table (9.1)- *Superconducting properties and relative percentage of different phases present in BiPbSrCaCuO films.*

The data in table (9.1) suggest that the length scale is independent of $T_{c,\ zero}$ of the films. By plotting the length scale as a function of the $(Sr,Ca)_{14}Cu_{24}O_{41}$ phase, shown in figure 9.2, it becomes apparent that the length scale increases as the $(Sr,Ca)_{14}Cu_{24}O_{41}$ phase decreases in proportion. The pattern also illustrates an increase in the value of length scale by nearly two orders of magnitude as the proportion of the $(Sr,Ca)_{14}Cu_{24}O_{41}$ phase decreases from 14 to 5%. It is not possible to determine without more data points whether this relationship is linear or that there is a threshold value below which the length scale increases rapidly. However, it may be concluded that the length scale, and consequently the J_c value of the films increases with a reduction in the proportion of the $(Sr,Ca)_{14}Cu_{24}O_{41}$ phase. Therefore, it is desirable to eliminate this phase from the films altogether.

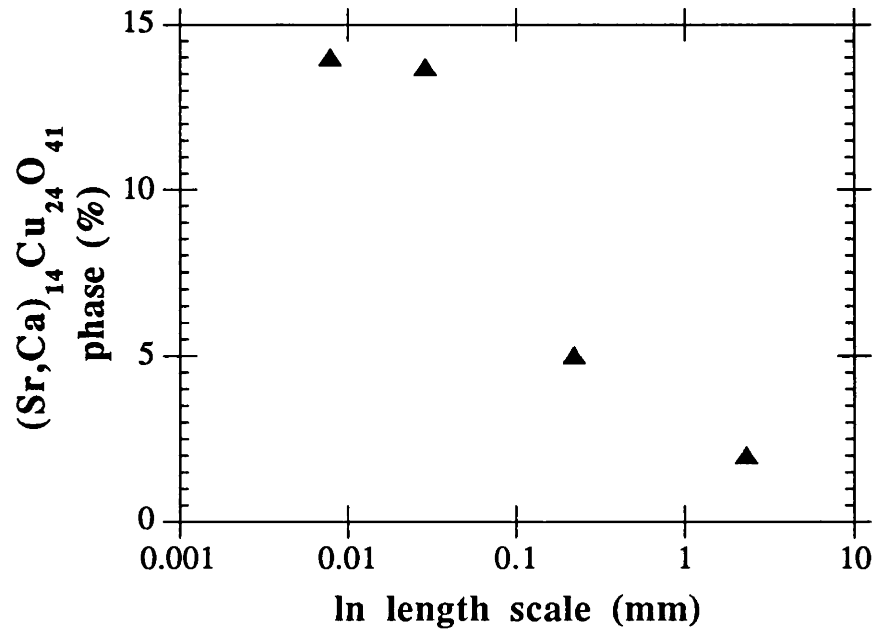

Figure 9.2-*$(Sr,Ca)_{14}Cu_{24}O_{41}$ phase proportion versus log of length scale. To avoid cofusion error bars (0.01mm) are not included.*

9.3.3 J_c calculations

The critical current density inside the single crystalline grains J_g and the whole of the film J_f could be determined by the Bean model [3]. The critical current density can be derived by considering the magnetic moment of a disk of radius R and thickness t. The magnetic moment of this disk is equal to integral of current loop, i.e.,

$$m = \oint IdA = \int_0^R Ir^2\pi \, dr \qquad (9.2)$$

current density J_c is defined as

$$J_c = \frac{I}{r\,t} \tag{9.3}$$

therefore:

$$m^{\pm} = J_c t \int_0^R \pi r^2 \, dr = \frac{\pi J_c t R^3}{3} \tag{9.4}$$

$$m^{+} - m^{-} = \Delta m = \frac{2 J_c t R^3 \pi}{3} \tag{9.5}$$

$$J_c = \frac{3\,\Delta m}{2 R^3 t \pi} \tag{9.6}$$

Where R and t are the radius and thickness of the film, respectively. The term $\Delta m/\pi R^2 t$ is the magnetic moment per unit volume, or magnetization ΔM. Where $\Delta M = M^+ - M^-$ is the irreversible magnetization, M^+ and M^- corresponds to the upper and lower branch of the hysteresis loops. Therefore equation (9.6) can be re-written as

$$J_c = \frac{3\Delta M}{2R} \tag{9.7}$$

The above formula is known as the Bean model and may be applied to estimate the critical current density of single crystal superconducting materials. However, in the case of polycrystalline superconducting thin films the current does not necessarily circulate through the entire film. Consequently the value of J_c depends on the length scale. If the length scale, Λ, obtained from equation (9.1) shows $\Lambda < R$, then R should be replaced with Λ in equation (9.7). This then can be used to estimate the intergrain critical current density of the superconducting films.

The low length scale values obtained for films with a high proportion of the $(Sr,Ca)_{14}Cu_{24}O_{41}$ phase, M82 and M80, indicate the granular nature of the films. In this case the superconducting grains are not very well connected and the grain boundaries could limit the transport critical current density and determine its dependence on applied magnetic field (H) and temperature (T). On the other hand, the fact that the length scale obtained for film with the lowest proportion of the $(Sr,Ca)_{14}Cu_{24}O_{41}$ phase, M142, is nearly identical to the sample effective radius, indicates that the corresponding J_c value is mainly a contribution of the film and not the individual superconducting grains.

The length scale value of the film with the highest proportion of the 2223 phase, M81, was found to 0.22mm at 30K which is in the intermediate range of mm and micron. Therefore it is not possible to be sure that the contribution to the critical current density is from the grains or from the film as a whole. One way to check this would have been to break the sample into different size pieces and measure their respective magnetic moments. If the measured magnetic moment is due to current circulating in the grains, then the calculated J_g would remain constant. Due to the time limitation on use of the VSM equipment, however, it was not possible to verify this. The critical current density of the $(BiPb)_2Sr_2Ca_2Cu_2O_x$ films calculated by inserting the length scale and ΔM values into equation (9.7) are summarised in table (9.2). It should be noted, however, that the Bean model is only an approximation and therefore the J_c values obtained by this model are not exact.

Film code	Length scale (mm)	J_c (A/cm^2) at (30K)	J_c (A/cm^2) at (70K)
M82	$7.8\text{x}10^{-3}$	$6.5\text{x}10^5$	not measured
M80	$2.87\text{x}10^{-2}$	$5.3\text{x}10^5$	$1.5\text{x}10^5$
M81	0.22	$1.4\text{x}10^4$	$3.7\text{x}10^3$
M142	2.3	$4.0\text{x}10^4$	$1.0\text{x}10^4$

Table (9.2)- *Length scale and the critical current density values of the BiPbSrCaCuO films.*

The large J_c values obtained for granular films are an indication of the intergrain critical current density, J_g. The large critical current density obtained for the films with the highest proportion of the 2223 phase and the lowest proportion of the $(Sr,Ca)_{14}Cu_{24}O_{41}$ phase are comparable to the best values recorded in recent literature [4-8]. These are summarised in table (9.3). The highest J_c value for BiSrCaCuO films reported in the literature is, $3.8x10^5$ A/cm^2, by Endo et al.[8]. This value was obtained for an in-situ grown BiSrCaCuO film on a $LaAlO_3$ substrate. They also reported a very small reduction in J_c of the film (from $3.8x10^5$ to 9.1×10^4 A/cm^2) in applied magnetic fields of 1-8 Tesla which is an indication that the film is weak link free.

Group	Deposition technique	$T_{c,\ zero}$ (K)	J_c (A/cm^2)
J. Levoska [4]	PLD	101	10^3 (77K)
A. Tanaka et al. [5]	rf magnetron sputtering	106.5	$4.1x10^4$ (77.3K)
K. Lee et al. [6]	surface diffusion process	104	10^3 (77K)
K. Tsukamoto et al. [7]	rf magnetron sputtering	107	$2.7x10^4$ (77.3K)
K. Endo et al. [8]	MOCVD	97	$3.8x10^5$ (77K)
A. Marino et al. [2]	rf magnetron sputtering	102	10^4 (10K)
A. Sajjadi [18]	PLD	105.5	$2.5x10^4$ (70K)

Table (9.3)- *J_c values of BiSrCaCuO films reported in recent literature.*

To investigate the effect of applied magnetic field on J_c, film M142 was subjected to a field as high as 8 Tesla at 4.9K. The critical current density of this film as a function of applied magnetic field in the range of 0-8Tesla is shown in figure 9.3.

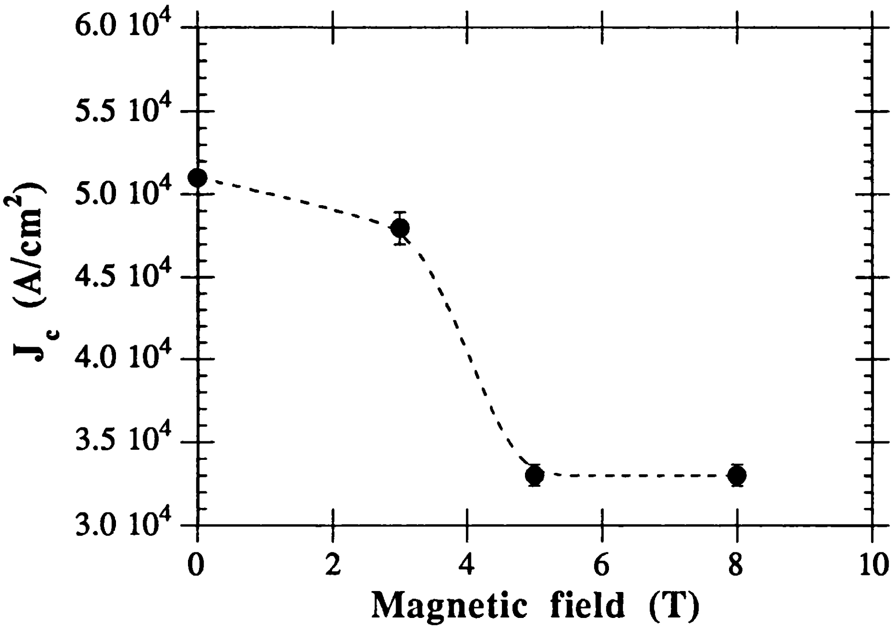

Figure 9.3- *Critical current density J_c of film M142 as a function of the magnetic field at 4.9K. Dotted line is a possible profile.*

The plot shows J_c decreases by 6% with an increase in applied magnetic field in the range of 0-3T. This is followed by a more pronounced reduction in J_c (≈33%) with the magnetic field in the range of 3-5 T succeeded by a plateau region in the range of 5-8T. The rapid decrease of J_c in these regions has been associated with a decoupling of the Josephson weak links between the superconducting grains. As a result, the critical current density in this region is believed to be a contribution of the superconducting grains [9].

The temperature dependence of the critical current density J_c (0T) for the films with the highest proportion of the 2223 phase and the lowest proportion of the $(Sr,Ca)_{14}Cu_{24}O_{41}$ phase are illustrated in figure 9.4. The patterns show, as expected, that the critical current density J_c is a decreasing function of temperature. The highest J_c value, of 5.1×10^4 and 1.6×10^4 A/cm^2 for film M142 and M81 are obtained at 4.9K and 26K, respectively.

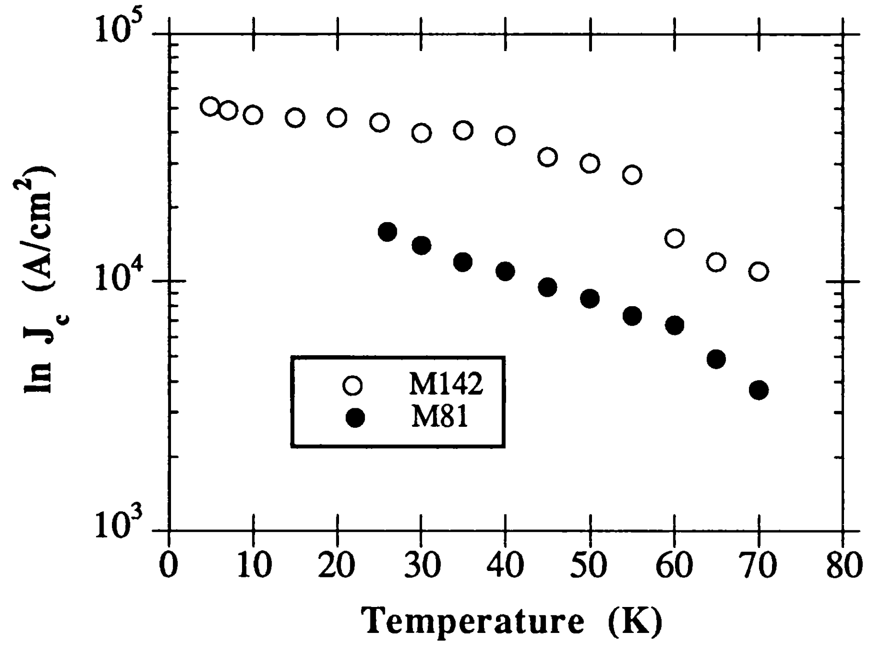

Figure 9.4- *Critical current density J_c versus temperature for films M81 and M142. Error bars are not included in order to avoid confusion.*

9.4 The coupling consideration

The coupling mechanism between superconducting grains in the film with the highest proportion of the 2223 phase, M81, can be realised from the temperature dependence of the critical current density J_c. In polycrystalline superconducting thin films the grains can be separated by a non superconducting material, which strongly determines the dependence of J_c on temperature T. Numerous studies have been done in order to understand the coupling mechanisms between superconducting grains in superconducting thin films [10-15]. In the case of grains separated by normal material forming superconducting-normal-superconducting (SNS) junctions de Gennes [12] showed that $J_c \propto (1-T/T_c)^{\alpha}$ with $\alpha \approx 2$ for T close to T_c. In the case of superconducting grains separated by insulating material , forming superconducting-insulating-superconducting (SIS) junctions, Ambegaokar and Baratoff [13] found that $\alpha \approx 1$ near T_c. Moreover, recently, Clem et al. [14] showed that, for this case, (SIS junctions), J_c versus temperature has Ambegaokor-Baratoff dependence at low temperatures ($\alpha \approx 1$), but exhibits a crossover near T_c ($\alpha \approx 1.5$). In the case of superconducting grains separated by insulating and normal material, Nagata et al. [15] showed that $\alpha \approx 1.5$ for T close to T_c.

Although J_c measurements of the sample was performed up to 70K, it may still be possible to get an indication on the nature of coupling of the grains with the existing values. To illustrate the coupling mechanism between the superconducting grains, J_c (0T) was plotted as a function of $1\text{-}T/T_c$. This is illustrated in figure 9.5.

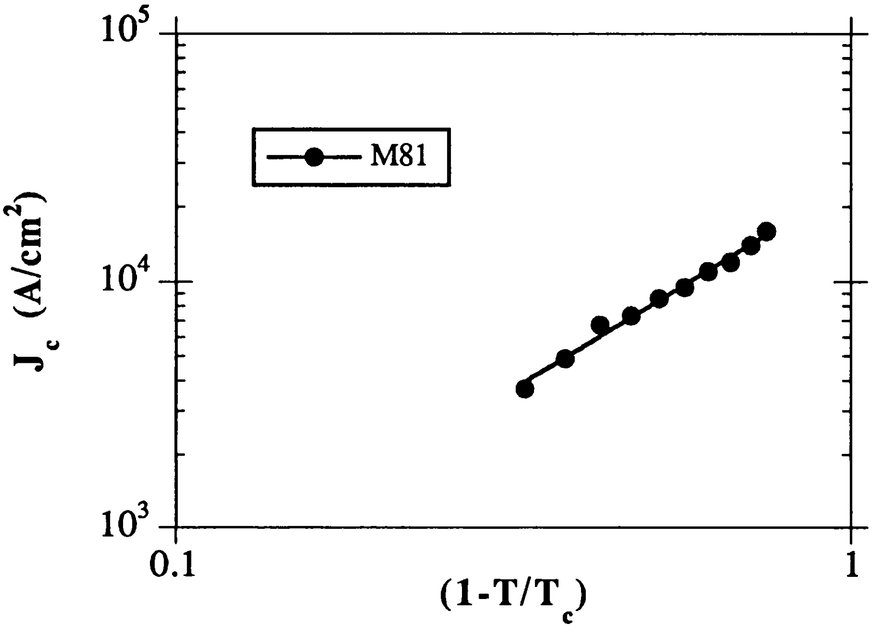

Figure 9.5- *Log plot of the critical current density J_c versus $(1\text{-}T/T_c)$ of film M81.*

The straight line represents the least-square fit of the experimental data to the power law $(1\text{-}T/T_c)^{1.8}$ in the range of $T_1<T<T_2$, where T is $(1\text{-}T/T_c)$. The nearly square law ($\alpha \approx 2$) suggests that the electrical transport mechanism is determined mainly by superconducting-normal-superconducting (SNS) junctions. The exponent value agrees with the experimentally determined value in 2223 BiSrCaCuO films by Setsune et al. [10] and others [16, 17]. The SNS behaviour may be attributed to the presence of layered structures in this film. It should be emphasized that the values of α obtained for this film corresponds to T=70K and not near $T_{c,\ zero}$. Due to the technical limitation with the VSM equipment at the time the measurements were taken it was not possible, however, to measure the value of α near $T_{c,\ zero}$.

9.5 Conclusion

The critical current density of pulsed laser deposited BiPbSrCaCuO films were measured by the magnetic technique using VSM. It was found that the proportion of the $(Sr,Ca)_{14}Cu_{24}O_{41}$ phase in the films would effect the length scale value. The length scale value of film M142 (2.3mm) was comparable to the effective radius of the film. This indicates that the contribution to the critical current density is from the whole of the film. The critical current density of the films was calculated by using the calculated length scale values and the Bean model. The critical current density of film M81 and M142 in zero field at 70K were 3.7×10^3 and 1.0×10^4 A/cm^2, respectively. These are comparable to the values obtained by others in recent literature.

The coupling mechanism in film with the highest proportion of the 2223 phase was examined by plotting J_c as a function of $1-T/T_c$. The nearly square law ($\alpha \approx 2$) suggests that the electrical transport mechanism is determined mainly by superconducting-normal-superconducting (SNS) junctions.

References

1- M. A. Angadi, A. D. Caplin, J. R. Laverty, and Z. X. Shen. Physica C 177, (1991), 479-486.

2- A. Marino, T. Yasuda, E. Holguin, and L. Rinderer, Physica C. 210, (1993),16-20.

3- C. P. Bean, Phys. Rev. Lett, 8, (1962), 260.

4- J. Levoska, T. Murtoniemi, and S. Leppavuori, J. Less-Common Metals, 164&165, 1362 (1990).

5- A. Tanaka, T. Machi, N. Kamehara, and K. Niwa, Appl. Phys. Lett. 54, 1362 (1990).

6- K. Lee, J. Lee, and G. Park. Jpn. J. Appl. Phys. 29(8), (1990), L1449-L1451.

7- K. Tsukamoto, H. Shimojima, M. Ishii, N. Enomoto, and C. Yamagishi. J. Am. Ceram. Soc. 76(4), (1993), 1031-1039.

8- K. Endo, H. Yamasaki, S. Misawa, S. Yoshida, and K. Kajimura. Nature. Vol 355, (1992), 327-328.

9- R. L. Peterson and J. W. Ekin. Physica C. 157, (1989), 325.

10- K. Setsune, K. Hirochi, H. Adachi, Y. Ishikawa and K. Wasa, Appl. Phys. lett. 53, (1988), 600.

11- H. E. Hong, J. C. Jao, H. C. Chen, H. C. Yang, H. H. Sung and F. C. Chen, Phys. Rev. B39, (1989), 9628.

12- P. G. de Gennes, Rev. Mod. Phys, 36, (1964), 225.

13- V. Ambergaokar and A. Baratoff, Phys. Rev. Lett, 10, (1963), 486.

14- J. R. Clem, B. Bumble, S. I. Raider, W. J. Gallagher and Y. C. Shih, Phys. Rev. B35, (1987), 6637.

15- S. Nagata and H. C. Yank, Phys, B108, (1981), 997.

16- D. W. Chung, I. Martense, T. L. Peterson and P. M. Hemenger, J. Appl. Phys. 68, (1990), 3772.

17- J. W. C.de Vries, M. a. M. Gijs, G. M. Stollman, T. S. Baller and G. N. A van Veen, J. appl. Phys. 64, (1988), 426.

18- Amin. Sajjadi and Ian. W. Boyd. Appld. Phys. Lett. 63(24), (1993), 3373-3375.

Chapter 10

Patterning & Application of The Superconducting BiPbSrCaCuO (2212, 2223) Films

10.1 Introduction

In this chapter the successful application of the wet chemical etchant *Ethylene-diamine-tetra-acetic acid (EDTA) in water in* patterning of the 2212 and 2223 BiPbSrCaCuO films is presented. The design and development of a band-pass microstrip filter using the 2223 films is attempted and its performance discussed.

Applications of superconducting films fall broadly into two categories: passive and active devices [1]. Passive devices tend to modify a single electrical signal or input, whereas active devices tend to have another signal controlling the modification of the input in a non linear fashion [1]. Passive devices such as microwave resonators, filters, and delay lines usually require a single-layer structure consisting of a patterned superconducting film. For these applications the interface region is unimportant over a thickness of a few unit cells. Microwave passive devices primarily utilize the low rf surface resistance, R_S, of superconducting films below T_C [1]. R_S is a measure of the quality of films and depends basically on scattering centres such as grain boundaries and other defects, especially at the substrate film interface. Among the various microwave passive devices mentioned above the resonators are the simplest. Although resonators can be constructed with cylindrical, coaxial or helical cavities, the resonator which will have the highest potential is a planar resonator. There are primarily four types of planar resonators namely, stripline, slotline, microstrip, and coplanar microstrip geometries [2]. A typical resonator consists of a length of planar transmission line which is open circuit at both ends and resonance occurs when the device length is an integral number of half wavelengths. In this configuration coupling can be achieved by using capacitive gaps or loops.

The resonating circuit can be implemented on a HTS film by a patterning process. High temperature superconducting films can be deposited on various substrates such as magnesium oxide MgO, zirconium oxide ZrO_2, strontium titanate $SrTiO_3$ and lanthanum aluminate $LaAlO_3$. Obviously, one of the main loss mechanism which limit the performance of microwave planar circuits is the dielectric loss. However, the dielectric loss can be maintained by choosing a correct dielectric with minimum loss tangent as a substrate. Table (10.1) summarises the details of permittivity and loss tangent at 77K for a range of suitable dielectric substrates (alumina is included for reference).

Type	Relative permittivity	dielectric loss at 77K
MgO	9.65	$6x10^{-6}$
$LaAlO_3$	25	10^{-4}
YSZ	20	$5x10^{-3}$
$SrTiO_3$	$300\text{-}10^4$	$5x10^{-2}$
Al_2O_3	9.5	10^{-6}

Table (10.1)- *Dielectric substrates for HTS [3].*

Active devices, best represented by Josephson junction, generally but not always require several layers, and in such structures the interface region is extremely critical to the behaviour of the device [1]. A common patterned structure is Superconducting Quantum Interference Devices (SQUID). These are capable of unprecedented measurement precision for a range of physical parameters such as magnetic flux variation. These devices in the operating conditions give rise to an output voltage signal, which is in periodic function of the flux threading a superconducting loop in which one or two weak links are inserted [1].

10.2 Patterning methods

Dry etching such as reactive ion etching and pulsed laser evaporation has been used by a number of groups in patterning superconducting thin films [4-7]. Although these processes are promising for producing micron size patterns, there are conflicting reports about the effect of these techniques on the superconducting properties of the films [4, 8]. For instance, in pulse laser evaporation a precise control of the etching depth is difficult to achieve due to rapid melting and evaporation of the film [8]. A viable alternative to the dry etching technique is the wet etching process. In this process various acids etchants such as solution of hydrochloric acid, nitric acid, and phosphoric acid could be used for patterning high-T_C films [9]. However, these etchants even at very low concentrations provide rapid removal of the superconducting films (0.5μm per minute) which is not suitable for thin film patterning where controlled film removal is required. To overcome this problem Shokoohi et al. [10] have applied EDTA, an organic solvent, on laser deposited Y-Ba-Cu-O thin films. EDTA provides a relatively slow and controllable rate of etching. The structural formula of EDTA is shown in figure 10.1.

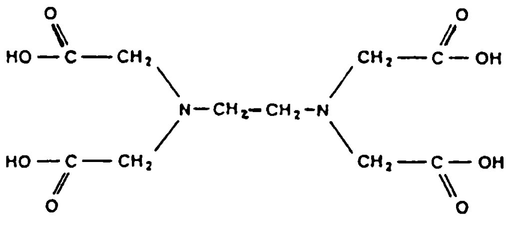

Figure 10.1- *Structural formula of EDTA*

10.3 Wet chemical etching process by EDTA

In the following sections patterning of the 2212 and 2223 BiPbSrCaCuO films by EDTA is presented. The crystal structure and electrical properties of the films before and after patterning process were investigated and the results presented. In general the patterns were generated on the superconducting BiPbSrCaCuO films by the following procedure. Prior to the application of the photoresist all superconducting films were cleaned in hot trichloroethylene (TRIC) for 5 minutes followed by a rinse in acetone, methanol, and de-ionised water (DI). Several layers of positive photoresist AZ1512 were then applied on the film surface. In order to obtain a uniform distribution of the photoresist the films were spun (on a rotating vacuum disk) at 4000rpm for 1 minute. The films were subsequently soft-baked at 85°C for 20 to 25 minutes. The films were carefully positioned under a well-focused mask aligner, supplying UV light (wave length 320nm) with an intensity of 5 mW/cm^2, and exposed to UV radiation for 8 seconds. The exposure duration of 8 seconds to UV light was found empirically ideal. The photoresist layer was subsequently developed for 10-15 seconds. This was followed by hard baking the films at 110°C for 20 minutes. The undesired area on the samples was etched by immersing the films into a saturated solution of EDTA/water for 5 minutes. Excess amounts of EDTA crystals were present in the solution to eliminate concentration degradation with time. The etching process was terminated by rinsing the sample in de-ionized water. To expose the pattern covered with photoresist the films were rinsed in acetone and then blown dry with nitrogen gas.

Figure 10.2 illustrates a plot of superconducting BiPbSrCaCuO film thickness removed as a function of etching time. The plot shows that in early stages the etching rate is quite high. However, the etching rate decreases as the film is left for longer time in the etchant solution. For instance, the etching rate being ≈13.3Å/s after 5 minuted is reduced to 3.3Å/s after 30 minutes of etching.

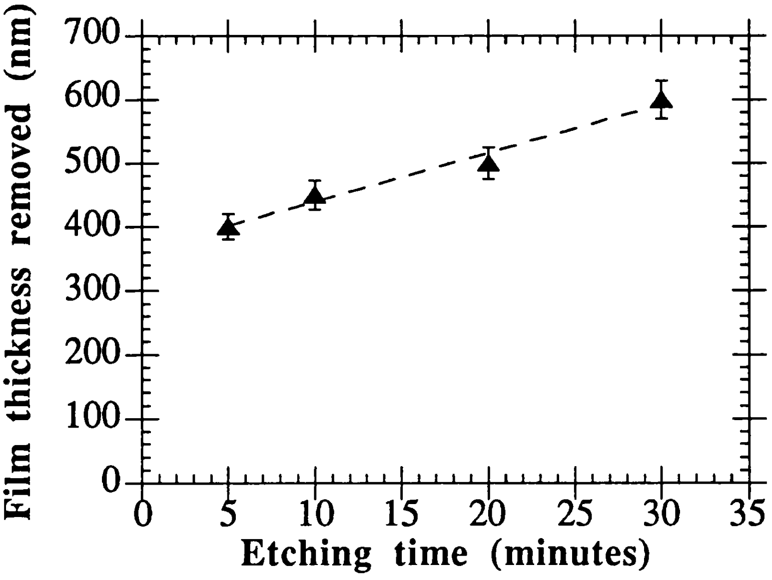

Figure 10.2- *Plot of film removed as a function of the etching time. Dotted line is a possible profile.*

The overall etching rate obviously depends on the microstructure of the BiPbSrCaCuO films. For instance, the thick dendrites on the films were found particularly difficult and time consuming to etch away. Conversely, platelets were easily removed. A similar observation has also been made by Joe Muller [11].

10.3.1 XRD characterisation

Figure 10.3 illustrates x-ray diffraction patterns of a mixed 2223/2212 phase BiPbSrCaCuO film before and after patterning. The patterns indicate that the crystal orientation and crystallinity of the film has not been effected by the patterning process.

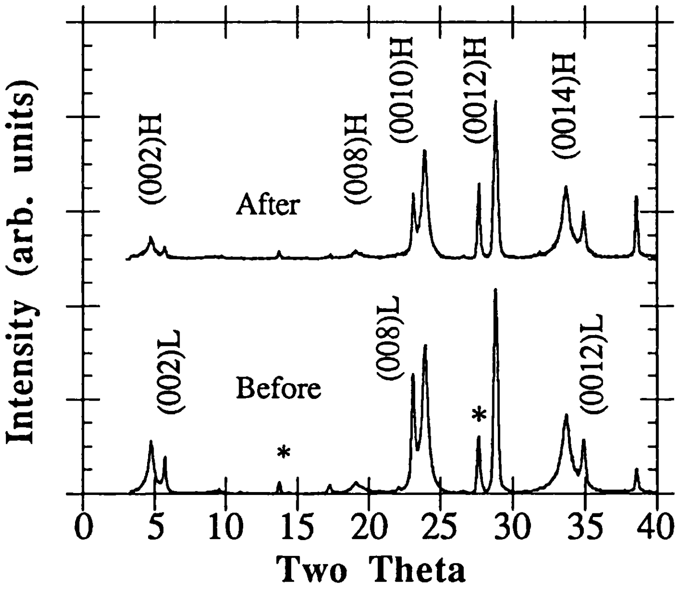

Figure 10.3- *X-ray diffraction patterns of a typical BiPbSrCaCuO 2223/2212 film before and after patterning.*

10.3.2 Resistivity measurements

The electrical properties, before and after patterning, were investigated on the 2212 BiPbSrCaCuO film. Figure 10.4 shows resistivity versus temperature curves of the 2212 film before and after patterning. The curves show an improvement in the $T_{c,\ onset}$ (from 85K to 90K) and $T_{c,\ zero}$ (from 80K to 85K) values by 5K after the patterning process. This increase in the superconducting temperature is probably due to the removal of low T_c

areas containing grains of lower $T_{c,\ zero}$. A similar observation of improvement in the $T_{c,\ onset}$ and $T_{c,\ zero}$ values of the 2212 BiPbSrCaCuO films after patterning by EDTA has been reported by Joe Muller et al.[11].

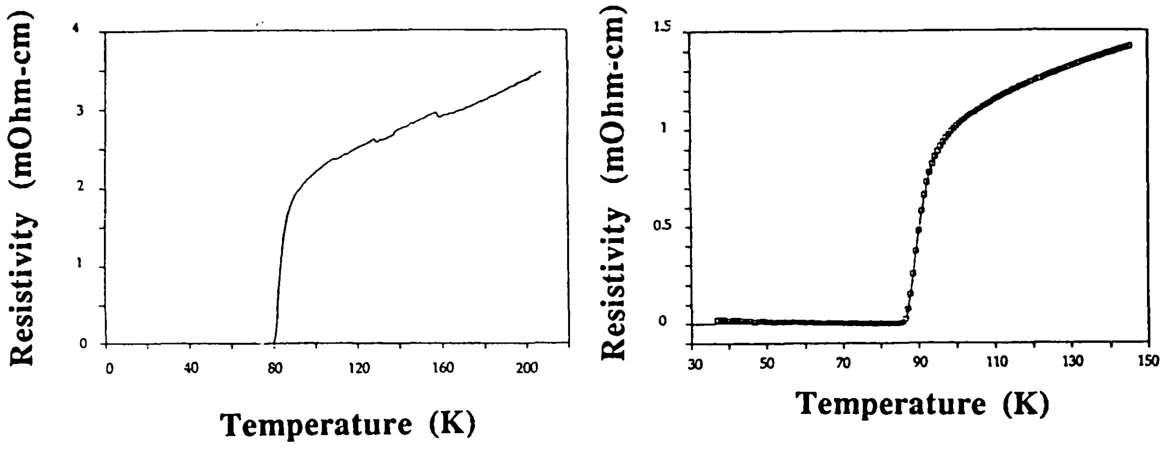

Before patterning

After patterning

Figure 10.4- *Resistivity versus temperature of the 2212 BiPbSrCaCuO film before and after patterning.*

10.3.3 Critical current density

The critical current density of the 2212 film was calculated from the magnetic measurements of the film on a vibrating sample magnetometer (VSM) (Oxford Instruments model 3001) before and after etching in EDTA. The critical current density at J_c (70K, 0T) was measured as $1.0\times10^3 A/cm^2$ before etching in EDTA and as $1.0\times10^3 A/cm^2$ afterwards. These results indicate that the patterning process did not degrade the crystallinity and superconducting properties of the BiPbSrCaCuO films.

10.3.4 SEM observation

SEM observation did not reveal any damage to the morfology of the films after the patterning process. The SEM micrograph of the patterned 2212 film is shown in figure

10.5. The patten shows three dc SQUIDs, each consisting of a round washer pocessing two symmetricaly arranged constrictions. The constrictions are either 200 or 400μm wide and the radii of the round washers are 20, 40, and 80μm.

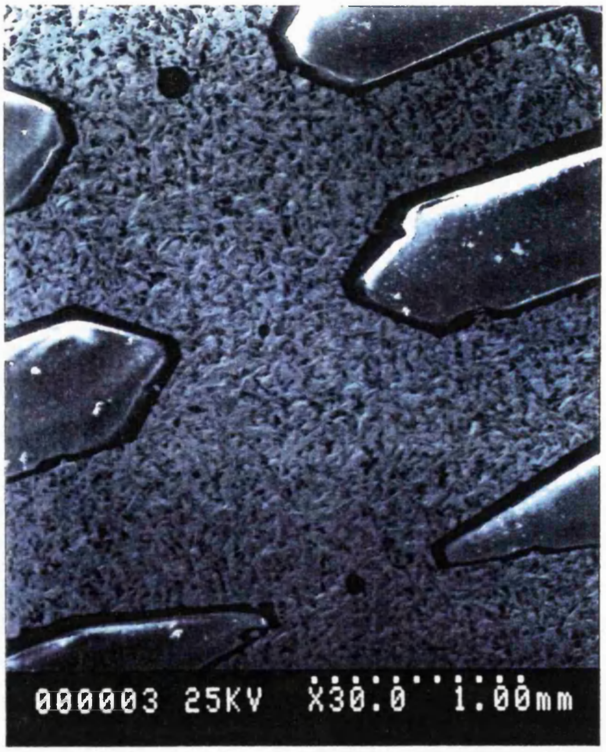

figure 10.5-*SEM micrograph of of the 2212 film patterned into three dc SQUIDs.*

10.4 Filter theory

A filter in general is a simple circuit which can change the input signal in time and frequency domain to an output signal. Mathematically, a filter can be described by a function that maps the input to the output in either the time or frequency domain, a transfer function. A more specific definition of a filter is a circuit that passes certain frequencies while rejects others, in a prescribed manner. Therefore a filter can have a specific frequency response. Several types of filters are shown schematically in the figure 10.6. An ideal filter would consist of a flat pass band with 100% transmission, a stop-band that transmitts no signal at all, and an infinitely sharp cut-off. Since this is quite impossible to achieve, approximating functions have to be used which are physically realisable at the expense of cut-off slope and band-pass [12].

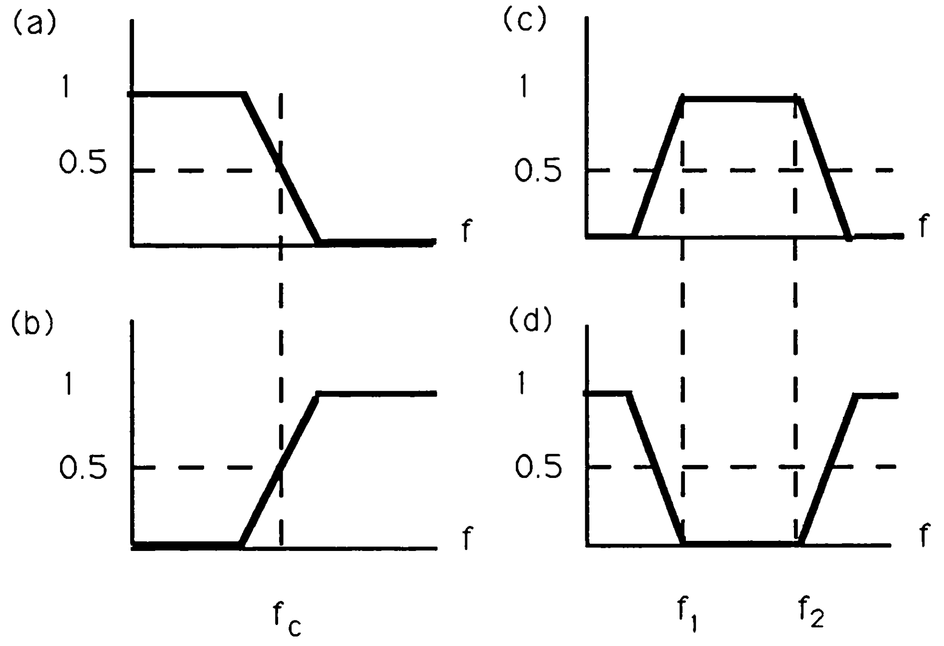

Figure 10.6- *Transmition versus frequency for various filter responses, (a) low pass, (b) high pass, (c) band pass, (d) band stop.*

Butterworth (also known as maximally flat) and Tchebyshev are the two most common approximating functions. Low-pass responses using these two functions can be expressed mathematically [12].

Butterworth low-pass filter response:

$$\left|S_{11}\right|^2(f) = \frac{K_n}{1+\left(\frac{f}{f_c}\right)^{2n}} \tag{10.1}$$

Tchebyshev low-pass filter response:

$$\left|S_{21}\right|^2(f) = \frac{K_n}{1+\varepsilon^2 C_n^2\left(\frac{f}{f_c}\right)} \tag{10.2}$$

where,

$$C_n(\omega) = \cos(n \cos^{-1}(\omega)) \qquad \text{for } 0 < \omega < 1 \tag{10.3}$$

$$= \cosh(n \cosh^{-1}(\omega)) \qquad \text{for } \omega > 1$$

Figure 10.7 shows graphical representation of the two functions. Pattern B illustrates the Butterworth characteristic which has a smooth pass-band, while pattern A shows the Tchebyshev which has a much sharper cut-off but with ripples in the pass-band. The Tchebyshev characteristic is often used since the Tchebyshev ripples can be made arbitrary small within physical limitations.

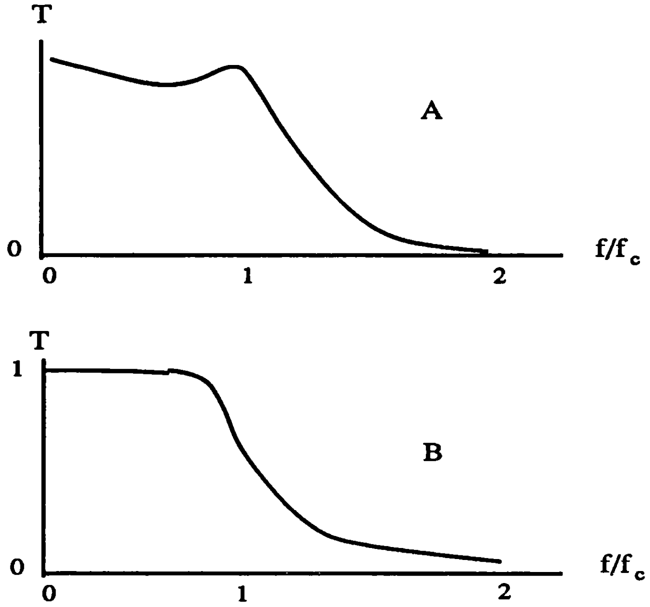

Figure 10.7- *Low pass filter transfer functions: (a) Tchebyshev response; (b) Butterworth response: plotted for n=3*

The response functions can be used to calculate the order of filter required in order to obtain certain attenuation at certain frequency [12]. Once the order of the filter, the approximate function, and the in-band ripple (for Tchebyshev) has been decided, a generating function can be used to derive the normalised prototype element values, g. Figure 10.8 shows lumped element low-pass prototype of order n. These element values correspond to the component values of a lumped low-pass filter. The values are normalised for a 1 Ω impedance at 1 rad/s and they need to be scaled up by the appropriate factor at a later stage.

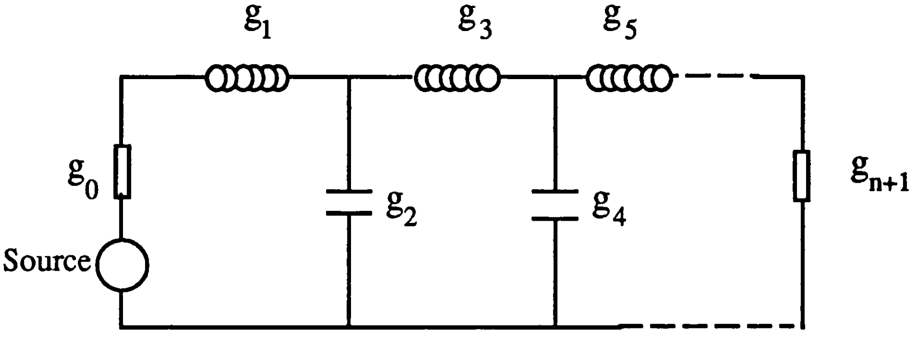

Figure 10.8- *Lumped element low-pass prototype of order n.*

It is now possible to convert the lumped low-pass circuit into a lumped band-pass circuit by considering the frequency transformation that maps the required pass-and stop-band and pass-and stop-band of the low-pass prototype. The frequency transformation is

$$\omega \rightarrow 1/\delta\ [\omega/\omega_0 - \omega_0/\omega] \qquad (10.4)$$

this transforms the admitance of the capacitor

$$j\omega C_{LP} \rightarrow jC_{LP}\ \omega/\delta\omega_0 - jC_{LP}\omega_0/\delta\omega \qquad (10.5)$$

This can be written in terms of a new capacitance and inductance

$$j\omega C_{BP} - j/\omega L_{BP} \qquad (10.6)$$

This represents a shunt inductance and capacitance, a parallel resonator, where,

$$C_{BP}=C_{LP}/\delta\omega_0 \quad \& \quad L_{BP}=\delta/\omega_0 C_{LP} \qquad (10.7)$$

A similar analysis shows that the series inductors of figure 10.8 are transformed into a series capacitor and inductor, a series resonator. The band-pass filter circuit is now shown in figure 10.9.

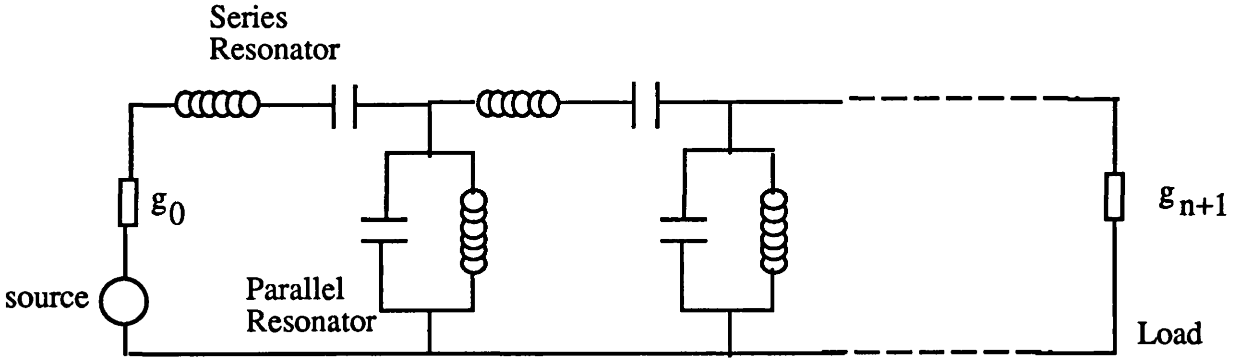

Figure 10.9- *Lumped element band-pass filter.*

The Band-pass filters can be constructed from lumped elements such as capacitors, inductors, and resistors for operation at low frequencies. However, for high frequency operations the lumped elements are not suitable as the high frequency yields small components values. This results in the inductance of the leads and the casings of the capacitance components to dominate and obscure the characteristics of the discrete component [12]. It is, however, possible to utilise transmission line such as microstrip and co-axial lines for this purpose.

10.6 Microstrip transition lines

In this section microstrip transmission lines are briefly described. For a detailed discussion on microstrip lines reference [2] should be consulted. Microstrip line is one of the most popular types of planar transmission lines, primarily because it can be fabricated by photolithographic processes and is easily integrated with other passive microwave devices. Figure10.10(a, b) shows the geometry and the field lines of a microstrip line. The figure shows a conductor of width w, grounded dielectric substrate of thickness h and relative permittivity ε_r.

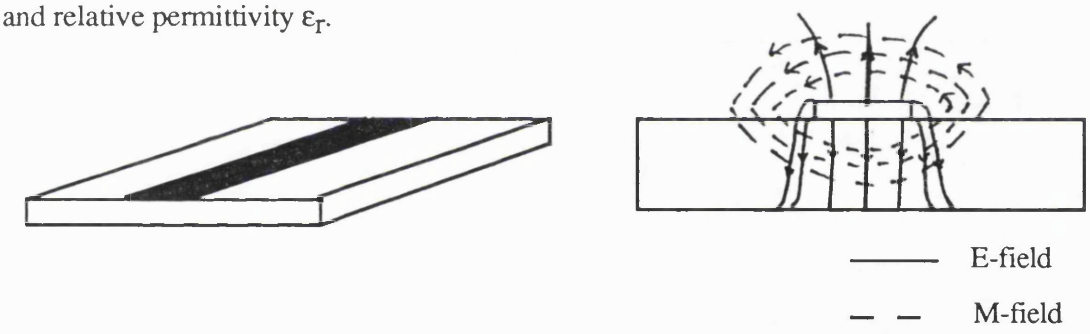

Figure 10.10 (a, b)- *Microstrip transmission line a) geometry, b) electric and magnetic field lines.*

The field lines in a microstrip line are mostly concentrated between the strip conductor and the ground plane with some fraction in the air region above the substrate. This means that the microstrip line can not support a pure TEM wave, since the phase velocity of TEM fields in the dielectric region would be $c/\sqrt{\varepsilon_r}$, but the phase velocity of TEM fields in the air region would be c. This indicates that a phase match at the dielectric-air interface would be impossible to attain for a TEM type wave [2]. The dominant mode in microstrip is, therefore, a quasi-TEM mode, a term used to indicate that the field patterns are distorted because of the mixed dielectric. Microstrip has several features including **(i)** an easy access to the surface of the microstrip. This makes it easy to mount both passive and active devices anywhere on the structure. Minor adjustment or tuning are possible after the circuit has been fabricated. **(ii)** the electromagnetic field distribution of a microstrip, as shown in figure 10.10(b), is asymmetrical, i.e., in the lower half the field is contained between the strip and ground plane, on the upper half it radiates into the air. Although this feature has been exploited, in the case of microstrip aerial, it is a drawback as it allows radiation and losses.

Calculation for microstrip involves a quantity known as effective dielectric constant (ε_{eff}). This quantity is related to the prorogation of field in the air relative to that in the dielectric. The effective dielectric constant is given by $C/C_{air}=(C/V_p)^2=\varepsilon_{eff}$, where V_p is the phase velocity of the signal travelling along the line and is equal to $V_p=1/(LC)^{1/2}$. For any wave prorogating in a transmission line the velocity of prorogation is

$$C=f\,\lambda_0 \quad \text{for free space} \qquad (10.8)$$

$$V_p=f\,\lambda_g \quad \text{for dielectrically loaded line} \qquad (10.9)$$

Therefore,

$$\varepsilon_{eff}=(\lambda_0/\lambda_g)^2 \qquad (10.10)$$

or

$$\lambda_g=\lambda_0/(\varepsilon_{eff})^{1/2}=c/f(\varepsilon_{eff})^{1/2} \qquad (10.11)$$

where λ_g is the guide wavelength, and c is the velocity of an electromagnetic wave travelling in air.

10.6 The parallel-coupled band-pass filter

There are two principal approaches to planar coupling between adjacent resonators namely end and edge coupling. With the end coupling configuration the energy interchange across the coupling gaps is insufficient and the sensitivity is poor, even for very small gaps [2]. With the parallel coupling configuration maximum coulping is obtained between the parallel microstrips when the length of the coupled region is $\lambda_g/4$, or some multiple thereof. The resonator strip is $\lambda_g/2$ in length or some multiple thereof [2].

There are four main design steps that should be taken into consideration for designing parallel coupled microstrip resonators [2]. These are: (i) determining the specification from the original prototype, (ii) evaluating the even and odd ordered characteristic impedances applicable to the parallel-coupled microstrip, (iii) relating the impedances values to microstrip widths and separations (w, s), and (iv) calculating the whole resonator length 2l.

The realisation of band-pass filter in microstip requires the design and interconnection of the series and parallel type resonators. In practice it is possible to convert all the series resonators into parallel resonators by using admittance inverters [2]. A network consisting of admittance inverters are usually called J-inverters. The parallel resonators can also be replaced with generalised parallel susceptances with the same frequency and the same suceptance slope. This means that the filter circuit can be represented by shunt susceptances and impedance inverters as shown in figure 10.11. The details of impedance or admittance inverter relationships is beyond the scope of this thesis and the excellent book by Matthaei, Young and Jones [12] should be consulted.

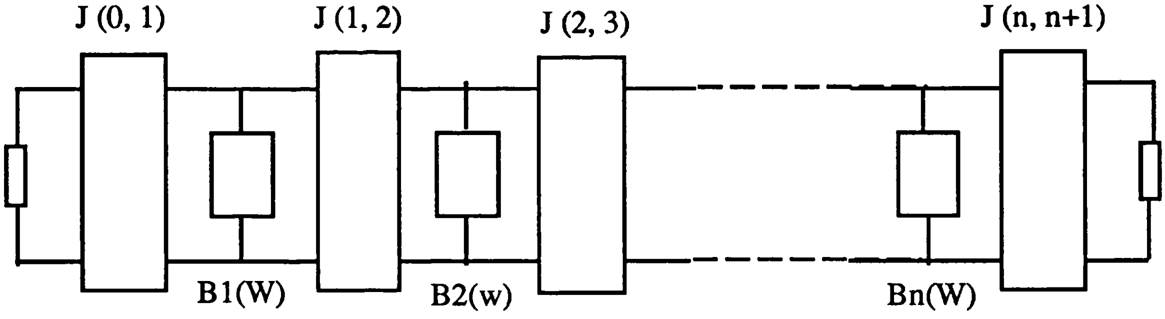

Figure 10.11- *Band-pass filter suitable for distributed circuit realisation, utilizing admittance inverters and generalised susceptances.*

The admittance inverter parameters (J) can be calculated from the filter's fractional bandwidth δ and the element values g_n [2]. For the first coupling structure:

$$\frac{J_{01}}{Y_0} = \sqrt{\frac{\pi\delta}{2g_0g_1}} \qquad (10.12)$$

For the intermediate couling structure:

$$\left.\frac{J_{j,\,j+1}}{Y_0}\right|_{j\,=\,1\text{ to }(n\,-1)} = \frac{\pi\,\delta}{2\omega_c\sqrt{g_j g_{j+1}}} \qquad (10.13)$$

For the final coupling structure:

$$\frac{J_{n,\,n+1}}{Y_0} = \sqrt{\frac{\pi\,\delta}{2g_n g_{n+1}}} \qquad (10.14)$$

In these equations, δ is the fractional bandwidth and is given as

$$\delta = \frac{f_2 - f_1}{f_0} \qquad (10.15)$$

To proceed with the microstrip design the odd-and even mode coupled-lined impedances are required [2]. The even mode coupling impedance is

$$(Z_{0e})_{j,\,j+1}=Z_0(1+aZ_0+a^2Z_0^2) \qquad (10.16)$$

and the odd mode coupling impedance is

$$(Z_{0o})_{j,\,j+1}=Z_0(1+aZ_0+a^2Z_0^2) \qquad (10.16)$$

where , $a=J_{j,\,j+1}$ and Z_0 is the system characteristic impedance (i.e. that of the lines feeding the filter). The two impedances represent the combined effect of two coupled lines. Having realised the values of Z_{0e} and Z_{0o}, the microstrip widths and separations can be determined by the synthesis technique of Akhtarzad et al [13] which consist of two distinct stages. In the first stage shaped ratios for equivalent single microstrip lines are determined. In the second stage the shape ratio w/h and the spacing ratio s/h for the desired coupled microstrip structue using the single-line shape ratios are obtained. The characteristic impedances (odd and even modes) for equivalent single microstrip line are defined as [2]

$$Z_{0se}=Z_{0e}/2 \text{ for single microstrip shape ratio } (w/h)_{se} \qquad (10.17)$$

$$Z_{0so}=Z_{0o}/2 \text{ for single microstrip shape ratio } (w/h)_{so} \qquad (10.18)$$

The single line equivalent to the coupled lines with odd and even impedances are given as

$$Z_{0se,so}=Z_{0\,(e,o)}/2 \qquad (10.19)$$

The width of the single lines with the even and odd impedances can be calculated from

$$(w/h)_{se,so}=2/\pi[D_{e,o}-1-\ln(2D_{e,o}-1)]+\varepsilon_r -1/\pi\varepsilon_r\ [\ln(D_{e,o}-1)+0.293-(0.517/\varepsilon_r)] \qquad (10.20)$$

where,

$$D_{e,o}=60\pi^2/Z_{0se,so}\sqrt{\varepsilon_r} \qquad (10.21)$$

This expression is general and can be used to determine the width of the 50Ω input line that is required for the parallel coupled microstrip. The final stage of the design process involves solving the approperiate shape ratio equations provided by Akhtarzad et al simultaneously. For $\varepsilon_r \geq 6$

$$(w/h)_{se}=2/\pi[\ \cosh^{-1}(2d-g+1/g+1)] \qquad (10.22)$$

$$(w/h)_{so}=2/\pi[\ \cos^{-1}(2d-g-1/g-1)]+1/\pi[\ \cosh^{-1}(1+2(w/h)/(s/h) \qquad (10.23)$$

where g= cosh (πs/2h) and d= cosh (πw/h+πs/2h). The solution of equations (10.22, 10.23) provides the shape ratios of the lines.

10.8 Superconductors in microwave circuits

The use of superconducting materials instead of conventional metals such as Cu and Au in microwave passive devises has been reported to increase their performance by at least an order of magnitude [3]. The main loss mechanism which limit the performance of microwave planar circuits are the ohmic, dielectric and radiation losses. The dielectric loss can be minimized by choosing a correct dielectric with minimum loss tangent. HTS can provide a substantial improvement in the insertion loss of a microstrip circuit. The improvement in the insertion loss provides an increase in the Q of the circuit. This is a highly desirable effect, since it provides a sharper cut-off and greater out-of-band rejection. Microwave devices primarily utilize the low rf surface resistance, R_s, of superconducting films below T_c. The surface resistance R_s is at least an order of magnitude smaller with superconductors than the conventional metal films. For pure superconductors the surface resistance is given by the following formula [3]:

$$R_s = RZ_s = \frac{1}{2}\omega^2\mu_0\lambda^2\frac{N_n}{N} \qquad (10.24)$$

where N_n is the proportion of normal electrons, λ is the London field penetration depth and R indicates that the real part of the complex quantity of surface impedance, Z_s. However, for the normal conductors R_s can be written as

$$R_s = \left(\frac{\omega\mu_0}{2\,\sigma}\right)^{1/2} \qquad (10.25)$$

This indicates that for a normal metal, $R_s \propto \omega^{1/2}$, while for a superconductor at frequencies well below the gap frequency, $R_s \propto \omega^2$. The ω^2 relationship applies to pure superconductors. Since in all high temperature superconducting thin films significant number of grain boundaries exists, the index is more close to 1.5 for these materials. Figure 10.12 illustrates the relationship between the surface resistance and the frequency for YBaCuO high temperature superconductor and copper at 77K.

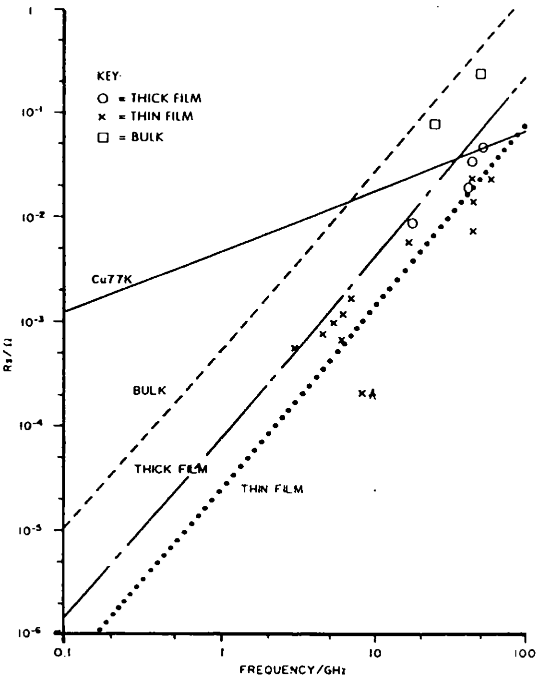

Figure 10.12- *RF surface resistance of YBCO at 77K. Figure after D. J. Cracknell [3].*

The graph illustrates that R_S values of superconducting YBaCuO (123) thin film at 77K are at least an order of magnitude smaller than those of Cu at low frequencies. Also the pattern shows that at constant temperature and above a certain frequency YBaCuO (123) superconductor could be more lossy than Cu. This frequency is known as the cross-over frequency. The cross-over frequency for thin YBaCuO film at 77K and low rf fields is of the order of 100s of GHz.

The London penetration depth λ may be considered to be equivalent to the skin depth δ in normal conductors. The London penetration depth is a measure of the extent to which applied magnetic field can penetrate the surface of a superconductor. Unlike skin depth which is proportional to $\omega^{-1/2}$, λ does not vary with frequency. The penetration depth λ increases progressively with temperature between absolute zero and the critical temperature according to the following expression:

$$\lambda(t) = \lambda(0)\{1-T/T_c)^4\}^{-1/2} \qquad (10.26)$$

10.9 Microwave filter application HTS

The application of high temperature superconductors (HTS) in microwave filters for satellite communications is one of the areas being investigated by researchers intensively. The background space temperature (3K) has allowed feasibility for the operation of superconducting microwave devices. A typical communications satellite receives a broad band uplink signal in the 6, 14,and 30GHz frequency bands. This signal is amplified, demultiplexed into individual carriers, frequency downconverted into the 4, 12, and 19 GHz downlink frequency band, amplified and multiplexed into the antenna system.

One of the main advantages of using HTS is to decrease the mass and volume of a microwave filter substantially. This can be achieved by using HTS in intrinsically low Q transmission line resonators such as microstrip or stripline. The cost of communication payload has been estimated to a about£14000/g. Therefore, the mass reduction is very attractive in cost savings. Another important advantage is the reduction in insertion loss of a microwave filter by substituting the metallic conductors with HTS materials in the filter design. The reduction in insertion loss of a resonant structure brings with it an increase in the Q of the circuit, which is a highly desirable effect. This means sharper cut-offs and greater out-band rejection, which could allow for closer packing of frequency channels in a communication system.

10.10 Design of parallel coupled microstrip filter & patterning

The circuit was simulated using standard CAD package (Microwave harmonica). The design was based on two-port capacitively coupled microstrip configuration. Both the feeder lines and the centre line was designed with a characteristic impedance of 50Ω. Since the wavelength and hence frequency of operation has direct implication on the length of the centre bar, this was designed to be approximately half a guided wavelength long. However, this length was constrained by the size of the superconducting 2223 BiPbSrCaCuO films which were 5.5x5.5mm in dimensions.

The signal was applied to the microstrip via co-axial cable. The co-axial connectors were connected to the feeder lines by silver paste.Taking various limitations such as the size of the superconducting films into account a final estimate for the maximum length of the centre bar was given as $l_{trans} \approx 4.4$mm. Thus the operating frequency can be estimated from equation (10.11) by considering the guided wavelength which is a function of free space wavelength and the effective dielectric constant. The minimum operating frequency is thus

$$f_{min} = \frac{c}{2l_{trans}\sqrt{\varepsilon_{eff}}} = 13.5\ \text{GHz} \tag{10.27}$$

Figure 10.13 illustrates schematic diagram of the band-pass microstrip filter.

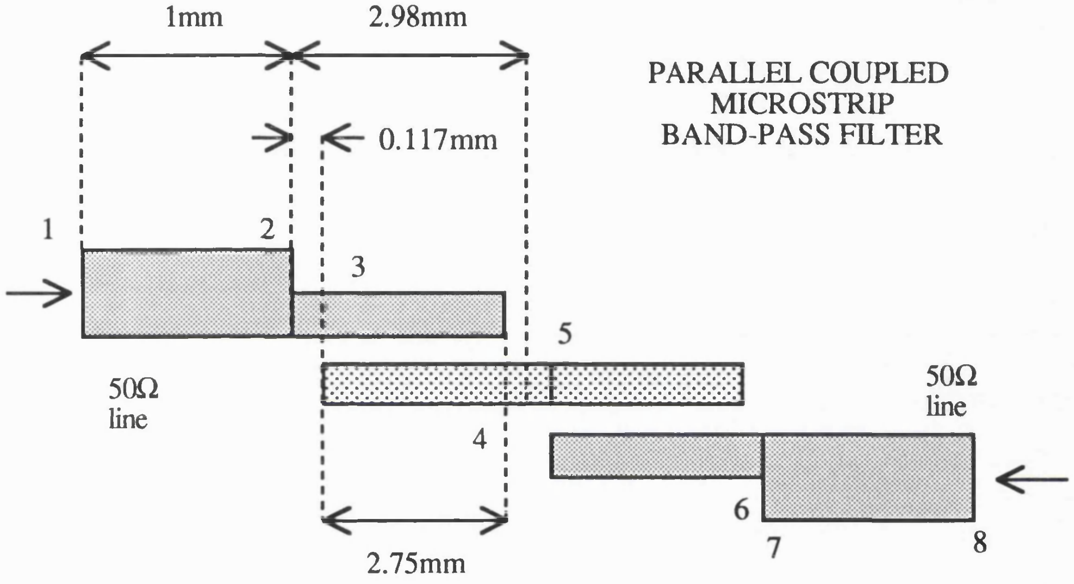

Figure 10.13- *Schematic diagram of parallel coupled microstrip band-pass filter. Note that the layout is symmetrical about the middle of nodes 4 and 5.*

The microwave test jig was home made and designed to take advantage of the maximum continuous length available on the filter. The jig was also designed as small and thin as possible so that upon insertion into liquid nitrogen the jig interior temperature would drop rapidly. Figure 10.14 shows schematic diagram of the band-pass microstrip filter mounted in its jig. In order to check the theoretical design procedure and optimise various parameters the circuit was simulated by using standard CAD package (Microwave Harmonica), an analogue circuit simulation package aimed specifically at high frequency design.

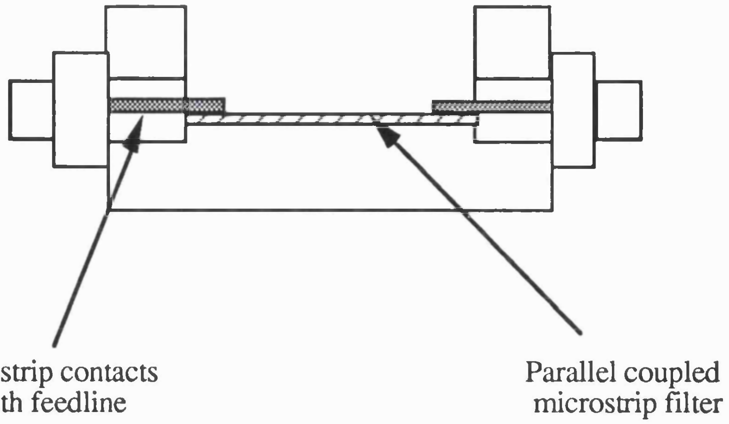

Figure 10.14- *Schematic diagram of BiPbSrCaCuO (2223) parallel coupled microstrip band-pass filter in its jig.*

The parallel coupled microstrip band-pass filter was imposed by photolithography technique on a BiPbSrCaCuO 2223 film deposited on MgO substrate according to the method described earlier. Cr/Au of $\approx 1\mu m$ in thickness was evaporated and electroplated on the back of the MgO substrate to act as the ground plane of the filter. This is a standard process and was done in the clean room. The process involved initial evaporation of thin layer of Cr on the back of MgO substrate followed by evaporation of Au in order to create the necessary adhesion of gold to MgO. This resulted in total film thickness of ≈ 100Å. Finally, more gold was electroplated onto the evaporated layer to bring the total thickness to $\approx 1\mu m$. Idealy the ground plate should also be made of a superconducting material. However, the stringent post-annealing process used for the growth of the 2223 BiPbSrCaCuO thin film did not allow for this.

The proportion of the 2223 phase in the BiPbSrCaCuO film was roughly estimated as 90% (±3%), using the ratio of the (0014) of the 2223 phase peak and the (0012) of the 2212 phase peak from the x-ray diffraction pattern. The corresponding x-ray diffraction pattern and R-T curve of the 2223 film is shown in figure 10.15. The pattern indicates a near single 2223 phase with a high degree of c-axis orientation perpendicular to the substrate. The inset in figure 10.15 shows the resistivity versus temperature of this film with $T_{c,\ onset}$ at 110 K and $T_{c,\ zero}$ at 105.5K.

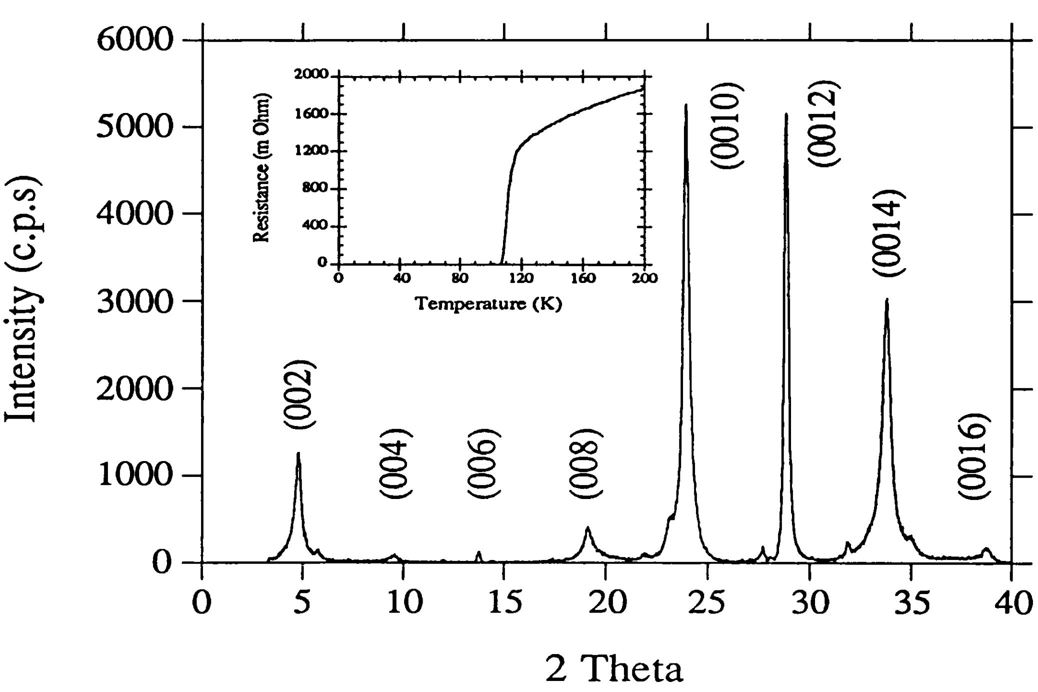

Figure 10.15- *X-ray diffraction pattern of a near BiPbSrCaCuO 2223 single phase grown on MgO substrate. The inset shows its respective resistivity versus temperature with $T_{c,\ onset}$ at 110 K and $T_{c,\ zero}$ at 105.5K.*

10.10 Microstrip filter measurements

Microwave measurements were carried out over a sweep rage of 10-16GHz using a vector network analyser, HP8510A. The frequency source used was a synthesized sweeper. The low temperature measurements of the 2223 BiPbSrCaCuO filter were carried at University College London (Department of Electrical &Electronic Eng) and at the National Physics Laboratory (NPL). The initial measurements were carried out by dipping the jig into a bath of liquid nitrogen at UCL. Figure 10.16 illustrate the computer simulation and the actual output of the network analyser of the filter pattern.

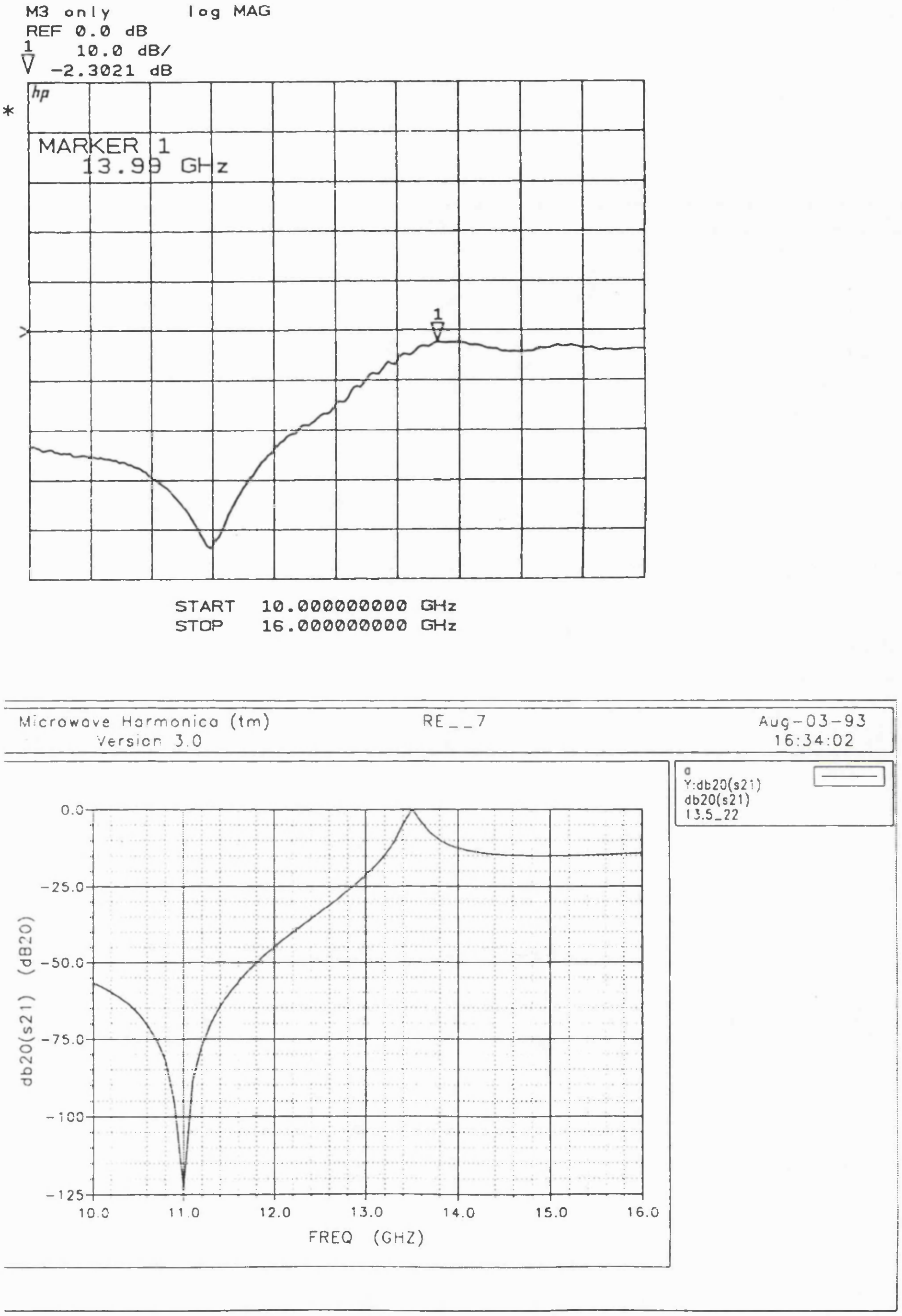

Figures 10.16- *Comparison between the out put analyser and the computer simulation.*

The computer simulation and the actual output of the network analyser of the filter pattern show that the measured response is very similar in shape to the simulated response, though no sharp band-pass response is measured. The most prominent feature of the measured response is the sharp dip at around 11.5GHz which corresponds well to the simulated filter which shows a very sharp dip at 11GHz. However, the magnitude of the dip in the measured response is much smaller than the simulated one. Also, the measured response tails off to a minimum insertion loss of approximately -2dB, at a frequency of 14GHz. Whereas the simulated response indicates that this should rise to zero dB and then settle down to -10dB.

The anomalies between simulated and measured response could be due to a possible leakage fields. This situation arises when the co-ax to the microstrip transition is equally a good radiator as well as a good transition. In this case at high frequencies, the coupling between the two co-ax lines provides an alternative path for the signal. In order to investigate this possibility the computer circuit listing was altered slightly. Two very small value capacitors were incorporated in the circuit, one was placed in parallel with the microstrip and another in parallel with the input line. Figure 10.17 illustrates the new circuit with the two capacitors included. After experimenting with different values, a new simulated response was obtained which is shown in figure 10.18

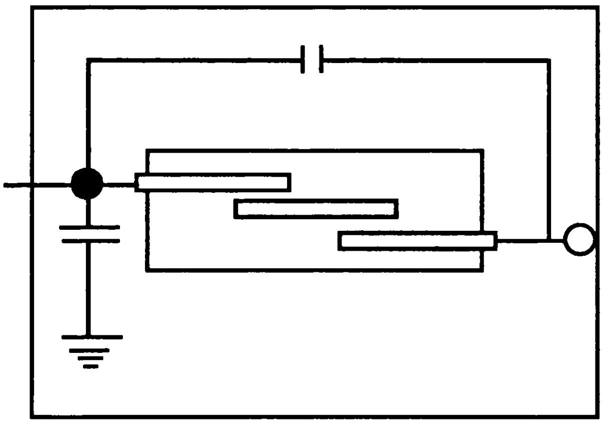

Figure 10.17- *Schematic diagram of the parallel coupled microstrip band-pass filter modelled for high frequency leakage.*

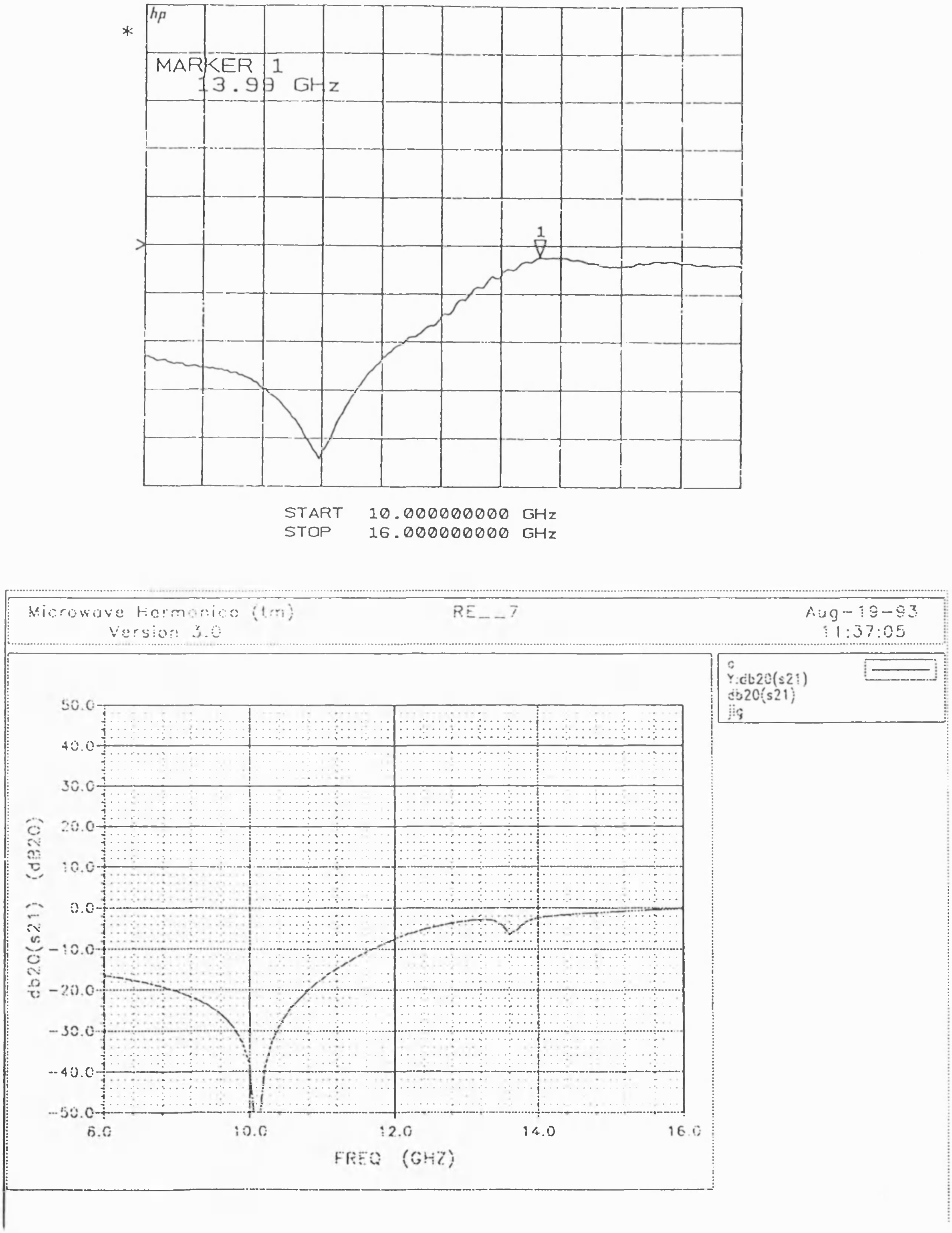

Figure 10.18- *Comparison between the measured response and leakage simulation.*

The figure shows a high frequency roll off as expected. However, the frequency shift is still present. This frequency shift could be due to the radiation from the open end resonator. This is a very well known effet which can be compensated using the CAD package. Interestingly when the axes of the new simulated response are moved to the left, which is equivalent to an upward shift in frequency, the similarity between the new simulated response and the measured response is remarkable. This shows that the microstrip is behaving as expected, and that the problem in measuring the band-pass response at such high frequencies is the main difficulty.

Microwave measurements on the filter were also carried out at NPL, with the help of Prof John Gallop. The jig containing the filter was cooled in a closed circuit liquid helium cryo-cooler from room temperature down to 20K. Table (10.2) summarises the results obtained.

Temperature (K)	Resonance frquency (f_0) GHZ	Δf_0 MHz
30	14	260
53	14.13	263
77	13.99	307

Table (10.2)- *Summarised resonance frequency and half width results for BiPbSrCaCuo (2223) parallel coupled microstrip filter at various temperatures.*

The response of the filter showed increasing half width and a reduction in the resonance peak magnitude with an increase in measured temperature. It also showed the presence of standing waves which is an indication of mismatch between the co-ax connections and the microstrips. The Q value of the filter was calculated to be around 55 from the measured data. The actual measured Q-factor will include conductor and dielectric losses which are accounted for by an unloaded Q-factor, Q_u. Therefore the total measured Q for the resonator is given by

$$\frac{1}{Q}=\frac{1}{Q_u}+\frac{1}{Q_e} \qquad (10.28)$$

The unloaded Q value may be calculated by considering the resonating line [14]. The length of the resonance line is given as $l=\lambda/2=c/2f\sqrt{\varepsilon_{eff}}$. Also, the propagation constant is given as $\beta=2\pi f/v_p=2\pi f\sqrt{\varepsilon_{eff}}/c$. To calculate the Q_u value the attenuation due to conductor loss, α_c, and dielectric loss, α_d, needs to be calculated. The attenuation due to conductor loss is given by

$$\alpha_c=\frac{R_s}{Z_0 w} \qquad (10.29)$$

and the attenuation due to dielectric loss is given by

$$\alpha_d=\frac{K_0\varepsilon_r(\varepsilon_e-1)\tan\delta}{2(\varepsilon_r-1)\sqrt{\varepsilon_e}} \qquad (10.30)$$

where $K_0=2\pi f/c$, ε_{eff} is the effective dielectric constant, $\tan\delta$ is the loss tangent, and R_s is the film's surface resistance. The attenuation due to conductor loss and dielectric loss is $\alpha=\alpha_c+\alpha_d$. The unloaded Q value is then given by

$$Q=\frac{\beta}{2\alpha} \qquad (10.31)$$

The surface resistance of the 2223 BiPbSrCaCuO film is unknown. However, by using the surface resistance value of YBaCuO film, shown in figure 10.12, it is conceivable to work out an approximate value for the unloaded Q value. Using the above equations the unloaded Q is found to be 7900.

10.11 Conclusion

BiPbSrCaCuO films patterned by wet chemical etching in EDTA did not show any sign of degradation in terms of crystalinity or electrical properties. This technique can be recommended for future patterning of superconducting films where control etching of the film is required. The parallel coupled microstrip filter was the first filter developed on BiPbSrCaCuO (2223) thin film. The computer simulation and the actual output of the network analyser of the filter showed that the measured response was very similar in shape to the simulated response, though no sharp band-pass response was measured. The anomalies between simulated and measured response was attributed to the leakage fields.

References

1- S. T. Ruggiero and D. A. Rudman. Superconducting Devices, (1990).
2- T. C. Edwards. Foundation for microstrip circuits, Wiley & Sons Publication, (1981).
3- D. J. Cracknell. GEC Journal of Research, vol 9 (3), (1992), 155-165.
4- A. Inam, X. D. Wu, T. Venkatesan, S. B. Ogale, C. C. Chang, and D. Dijkkamp. Appl. Phys. Lett. 51 (14), (1987), 1112-1114.
5- N. Khare, A. K. Gupta, D. K. Walia, V. S. Tomar, V. N. Ojha, H. C. Pandey, S. K. Bhatnagar, and Y.K. Jain. Supercon. Sci. Technol. 3 (1990), 191-193.
6- H. Schneidewind, J. Arnold, J. Borck, U. Hubner, S. Linzen, F. Schmidl, T. Schuler, P. Seidel. "Private communication".
7- R. Yusa, M. Nakao, S. Fujiwara, K. Kaneda, S. Suzuki, and A. Mizukami, Extended abstract of fifth Int. Workshop On Future Electron Devices, 245, (1988).
8- T. Oohira, S. Sakai, Y. Kasai, N. Atoda, and K. Shimizu. Jpn. J. Appl. Phys. 30 (3A), (1991), L355-L357.
9- G. C. Hilton, P. A. Polakos, C. E. Rice. Appl. Phys. Lett. 55, (1989), 495.
10- F. K. Shokoohi, L. M. Schiavone, C. T. Rogers, A. Inam, X. D. Wu, L. Nazar, and T. Venkatesan. Appl. Phys. Lett. 55 (25), (1989), 2661-2663.
11- J. Muller. PhD thesis, Imperial College, London, (1993).
12- Microwave Filters, edited by G. L. Matthaei, L. Young, E. M. T. Jones. McGraw-Hill Book Company, (1964).
13- S. Akhtarzad, T. R. Rowbotham, P. B. Jones. IEEE, Trans, MTT-23, No6, (1975), 486-492.
14- D. M. Pozar. Microwave Engineering, Addison-Wesley, (1990).

Chapter 11

Conclusions and Future Work Suggestions

In this chapter the general conclusions to this thesis is presented and the key results obtained during the course of this research project are high lighted.

11.1 Conclusions

In this thesis growth and properties of high temperature superconducting thin films of the $Bi_2Sr_2Ca_{n-1}Cu_nO_{4+2n+\delta}$ system deposited with pulsed laser deposition (PLD) technique have been investigated. Research efforts were concentrated on the thin film growth of the 2212 phase and in particular the 2223 phase of this system.

PLD is one of the main thin film growth techniques increasingly being used now a days for the growth of high temperature superconductors (HTS). However, in order to deposit high temperature superconducting films uniformly over large areas a new deposition geometry was developed. The suggested geometry was to simply tilt the target away from its normal horizontal position and hence create an angle of wobble on the target. Detailed mathematical modelling with supporting experimental results of the geometry has been presented, that produces homogenous films over an area of several square centimetres. The film uniformity and thickness, however, has been shown to be dependent on the angle of tilt, θ, and the substrate-target distance, **a**. For instance, it has been shown that for $\theta=0°$ the data was consistent with a $\cos^{10}\phi$ distribution over the central region of the substrate. As θ was increased a wider area in uniformity was obtained over this region. Also, film uniformity increased with larger substrate-target distance. However, this resulted in a reduction in film thickness.

Both ex-situ and in-situ thin film growth of the 2212 phase of the $Bi_2Sr_2Ca_{n-1}Cu_nO_{4+2n+\delta}$ system by PLD has been investigated. In the ex-situ process, growth parameters such as annealing temperature and duration, and for in-situ process, oxygen pressure and substrate temperature, have been optimised. It has been shown that with both processes 2212 films could be grown on MgO (001) oriented substrates. With ex-situ process the annealing temperature is crucial for obtaining a highly c-axis 2212 film. Also, the superconducting properties of the films improves substantially with increasing annealing period. For instance, the XRD pattern of the film annealed at 845°C showed an almost pure 2212 phase, however, the zero resistance value of this film did not exceed 65K, which is 15K below the ideal value (80K) for the 2212 phase. By annealing the film next to the pellet for 16 hours at 840°C the zero resistivity increased to 80K with the XRD pattern showing a highly c-axis oriented film. The critical current density of this film measured by magnetic technique was found to be 1000 A/cm^2 in zero field at 70K.

With in-situ processing phase control of BiPbSrCaCuO films is possible by varying the substrate temperature and oxygen pressure. For instance, BiPbSrCaCuO films deposited in the temperature range of 660-740°C under oxygen pressure of 2x10^{-2}mbar showed mixed phases of 2201/2212, with the 2201 phase being the main constituent. At substrate temperatures of 720-740°C range and oxygen pressures of 0.06-0.08mbar both phases were still present, however, in this region the 2212 phase was the main constituent. This pattern continued with increase in oxygen pressure and at pressures of around 0.1mbar a pure 2212 film was obtained. Keeping the substrate temperature constant whilst increasing the oxygen pressure further resulted in the formation of BiPbSrCaCuO mixed films of 2201/2212. The oxygen partial pressure-substrate temperature phase diagram for BiPbSrCaCuO films indicated that in order to obtain a pure c-axis 2212 BiPbSrCaCuO films both substrate temperature and oxygen pressure should be optimised. However, the conditions required for the growth of the crystalline 2212 phase did not necessary correspond to the conditions needed for superconductivity of the film. This therefore entails adjustment of the target composition for a set of deposition parameters that yield superconductivity as well as crystallinity.

The 2223 phase of the $Bi_2Sr_2Ca_{n-1}Cu_nO_{4+2n+\delta}$ system has especially attracted the attention of the scientific community for its high T_c (110K). The growth of 2223 in pure form, however, has not been an easy task due to a number constraints associated with this phase which were out lined in chapter eight. In the initial programme of thin film growth of the 2223 phase, BiPbSrCaCuO films were deposited on MgO substrates from a single (BiPb)SrCaCuO target. However, this approach was not effective in obtaining a high proportion of the 2223 phase (> 50%), due to the evaporation of Pb at an early annealing stages from the film (due to low melting point and high vapour pressure of Pb). To overcome this problem an approach of depositing multilayers of PbO between several layers of BiPbSrCaCuO has been utilised. Using the multilayered (BiPb)SrCaCuO/PbO technique Pb could in sufficient quantity be doped in the BiSrCaCuO films to facilitate the growth of the 2223 phase. With this multilayered method, superconducting $Bi_2Sr_2Ca_2Cu_3O_{10+\delta}$ films containing more than 85% 2223 phase could be grown by annealing at 854°C for 15 hours in air.

Several key conclusions have been drawn from the results presented in this study. It has been demonstrated that addition of Pb was essential for the formation of the 2223 phase in high proportions. The use of Pb was found to lower the formation temperature of the 2223 phase and the melting temperature of the $Bi_2Sr_2Ca_2Cu_3O_{10+\delta}$ films. The effect of target composition on the thin film growth of the 2223 phase indicated that an excess Ca and Cu over the stoichiometric composition has been effective in promoting the formation of the 2223 phase significantly, however, excess Cu was found to also favour the formation of the $(Sr_{14-x,}Ca_x)Cu_{24}O_{41-y}$ phase. This indicated that in order to grow thin films of the 2223 phase without the impurity phase it is essential to optimise the starting composition.

It has been demonstrated that the growth of the 2223 phase strongly depends on the annealing temperature and duration and that the temperature range in which the 2223 phase is preferentially produced was exceedingly narrow, being 854°C (±1°C) for 15 hours in air. At temperatures higher than 854°C or for annealing temperatures longer than 15 hours the 2223 phase decomposes to form the 2212 phase and a Bi deficient phase. The presence of the 2212 phase in the microstructure of the films even under the optimum conditions, demonstrated that the 2223 and the 2212 phases can coexist thermodynamically. Annealing the multilayered films in $Ar:O_2$ lowered the melting point of the BiPbSrCaCuO films considerably. Also, the re-annealing of the BiPbSrCaCuO films containing a high proportion of the $(Sr_{14-x,}Ca_x)Cu_{24}O_{41-y}$ phase in $Ar:O_2$ atmosphere illustrated that the $(Sr_{14-x,}Ca_x)Cu_{24}O_{41-y}$ phase is unstable in a low oxygen atmosphere.

The critical current density of the pulsed laser deposited 2223 BiPbSrCaCuO films measured by the magnetic technique using VSM were found to be as high as $3.7x10^3$ and

1.0×10^4 A/cm^2, in zero field at 70K which were comparable to the values obtained by other groups reported in recent literature. It has been found that the proportion of the $(Sr,Ca)_{14}Cu_{24}O_{41}$ phase in the films lowered the length scale value and hence the critical current density of the films.

The successful patterning of 2212 and 2223 films by wet etching process (EDTA) for devise application has been demonstrated in chapter ten. Also, the design and development of a superconducting microstrip filter for space applications using the 2223 films has been attempted. Although the devise did not fully show the filter characteristic, the measured response was very similar in shape to the simulated response, though no sharp band-pass response was measured.

11.2 Suggestions for further work

(a) Growth of the 2212 thin films

Thin films of the 2212 phase have been grown by ex-situ and in-situ processes using a Nd-YAG laser operating at 532nm. The next step is to use stronger oxidizing agents such as ozone and N_2O instead of O_2 as the growth medium. Also, in-situ techniques such as RHEED and XPS could be used to investigate the growth mechanism of the films. In-situ RHEED could be used to monitor the crystal growth and XPS could be used to monitor the oxidation states of the elements.

(b) Growth of the 2223 thin films

It has been clearly demonstrated that a dependence exist between the starting composition and the volume fraction of the 2223 phase in the film. It has been shown that a target of $Bi_{1.7}Pb_{0.4}Sr_{1.6}Ca_{2.4}Cu_{3.6}O_x$ composition produces acceptable films containing >85% 2223 phase with the rest being 2212 and $(Sr_{14-x},Ca_x)Cu_{24}O_{41-y}$ phases. However, it would be interesting to investigate stoichiometries close to this one in order to isolate the optimum composition of the target.

(c) Superconducting devices

The small dimensions of the superconducting BiPbSrCaCuo (2223) films only supports high frequency circuits which can cause problems in measurements. An alternative approach would be to design miniature structures such as hair pin resonators. These circuits take up less space for a given frequency.